Base cation mass budgets and stable isotope ratios of Mg along a 127-year glacial retreat chronosequence in the subtropical Hailuogou region

Zur Erlangung des akademischen Grades einer
DOKTORIN DER NATURWISSENSCHAFTEN (Dr. rer. nat.)
von der KIT-Fakultät für
Bauingenieur-, Geo- und Umweltwissenschaften des

Karlsruher Instituts für Technologie (KIT)
genehmigte

DISSERTATION

von

Nuria Basdediós Prieto

Tag der mündlichen Prüfung: 05.07.2023

Referent: Prof. Dr. Wolfgang Wilcke
Korreferent: Prof. Dr. Moritz Bigalke

Karlsruhe (2023)

Contents

Acknowledgments

I would like to express my gratitude to all people who have helped and supported me along this journey.

First of all, I am indebted to Wolfgang Wilcke for providing guidance and continuous feedback throughout this project, and for his unwavering support and belief in me. I would like to extend my sincere thanks to Yanhong Wu for his continuous support.

Thanks to Z. Zhong for her indefatigable assistance during my stay in China, as well as J. Wang, H. Bing, J. Zhou, Q. He and numerous students of the Chinese Academy of Science, not only for their support in the field, but also for introducing me to the fascinating Chinese culture and traditions.

I am grateful to all my working colleagues in the Soil Science Group of the Institute of Geography and Geoecology, both those who accompanied me all along the entire way and those who only shared a stretch. Thanks to Bastian, Stefan and Esthela, my office colleagues, for motivating me every day, and to Pablo and José for sharing so many feedback sessions and nice time. I am also grateful to Tobias W. for patiently introducing me to soil sampling, to Martin K. for his constant support during my work at the Westhochschule, to Aiaz for being a tireless learner and for accompanying me during long hours in the clean-air lab, and to Andre and Tobias F. for their assistance during so many late-night sessions at the FZU lab. I'd like to recognize Sophia, Soni, Svenja, Eva, Peter, Melanie, Benjamin, Simon, and all other former members of the working group, because from each of them I had always something to learn. I am also thankful to Rita and Petra for their kind assistance with every administrative task. Thanks also go to Armin Zeh for showing me so patiently how to identify minerals under the microscope, to Stephan Unrein for providing the thin sections and explaining how they are prepared, and to all my colleagues from the Vegetation Science Group and the Human Geography Group for all cherished time we spent together.

My gratitude extends to all members of the Soil Science group at the Institute of Geography at the University of Bern, Switzerland, for welcoming me during my research stay and making me feel like at home from the very first day: Moritz, Sabman, Alex, Evelyne, Anna, Jaime, Adrien, Miquel, Lorenz, Teresa, Martin I., Hang, Klaus, Milo, Patrick, Daniela,… not forgetting Isabella and Marlis, for all their administrative support.

I acknowledge the funding of the Deutsche Forschungsgemeinschaft (DFG, Wi 1601/25-1) and the Karlsruhe House of Young Scientists (KHYS) which enabled my research at the University of Bern during three months.

I would like to acknowledge all my friends for their continuous motivation and their interest in my research. Special thanks to Diego, for inspiring me to start this adventure, and to Rene, Zeynep and Patrick, for becoming my family during my time in Karlsruhe.

Last but not least, my appreciation also goes to my parents, Antonio and Esther, and my sister, Ana, for their continuous encouragement and support all through my studies.

Summary

Many glaciers in high mountain areas all over the world are retreating because of the increasing temperatures. Following glacial retreat, glacial debris is continuously deposited in the whole retreat area allowing us to study early soil and ecosystem development with a space-for-time substitution approach. Fast vegetation succession in the globally expanding glacial retreat areas helps to prevent mountain risks such as landslides, erosion, or flooding. Although pioneer plants usually start colonizing young surfaces a few years after glacier melt, it usually takes various decades, if not centuries, to develop a full vegetation cover. Surprisingly, in the subtropical Hailuogou glacial retreat area (ca. 3000 m a.s.l., 1950 mm precipitation, mean annual temperature 4.2 °C), Sichuan, southwest China, a development from bare soil to full coniferous forest occurred in only 80 yr. A striking difference to many other glacial retreat areas, where vegetation development is slow, is the presence of a low concentration of carbonates in the mainly granitic moraine material, which are dissolved in ~50 yr.

In this thesis, I studied a possible link between soil properties and vegetation development along the Hailuogou glacial retreat chronosequence. To this end, I (i) evaluated a possible relationship between base metal (Ca, Mg, K and Na) supply and vegetation establishment, (ii) determined soil and plant base metal stocks, (iii) estimated the size of the main base metal fluxes, (iv) characterized the composition of the glacial debris to elucidate the sources of base cations, (v) determined the base cation release kinetics from topsoils along the chronosequence with a weathering experiment, and (vi) measured stable Mg isotope ratios in different compartments.

Total ecosystem Ca and Mg stocks decreased along the chronosequence, while those of K and Na were unrelated with ecosystem age. The decrease in Ca and Mg stocks mostly occurred during the first 47 years, when Ca and Mg were leached at rates of 130±10.6 and 35±3.1 g m^{-2} $year^{-1}$, respectively. Carbonate weathering determined the rapid initial Ca release but not that of Mg, which was attributed to the weathering of silicate minerals. The base cation release kinetics in the mineral soil followed the order Ca>>Mg>K>>Na. The initial high Ca bioavailability because of the moderately alkaline soil pH and carbonate depletion, together with the dissolution of easily-weatherable silicates providing enough Mg and K to the pioneer vegetation, contributed to the rapid establishment of a deciduous forest in less than 47 years. After the carbonates were leached, the net weathering rates decreased because less soluble minerals remained in the soil, which occurred in line with the vegetation change from deciduous to coniferous trees and their associated lower nutrient demand and slower nutrient cycle. The Mg depletion rate from the mineral topsoil along the chronosequence could be traced by the measurement of Mg isotope ratios, which could also be used to identify chlorite as the major source of the fast initial Mg loss.

My results suggest that the well synchronized interplay between carbonate and silicate weathering facilitated the fast vegetation succession along the glacial retreat chronosequence. In addition, I found that Mg isotope ratios can be used to estimate Mg loss rates from the topsoil during the early phase of soil development and to identify the sources of this loss.

Zusammenfassung

Weltweit ziehen sich Gletscher in Hochgebirgsregionen aufgrund steigender Temperaturen zurück. In ihrem Rückzugsgebiet hinterlassen sie Till, auf dem sich ein neues Ökosystem entwickelt. Die Entwicklung der Ökosystem-Sukzession kann mit Hilfe der Raum-für-Zeit-Substitution untersucht werden. Eine schnelle Vegetationssukzession in den global größer werdenden Gletscherrückzugsgebieten verringert Gebirgsrisiken wie Erdrutsche, Erosion oder Überschwemmungen. Obwohl sich in der Regel bereits wenige Jahre nach der Gletscherschmelze Pionierpflanzen auf den jungen Rückzugsflächen ansiedeln, dauert es oft Jahrzehnte, wenn nicht Jahrhunderte, bis sich eine vollständige Vegetationsdecke entwickelt hat. Überraschenderweise hat sich im von mir untersuchten subtropischen Hailuogou-Gletscherrückzugsgebiet (ca. 3000 m ü. NN, 1950 mm Niederschlag, Jahresmitteltemperatur 4,2 °C) in Sichuan, Südwestchina in nur 80 Jahren ein reifer Nadelwald entwickelt. Ein auffälliger Unterschied zu vielen anderen Gletscherrückzugsgebieten, in denen sich die Vegetation langsam entwickelt, ist die Präsenz eines niedrigen Karbonat-Gehalts im überwiegend granitischen Moränenmaterial Diese Karbonate werden innerhalb von ca. 50 Jahren aufgelöst.

In meiner Dissertation habe ich einen möglichen Zusammenhang zwischen den Bodeneigenschaften und der schnellen Vegetationsentwicklung entlang der Hailuogou-Chronosequenz untersucht. Dazu habe ich (i) einen möglichen Zusammenhang zwischen der Freisetzung von basischen Kationen (Ca, Mg, K und Na) und der Vegetationsentwicklung untersucht, (ii) die Vorräte an basischen Kationen im Boden und in den Pflanzen bestimmt, (iii) die wichtigsten Flüsse der basischen Kationen quantifiziert, (iv) die Zusammensetzung des Tills untersucht, um die Mineral-Quellen der basische Kationen zu identifizieren, (v) die Freisetzungskinetik der basischen Kationen aus den Oberböden entlang der Chronosequenz mit einem Verwitterungsexperiment bestimmt und (vi) stabile Mg-Isotopenverhältnisse in verschiedenen Kompartimenten entlang der Chronosequenz gemessen.

Die Gesamtvorräte an Ca und Mg im Ökosystem nahmen entlang der Chronosequenz ab, während die Vorräte an K und Na nicht mit dem Alter des Ökosystems zusammenhingen. Der Rückgang der Ca- und Mg-Vorräte erfolgte hauptsächlich in den ersten 47 Jahren, in denen Ca und Mg mit Raten von 130±10,6 und 35±3,1 g m^{-2} $Jahr^{-1}$ ausgewaschen wurden. Die Karbonatverwitterung war für die rasche anfängliche Freisetzung von Ca, nicht aber von Mg verantwortlich. Die schnelle anfängliche Freisetzung von Mg erfolgte aus leicht verwitterbaren Silikaten. Die Kinetik der Freisetzung von basischen Kationen im Mineralboden folgte der Reihenfolge Ca>>Mg>K>>Na. Die anfänglich hohe Ca-Bioverfügbarkeit aufgrund des mäßig alkalischen pH-Werts des Bodens und der Karbonatauswaschung trugen zusammen mit der Auflösung von leicht verwitterbaren Silikaten, die der Pioniervegetation genügend Mg und K lieferten, zur raschen Etablierung eines Laubwaldes in weniger als 47 Jahren bei. Nach der Auswaschung der Karbonate nahmen die Nettoverwitterungsraten ab, weil weniger lösliche Mineralien im Boden verblieben, was mit dem Vegetationswechsel von Laub- zu Nadelbäumen und dem damit verbundenen geringeren Nährstoffbedarf und langsameren Nährstoffkreislauf zusammenhing. Die Mg-Verarmungsrate aus dem mineralischen Oberboden entlang der Chronosequenz konnte durch die Messung von Mg-Isotopenverhältnissen nachvollzogen

werden, mit deren Hilfe außerdem Chlorit als Hauptquelle der anfänglich schnellen Mg-Freisetzung identifiziert wurde.

Meine Ergebnisse deuten darauf hin, dass das gut synchronisierte Zusammenspiel von Karbonat- und Silikatverwitterung die schnelle Vegetationssukzession entlang der untersuchten Gletscherrückzugs-Chronosequenz ermöglicht hat. Außerdem fand ich, dass die Mg-Isotopenverhältnisse die Schätzung der Mg-Verluste aus dem Oberboden während der frühen Phase der Bodenentwicklung ermöglichen und verwendet werden können, um die Mineral-Quellen des Mg-Verlustes zu identifizieren.

List of tables

List of figures

List of abbreviations

AAS	atomic absorption spectroscopy
ANOVA	analysis of variance
a.s.l.	above sea level
B_C	biomass of the ecosystem compartment *c*
BCR	basalt of the Columbia river (reference material)
BD	bulk density
BDep	bulk deposition
ca.	lat. circa, i.e., approximately
CRM	certified reference material
DD	dry deposition
DI	deionized water
ECEC	effective cation-exchange capacity
Eq	equation
Fig	figure
HSD	honestly significant difference
ICP	inductively-coupled plasma
k_a	rate constant (h^{-1}) of Pool A
k_b	rate constant (h^{-1}) of Pool B
LIA	little ice age
LOI	loss on ignition
MC-ICP-MS	multicollector inductively-coupled plasma mass spectrometer
MS	mass spectrometer
NIST	National Institute of Standards and Technology
OES	optical emission spectroscopy
PE	polyethylene
pH_{stat}	method to measure the base cation release kinetics at a constant pH
Pool A	estimate of the fast-reacting pool (mg kg^{-1})
Pool B	estimate of the slow-reacting pool (mg kg^{-1})
Pr	precipitation (L m^{-2} $year^{-1}$ = mm)
SD	standard deviation
SRM	standard reference material

SW	southwest
t	time
T_i	thickness of the horizon *i*
TD	total deposition
VDV	vertical dual view

A. Summarizing overview

1. Introduction

The ongoing increase in global average temperatures since the end of the Little Ice Age (LIA; IPCC 2021) have resulted in the retreat of high mountain glaciers from polar to tropical regions in the past few decades. Particularly, the rate at which glaciers outside ice sheet peripheries (i.e., Antarctica and Greenland) are retreating has doubled over the past two decades (Hugonnet et al. 2021). Glacial retreat is expected to continue during the twenty-first century (Hock et al. 2019; Nogués-Bravo et al. 2007). Following glacial retreat, glacial debris is continuously deposited in the retreat areas serving as new substrate for soil and ecosystem development. The abundance of unconsolidated material and the lack of a vegetation cover render these regions especially susceptible to natural hazards such as landslides, debris flows and erosion, and water risks such as flooding and sediment loading of rivers, mainly derived from the lack of transpiration, higher surface runoff and reduced infiltration on the newly formed bare soil areas. Thus, the knowledge of the processes that drive vegetation succession is crucial to cope with the risks originating from the globally increasing glacial retreat areas.

Chronosequences and associated space-for-time substitution approaches consist of a set of sites formed on similar parent materials and relief developing under the same climatic conditions, that differ in the time since they were formed (soil age), so that the observed changes can be interpreted as a sole consequence of the different ages (Schaetzl and Anderson 2005; Walker et al. 2010). This approach has been widely used in the past years for studying temporal dynamics of soil development and plant succession across multiple time scales and many landscapes (Bockheim 1980; Huggett 1998; Walker et al. 2010).

For the subtropical Gongga region, a remote location in the Chinese Province of Sichuan on the eastern rim of the Tibetan plateau, Wu et al. (2013) have shown that the annual precipitation decreased while the annual mean temperature increased in the past two decades. This resulted in the retreat of the Hailuogou glacier, one of the largest glaciers at the foot of the Gongga Mountain (summit: 7,556 m a.s.l.; Zhou et al. 2013). The Gongga massif is mainly composed of a granitoid complex (i.e., granite and granodiorite) intruded into the Palaeozoic-Triassic meta-sediments and meta-volcanic rocks of the Songpan-Ganze terrane (Roger et al. 1995; Searle et al. 2016). Many young primary successions developed under different climates are dominated by pioneer mosses, dwarf shrubs and shrubs but lack fully developed forests (see compilation of studies in **Table B-S1**).

However, the primary succession developing along the Hailuogou glacial retreat area has surprisingly achieved the average biomass estimated for mature temperate coniferous forests (307 tones ha^{-1}, Cole and Rapp 1981) within a period of only ~80 years (Luo et al. 2004).

Previous research on biologically relevant elements in the Hailuogou region have mainly focused on the change in C, N and P concentrations, stoichiometric ratios and stocks (e.g., Bing et al. 2016, He and Tang 2008; Wu et al. 2015; Yang et al. 2021; Zhang et al. 2021; Zhou et al. 2013). Although N and P are considered the most commonly limiting nutrients affecting biomass production in terrestrial ecosystems (Elser et al. 2007; LeBauer and Treseder 2008; Vitousek and Howarth 1991; Lei et al. 2021; Yang et al. 2021), previous studies have also shown that Ca, Mg and K can have a great influence on tree growth and vegetation development (Baribault et al. 2012; Burstrom 1968; Epron et al. 2012; Federer et al. 1989; McLaughlin and Wimmer 1999; Paoli and Curran 2007; Wright et al. 2011).

The mobilization of nutrients from parent materials by chemical weathering plays a key role in vegetation succession (Chadwick et al. 1999). Among the rock-bound elements, calcium (Ca), magnesium (Mg) and potassium (K) are three macronutrients with crucial physiological and structural functions in plants. Calcium is needed by all plants for the formation of cell walls and cell membranes, controlling the mechanisms of plant growth and development (Wyn Jones and Lunt 1967; Burstrom 1968). Magnesium is required mainly for chlorophyll and protein synthesis, as well as enzyme activation, while K promotes metabolism, is needed for photosynthesis and participates in regulating water flow for stomatal aperture in leaves (Epron et al. 2015, Tränker et al. 2018). Sodium (Na) can also be taken up and used by plants (Amtmann and Sanders 1999). Sodium regulates cellular osmotic balance of microorganisms and thereby influences the decomposition of soil organic matter (Jia et al. 2015; Kaspari et al. 2009, 2014) and the resupply of bioavailable mineral nutrients. However, at high concentrations in soil (>1 mg kg^{-1}; Marschner 2012) Na can hinder plant growth, interfere with K and Ca nutrition and disturb efficient stomatal regulation (Tavakkoli et al. 2010). Moreover, high concentrations of any of these elements (i.e., Ca, Mg, K and/or Na) can lower or even inhibit the uptake of the others, which is known as cationic antagonistic effect (Diem and Godbold 1993; Ertiftik and Zengin 2017; Fageria 1983; Rhodes et al. 2018). During mineral weathering processes, these elements are released from minerals to soil solution as cations, which can readily move between the various geochemical and biological reservoirs and be lost with stream

water (Fantle and Tipper 2014). Plants influence the biogeochemical cycle of nutrients by affecting their bioavailability in soils, taking up nutrients from the soil solution via their roots and their associations with mycorrhiza, storing them in tissues, and finally returning them to the soil system and to streams via canopy leaching, litterfall, and organic matter decomposition (Vogt et al. 1986). The formation of a soil organic layer on top of the mineral soil also plays an important role in forest nutrition, because it stores nutrients which can be slowly released and reiteratively taken up by plants (Lilienfein et al. 2001; Wilcke et al. 2002).

The elemental analysis of different tree and plant compartments (i.e., bark, wood, branches, roots and leaves/needles) and organic and mineral soil horizons, complemented with measurements of tree biomass, bulk density of the soils, and thickness of the soil horizons allow us to calculate elemental budgets and to estimate element fluxes at each ecosystem age, and to study their development with time by applying a space-for-time substitution.

Batch and column techniques are widely used to examine buffer capacities and reaction kinetics of soils (e.g., Alt et al. 2013; Hacker et al. 2017; Selim and Amacher 1997). Frequently, the analyzed mineral material is exposed to a constant elevated H^+ pressure in so-called pH_{stat} experiments, which can be realized as a batch experiment with ion exchangers or in automatic titroprocessors. In experiments with tritroprocessors, the released ions accumulate in the solution with the risk that secondary mineral precipitation occurs if dissolution constants are surpassed. However, in the pH_{stat} method of Kaupenjohann and Wilcke (1995) ions are released into solution during H^+ buffering at constant pH and immediately removed from the system using ion exchange resins, not affecting further reactions (Alt et al. 2013; Hacker et al. 2017; Schwarz et al. 1999). Süsser (1987) described buffer reactions in soils during pH_{stat} experiments as the sum of two independent reactions both following first order kinetics. This allows to distinguish a fast- and a slow-reacting mineral pool and the release rate constants associated to each of them by applying a nonlinear regression model. The combination of this approach with our space-for-time substitution allows us to study the change in pool size and the base cation release kinetics all along the glacial retreat area.

Furthermore, the access to the stable isotope ratios of "non-traditional" isotopes (i.e., isotopes beyond C, H, O, N, and S), which became increasingly available in the beginning

of this century, offers the opportunity to deepen our understanding of the processes underlying temporal changes such as weathering and the mobilization of nutrients into the biotic cycles. As one of the most abundant elements in the Earth's continental crust, magnesium (Mg) is widely distributed among the lithosphere, hydrosphere, and biosphere (Rudnick and Gao, 2003; Taylor and McLennan, 1985). Three stable Mg isotopes exist in nature: ^{24}Mg (79%), ^{25}Mg (10%) and ^{26}Mg (11%) (Mejia et al. 2013), which are fractionated through diverse processes, such as weathering of the continental crust (Pogge von Strandmann et al. 2008; Teng et al. 2010; Tipper et al. 2006), Mg incorporation in secondary Mg-bearing minerals (Opfergelt et al. 2012), magma differentiation (Teng et al. 2007; Richter et al. 2008; Ryu et al. 2011), plant uptake (Black et al. 2008; Bolou-Bi et al. 2010), or chlorophyll biosynthesis (Black et al. 2006). The resulting natural variation in Mg isotope ratios of different mineral and ecosystem pools may be used to elucidate the origin of Mg pools with different isotopic composition and to trace ecosystem processes.

Different dissolution rates of the diverse minerals in the parent material of soils have also an effect on the fractionation of Mg isotopes in soil through weathering. Previous studies showed that rivers draining carbonate watersheds have a similar Mg isotope composition as the carbonate bedrock (Galy et al. 2002; Tipper et al. 2008), while Mg in watersheds draining silicate bedrock, which dissolves more slowly (Lasaga 1984), is usually isotopically lighter (Brenot et al. 2008, Lee et al. 2014; Tipper et al. 2008). Conversely, some studies reported that during silicate weathering lighter Mg isotopes are preferentially incorporated into secondary phases (e.g., Pogge von Strandmann et al. 2008; Wimpenny et al. 2010) resulting in higher δ^{26}Mg values in solution. This suggests that the direction of Mg isotope fractionation during weathering might depend on the dissolution and formation of specific minerals (Pogge von Strandmann et al. 2008; Hindshaw et al. 2019, 2020). The Mg isotope fractionation associated with cation exchange in soil leaves isotopically light Mg in the exchangeable Mg pool because of the preferential removal of heavy Mg isotopes during adsorption-desorption processes (e.g., Gao et al. 2018; Huang et al. 2012; Opfergelt et al. 2014).

Likewise, Mg isotopes are fractionated during plant uptake and during Mg retranslocation through the various plant compartments. Typically, the Mg in plant roots is isotopically heavier than in the soil solution, while the light Mg isotopes are preferentially incorporated into chlorophyll and thus accumulate in leaves and shoots (Black et al. 2008;

Bolou-Bi et al. 2010, 2012). The return of this isotopically light Mg pools via litterfall can influence the Mg isotopic composition of the topsoils.

The overall goal of this thesis was to improve the understanding of the drivers of vegetation development on glacial debris. To this end, I addressed the following research questions:

(1) Is there a link between base metal (Ca, Mg, K and Na) supply and vegetation establishment along the 127-year Hailuogou glacial retreat chronosequence? (**Section B**)

(2) Which are the main base metal sources and how are base metals released along the Hailuogou chronosequence? (**Sections B and C**)

(3) Can stable Mg isotope ratios be used to elucidate the mineral sources of Mg release by weathering and as tracer of Mg loss from the soil? (**Section D**)

(4) Do stable Mg isotope ratios in ecosystem compartments reflect the increasing incorporation of Mg into biotic cycles with advancing vegetation succession? (**Section 3.4**)

2. Materials and methods

2.1. Study area and field sampling

Located on the eastern slope of the Gongga Mountain, in the transition zone of the Sichuan Basin and the Tibetan Plateau (southwest China), the Hailuogou Glacier has markedly retreated since late 19th century (Li et al. 2010), developing a 2 km long and 50–200 m wide chronosequence, which spans an elevational range from 2800 to 2950 m a.s.l. (**Figure A-1**). The parent material of soil formation is moraine and consists mainly of a mixture of silicates (87%), including plagioclase (28.5%), quartz (24.5%), biotite (12%), hornblende (12%) and K-feldspar (10%), carbonates (<10%), and a minor contribution of apatite (<2.1%) (Yang et al. 2015; Zhou et al. 2016a). The short time of pedogenesis (<130 years) formed soils without B horizon classified from youngest to oldest as Leptic Calcaric to Folic Dystric Regosols (IUSS Working Group WRB, 2022; **Figure A-2**). With increasing time, the soils have developed A and O horizons of increasing thickness. The mean annual

temperature and precipitation are 4.2 °C and 1947 mm, respectively. Rain falls mainly during the vegetation period (May to September, Wu et al. 2013).

Our study included seven sites, de-glaciated between 0 (Site 1; 2982 m a.s.l.) and 127 years ago (Site 7; 2855 m a.s.l.; **Figure A-3**), previously described by Zhou et al. (2013). A primary vegetation succession has developed along the chronosequence, from pioneer shrubs (i.e., *Hippophae rhamnoides* L., Site 3; 37 yr-old site), over half mature broad-leaved tree forests dominated by *Populus purdomii* Rehder (Site 4; 47 yr-old site), to a full forest dominated by *Abies fabri* (Mast.) Craib (Sites 5-6; 59 and 87 yr-old sites, respectively) and *Picea brachytyla* (Franch.) E. Pritz. (Site 7; 127 yr-old site).

Figure A-1. Aerial view of the Hailuogou Chronosequence.

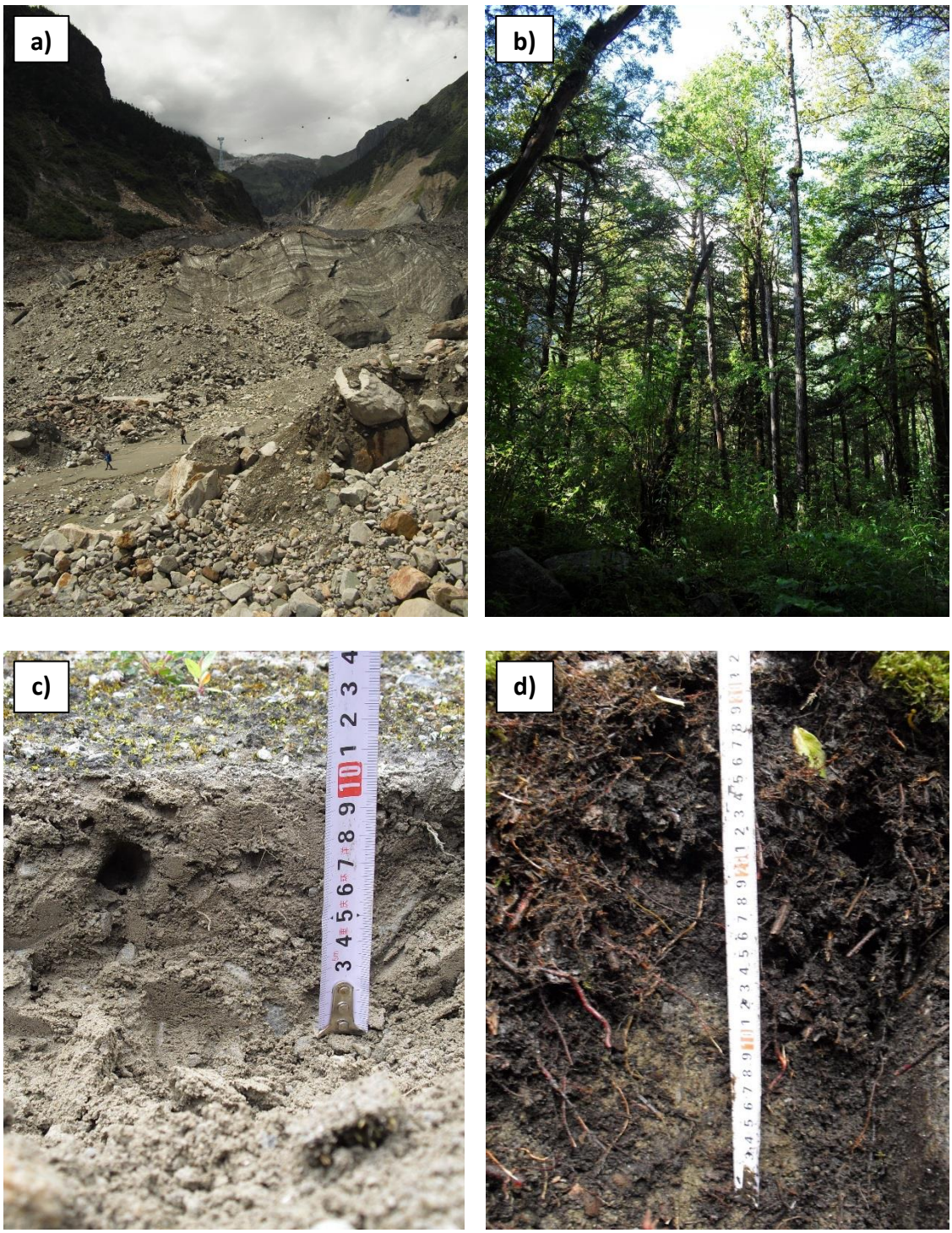

Figure A-2. View of the bare 0-yr old site (a) and the fully developed conifer-dominated mixed forest at the 87-yr old site (b) of the Hailuogou chronosequence, together with characteristic soil profiles, i.e., a Leptic Calcaric Regosol (5-yr old site; c) and a Folic Dystric Regosol (87-yr old site; d).

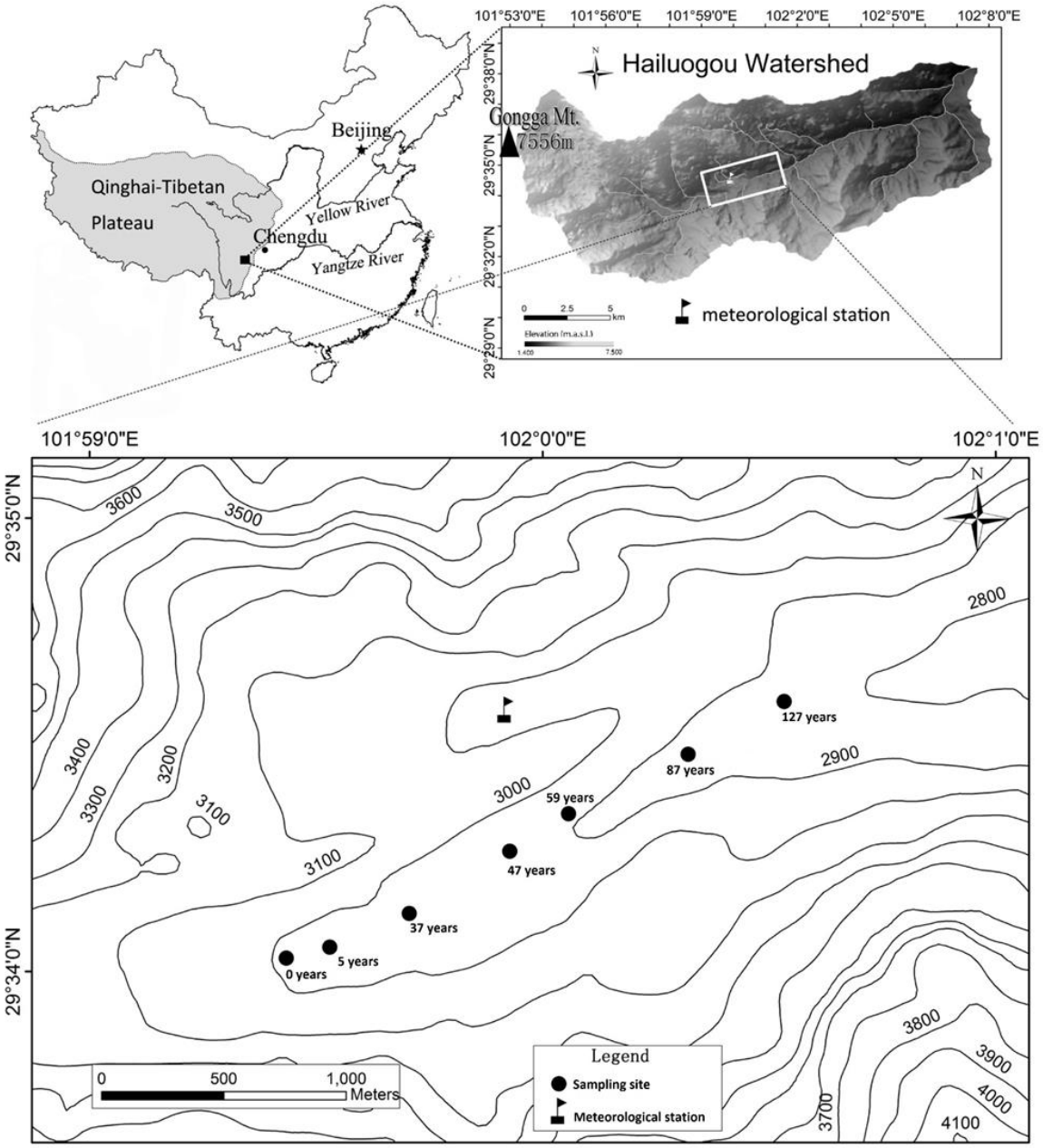

Figure A-3. Location of the Hailuogou Chronosequence and study sites.

Soil samples were collected in August 2017 from the seven ecosystem succession stages, which were exposed for 0, 5, 37, 47, 59, 87 and 127 years since glacial retreat (**Figure A-3**). Each ecosystem succession stage was sampled in triplicate. The distance between the sampled soil profiles was at least 20 m, except at the 0 and 5 year-old sites, where the distance was reduced to 10 m because the studied valley is narrower in the proximity of the glacier. Soil profiles were hand-dug and five soil horizons sampled: Oi (fresh litter), Oe (shredded litter), Oa (dark layer of decomposed humus), A (surface

mineral soil with humus enrichment), and C (weathered soil parent material). No organic layers were present at the 0 and 5 year-old sites. Sixteen different rock samples were collected close to the current glacier front, which were considered as representative of the composition of the glacial debris forming the substrate for soil development (**Figure A-4**).

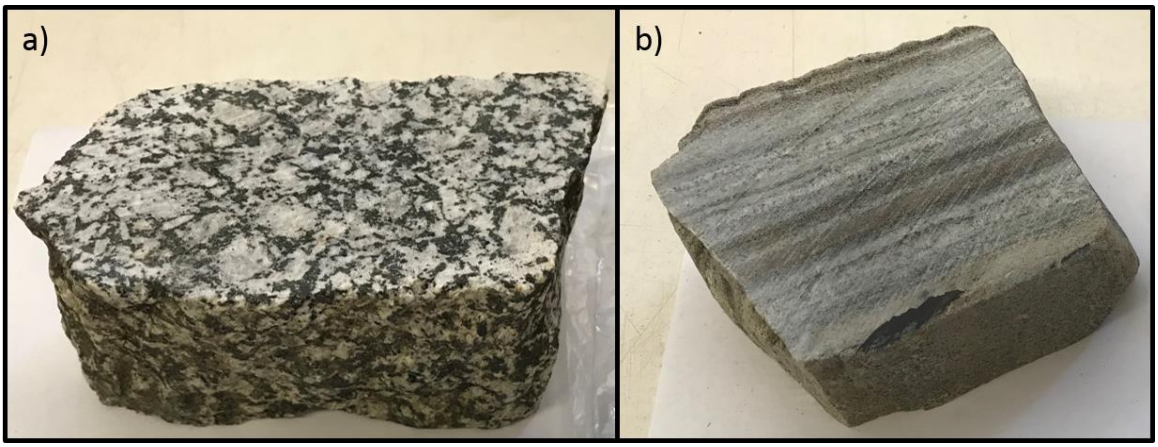

Figure A-4 Samples of granite (a) and meta-sedimentary rock (b) collected from the glacial debris of the Hailuogou chronosequence. Foto Credit: Qingqing He.

Between August and October 2017, we collected freshly cut leaves, 1 and 3 year-old needles, bark, branches, trunk, and roots of the dominant tree and shrub species in the surrounding of our replicate soil profiles. To achieve a more representative sample of each replicate, a minimum of three individuals were randomly sampled from the trees of the same area. Four species were sampled along the chronosequence: *H. rhamnoides* (Site 3, 37 years), *P. purdomii* (Site 4, 47 years), *A. fabri* (Sites 5-6, 59 and 87 years), and *P. brachytyla* (Site 7, 127 years). Tree branches were randomly sampled from the tree canopy using pole shears. Bark samples were collected using an outdoor knife. The depth of cut was adjusted depending on the bark thickness in order to take a representative sample without reaching the cambium. Trunk samples were collected using a tree corer.

Soil samples (mineral and organic horizons) were air-dried to constant weight in a drying room located in the research station. Mineral samples were sieved to collect the two fractions fine earth (<2 mm) and stones (>2 mm). To collect unweathered rock material, we removed the outer shell of each rock sample by cutting with an automated core slabbing saw. Leaf, needle, branch, bark, trunk and root samples were oven-dried to constant weight

at 40°C during 72 hours and stored in sealed bags. Trunk and root samples were manually homogenized using an agate pestle and mortar. Bark and branch samples were homogenized using a blade grinder equipped with a 3.0 mm sieve. Aliquots of all samples were ground using a ball mill equipped with a zirconium oxide jar. The stone fraction of the soils (>2 mm) and the rock samples were ground in an agate grinding set using a vibratory disk mill.

2.2. Chemical analysis

Soil pH was determined by a glass electrode in a 1:5 (v/v) air-dried fine earth (<2 mm):water suspension. The carbonate concentration (CO_3^{2-}) in the fine earth was determined by measuring the volume of emitted carbon dioxide after reaction of the sample with 10% HCl in a Scheibler calcimeter. The grain-size distribution of the fine earth was determined according to DIN ISO 11277:2002-08. The effective cation-exchange capacity (ECEC) was determined by summing the charge equivalents of K, Na, Ca, Mg and Al after extraction with 1M NH_4NO_3 (1:25 soil:solution ratio; Zeien and Brümmer 1989). Total element concentrations in the organic horizon, fine earth and stones were determined after complete digestion with concentrated HNO_3/HF/H_2O_2 (4:1.5:1, v:v:v) and in the plant compartments after complete digestion with 8 mL of concentrated HNO_3 and 2 mL of concentrated H_2O_2 in a microwave oven (MARS6Xpress, CEM). Elemental concentrations in the digests were analyzed using an inductively-coupled plasma optical-emission spectrometer (ICP-OES, 5100 VDV, Agilent). The inorganic C concentrations and $\delta^{13}C$ values in the rocks were determined with an Elemental Analyzer – Isotope Ratio Mass Spectrometer (Flash 2000 HT Plus-Delta V Advantage, ThermoFisher Scientific) after muffling the samples at 550°C. Loss on ignition (LOI) was determined by weighing before and after muffling the samples at 550°C (**Sections B and C)**.

To determine the release kinetics of the base cations (i.e., Ca, Mg, K, and Na), I conducted a weathering experiment using the resin-based pH_{stat} approach of Schwarz et al. (1999) including modifications of Alt et al. (2013) to handle the carbonates. Briefly, the base cations were released from the fine earth into solution during H^+ buffering at constant pH, and removed from the system using a mixed ion-exchange resin, which was further extracted with 2 M HNO_3. Samples were shaken during 10 min, 30 min, 1 h, 2 h, 4 h, 12 h, 24 h, 48 h, 96 h and 168 h, respectively, to determine the element release over time. Based

on the element release over time, I applied a nonlinear regression model to estimate the size of two differently reactive pools (slow/fast) and the corresponding release rate constants. At each site age, I analyzed three independent soil samples collected from the uppermost 10 cm of the soils. In total, 210 samples were processed (7 sites x 3 replicates x 10 aliquots for the different shaking times). Exchanged element concentrations were determined by ICP-OES. (**Section C**).

For Mg isotope analysis, soil samples were digested with concentrated HF-HNO_3 (3:1) in Teflon Savillex screw-top beakers on a hot plate at 120°C for 72 h, and dried down, before they were purified. I produced and purified digests of bulk soils (<2mm) from the C1 and C2 mineral horizon at the 0 yr-old site, the A and C mineral horizons at the 37, 47, 87 and 127 yr-old sites, the exchangeable Mg fraction along the chronosequence (5 samples) and resin extracts derived from the pH_{stat} experiment corresponding to the three independent soil samples collected at each of the 0 yr- and 127 yr-old sites, extracted at three different times (after 30 min, 48 h, and 168 h). The remaining residues were treated with concentrated HCl-HNO_3 (3:1) at 120°C for 24 h, evaporated to dryness, and taken up in 1 M HNO_3. Aliquots of the exchangeable cation extracts were dried down and treated with HCl-HNO_3 (3:1, v:v) at 120°C for 24 h in order to digest the high salt concentration of the matrix (1 M NH_4NO_3), before re-dissolution in 10 M HCl. A fraction of each sample containing 10-15 µg of Mg was evaporated and taken up in the acid needed for purification (i.e., 2 mL 1 M HNO_3 – resin extracts – or 0.25 mL 10 M HCl – mineral soil digests and exchangeable Mg fraction – **Section D**).

Resin extracts derived from the pH_{stat} experiment were purified for Mg isotope analysis according to the procedure described by Teng et al. (2007), in which I used slightly longer columns to increase the retention time of the eluted elements and obtain sharper breakthrough curves. Following this method, the Mg fraction and the potential interferences (e.g., Na, Ca or Ti; **Table A-1**), were eluted from the column at different times using 1 M HNO_3 as eluent. Sodium was eluted with the first 10 mL after loading the sample, Mg was collected in the next 16 mL, and Ca was lastly eluted (**Figure A-5**). The procedure was repeated 2-3 times for each sample to obtain a pure Mg solution (i.e., showing a ratio of the concentration of the interferences to that of Mg <0.05). However, because of the more complex matrix of our soil samples, I found that when using the method of Teng et al. (2007) part of the Ti contained in the samples was eluted at the same time as the Mg, which

potentially creates an interference on the stable isotope ratio of Mg because the double charged ions of Ti ($^{48}Ti^{2+}$, $^{50}Ti^{2+}$) have the same mass/charge ratio as Mg isotopes (**Table A-1**). Therefore, soil samples and soil exchangeable fractions were purified following the two-step method described by Opfergelt et al. (2012), in which most of the Fe and Ca was removed from the sample using 10 M HCl as eluent in the first step. The second step separates Mg from the rest of the matrix with successively 0.4 M HCl, 0.15 M HF, 95% acetone/0.5 M HCl and 1 M HCl as eluents (**Figure A-6**). The resin was cleaned with 1 M HCl, 4 M HCl, 1 M HNO_3, and deionized water >18.2 MΩ cm^{-1} before filled into columns (10 mL Bio-Rad® polypropylene columns), and further cleaned in the columns with 20 mL of 4 M HCl and 10 mL of deionized water before it was conditioned with the required acid (1 M HNO_3 or 10 M HCl) prior to loading the sample (**Section D**).

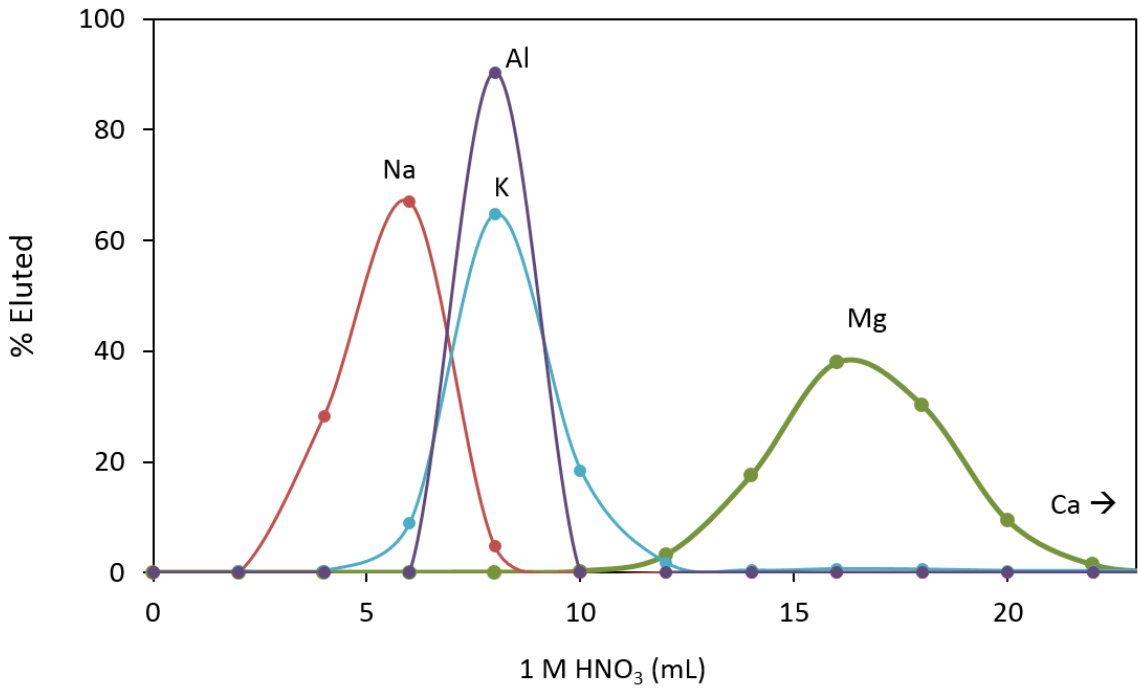

Figure A-5. Elution curves of Na, Al, K, and Mg for a resin extract derived from the pH_{stat} experiment according to the procedure described by Teng et al. (2007), in which we used slightly longer columns (filled with 1.2 mL of resin instead of 1 mL).

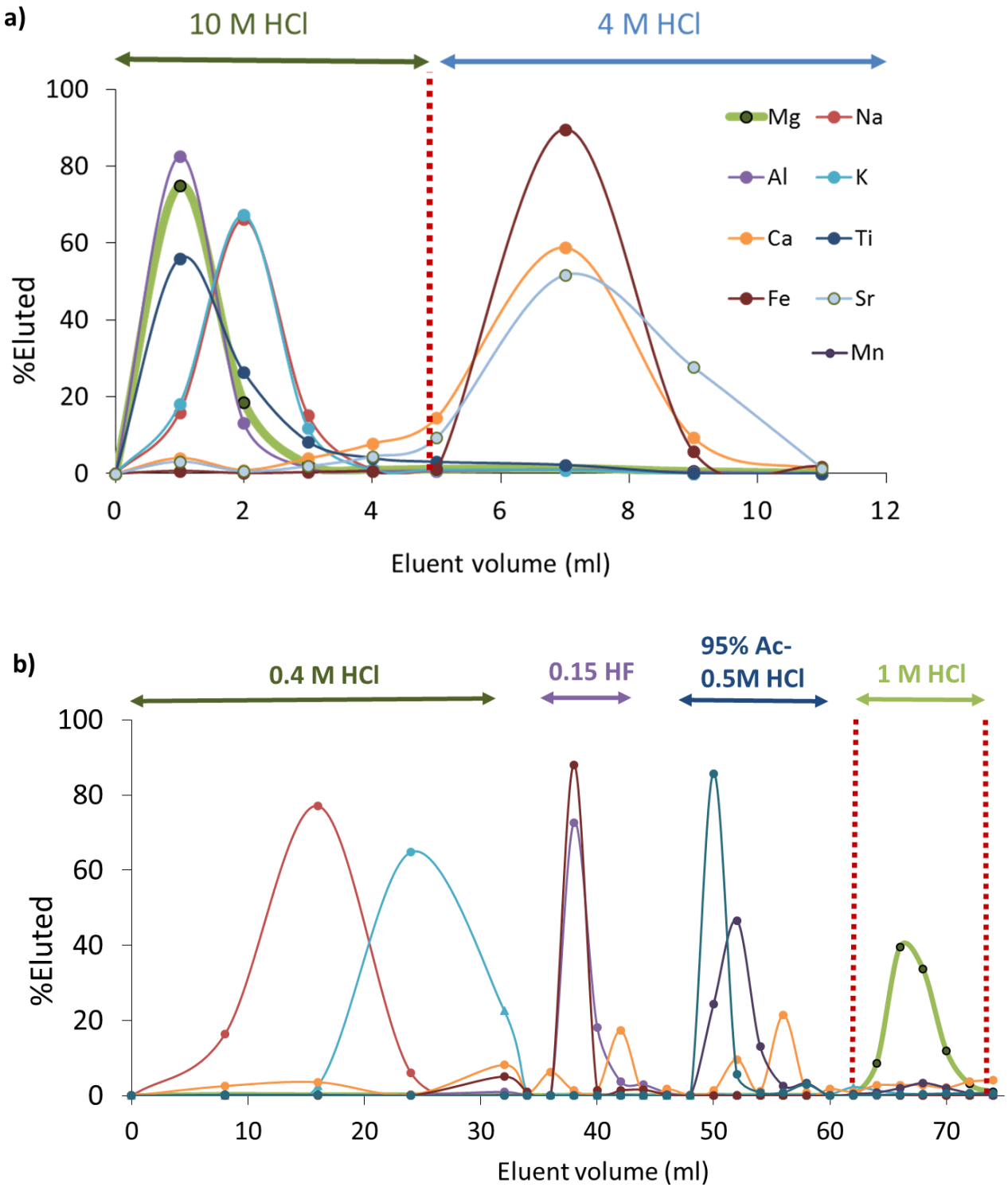

Figure A-6. Elution curves of Mg and potentially interfering elements for Step 1 (a) and Step 2 (b) of a mineral soil sample analyzed in this study following the method of Opfergelt et al. (2012).

2.3. Mg isotope measurements

Figure A-7: Thermo Scientific Neptune MC-ICP-MS in the Soil Biogeochemistry laboratory of the KIT-Institute of Geography and Geoecology.

The three stable Mg isotope signals (^{24}Mg, ^{25}Mg and ^{26}Mg) were measured simultaneously with a Thermo Scientific Neptune MC-ICP-MS (**Figure A-7**) on Faraday detectors using a 10^{11} Ohm Faraday cup current amplifier in five blocks of 30 cycles per block, with an integration time of 4 s per cycle. All samples and standards were introduced into the plasma dissolved in 0.37 M HNO_3 at Mg concentrations of 500 ppb to avoid instrumental mass bias (Teng and Yang, 2014), and were measured using the standard-sample bracketing technique. Magnesium isotope data are reported relative to DSM-3 (Galy et al. 2003, **Eq. A-1**):

$$\delta^{x}Mg = \{[{}^{x}Mg/{}^{24}Mg)_{sample} / ({}^{x}Mg/{}^{24}Mg)_{DSM\text{-}3}] -1\} \times 10^{3} \quad \textbf{(A-1)}$$

where x is either mass 26 or 25.

An in-house $Mg(NO_3)_2$ standard was used for the bracketing. The composition of the in-house standard was determined by repeated measurements (n=45) relative to ERM-AE143, which has recently been used as new reference material for δ^{26}Mg values (Vogl et al. 2016) after the DSM-3 standard established by Galy et al. (2003) was exhausted, and had a δ^{26}Mg value of 3.61 ± 0.24‰ and a δ^{25}Mg value of 1.87 ± 0.14‰ (± 2 standard deviations, SD). The data relative to ERM-AE143 were normalized to the international DSM-3 Mg standard scale according to González de Vega et al. (2020) by subtracting 3.295±0.064 for δ^{26}Mg and 1.666±0.043 for δ^{25}Mg.

All samples analyzed in this study showed a mass-dependent isotope fractionation, as indicated by the positive correlation of the $\delta^{26}Mg$ with the $\delta^{25}Mg$ values. The regression line of the $\delta^{25}Mg$ on the $\delta^{26}Mg$ values showed a slope of 0.521±0.012 (2 SD); **Figure A-8**), in line with the theoretical kinetic slope of 0.511 and the theoretical equilibrium slope of 0.521 (Young and Galy 2004).

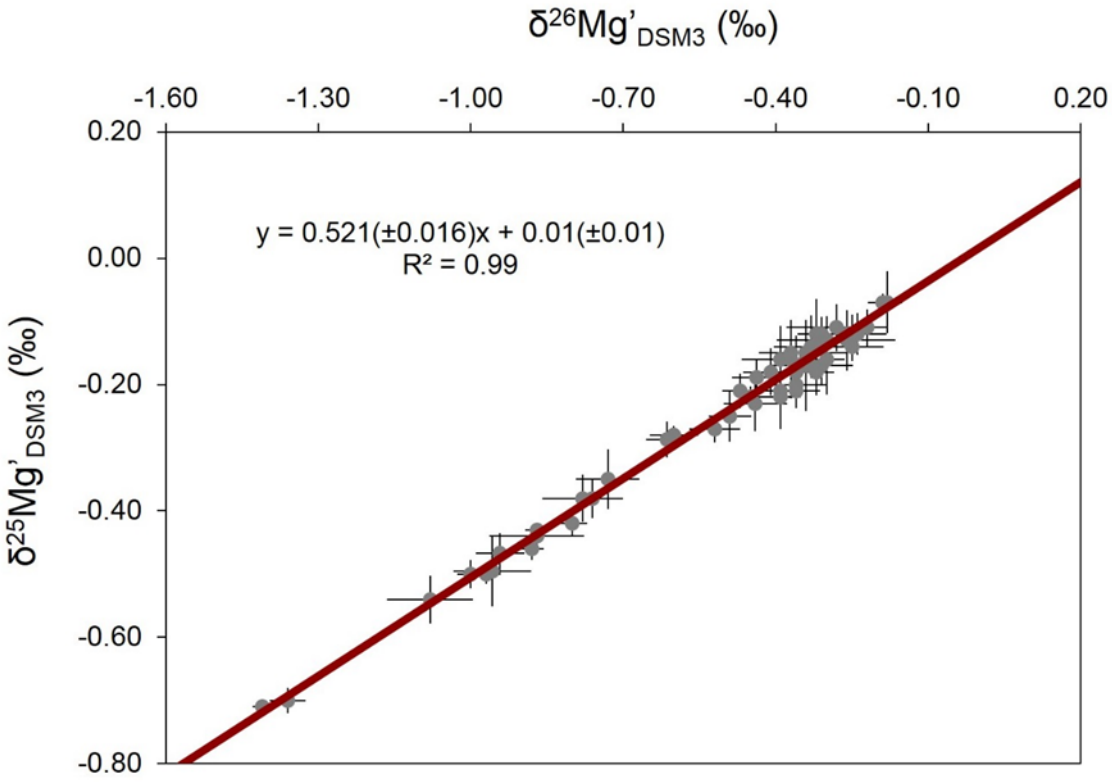

Figure A-8 Magnesium three-isotope plot of all samples analyzed in this study. The solid line represents the mass-dependent fractionation, in line with the theoretical kinetic slope of 0.511 and the theoretical equilibrium slope of 0.521 (Young and Galy 2004). The error bars indicate 2SD of repeated measurements. The slope and intercept of the regression equation are shown with their errors (2SD).

2.4. Calculations and statistical analysis

A detailed description of the equations used in this study to calculate Ca, Mg, K and Na stocks in the different compartments (leaves/needles, branches, trunk, bark, roots, organic and mineral horizons) along the Hailuogou chronosequence, as well as the associated fluxes (atmospheric deposition, plant uptake, accumulation in the organic layer and export with the stream) can be found in **Section B-3**. Briefly, I used the element concentrations I

measured in the considered compartments and relied on existing data concerning biomass and soil bulk density from our Chinese partners. Total biomass was estimated for our study sites based on total biomass measured by Luo et al. (2004), after applying a logistic fitting to account for the increasing biomass until the year 2017, when our samples were collected. Similarly, the net primary productivity (NPP) was calculated for our sites from data published by Luo et al. (2004) for the same study area. The proportional contribution of the different tree compartments (trunk, bark, branches, leaves, roots) to the total tree biomass was taken from Zhou (2013). Bulk density of the soils and stone volume were taken from Zhou et al. (2016a) and Wang et al. (2020), who studied the same sites. Thickness of the organic and mineral horizons was measured at each of the soil profiles before sampling. I calculated the total soil and ecosystem stocks to a mineral soil depth of 0.1 m. Total stocks (g m^{-2}) at each plot were calculated by summing the individual stocks of the different plant compartments, the organic horizons and the uppermost mineral horizons. For the estimation of the fluxes, we obtained bulk deposition data from the Gongga Mountain Alpine Ecosystem Observation Station (Zhou et al. 2016b), mean annual precipitation from Wu et al. (2013), and base cation concentrations of the stream water of the Hailuogou region together with the mineral composition of our study soils from Zhou et al. (2016a) (**Section B**).

The release kinetics of the base cations in soils was described as a two-step first-order reaction by Süsser (1987). Therefore, I applied **Eq. A-2** to determine the release kinetics of Ca, Mg, K and Na along the chronosequence, based on the samples derived from the pH_{stat} experiment.

$$Y(t) = \text{Pool A}\ (1-e^{-kat}) + \text{Pool B}\ (1-e^{-kbt}) \qquad (\mathbf{A\text{-}2})$$

where Y(t) represents the element release from soil (mg kg^{-1}) at time t. Pool A and Pool B are the estimates of the two differently reactive pools (slow/fast; mg kg^{-1}) and k_a and k_b are the corresponding rate constants (h^{-1}) of each pool, estimated by a nonlinear regression model using sequential quadratic optimization. We used the coefficient of determination (R^2) as measure of the fit between our data and the function (**Section C**).

I applied a two-end-member mixing model (**Eq. A-3** and **Eq. A-4**) to calculate the $\delta^{26}Mg$ value of the upper 10 cm of the mineral soil ($\delta^{26}Mg_{10cm}$) and to calculate the $\delta^{26}Mg$ composition of the slow-reacting Mg pool (**Section D**).

$$\delta^{26}Mg_M = f_A \delta^{26}Mg_A + f_B \delta^{26}Mg_B \quad \textbf{(A-3)}$$

$$1 = f_A + f_B \quad \textbf{(A-4)}$$

In which A and B represent the different end members contributing to the total mixture (M) and f represents the respective contribution of each source.

Normal distribution of the data was checked with the Shapiro-Wilk test. Pearson correlation, linear regression, and non-linear function fitting were used to evaluate relationships between variables. Significant differences between paired samples were tested with a t-test. One-way analysis of variance (ANOVA) followed by Tukey's HSD post-hoc test was applied to detect significant differences in mean total stocks, sizes of the modelled pools and k_a and k_b values among the various study sites. Normal distribution of residuals was visually inspected. Homoscedasticity was confirmed for our data after applying the Levene's test. Significance was set at $p < 0.05$ (**Sections B to D**).

3. Results and discussion

3.1. Base metal stocks and fluxes (Section B)

To improve our understanding of the fast vegetation development along the Hailuogou chronosequence, I studied the influence of base cation (Ca, Mg, K and Na) supply and vegetation establishment along the Hailuogou chronosequence **(Figure A-9**). Total ecosystem Ca and Mg stocks decreased along the chronosequence. Fortyfour and 30% of the initial stocks of Ca and Mg, respectively, were leached during the first 47 years, at rates of 130±10.6 g m^{-2} $year^{-1}$ Ca and 35±3.1 g m^{-2} $year^{-1}$ Mg, paralleling the pH decrease from 8.0 to 5.8 in the mineral topsoil and the loss of carbonates, mainly calcite. The Mg release could not be attributed to the carbonate weathering because the low dolomite concentrations did not change along the chronosequence (Zhou et al. 2016) and no other Mg carbonate mineral was detected in the parent material.

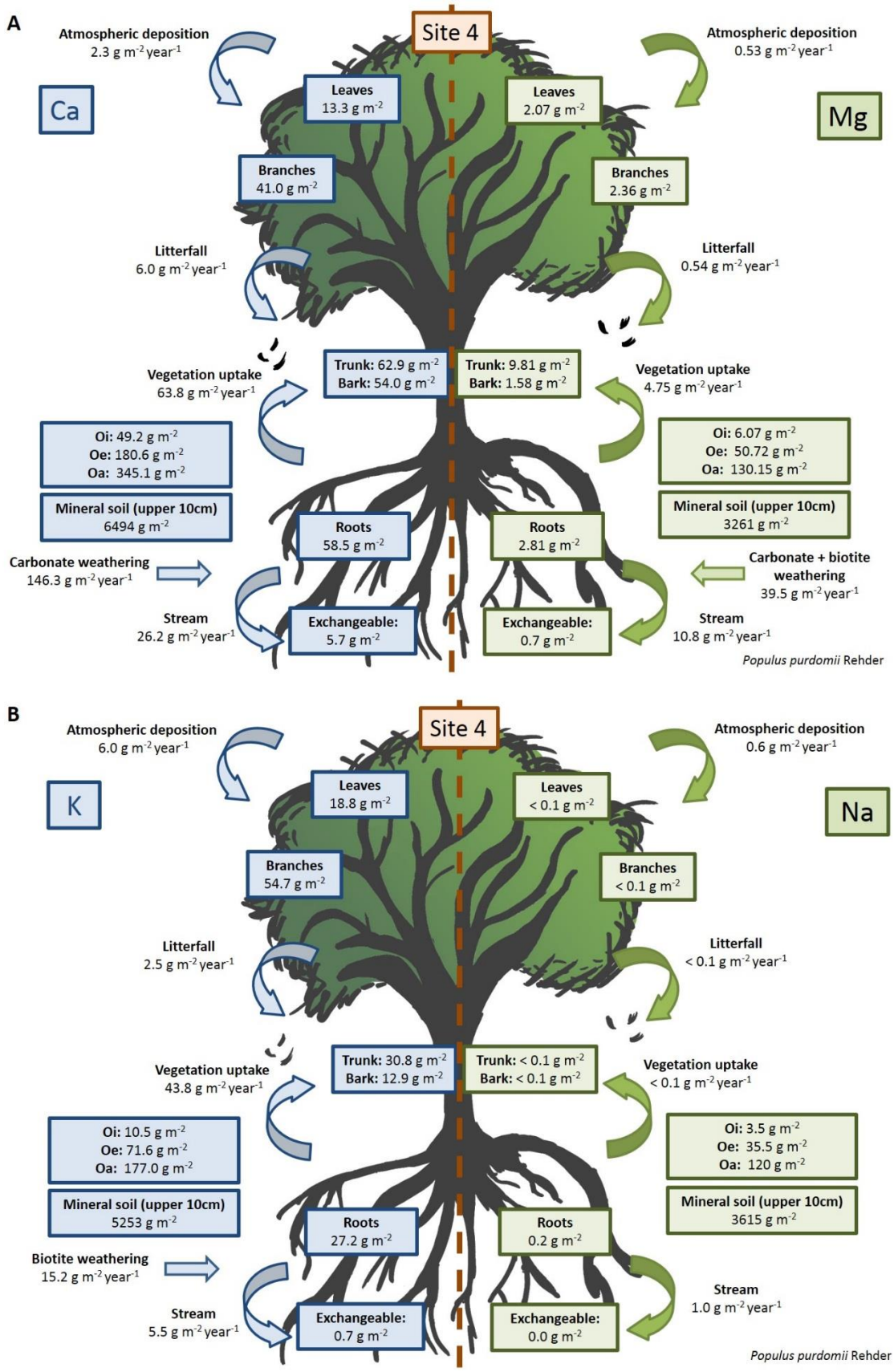

Figure A-9. Stocks (boxes) and fluxes (arrows) of Ca (A, left), Mg (A, right), K (B, left) and Na (B, right) at the 47 yr-old site with *P. purdomii*-dominated forest.

Therefore, the fast initial Mg release must be related to other easily weatherable Mg-containing minerals such as biotite, hornblende or chloride. Stocks of K and Na were unrelated with ecosystem age and remained similar at on average 5162 ± 710 g m^{-2} K and 3530 ± 429 g m^{-2} Na along the chronosequence.

The organic layer accumulated at a mean rate of 288 g m^{-2} $year^{-1}$ providing a bioavailable base metal stock, in which the accumulation of base cations decreased in the order Ca > K > Mg > Na along the chronosequence. Annual losses of Ca and Mg via the stream were between one and two orders of magnitude higher than the estimated bulk deposition, while those of K and Na were in a similar range. Annual plant uptake did not show a consistent temporal trend along the chronosequence and was higher at those sites where deciduous trees were growing (37 to 59 year-old sites) than at the older sites (> 87 years), after the stabilization of a conifer-dominated mixed forest.

3.2. Base cation sources, pool sizes and release kinetics (Section C)

To explore the reasons for the fast depletion of Ca and Mg in only a few decades, while the K and Na stocks remained similar, I conducted a weathering experiment using a resin-based pH_{stat} approach, in which ions were released into solution during H^+ buffering at constant pH and removed from the system using ion exchange resins. I found that the main source of weathered Ca was calcite ($CaCO_3$), which was mainly present in the pores of metasedimentary rocks, as revealed by the visual analysis of photomicrographs of thin sections of rocks collected at the terminus of the glacier (**Figures A-10 and C-2**). Low concentrations of carbonates were also detected in granites (3 – 57 g kg^{-1} $CaCO_3$), while the sample with the highest calcite concentration was the meta-volcanic rock (300 g kg^{-1} $CaCO_3$), which was characterized by layers mainly consisting of calcite, plagioclase and quartz (**Figures A-11** and **C-2**).The size of the fast-reacting Ca pool decreased with increasing site age, in line with the rapid weathering of $CaCO_3$. After carbonates had been leached (>47 yr), the size of the fast-reacting Ca pool was comparable to that of the exchangeable Ca pool. The release rate constant associated with the slow-reacting pool of Ca, k_{b_Ca}, did not significantly change with increasing site age, although the size of the pool tended to decrease, indicating that the slow-reacting Ca pool was weathered at a constant rate along the chronosequence.

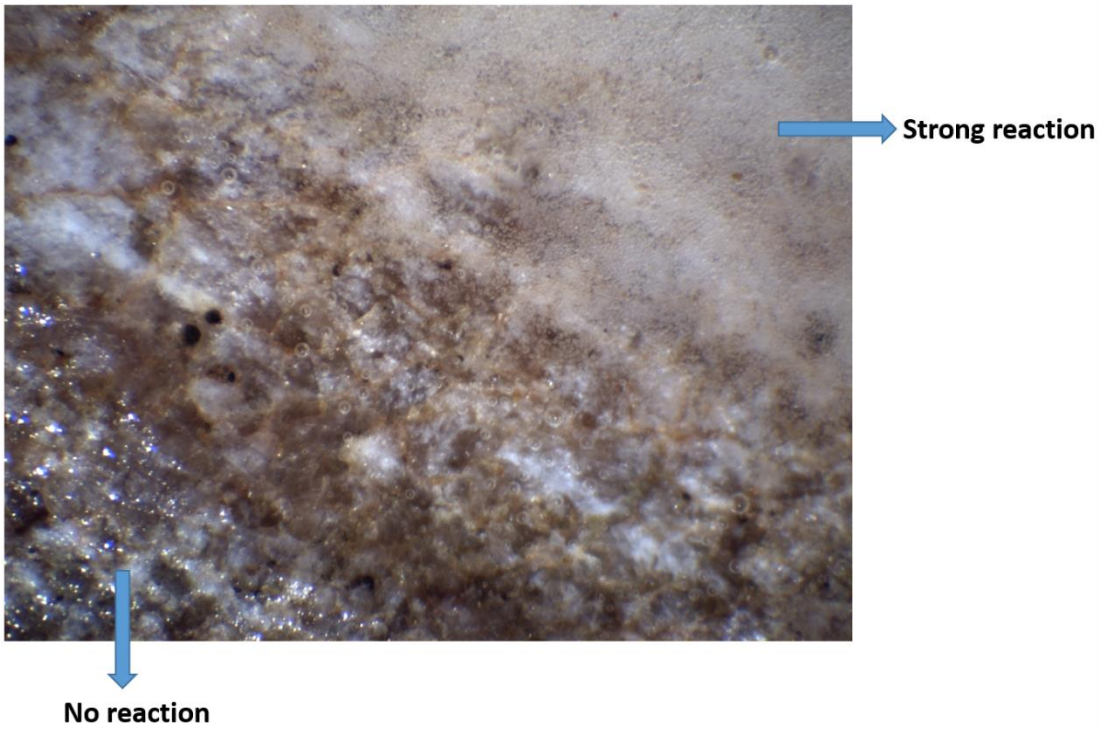

Figure A-10. Reaction to adding some drops of 10% HCl to a meta-sedimentary rock collected at Site 1 (0 years old) at the Hailuogou chronosequence, observed by optical microscopy.

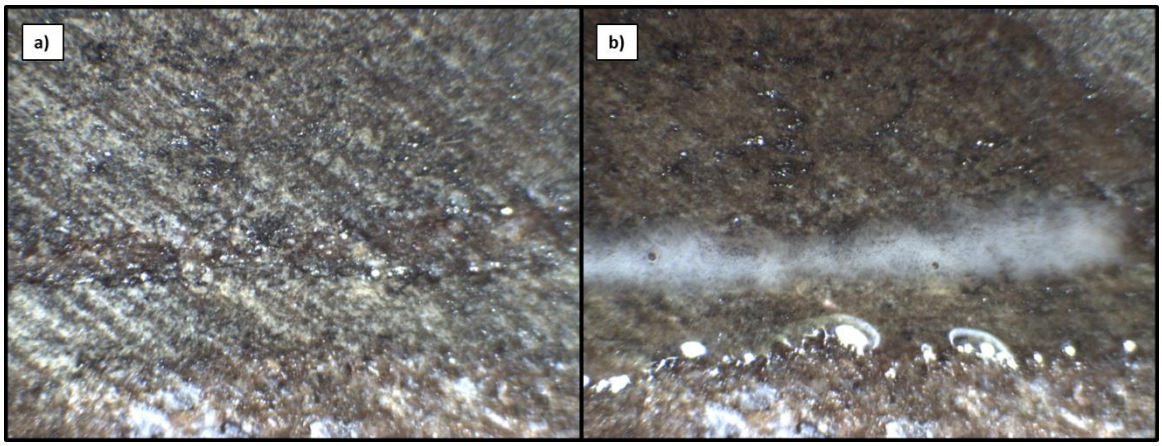

Figure A-11. Meta-volcanic rock before (a) and after (b) addition of 10% HCl, observed by optical microscopy. The reaction $CaCO_3 + 2HCl \rightarrow Ca^{2+} + 2Cl^- + H_2O + CO_2$ occurred only along a defined cross section of the rock.

The main sources of weathered Mg, K and Na were silicate minerals, whose release rates followed the order Mg > K >> Na. The release rate constant associated with the fast-reacting Mg pool, k_{a_Mg}, did not significantly change along the chronosequence, nor did the size of the fast-reacting Mg pool. The size of the fast-reacting Mg pool correlated with the exchangeable Mg concentration in soil, except at the younger sites (0 and 5 years old), where the fast-reacting Mg pool was significantly larger than the exchangeable Mg pool, indicating the contribution of one or more easily weatherable Mg-containing mineral(s) to that pool. The release rate constant associated with the slow-reacting Mg pool, k_{b_Mg}, marginally significantly ($p < 0.1$) decreased with time. The slow-reacting Mg pool seemed to only become active 4-12 hours after the start of the experiment and not simultaneously with the fast pool as was the case for Ca, K and Na, which may indicate that the little reactive Mg was more strongly bound in soil than the little reactive Ca, K and Na. The latter was corroborated by the finding that 2 h after the start of the pH_{stat} experiment, before the slow-reacting pool of Mg was activated, the molar K:Mg ratio significantly decreased with site age from 3.4±0.2 to 1.2±0.3, while after 168 h the K:Mg ratios did not correlate with site age anymore and averaged to 0.4±0.1. This indicated that more Mg was leached relative to K, although more K than Mg was originally stored in the mineral soil (K:Mg ratio in the mineral soil: 1.3±0.1).

3.3. Mg isotope ratios of minerals and soil Mg pools (Section D)

In the third section of my thesis, I tried to reveal if Mg isotope ratios can be used to further elucidate the mineral sources of Mg release by weathering, and as tracer of Mg loss from the soil along the 127-yr old glacial retreat chronosequence. To achieve that, I determined the δ^{26}Mg values of bulk soils and exchangeable Mg along the chronosequence, and in the differently reactive pools derived from the pH_{stat} experiment. I found a close negative correlation between the δ^{26}Mg values of the bulk topsoils (0-10 cm) and annual Mg depletion rates ($r=0.98$, $p<0.001$). The particularly fast Mg loss in the first 37 yr was attributable to leaching of exchangeable Mg and the fast dissolution of labile chlorite as revealed by the lower δ^{26}Mg values of the fast- (-1.28±0.10‰) than the slow-reacting (-0.64±0.11‰) Mg pool at the 0 yr-old site. The different δ^{26}Mg values of the fast-reacting Mg pool in the youngest and oldest soils indicated that the mineral sources of this pool also changed with time. The fact that the δ^{26}Mg values of the exchangeable Mg pool correlated

significantly with the release rate constant of the slow-reacting pool in the five oldest soils illustrated that the exchangeable pool was continuously fed by the weathering of biotite and hornblende, once the labile chlorite, with a lighter Mg isotopic composition, was dissolved. Therefore, these results support that the δ^{26}Mg values can be used as proxy of Mg loss and to identify the mineral sources of this loss during the early phase of soil development.

3.4. Mg isotope ratios of plant compartments

I have also analyzed the Mg isotope ratios of the organic horizon as well as diverse plant compartments (i.e., leaves, needles and roots) of the dominant tree species growing along the Hailuogou Chronosequence (**Figure A-12**), in order to further elucidate the increasing Mg incorporation into the biotic cycles with increasing vegetation biomass.

The tree roots were Mg-isotopically heavier than the exchangeable Mg pool in the mineral soil, supporting previous findings that plants prefer to incorporate ^{26}Mg relative to ^{24}Mg via root uptake, mainly because of the equilibrium fractionation by Mg binding to the root surfaces prior to uptake into the cells (Black et al. 2008; Bolou-Bi et al. 2010, 2012; Uhlig et al. 2017). With increasing ecosystem age, the roots increasingly accumulated isotopically heavy Mg, which is in line with the fact that the bioavailable Mg pool became isotopically heavier (**Section D**).

The δ^{26}Mg values of the organic layer remained mostly unchanged along the chronosequence at an average of -0.34 ± 0.10 ‰ (n=15). These δ^{26}Mg values were similar to the δ^{26}Mg values in tree leaves (-0.37 ± 0.27 ‰, n=9) and higher than the δ^{26}Mg values in old needles (-1.18 ± 0.27 ‰, n=15).

In *A. fabri*, the Mg concentration in 1 year-old needles was higher than in 3 year-old needles (**Figure A-13**). For the synthesis of new needles, conifers primarily acquire Mg from two sources. They take up Mg^{2+} from the soil solution through the roots (via xylem sap) or remobilize it from old to new compartments (via phloem sap). The Mg remobilization from old to young plant compartments mainly occurs as organo-complex. In organo-complexes Mg^{2+} forms highly coordinated, strong covalent bonds. For this reason, at chemical and isotope equilibrium, organo-Mg complexes prefer ^{26}Mg relative to ^{24}Mg that accumulates in the free cytosolic Mg^{2+} (Pokharel et al. 2017). The δ^{26}Mg values were higher in young (δ^{26}Mg = -0.59 ± 0.23, n=12) than in old needles (δ^{26}Mg = -1.26 ±

0.21, n=12) presumably because their major Mg source was the retranslocation of Mg-isotopically heavy organo-Mg complexes from older tissue. The latter might have been favored by the pronounced plant uptake of K, which was an order of magnitude larger than that of Mg along the chronosequence (**Section C**), because high plant K concentrations promote the Mg redistribution as organo-complexes from leaves prior to abscission or from old to young needles (Mengel et al. 2001). The even higher δ^{26}Mg value of leaves of the deciduous tree *P. purdomii* than of the one year-old needles might indicate that most of the comparatively high Mg demand of the leaves of this species is covered by Mg, which was retranslocated prior to leaf abscission and reused by the following generation of leaves, while less Mg was taken up from the exchangeable soil pool with its light δ^{26}Mg value (-0.86 ± 0.13‰; **Figure A-13**).

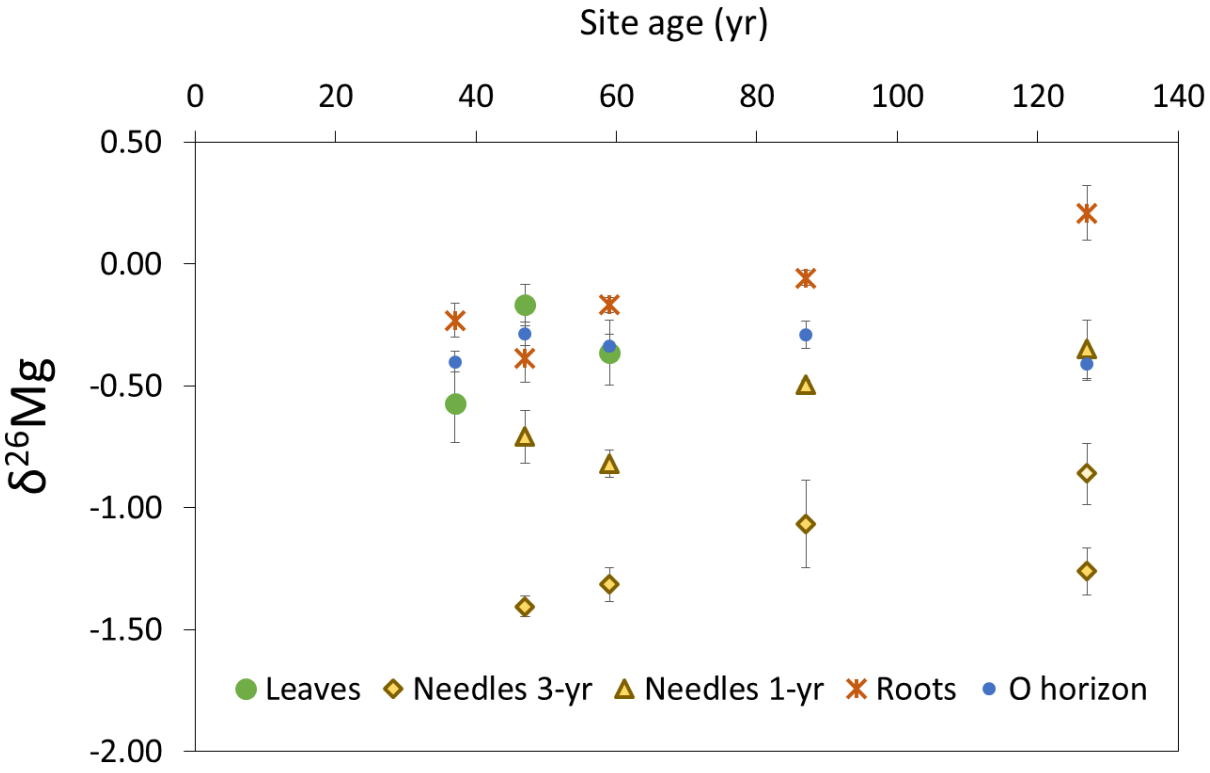

Figure A-12. Mean δ^{26}Mg values of the organic horizons (O horizon), roots, and leaves and needles of the dominant tree species i.e., the deciduous shrub *Hippophae rhamnoides* L. (Site 3, 37 yr) and tree *Populus purdomii* Rehder (Site 4, 47 yr) and the coniferous trees *Abies fabri* (Mast.) Craib (Site 5, 59 yr and Site 6, 87 yr) and *Picea brachytyla* (Franch.) E. Pritz. (Site 7, 127 yr). δ^{26}Mg values of needles of *A. fabri* at Site 4 (47 yr) and site 7 (127 yr) and leaves of *P. purdomii* at site 5 (59 yr) are additionally shown. The upper yellow rhombus showing the mean δ^{26}Mg values of 3 yr-old needles at site 7 (127 yr) corresponds to *P. brachytyla* and the lower yellow rhombus to *A. fabri*. Error bars represent the standard error of three spatially independent replicates (n=3).

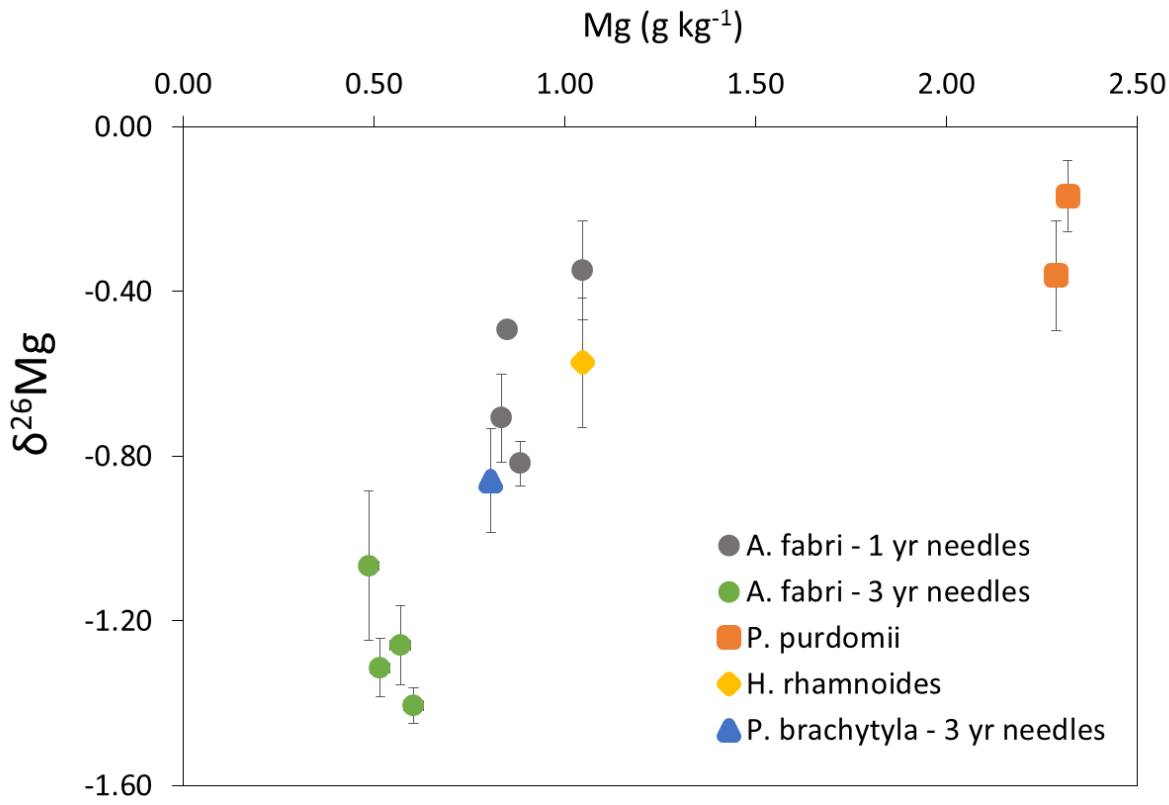

Figure A-13. Mean δ^{26}Mg values of leaves (*P. purdomii* and *H. rhamnoides*) and needles (*A. fabri* and *P. brachytyla*) of the dominant tree species growing along the Hailuogou chronosequence in relation to their Mg concentration (g kg^{-1} dry matter). Error bars represent the standard error of three spatially independent replicates (n=3).

3.5. Error discussion

In combined field and laboratory work, errors can occur during sampling and in the laboratory. To limit the sampling errors, replicates are necessary to account for the natural spatial heterogeneity. To limit measurement errors, a quality control including the determination of possible background contaminations, accuracy (or trueness) and precision is necessary.

3.5.1. Sampling errors

Natural heterogeneity may affect the results and the conclusions drawn from them if the sampling is not sufficiently representative. To account for the spatial heterogeneity of our research area, each study ecosystem succession stage was sampled in triplicate. To achieve a thoroughly representative sample of each replicate of the diverse plant compartments (i.e., leaves, needles, bark, branches, trunk, and roots), a minimum of three individuals were randomly sampled from the trees of the same area, and mixed well to create a composite sample before grinding. Three soil profiles were dug and each horizon was manually sampled. To account for the heterogeneity of the soil surface, the distance between soil profiles at each ecosystem age was at least 20 m, except at the younger sites (0 and 5 years old), that was reduced to 10 m because the valley is narrower in the proximity of the glacier. The differences in element concentrations measured in the diverse ecosystem compartments among the plots of the same ecosystem age site is frequently larger than measurement errors.

In my thesis, fluxes have been estimated by measuring changes in the respective pool sizes with increasing site age, based on the base metal stocks described in **Section B**. I relied on existing climate data from our partners from the Chinese Academy of Sciences to estimate total element deposition and element leaching fluxes, and on previously published net primary productivity and biomass data to estimate annual plant uptake and plant stocks along the chronosequence. My estimate of the base metal leaching losses is based on the assumptions that all water passes through the deep subsoil and that during this passage chemical equilibrium of the soil solution with the substrate is reached, which is reasonable because the length of the water path from the study soils to the stream is longer than 1 m. Uncertainties were calculated by error propagation, considering the uncertainties reported in the publications of my colleagues. When the error was not reported, a standard deviation of 10% of the value was assumed (**Section B**).

3.5.2. Contaminations, accuracy and precision

Different matrices (e.g., mineral soil, organic horizons, plant material, etc.) and even different acid digestion methods can release a different fraction of elements from the matrix (Chen and Lena 2001), potentially resulting in too low measured element concentrations if the digestion is not complete. To prevent this, all digests were visually checked and only accepted if they were translucent and no solids could be observed (**Sections B and D**).

Sample preparation for Mg isotope ratio analysis, purification and measurements were performed in a clean air lab to avoid sample contamination. We used distilled acids (DST-1000 Savillex ®) to remove any impurities. All labware used during sample treatment was previously acid-cleaned and rinsed with deionized water to prevent sample contamination. The ^{24}Mg signal of the procedural blanks was < 0.5% of the total ^{24}Mg signal and was therefore considered negligible (**Section D**).

Commercial resins usually contain impurities that can affect our results. Since base cations are usually ubiquitous, I carefully cleaned the mixed ion-exchange resin used for the pH_{stat} experiment (Amberlite MB-20, Rohm and Haas) before loading it into the homemade PE-bags. In general, 250 g of resin were shaken with 500 mL of 2 M HNO_3 for at least 2 hours and rinsed with deionized water (>18.2 MΩ cm^{-1}). After repeating this procedure for 5 times, I achieved concentrations of Ca, Mg, K and Na that were below the detection limit of our measurement, confirming that the resin will not be a source of contamination. I performed preliminary tests with standard solutions to achieve a complete element recovery from the resin. The most satisfying results were achieved using 30 mL of 2 M HNO_3 for 10 min in the first and second step and for 30 min in the last one (Ca: 101 ± 3%, Mg: 99 ± 1%, K: 106 ± 3%, Na: 99 ± 1%; n = 3). I also measured the extract corresponding to the fourth step, which contained none of the analytes. Therefore, the results achieved with the performed extractions were satisfying for all the studied elements (**Section C**).

Mg purification from matrix elements was achieved by cation-exchange chromatography, using Bio-Rad AG50W-X8 resin, which I also carefully cleaned with 1 M HCl, 4 M HCl, 1 M HNO_3, and deionized water >18.2 MΩ cm^{-1} before I filled the resin into columns. Once in the columns, I further cleaned the resin with 30 mL of 4 M HCl and 10 mL of deionized water before it was conditioned with the acid required for sample purification (**Section D**).

In each rack (with between 15 and 30 samples) of microwave-digested samples, at least one certified reference material matching the matrix of the samples was included (i.e., SRM1547 and SRM1515 for organic samples and BCR-2 for soil samples), as well as one replicate of a selected sample, and one blank to control for background contamination. Average recoveries ± SD were 100 ± 10% for all certified element concentrations and the relative standard deviation between duplicate measurements of the same sample was <5%. Therefore, elemental concentrations reported in this thesis are considered sufficiently accurate and precise (**Section B**).

Accuracy and precision of the whole clean air lab procedure was assessed by digestion and purification of the certified reference materials BCR-2 and NIST 1515. The results obtained with our method were δ^{26}Mg = -0.25±0.06‰ and δ^{25}Mg = -0.10±0.02‰ (2 SD, n=13) for BCR-2, and δ^{26}Mg = -1.22±0.13‰ and δ^{25}Mg = -0.59±0.08‰ for NIST 1515 (2 SD, n=8). These results are in close agreement with corresponding measurements reported by previous studies (e.g., δ^{26}Mg = -0.27±0.03 ‰ and δ^{25}Mg = -0.12±0.02‰ for BCR-2, Teng, 2017 and δ^{26}Mg = -1.22±0.05‰ and δ^{25}Mg = -0.62±0.05‰ and for NIST SRM 1515, Shalev et al. 2017) (**Section D**).

The most important isobaric interferences on the measurement of Mg isotopes include molecular ones (e.g., C_2^+, CN^+ and NaH^+) and double charged ions with the same mass/charge ratios as the Mg isotopes (e.g., $^{48}Ca^{2+}$, $^{48}Ti^{2+}$, $^{50}Ti^{2+}$, $^{50}V^{2+}$, $^{50}Cr^{2+}$ and $^{52}Cr^{2+}$; **Table A-1**). The accuracy of the Mg cut in soil extracts and digests with different matrices was checked by measuring the Mg concentration in 1 mL before and 3 mL after the Mg cut, in a sample with high and a sample with low $CaCO_3$ concentration. The Mg recovery in this test was ~98% and the Mg recovery in the pre- and after-cut was <1% (**Section D**).

Mg isotopes can be fractionated during ion-exchange reactions with heavy Mg isotopes eluted first from the column (Teng et al. 2007), therefore, I accepted a chromatographic run for purification only if the Mg recovery was >95% and if the ratio of any potential interference to that of Mg was lower than 0.05. If all these requirements were not achieved, the whole purification procedure was repeated (**Section D**).

Table A-1: Potential elemental and molecular interferences on the measurement of Mg isotopes with Inductively-coupled Plasma Multicollector Mass Spectrometry.

^{24}Mg		^{25}Mg		^{26}Mg	
Mass	**Formula**	**Mass**	**Formula**	**Mass**	**Formula**
23.47588	$^{47}Ti^{2+}$	24.47393	$^{49}Ti^{2+}$	25.47198	$^{51}V^{2+}$
23.97398	$^{48}Ti^{2+}$	24.97239	$^{50}Ti^{2+}$	25.97025	$^{52}Cr^{2+}$
23.97627	$^{48}Ca^{2+}$	24.97303	$^{50}Cr^{2+}$	**25.98260**	**Mg^{+}**
23.98504	**Mg^{+}**	24.97358	$^{50}V^{2+}$	26.00307	$^{14}N^{12}C^{+}$
23.99760	$^{23}Na^{1}H^{+}$	**24.98584**	**Mg^{+}**	26.00670	$^{13}C^{13}C^{+}$
24.00000	$^{12}C^{12}C^{+}$	25.00335	$^{12}C^{13}C^{+}$	26.00785	$^{10}B^{16}O^{+}$
24.01229	$^{9}Be^{15}N^{+}$	25.00387	$^{23}Na^{2}H^{+}$	26.00942	$^{11}B^{15}N^{+}$
24.01266	$^{11}B^{13}C^{+}$	25.00709	$^{9}Be^{16}O^{+}$	26.01131	$^{9}Be^{17}O^{+}$
24.01428	$^{6}Li^{18}O^{+}$	25.01238	$^{11}B^{14}N^{+}$	26.01440	$^{7}Li^{19}F^{+}$
24.01513	$^{7}Li^{17}O^{+}$	25.01305	$^{10}B^{15}N^{+}$	26.01492	$^{9}Be^{16}O^{1}H^{+}$
24.01601	$^{10}B^{14}N^{+}$	25.01352	$^{6}Li^{19}F^{+}$	26.02021	$^{11}B^{14}N^{1}H^{+}$
24.01874	$^{7}Li^{16}O^{1}H^{+}$	25.01516	$^{7}Li^{18}O^{+}$	26.02299	$^{7}Li^{18}O^{1}H^{+}$
24.02308	$^{9}Be^{14}N^{1}H^{+}$	25.02012	$^{9}Be^{15}N^{1}H^{+}$	26.47033	$^{53}Cr^{2+}$
24.47393	$^{49}Ti^{2+}$	25.02211	$^{6}Li^{18}O^{1}H^{+}$		
		25.02296	$^{7}Li^{17}O^{1}H^{+}$		
		25.02384	$^{10}B^{14}N^{1}H^{+}$		
		25.02501	$^{7}Li^{16}O^{2}H^{+}$		
		25.47198	$^{51}V^{2+}$		

Instrumental mass bias, which is caused by differential transmission of the different Mg isotopes during the measurement with MC-ICP-MS, was corrected by applying the sample-standard bracketing technique. Because Mg has only three stable isotopes (^{24}Mg, ^{25}Mg and ^{26}Mg), double-spike methods, which require at least four stable isotopes of the same element, could not be applied. I used an in-house $Mg(NO_3)_2$ standard for our sample bracketing. The Mg-isotopic composition of the in-house $Mg(NO_3)_2$ standard was determined by repeated measurements (n=45) relative to ERM-AE143. The in-house standard had a δ^{26}Mg value of 3.61 ± 0.24‰ and a δ^{25}Mg value of 1.87 ± 0.14‰ (2 SD). The long-term reproducibility of the Mg isotope ratio measurements was checked by performing repeated measurements (n=16) of the in-house $Mg(NO_3)_2$ standard of the Observatoire Midi-Pyrenées/Laboratoire Geosciences Environnement Toulouse (GET), France. My values of δ^{26}Mg = 0.28±0.13‰ and δ^{25}Mg = 0.18±0.09‰ matched those

reported by Stamm et al. (2022) well ($\delta^{26}Mg$ = 0.32±0.14‰ and $\delta^{25}Mg$ = 0.16±0.08‰). Since differences in the Mg concentrations between samples and standards can also affect instrumental mass bias and deteriorate the quality of the Mg isotope analysis, all samples and standards were introduced into the plasma dissolved in 0.37 M HNO_3 at Mg concentrations of 500 ppb. Mg isotope signals (^{24}Mg, ^{25}Mg and ^{26}Mg) were measured simultaneously on Faraday detectors using a 10^{11} Ohm Faraday cup current amplifier in five blocks of 30 cycles per block, with an integration time of 4 s per cycle (**Section D**).

4. General conclusions

The initial high Ca bioavailability because of the moderate alkaline soil pH and carbonate depletion together with the dissolution of easily weatherable silicates providing enough Mg and K to the pioneer vegetation contributed to the establishment of a deciduous forest in the early stage of the Hailuogou chronosequence. The slower element release by weathering after leaching of carbonates occurred synchronously with the vegetation change from deciduous to coniferous forests, which usually have a lower nutrient demand. Consequently, nutrient supply by weathering and nutrient demand by the vegetation seemed to be well synchronized to promote vegetation development along the Hailuogou glacial retreat chronosequence (**Section B**).

Calcite ($CaCO_3$) occurred in the mainly granitic substrate of the Hailuogou chronosequence, which originated from meta-sedimentary and meta-volcanic rocks in the glacial debris and provided a high amount of bioavailable Ca in the early stage of the chronosequence. Carbonate weathering determined the rapid initial Ca but not Mg release. The latter was attributed to the easily weatherable Mg-containing silicate mineral chlorite. Although less Mg than K was originally stored in the mineral soil, Mg was leached faster. The main sources of weathered K and Na were silicate minerals. The release of K was one order of magnitude higher than that of Na, although the total concentrations of both elements were similar in the parent material. The base cation release rates along the chronosequence followed the order Ca >> Mg > K >> Na (**Sections B and C**).

The significant negative correlation between the $\delta^{26}Mg$ values of bulk soils and the Mg depletion rates along the chronosequence suggest that Mg isotope ratios can be used to trace Mg loss from the topsoil during the early phase of soil development. The different

δ^{26}Mg values of the minerals contained in the parent material combined with the δ^{26}Mg values of the two differently reactive Mg pools (fast/slow) could be used to identify the mineral sources of this loss. Because the low δ^{26}Mg value of chlorite explained the similarly low δ^{26}Mg values of the fast-reacting Mg pool of the weathering experiment (pH_{stat}), chlorite was confirmed as the major Mg source in the young soils (**Section D**).

With increasing ecosystem age, roots and young needles accumulated isotopically heavy Mg, probably as a result of the decreasing size of the Mg-isotopically light bioavailable pool and its increasing δ^{26}Mg value. Generally, increasing Mg concentrations in leaves and needles resulted in ^{26}Mg enrichment, regardless of tree species (**Section A-3.4**).

In my thesis, I found promising relationships between the δ^{26}Mg values of soils and plant compartments that might be used as tracers of Mg fluxes in ecosystems including e.g., the Mg loss from the entire ecosystem or the Mg uptake by plants. However, my findings are based on a limited number of sites along a comparatively homogeneous chronosequence of young ecosystems. Therefore, future research should address the question whether my findings can be extrapolated to more diverse soils and longer time scales by studying longer chronosequences on diverse parent materials.

5. Author contributions

I collected all samples treated in this thesis with the particular support of Zhilin Zhong and other colleagues from the Chinese Academy of Science during a sampling campaign that took place between August and October 2017 in the Hailuogou retreat area. Once in Germany, I sieved, ground and digested all samples myself, realized the measurement of diverse soil properties (i.e., pH, CO_3^{2-}, ECEC, grain size distribution, etc.), conducted the pH_{stat} weathering experiment and measured all extracts and digests (**Sections B and C**). I performed the data curation, formal analysis of the results and all statistical analyses (**Sections B to D**) and wrote the original drafts (**Sections A to D**). I tested diverse methods to purify Mg isotopes by cation-exchange chromatography in the clean air lab and implemented the method to measure Mg isotopes in our newly installed MC-ICP-MS (**Section D**). I wrote all first manuscript drafts.

Zhilin Zhong contributed to the field sampling and to writing review and editing (**Section B**).

Yanhong Wu was responsible for the conceptualization of the project, project administration, funding acquisition, investigation, supervision, and writing review and editing (**Sections B to D**).

Wolfgang Wilcke contributed to the methodology, conceptualization, project administration, funding acquisition, investigation, writing review and editing, and supervision of this thesis (**Sections A to D**).

6. References

Alt F, Oelmann Y, Schoning I, Wilcke W (**2013**) Phosphate release kinetics in calcareous grassland and forest soils in response to H+ addition. Soil Science Society of America Journal, 77, 2060–2070. *https://doi.org/10.2136/sssaj2013.02.0072*

Amtmann A, Sanders D (**1999**) Mechanism of Na+ uptake by plant cells. Advances in Botanical Research 29:75–112. https://doi.org/10.1016/S0065-2296(08)60310-9

Baribault TW, Kobe RK, Finley AO (**2012**) Tropical tree growth is correlated with soil phosphorus, potassium, and calcium, though not for legumes. Ecol Monogr 82:189–203. *https://doi.org/10.2307/41739364*

Bing H, Wu Y, Zhou J, Sun H, Luo J, Wang J, Yu D (**2016**) Stoichiometric variation of carbon, nitrogen, and phosphorus in soils and its implication for nutrient limitation in alpine ecosystem of Eastern Tibetan Plateau. J Soils Sediments 16:405–416. *https://doi. org/10.1007/s11368-015-1200-9*

Black JR, Yin QZ, Casey WH (**2006**) An experimental study of magnesium-isotope fraction in chlorophyll-a photosynthesis. Geochim. Cosmochim. Acta 70, 4072-4079. *https://doi.org/10.1016/j.gca.2006.06.010*

Black JR, Epstein E, Rains WD, Yin QZ, Casey WH (**2008**) Magnesium-Isotope fractionation during plant growth. Environmental Science and Technology 42 (21), 7831-7836. *https://doi.org/10.1021/es8012722*

Bockheim JG (**1980**) Solution and use of chronofunctions in studying soil development. Geoderma, 24, 71–85. *https://doi.org/10.1016/0016-7061(80)90035-X*

Bolou-Bi EB, Poszwa A, Leyval C, Vigier N (**2010**) Experimental determination of magnesium isotope fractionation during higher plant growth. Geochim. Cosmochim. Acta 74(9), 2523-2537. *https://doi.org/10.1016/j.gca.2010.02.010*

Bolou-Bi EB, Vigier N, Poszwa A, Boudot JP, Dambrine E (**2012**) Effects of biogeochemical processes on magnesium isotope variations in a forested catchment in the Vosges Mountains (France). Geochimica et Cosmochimica Acta 87, 341-355. *https://doi.org/10.1016/j.gca.2012.04.005*

Brenot A, Cloquet C, Vigier N, Carignan J, France-Lanord C (**2008**) Magnesium isotope systematics of the lithologically varied Moselle river basin, France. Geochim. Cosmochim. Acta 72, 5070–5089. *https://doi.org/10.1016/j.gca.2008.07.027*

Burstrom HG (**1968**) Calcium and plant growth. Biol Rev 43(3):287–316. *https://doi.org/10. 1111/j.1469-185X.1968.tb00962.x*

Chadwick OA, Derry LA, Vitousek PM, Huebert BJ, Hedin LO (**1999**) Changing sources of nutrients during four million years of ecosystem development. Nature 397-491:497. *https://doi.org/ 10.1038/17276*

Chen M, Lena QM (**2001**) Comparison of three aqua regia digestion methods for twenty Florida soils. Soil Sci Soc Am J 65:491–499

Cole DW, Rapp M (**1981**) Elemental cycling in forest ecosystems. Cambridge University Press, Cambridge, Dynamic Principles of Forest Ecosystems.

Diem B, Godbold DL (**1993**) Potassium, calcium and magnesium antagonism in clones of Popolus trichocarpa. Plant Soil 155(156):411-414. *https://doi.org/10.1007/BF00025070*

Elser JJ, Bracken MES, Cleland EE, Grunder S, Harpole WS, Hillebrandt H, Ngai JT, Seabloom EW, Shurin JB, Smith JE (**2007**) Global analysis of nitrogen and phosphorus limitation of primary producers in freshwater, marine and terrestrial ecosystems. Ecol Lett 10(12):1135–1142. *https://doi.org/10.1111/j.1461-0248.2007.01113.x*

Epron D, Laclau J-P, Almeida JCR, Gonçalves JLM, Ponton S, Sette CR, Delgado-Rojas JS, Bouillet J-P, Nouvellon Y (**2012**) Do changes in carbon allocation account for the growth response to potassium and sodium applications in tropical Eucalyptus plantations? Tree Physiol 32:667–679. *https://doi.org/10.1093/treephys/tpr107*

Epron D, Cabral OMR, Laclau J-P, Dannoura M, Packer AP, Plain C, et al. (**2015**) In situ 13CO2 pulse labelling of field-grown eucalypt trees revealed the effects of potassium nutrition and throughfall exclusion on phloem transport of photosynthetic carbon. Tree Physiology,36:6–21. *https://doi.org/10.1093/treephys/tpv090*

Ertiftik H, Zengin M (**2017**) Response of maize for grain to potassium and magnesium fertilizers in soils with high lime contents. Journal of Plant Nutrition 40:93–103. *https://doi.org/10.1080/01904167.2016.1201493*

Fageria NK (**1983**) Ionic Interactions in Rice Plants from Dilute Solutions. Plant Soil 70: 309–316. *https://doi.org/10.1007/BF02374887*

Fantle MS, Tipper ET (**2014**) Calcium isotopes in the global biogeochemical Ca cycle: Implications for development of a Ca isotope proxy. Earth-Science Reviews 129:148–177. *https://doi.org/10.1016/j.earscirev.2013.10.004*

Federer CA, Hornbeck JW, Tritton LM, Martin CW, Pierce RS, Smith CT (**1989**) Long-term depletion of calcium and other nutrients in eastern US forests. Environ Manag 13:593–601. *https://doi.org/10.1007/BF01874965*

Galy A, Bar-Matthews M, Halicz L, O'Nions RK (**2002**) Mg isotopic composition of carbonate: insight from speleothem formation. Earth and Planetary Science Letters 201(1):105-115. *https://doi.org/10.1016/S0012-821X(02)00675-1*

Galy A, Yoffe O, Janney PE, Williams RW, Cloquet C, Alard O, Halicz L, Wadhwa M, Hutcheon ID, Ramon E, Carignan J (**2003**) Magnesium isotope heterogeneity of the isotopic standard SRM980 and new reference materials for magnesium-isotope-ratio measurements. J Anal At Spectrom 18:1352. *https://doi.org/10.1039/b309273a*

Gao T, Ke S, Wang SJ, Li FB, Liu CS, Lei J, Liao C, Wu F (**2018**) Contrasting Mg isotopic compositions between Fe-Mn nodules and surrounding soils: accumulation of light Mg isotopes by Mg-depleted clay minerals and Fe oxides. Geochim. Cosmochim. Acta, 237, 205–222. *https://doi.org/10.1016/j.gca.2018.06.028*

González de Vega C, Chernonozhkin SM, Grigoryan R, Costas-Rodríguez M, Vanhaecke F (**2020**) Characterization of the new isotopic reference materials IRMM-524A and ERM-AE143 for Fe and Mg isotopic analysis of geological and biological samples. J. Anal. At. Spectrom. 35:2517-2529. *https://doi.org/10.1039/D0JA00225A*

Hacker N, Gleixner G, Lange M, Wilcke W, Oelmann Y (**2017**) Phosphorus release from mineral soil by acid hydrolysis: method development, kinetics, and plant community composition effects. Soil Sci. Soc. Am. J. 81, 1389–1400. *https://doi.org/10.2136/sssaj2017.02.0064*

He L, Tang Y (**2008**) Soil development along primary succession sequences on moraines of Hailuogou Glacier, Gongga Mountain, Sichuan, China. Catena 72, 259–269. *https://doi. org/10.1016/j.catena.2007.05.010*

Hindshaw RS, Rickli J, Leuthold J (**2019**) Mg and Li stable isotope ratios of rocks, minerals, and water in an outlet glacier of the Greenland Ice Sheet. Frontier in Earth Science, 7: 316. *https://doi.org/10.3389/feart.2019.00316*

Hindshaw RS, Tosca R, Tosca NJ, Tipper ET (**2020**) Experimental constraints on Mg isotope fractionation during clay formation: Implications for the global biogeochemical cycle of Mg. Earth Planet Sc. Lett., 531, 115980. *https://doi.org/10.1016/j.epsl.2019.115980*

Hock R, Rasul G, Adler C, et al. (**2019**) High Mountain Areas. In: IPCC Special Report on the Ocean and Cryosphere in a Changing Climate [H.-O. Pörtner, D.C. Roberts, V. Masson-Delmotte, P. Zhai, M. Tignor, E. Poloczanska, K. Mintenbeck, A. Alegría, M. Nicolai, A. Okem, J. Petzold, B. Rama, N.M.

Huang KJ, Teng FZ, Wei GJ, Ma JL, Bao ZY (**2012**) Adsorption- and desorption-controlled magnesium isotope fractionation during extreme weathering of basalt in Hainan Island, China. Earth Planet. Sci. Lett., 359–360, 73–83. *https://doi.org/10.1016/j.epsl.2012.10.007*

Huggett RJ (**1998**) Soil chronosequences, soil development, and soil evolution: A critical review. Catena, 32, 155–172. *https://doi.org/10.1016/S0341-8162(98)00053-8*

Hugonnet R, McNabb R., Berthier E., et al. (**2021**) Accelerated global glacier mass loss in the early twenty-first century. Nature 592, 726–731. *https://doi.org/10.1038/s41586-021-03436-z*

IPCC (**2021**) Climate Change 2021: The Physical Science Basis. Contribution of Working Group I to the Sixth Assessment Report of the Intergovernmental Panel on Climate Change [Masson-Delmotte, V., P. Zhai, A. Pirani, S.L. Connors, C. Péan, S. Berger, N. Caud, Y. Chen, L. Goldfarb, M.I. Gomis, M. Huang, K. Leitzell, E. Lonnoy, J.B.R. Matthews, T.K. Maycock, T. Waterfield, O. Yelekçi, R. Yu,and B. Zhou (eds.)]. Cambridge University Press, Cambridge, United Kingdom and New York, NY, USA, 2391 pp. *https://doi.org/10.1017/9781009157896*

IUSS Working Group WRB (**2022**) World Reference Base for Soil Resources. International soil classification system for naming soils and creating legends for soil maps. 4th edition. International Union of Soil Sciences (IUSS), Vienna, Austria.

Jia Y, Kong X, Weiser MD, Lv Y, Akbar S, Jia X, et al. (**2015**) Sodium limits litter decomposition rates in a subtropical forest: additional tests of the sodium ecosystem respiration hypothesis. Appl Soil Ecol 93:98e104. *https://doi.org/10.1016/j.apsoil.2015.04.012*

Kaspari M., Yanoviak SP, Dudley R, Yuan M, Clay NA (**2009**) Sodium shortage as a constraint on the carbon cycle in an inland tropical rainforest. Proc Natl Acad Sci USA 106: 19405e19409. *https://doi.org/10.1073/pnas.0906448106*

Kaspari M, Clay NA, Donoso DA, Yanoviak SP (**2014**) Sodium fertilization increases termites and enhances decomposition in an Amazonian forest. Ecology 95:795e800. *https://doi.org/10.1890/13-1274.1*

Kaupenjohan M, Wilcke W (**1995**) Heavy metal release from a serpentine soil using a pH-stat technique. Soil Sci. Soc. Am. J. 59, 1027-1031. *https://doi.org/10.2136/sssaj1995.03615995005900040010x*

Lasaga AC (**1984**) Chemical kinetics of water-rock interactions. Journal of Geophysical Research: Solid Earth, 89, B6 4009:4025. https://doi.org/10.1029/JB089iB06p04009

LeBauer DS, Treseder KK (**2008**) Nitrogen limitation of net primary productivity in terrestrial ecosystems is globally distributed. Ecology 89:379–379. *https://doi.org/10.1890/06-2057.1*

Lee SW, Ryu JS, Lee KS (**2014**) Magnesium isotope geochemistry in the Han River, South Korea. Chem Geol 364: 9–19. https://doi.org/10.1016/j.chemgeo.2013.11.022

Lei Y, Du L, Chen K, Plenkocić-Moraj SG (**2021**) Optimizing foliar allocation of limiting nutrients and fast-slow economic strategies drive forest succession along a glacier retreating chronosequence in the eastern Tibetan Plateau. Plant Soil 462:159–174. *https://doi.org/10.1007/s11104-020-04827-3*

Li Z, He Y, Yang X, Theakstone WH, Jia W, Pu T, Liu Q, He X, Song B, Zhang N, Wang S, Du J (**2010**) Changes of the Hailuogou glacier, Mt. Gongga, China, against the background of climate change during the Holocene. Quat Int 218:166–175. *https://doi. org/10.1016/j.quaint.2008.09.005*

Lilienfein J, Wilcke W, Thomas R, Vilela L, Lima SdC, Zech W (**2001**) Effects of Pinus caribaea plantations on the C, N, P, and S status of Brazilian savanna Oxisols. Forest Ecology and Management 147:171-182. *https://doi.org/10.1016/S0378-1127(00)00472-2*

Luo J, Li W, Liao X, He Z (**2004**) CO_2 emissions from soils of the deglaciered region on Hailuogou glacier in the past 100 years. J Mount Res 22:421–427

Marschner P (**2012**) Marschner's Mineral Nutrition of Higher Plants. Edition No. 3.

McLaughlin SB, Wimmer R (**1999**) Tansley review no. 104. Calcium physiology and terrestrial ecosystem processes. New Phytol 142(3):373–417. *https://doi.org/10.1046/j. 1469- 8137.1999.00420.x*

Mejia J, Coplen T, Berglund M, Brand W, De Bièvre P, Gröning M, Holden N, Irrgeher J, Loss R, Walczyk T, Prohaska T (**2016**) Isotopic compositions of the elements 2013 (IUPAC Technical Report). Pure and Applied Chemistry, 88(3), 293-306. *https://doi.org/10.1515/pac-2015-0503*

Mengel K, Kirkby EA, Kosegarten H, Appel T (**2001**) Principles of Plant Nutrition, fifth ed. Springer-Verlag and Heidelberg GmbH & Co. K, Berlin.

Nogués-Bravo D, Araújo MB, Errea MP, Martínez-Rica JP (**2007**) Exposure of global mountain systems to climate warming during the 21st Century. Glob Environ Chang 17:420–428. *https://doi.org/10.1016/j.gloenvcha.2006.11.007*

Opfergelt S, Georg RB, Delvaux B, Cabidoche YM, Burton KW, Halliday AN (**2012**)

Mechanisms of magnesium isotope fractionation in volcanic soil weathering sequences, Guadeloupe. Earth Planet. Sci Lett., 341-344, 176-185. *https://doi.org/10.1016/j.epsl.2012.06.010*

Opfergelt S, Burton KW, Georg RB, West AJ, Guicharnaud RA, Sigfusson B, Siebert C, Gislason SR, Halliday AN (**2014**) Magnesium retention on the soil exchange complex controlling Mg isotope variations in soils, soil solutions and vegetation in volcanic soils, Iceland. Geochim. Cosmochim. Acta, 125, 110:130. *https://doi.org/10.1016/j.gca.2013.09.036*

Paoli GD, Curran LM (**2007**) Soil nutrients limit fine litter production and tree growth in mature lowland forest of southwestern Borneo. Ecosystems 10:503–518. *https://doi.org/ 10.1007/s10021-007-9042-y*

Pogge von Strandmann PA, Burton KW, James RH, van Calsteren P, Gislason SR, Sigfússon, B (**2008**) The influence of weathering processes on riverine magnesium isotopes in a basaltic terrain. Earth Planet. Sci. Lett. 276(1-2), 187-197. *https://doi.org/10.1016/j.epsl.2008.09.020*

Pokharel R, Gerrits R, Schuessler JA, Frings PJ, Sobotka R, Gorbushina AA, von Blanckenburg F (**2018**) Magnesium stable isotope fractionation on a cellular level explored by Cyanobacteria and black fungi with implications for higher plants. Environ Sci Technol 52:12216-12224. *https://doi.org/10.1021/acs.est.8b02238*

Rhodes R, Miles N, Hughes, JC (**2018**) Interactions between potassium, calcium and magnesium in sugarcane grown on two contrasting soils in South Africa. Field Crops Research,223:1–11. *https://doi.org/10.1016/j.fcr.2018.01.001*

Richter FM, Watson EB, Mendybaev RA, Teng FZ, Janney PE (**2008**) Magnesium isotope fractionation in silicate melts by chemical and thermal diffusion. Geochim. Cosmochim. Acta 72(1), 206-220. *https://doi.org/10.1016/j.gca.2007.10.016*

Roger F, Calassou S, Lancelot J, Malavieille J, Mattauer M, Zhiqin X, Ziwen H, Liwei H (**1995**) Miocene emplacement and deformation of the Konga Shan granite (Xianshui He fault, west Sichuan, China): Geodynamic implications. Earth and Planetary Science Letters, 130, 201–216. *https://doi.org/10.1016/0012-821X(94)00252-T*

Rudnick RL, Gao S (**2003**) The Composition of the Continental Crust. In: Holland, H.D. and Turekian, K.K., Eds., Treatise on Geochemistry, Vol. 3, The Crust, Elsevier-Pergamon, Oxford, 1-64. *http://dx.doi.org/10.1016/b0-08-043751-6/03016-4*

Ryu JS, Jacobson AD, Holmden C, Lundstrom C, Zhang Z (**2011**) The major ion, δ 44/40 Ca, δ 44/42 Ca, and δ 26/24 Mg geochemistry of granite weathering at pH = 1 and T

=25°C: power-law processes and the relative reactivity of minerals. Geochim. Cosmochim. Acta 75(20), 6004–6026. *https://doi.org/10.1016/j.gca.2011.07.025*

Schaetzl RJ, Anderson S (**2005**) Soils: Genesis and Geomorphology. Cambridge University Press, New York.

Schwarz A, Wilcke W, Styk J, Zech W (**1999**) Heavy metal release from soils in batch pH(stat) experiments. Soil Science Society of America Journal, 63, 290–296. *https://doi.org/10.2136/sssaj1999.03615995006300020006x*

Searle MP, Roberts NMW, Chung SL, Lee YH, Cook KL, Elliott JR, Weller OM, St-Onge MR, Xu XW, Tan XB, Li K (**2016**) Age and anatomy of the Gongga Shan batholith, eastern Tibetan Plateau, and its relationship to the active Xianshui-he fault. Geosphere, 12, 948–970. *https://doi.org/10.1130/GES01244.1*

Selim HM, Amacher MC (**1997**) Reactivity and transport of heavy metals in soils. CRC press, Boca Raton, FL.

Stamm FM, Méheut M, Zambardi T, Chmeleff J, Schott J, Oelkers EH (**2022**) Determination of the equilibrium magnesium isotope fractionation factors between brucite and aqueous inorganic and organic species. Geochim. Cosmochim. Acta 336, 33–49. *https://doi.org/10.1016/j.gca.2022.09.003*

Süsser P (**1987**) Art, Menge und Wirkungsweise von Puffersubstanzen in Mineralbodenhorizonten forstlich genutzter Böden des Fichtelgebirges [PhD dissertation at the Chair of Soil Science, Technical University Munich, TUM].

Tavakkoli E, Rengasamy P, McDonald GK (**2010**) High concentrations of Na+ and Cl- ions in soil solution have simultaneous detrimental effects on growth of faba bean under salinity stress. Journal of experimental botany 61(15):4449–4459. *https://doi.org/10.1093/jxb/erq251*

Taylor SR, McLennan SM (**1985**) The Continental Crust: Its Composition and Evolution. Blackwell, Oxford, 1-312

Teng FZ, Wadhwa M, Helz RT (**2007**) Investigation of magnesium isotope fractionation during basalt differentiation: implications for a chondritic composition of the terrestrial mantle. Earth Planet. Sci. Lett. 261(1-2), 84-92. *https://doi.org/10.1016/j.epsl.2007.06.004*

Teng FZ, Li WY, Rudnick RL, Gardner LR (**2010**) Contrasting lithium and magnesium isotope fractionation during continental weathering. Earth Planet. Sci. Lett. 300 (1–2), 63-71. *https://doi.org/10.1016/j.epsl.2010.09.036*

Teng FZ, Yang W (**2014**) Comparison of factors affecting the accuracy of high-precision magnesium isotope analysis by multi-collector inductively coupled plasma mass spectrometry. Rapid Commun. Mass Spectrom. 28 (1), 19-24. *https://doi.org/10.1002/rcm.6752*

Tipper ET, Galy A, Gaillardet J, Bickle MJ, Elderfield H, Carder EA (**2006**) The magnesium isotope budget of the modern ocean: constraints from riverine magnesium isotope ratios. Earth Planet. Sci. Lett. 250(1-2), 241-253. *https://doi.org/10.1016/j.epsl.2006.07.037*

Tipper ET, Galy A, Bickle MJ (**2008**) Calcium and magnesium isotope systematics in rivers draining the Himalaya–Tibetan–Plateau region: lithological or fractionation control? Geochim. Cosmochim. Acta, 72, 1057–1075. *https://doi.org/10.1016/j.gca.2007.11.029*

Tränkner M, Tavakol E, Jákli B (**2018**) Functioning of potassium and magnesium in photosynthesis, photosynthate translocation and photoprotection. Physiol Plantarum 163: 414-431. *https://doi.org/10.1111/ppl.12747*

Uhlig D, Schuessler JA, Bouchez J, Dixon JL, von Blanckenburg F (**2017**) Quantifying nutrient uptake as driver of rock weathering in forest ecosystems by magnesium stable isotopes. Biogeosciences 14, 3111-3128. *https://doi.org/10.5194/bg-14-3111-2017*

Vitousek PM, Howarth RW (**1991**) Nitrogen limitation on land and in the sea—how can it occur? Biogeochemistry 13:87–115. *https://doi.org/10.1007/BF00002772*

Vogl J, Brandt B, Noordmann J, Rienitz O, Malinovskiy D (**2016**) Characterization of a series of absolute isotope reference materials for magnesium: ab initio calibration of the mass spectrometers, and determination of isotopic compositions and relative atomic weights. J. Anal. At. Spectrom., 31, 1440. *https://doi.org/10.1039/c6ja00013d*

Vogt KA, Grier CC, Vogt DJ (**1986**) Production, turnover, and nutrient dynamics of above- and belowground detritus of world forests. Adv Ecol Res 15:303–377. *https://doi.org/10.1016/S0065-2504(08) 60122-1*

Walker LR,Wardle DA, Bardgett RD, Clarkson BD (**2010**) The use of chronosequences in studies of ecological succession and soil development. Journal of Ecology, 98, 725–736. *https://doi.org/10.1111/j.1365-2745.2010.01664.x*

Wang J, Wu Y, Zhou J, Bing H, Sun H, He Q, Li J, Wilcke W (**2020**) Soil microbes become a major pool of biological phosphorus during the early stage of soil development with little evidence of competition for phosphorus with plants. Plant Soil 446:259–274. *https://doi.org/10.1007/s11104-019-04329-x*

Wilcke W, Yasin S, Abramowski U, Valarezo C, Zech W (**2002**) Nutrient storage and turnover in organic layers under tropical montane rain forest in Ecuador. Eur J Soil Sci 53:15–27. *https://doi.org/10.1046/j.1365-2389.2002.00411.x*

Wimpenny J, Gíslason SR, James RH, Gannoun A, Pogge Von Strandmann PAE, Burton KW (**2010**) The behaviour of Li and Mg isotopes during primary phase dissolution and secondary mineral formation in basalt. Geochim. Cosmochim. Acta, 74, 5259–5279. *https://doi.org/10.1016/j.gca.2010.06.028*

Wright SJ, Yavitt JB, Wurzburger N, Turner BL, Tanner EVJ, Sayer EJ, Santiago LS, Kaspari M, Hedin LO, Harms KE, Garcia MN, Corre MD (**2011**) Potassium, phosphorus, or nitrogen limit root allocation, tree growth, or litter production in a lowland tropical forest. Ecology 92:1616–1616. *https://doi.org/10.1890/10-1558.1*

Wu Y, Li W, Zhou J, Cao Y (**2013**) Temperature and precipitation variations at two meteorological stations on eastern slope of Gongga Mountain, SW China in the past two decades. J Mt Sci 10:370–377. *https:// doi. org/ 10. 1007/s11629- 013- 2328-y*

Wyn Jones RG, Lunt OR (**1967**) The function of calcium in plants. Bot Rev 33:407–426

Yang Z, Bing H, Zhou J, Wu Y, Sun H, Luo J, Sun S, Wang J (**2015**) Variation of mineral composition along the soil chronosequence at the Hailuogou glacier foreland of Gongga Mountain. Acta Pedol Sin 52(3):507–516. *https://doi.org/10.11766/trxb201406180301*

Yang D, Luo J, Peng P, Li W, Shi W, Jia L et al (**2021**) Dynamics of nitrogen and phosphorus accumulation and their stoichiometry along a chronosequence of forest primary succession in the Hailuogou glacier retreat area, eastern Tibetan Plateau. PLoS One 16(2):e0246433. *https:// doi.org/10.1371/journ al.pone.02464 33*

Young E and Galy A (**2004**) The isotope geochemistry and cosmochemistry of magnesium. Rev. Mineral. Geochem. Miner. Soc. Am., 55, 197–230. *https://doi.org/10.2138/gsrmg.55.1.197*

Zeien H, Brümmer GW (**1989**) Chemische Extraktion zur Bestimmung der Schwermetallbindungsformen in Böden. Mittlgn. Dtsch. Bodenkundl. Gesellsch. Sonderh. 59/I, Kongreßbd. Münster, 505–510

Zhang J, Luo J, DeLuca TH, Wang G, Sun S, Sun X, Hu Z, Zhang W (**2021**) Biogeochemical stoichiometry of soil and plant functional groups along a primary successional gradient following glacial retreat on the eastern Tibetan Plateau. Glob Ecol Conserv 26:e01491. *https://doi.org/10.1016/j.gecco.2021.e01491*

Zhou J, Wu YH, Prietzel J, Bing H, Yu D, Sun S, Luo J, Sun H (**2013**) Changes of soil phosphorus speciation along a 120-year soil chronosequence in the Hailuogou glacier retreat area (Gongga Mountain, SW China). Geoderma 195–196:251–259. *https://doi.org/10.1016/j. geoderma.2012.12.010*

Zhou J, Bing H, Wu Y, Yang Z, Wang J, Sun H, Luo J, Liang J (**2016a**) Rapid weathering processes of a 120-year-old chronosequence in the Hailuogou glacier foreland, Mt. Gongga, SW China. Geoderma 267:78–91. *https://doi.org/10.1016/j.geoderma.2015.12.024*

Zhou J, Wu, Y, Bing H, Yang Z, Wang J, Sun, H, Sun, S, Luo J (**2016b**) Variations in soil phosphorus biogeochemistry across six vegetation types along an altitudinal gradient in SW China. Catena 142:102-111. *https://doi.org/10.1016/j.catena.2016.03.004*

Zhou P (**2013**) The differentiation and influence factors of carbon sequestration of typical vegetation types in altitudinal belts of Gongga Mountain. Master thesis, University of Chinese Academy of Sciences, Beijing, China, pp. 32

B. Base cation stocks and fluxes

Initial carbonate weathering is linked with vegetation development along a 127-year glacial retreat chronosequence in the subtropical high mountainous Hailuogou region (SW China)

Nuria Basdediós[1], Zhilin Zhong[2], Yanhong Wu[2], Wolfgang Wilcke[1]

[1]Karlsruhe Institute of Technology (KIT), Institute of Geography and Geoecology, Reinhard-Baumeister-Platz 1, 76131 Karlsruhe, Germany

[2] Key Laboratory of Mountain Surface Processes and Ecological Regulation, Institute of Mountain Hazards and Environment, Chinese Academy of Sciences, Chengdu 610041, China

Plant and Soil (2022): 471, 609–628

DOI: 10.1007/s11104-021-05250-y

1 Abstract

Aims The retreat of glaciers is exposing new terrains to primary plant succession around the globe. To improve the understanding of vegetation development along a glacier retreat chronosequence, we (i) evaluated a possible link between base metal (Ca, Mg, K, Na) supply and vegetation establishment, (ii) determined the rates of the establishment of soil and plant base metal stocks, and (iii) estimated the size of the main base metal fluxes.

Methods We determined base metal stocks in the soil organic layer, the mineral topsoil (0-10 cm), and in leaves/needles, trunk, bark, branches and roots of the dominating shrub and tree species and estimated fluxes of atmospheric deposition, plant uptake and leaching losses along the 127-yr Hailuogou chronosequence.

Results Total ecosystem Ca and Mg stocks decreased along the chronosequence, while those of K and Na were unrelated with ecosystem age. Fortyfour and 30% of the initial stocks of Ca and Mg, respectively, were leached during the first 47 years, at rates of 130±10.6 g m^{-2} $year^{-1}$ Ca and 35±3.1 g m^{-2} $year^{-1}$ Mg. The organic layer accumulated at a mean rate of 288 g m^{-2} $year^{-1}$ providing a bioavailable base metal stock, which was especially important for K cycling.

Conclusions We suggest that the initial high Ca bioavailability because of a moderately alkaline soil pH and carbonate depletion in 47 years, together with the dissolution of easily-weatherable silicates providing enough Mg and K to the pioneer vegetation, contributed to the establishment of the mature forest in ca. 80 years.

2. Introduction

The worldwide increasing temperatures since the end of the Little Ice Age (LIA; IPCC 2021) have resulted in the retreat of high mountain glaciers in polar (Kabala and Zapart 2012; Moreau et al. 2008; Wietrzyk et al. 2018) and tropical regions (Cullen et al. 2013; Seehaus et al. 2019). Following glacial retreat, glacial debris is continuously deposited in the retreat areas serving as new substrate for soil and ecosystem development. Particularly during the time between deposition of the glacial debris and establishment of a vegetation cover, there is an enhanced risk of natural hazards typical for mountain areas, such as landslides, debris flows, erosion, and flooding. The main causes of this are the abundance of unconsolidated material and the lack of a vegetation cover which reduces surface runoff and wind and water erosion (Crozier 2010; Haeberli et al. 2017; Keiler et al. 2010; Portes et al. 2018; Richardson and Reynolds 2000). The similar climatic and geological conditions of a glacial retreat area allow us to apply space-for-time substitution approaches (Pickett 1989). Studies on primary succession on glacial moraines have been performed since the end of the 19th century (e.g., Coaz 1887; Crocker and Major 1955; Dickson BA and Crocker 1953; Friedel 1938) and continue to date (see compilation of studies in **Table B-S1**). Glacial retreat has accelerated during the second half of the 20th century (Zemp et al. 2008; Zhou et al. 2013) and is expected to continue for global mountain systems during the 21st century (Hock et al. 2019; Nogués-Bravo et al. 2007). Thus, the knowledge of the processes that drive vegetation succession is crucial to cope with the risks originating from the globally increasing glacial retreat areas.

Because of the harsh, high-elevation site conditions, glacier forelands are challenging environments for vegetation development. Although pioneer plants usually start colonizing young surfaces a few years after glacier melt, it needs various decades, if not centuries to develop a full vegetation cover (Burga et al. 2010; Conen et al. 2007; Vilmundardóttir et al. 2015). Many young primary successions (<200 yr) developing on different parent materials in different climate zones are dominated by pioneer mosses, dwarf shrubs and shrubs but lack fully developed forests (see compilation of studies in **Table B-S1**). The primary succession developing in the Hailuogou glacial retreat area has, however, surprisingly achieved the average biomass estimated for mature temperate coniferous forests (307 tones ha^{-1}, Cole and Rapp 1981) within a period of ~ 80 years (**Figure B-S1,** Luo et al. 2004).

Besides nitrogen (N) supply by microbial fixation from the atmosphere, the release of nutrients from parent materials by chemical weathering also plays a key role in vegetation succession (Chadwick et al. 1999). During chemical weathering processes, nutrients are released from minerals to soil solution as ions, which can readily move among the various geochemical and biological reservoirs and be lost via deep infiltration and stream water (Likens 2013). Plants can influence chemical weathering rates by a factor of two to five compared to the rates when plants are absent (Berner et al. 2004; Drever and Stillings 1997). Plants influence the biogeochemical cycle of nutrients by affecting their bioavailability in soils, taking up nutrients from the soil solution via their roots and their associations with mycorrhiza, storing them in tissues, and finally returning them to the soil via canopy leaching, litterfall, and organic matter decomposition. In this context, the formation of a soil organic layer on top of the mineral soil plays an important role, because it stores nutrients and slowly releases them for re-use by plants (Lilienfein et al. 2001; Wilcke et al. 2002). Different tree species can further influence nutrient cycling in soil, because of their different nutrient requirements (Larcher 2003). Deciduous tree species usually have higher Ca, Mg and K concentration in leaves and greater foliar biomass than coniferous tree species (Ericsson 1994), which causes larger metal fluxes with litterfall in deciduous than coniferous forests (Carnol and Bazgir 2013). Although N and phosphorous (P) are considered the most commonly limiting nutrients affecting biomass production in terrestrial ecosystems (Elser et al. 2007; LeBauer and Treseder 2008; Vitousek and Howarth 1991; Lei et al. 2021; Yang et al. 2021), previous studies have shown that Ca, Mg and K can have a great influence on tree growth and vegetation development (Baribault et al. 2012; Burstrom 1968; Epron et al. 2012; Federer et al. 1989; McLaughlin and Wimmer 1999; Paoli and Curran 2007; Wright et al. 2011). Sodium (Na) can also be taken up and used by vegetation (Amtmann and Sanders 1999). Sodium regulates cellular osmotic balance of microorganisms and thereby influences the decomposition of soil organic matter (Jia et al. 2015; Kaspari et al. 2009, 2014) and the resupply of bioavailable mineral nutrients. However, when high concentrations accumulate in the cytoplasm, Na interferes with K and Ca nutrition and disturbs efficient stomatal regulation (Marschner 2012; Tavakkoli et al. 2010). Moreover, high concentrations of any of these elements (i.e., Ca, Mg, K and/or Na) can lower or even inhibit the uptake of the others, which is known as cationic antagonistic effect (Diem and Godbold 1993; Ertiftik and Zengin 2017; Fageria

1983; Rhodes et al. 2018). Thus, at high Ca availability, e.g., in soils on limestone, Mg and K uptake can be limited (Ertiftik and Zengin 2017).

Our overall goal was to improve the understanding of the drivers of vegetation development on glacial debris. We hypothesized that (i) the vegetation establishment in the Hailuogou area, which surprisingly reaches the stage of a mature forest in only ~80 years, is linked with changes in total base metal stocks of the ecosystems attributable to a high initial bioavailability of Ca, Mg, K and Na, because the carbonic acid/carbonate buffer system maintains a near-neutral soil pH with a high base saturation in the early phase of the vegetation establishment. (ii) This high base metal availability allowed for the faster buildup of large base metal stocks in plants and in the soil organic layers than at other <200 yr-old glacial retreat chronosequences (**Table B-S1**), driven by particularly high base metal fluxes between soils and plants. (iii) After the carbonates and easily weatherable silicates have been dissolved, the base metal supply decreases considerably. However, this is compensated by the presence of an organic layer which provides plant-available nutrients to the vegetation and by a shift in the vegetation composition from deciduous to coniferous trees which reduces the base metal demand of the vegetation. The Hailuogou chronosequence has not been strongly disturbed by human activities, making this an ideal area to study biogeochemical element cycling in the early stage of soil and vegetation development at decadal scale.

3. Materials and methods

3.1. Study Area

The Hailuogou Glacier flows down the eastern slope of the Gongga Mountain, in the transition zone of the Sichuan Basin and the Tibetan Plateau, southwest China (**Figure A-3**). Because of a temperature increase, the Hailuogou Glacier has markedly retreated since the late 19th century (Li et al. 2010), developing an approximately 2 km-long, 50–200 m wide chronosequence, with an elevational difference of ~130 m. The climate is mainly controlled by the Southeast Monsoon. The mean annual temperature and precipitation at the Gongga Mountain Alpine Ecosystem Observation Station, Chinese Academy of Sciences, which is located in the same Hailuogou catchment (**Figure A-3**) are 4.2 °C and 1947 mm, respectively. For the eastern slope of the Gongga Mountain, where our study site

is located, Zhou et al. (2016) have reported a mean annual temperature of 5.6°C and 3.9°C at 2772 m.a.s.l. and 3060 m.a.s.l., i.e., an elevational temperature gradient of ca. 0.006°C m^{-1} or 0.77°C for the ca. 130 m elevational difference. In the same study, the mean annual precipitation was 1923 mm at 2772 m.a.s.l. and 1933 mm at 3060 m.a.s.l. resulting in a difference of ca. 4.5 mm (or 0.23% of the rainfall at 2772 m a.s.l.) between the youngest and oldest study sites. Rain falls mainly during the vegetation period (May to September; Wu et al. 2013). The parent material of soil formation is moraine and is mainly composed of silicates, including plagioclase (285 mg g^{-1}), quartz (245 mg g^{-1}), biotite (120 mg g^{-1}), hornblende (120 mg g^{-1}) and K-feldspar (100 mg g^{-1}) and non-silicatic carbonates (<103 mg g^{-1}) and apatite (<21 mg g^{-1}) (Yang et al. 2015; Zhou et al. 2016). The short time of pedogenesis (<130 years) resulted in the formation of initial soils without B horizon classified from the youngest to the oldest soils as Leptic Calcaric to Folic Dystric Regosols according to the World Reference Base for Soil Resources (IUSS Working Group WRB, 2014). The intense carbonate weathering and the rapid establishment of the vegetation decreased the pH of the mineral soil from 8.3 to 6.0 in only 47 years (**Table B-S2**).

Exposure ages of the different sites and trees ages at the Hailuogou Chronosequence have been determined based on historic records including aerial fotos and tree rings, respectively (Zhong et al. 1999). This study includes seven dated sites, de-glaciated between 0 (Site 1; 2982 m a.s.l.) and 127 years before our sampling (Site 7; 2855 m), which were previously described by Zhou et al. (2013). A complete primary vegetation successional sequence has rapidly developed along the retreat area, from bare land with pioneer mosses via a bush stage to forests successively dominated by the shrub species *Hippophae rhamnoides* L., which had a tree-like habit (i.e., it showed a single main trunk), reaching heights >5 m (Site 3, 37 yr, ~35% canopy cover, accompanied by scarce *Populus purdomii* Rehder and *Salix* spp. trees and the herb *Astragalus adsurgens* Pall. with a growth height <40 cm and 10% uncovered soil), the broad-leaved tree species *Populus purdomii* Rehder (Site 4, 47 yr, ~50% canopy coverage accompanied by the deciduous tree *Betula albosinensis* Burkill and scarce *H. rhamnoides* shrubs and *Abies fabri* (Mast.) Craib trees; Site 5, 59 yr, ~40% canopy coverage), and the coniferous tree species *Abies fabri* (Mast.) Craib (Site 5, 59 yr, ~40% canopy coverage; Site 6, 87 yr, ~60% canopy coverage; Site 7, 127 yr, ~40% canopy coverage) and *Picea brachytyla* (Franch.) E. Pritz. (Site 6, 20% canopy coverage; Site 7, 127 yr, 40% canopy coverage) (**Table B-1**). The percent canopy cover was estimated visually for each individual tree on three replicate 20 m x 20 m plots at each site by Luo et al. (2014).

Table B-1. Dominant tree species and their percentage cover, pH and CO_3^{2-} concentrations in the uppermost 10 cm of the mineral soil at the study sites of the Hailuogou chronosequence.

Site number	1	2	3	4	5	6	7
Site age (years)	0	5	37	47	59	87	127
Dominant tree species (percentage cover)	Bare land	Bare land	*H. rhamnoides* L. (30%)	*P.purdomii* R. (50%)	*A. fabri (*40%)	*A. fabri (*60%)	*P.brachytyla* (Franch.) *(*40%)
pH(H_2O)	8.0 ± 0	8.1 ± 0	6.1 ± 0.1	5.8 ± 0.2	5.9 ± 0.1	4.9 ± 0.1	5.2 ± 0.2
CO_3^{2-} (mg g^{-1})	19 ± 1	17 ± 1	2 ± 1	Not detected	Not detected	< 0.5	0.2 ± 0.1

Previous research on biologically relevant elements in the Hailuogou region focused on the change in C, N and P mass ratios and stocks (e.g., Bing et al. 2016b, He and Tang 2008; Wu et al. 2015; Yang et al. 2021; Zhang et al. 2021; Zhou et al. 2013) or contamination by trace metals (e.g. Bing et al. 2016a, 2019; Luo et al. 2015; Wang et al. 2020a). The latter studies described a rapid accumulation of organic matter and N in the topsoil, while the soil formation rate along the Hailuogou chronosequence decreased with increasing ecosystem age (He and Tang 2008). Zhou et al. (2016) reported that weathering processes in the Hailuogou are initially dominated by the weathering of carbonates followed by a more intense biogeochemical weathering (>80 yr) because of lower pH values. In a recent study, Yang et al. (2021) suggested that N is the main growth-limiting element in the Hailuogou area based on N:P stoichiometric ratios in leaves. Wang et al. (2021) recently reported a positive effect of pioneer N_2-fixing plants on the establishment of other non-N_2-fixing species after glacier retreat. However, the relationship between the bioavailability of base metals (Ca, Mg, K, Na) and vegetation development in this area have not yet been evaluated.

3.2. Field sampling

Soil samples were collected in August 2017 from seven ecosystem succession stages (Sites 1-7), which were exposed for 0, 5, 37, 47, 59, 87 and 127 years since glacier retreat (**Figure A-3**). Each ecosystem succession stage was sampled in triplicate. The distance between the sampled soil profiles was at least 20 m, except at Sites 1 and 2, where the distance was reduced to 10 m because the studied valley is narrower in the proximity of the glacier. Soil

profiles were hand-dug and five soil horizons sampled: Oi (fresh litter), Oe (shredded litter), Oa (dark layer of decomposed humus), A (surface mineral soil with humus enrichment), and C (weathered soil parent material). No organic layers were present at Sites 1 and 2 (0 and 5 years old, respectively).

Freshly cut leaves, 3-year-old needles, bark, branches, trunk, and roots of the dominant tree and shrub species were collected in triplicate for elemental analysis, in the surrounding of our replicate soil profiles, between August and October 2017 at each study site. To achieve a more representative sample of each replicate, a minimum of three individuals were randomly sampled from the trees of the same area. Four species were sampled along the chronosequence: *H. rhamnoides* (Site 3, 37 years), *P. purdomii* (Site 4, 47 years), *A. fabri* (Sites 5-6, 59 and 87 years), and *P. brachytyla* (Site 7, 127 years). Tree branches were randomly sampled from the tree canopy using pole shears. Bark samples were collected using an outdoor knife. The depth of cut was adjusted depending on the bark thickness in order to take a representative sample without reaching the cambium. Trunk samples equivalent to the radius of the sampled tree were collected using a tree corer with a diameter of 5.15 cm. Roots were manually washed out of a soil sample with defined volume.

Soil samples (mineral and organic horizons) were air-dried to constant weight in a drying room located in the research station. Mineral samples were sieved to collect the two fractions fine earth (<2 mm) and stones (soil >2 mm). Plant residues were removed from the soil. Leaf, needle, branch, bark, trunk and root samples were oven-dried to constant weight at 40°C during 72 hours and stored in sealed bags. Trunk and root samples were manually homogenized using an agate pestle and mortar. Bark and branch samples were homogenized using a blade grinding (Polymix PX-MFC 90 D) equipped with a 3.0 mm mesh size sieve. Aliquots of all samples were ground using a ball mill equipped with a zirconium oxide jar.

3.3. Chemical analyses

Soil pH was determined from the air-dried samples (<2 mm) by a glass electrode (WTW SenTix 81) in a 1:5 (v/v) soil:water suspension. Total element concentrations in the organic horizon, fine earth and stones were determined after digestion with concentrated HNO_3/HF/H_2O_2 (4:1.5:1, v:v:v) and in the plant compartments after digestion with 8 mL

of concentrated HNO_3 and 2 mL of concentrated H_2O_2 in a microwave oven (MARS6Xpress, CEM, Kamp-Lintfort, Germany). Elemental concentrations in the digests were analyzed using an inductively-coupled plasma optical-emission spectrometer (5100 VDV ICP-OES, Agilent, Waldbronn, Germany). Accuracy was assessed by the analysis of certified reference materials: SRM1547 (peach leaves) and SRM1515 (apple leaves) for organic samples and BCR2 (Columbia River Basalt 2) for soil samples. Average recoveries ± single standard deviation were 100 ± 10% for all certified element concentrations. Precision determined by duplicate measurements was <5%.

Carbonate content (CO_3^{2-}) in the fine earth was determined by measuring the volume of emitted carbon dioxide after reaction of the sample with 10% HCl in a Scheibler calcimeter. Inorganic C concentrations in the stones were measured with an elemental analyser (EuroEA Elemental Analyzer, HEKAtech, Wegberg, Germany), after muffling at 550°C.

Exchangeable cations (Ca, Mg, K, Na, and Al) in the mineral soil (2 g) were extracted with 1 M NH_4NO_3 in a 1:25 soil to solution ratio following the method described by Zeien and Brümmer (1989) and measured by ICP-OES. All our element concentrations and stocks refer to the air-dry mass of the samples.

3.4. Calculations and statistical analyses

Stocks

Stocks ($E_{plant\ compartment}$) of the respective element E (i. e., Ca, Mg, K or Na) in the different tree compartments (leaves/needles, branches, trunk, bark and roots) of the dominant shrub or tree species at each site were calculated by multiplying the corresponding compartment biomass (B_c) with the element concentrations measured in the different compartments (C_E) (**Eq. B-1**).

$$E_{plant\ compartment}\ (g\ m^{-2}) = B_c\ (g\ m^{-2}) \times C_E\ (g\ g^{-1}) \quad \textbf{(B-1)}$$

The B_c was calculated by multiplying the total biomass at each plot (**Table B-S3**), estimated for our study site from Luo et al. (2004) after applying a logistic fitting (**Figure B-S1**), with the proportional contribution of the tree compartments to total biomass taken from Zhou (2013) and for partitioning between trunk and bark from Wilcke and Lilienfein (2004) (**Table B-S4**). Tree biomass published by Luo et al. (2004) was calculated with the

allometric equations reported by Zhong et al. (1997), which are based on tree height and diameter at breast height. The biomass of the shrub species was obtained by Luo et al. (2004) through destructive sampling after harvesting and drying. With this approach, we assumed that the mean base metal concentrations of the dominant species was representative for the whole vegetation on the considered plot. To support this assumption, we calculated according to the mass contributions of the various tree compartments (leaves/needles, branches, bark, trunk, roots) weighted mean base metal concentrations of the dominant species (**Figure B-S2**). The results illustrate that the nutrient concentrations in the shrub and trees were low at Sites 3, 6, and 7 and higher at Sites 4 and 5. The coniferous tree species *A. fabri* showed significantly higher base metal concentrations at Site 5 than at Site 6. Moreover, at Site 3 the tree-like shrub *H. rhamnoides* contributed more to the total biomass than can be expected from its cover (**Table B-1**), because of its multiple branches and much taller stature than the second most abundant herb *A. adsurgens*. At Sites 6 and 7, the cover of the two coniferous tree species *A. fabri* and *P. brachytyla* together was >80% of the total cover, which we took as approximate measure of the contribution of the individual species to the total biomass on the respective plot. The two coniferous tree species did not show significantly different mass-weighted mean base metal concentrations (**Figure B-S2**). With respect to our extrapolation, the most critical study sites were Sites 4 and 5 with a mixed vegetation. To assess the validity of our extrapolation, we compared the base metal stocks of an assumed 100% cover of *A. fabri* with an assumed 100% cover of *P. purdomii* and did not find significant differences in the Ca, Mg and K stocks in the biomass (**Figure B-S3**). The estimate of the Ca, Mg and K stock in *P. purdomii* on Site 5 is based on the assumption that the lack of a difference in the concentrations of these elements in the leaves between Sites 4 and 5 implies that the concentrations in all other plant compartments are also similar.

Element stock in each soil organic layer ($E_{Oa/Oe/Oi}$) was calculated considering the elemental concentration ($C_{E\ Oa/Oe/Oi}$), the bulk density (BD_i) and the thickness (T_i) of the respective horizon (Oa, Oe, Oi) (**Eq. B-2**). Total organic horizon stock at each plot was calculated by summing up all individual horizons (**Eq. B-3**).

$$E_{Oa/Oe/Oi}\ (g\ m^{-2}) = C_{E\ Oa/Oe/Oi}\ (g\ g^{-1}) \times BD_i\ (g\ m^{-3}) \times T_i\ (m) \qquad \textbf{(B-2)}$$

$$E_{organic\ horizons} = E_{Oa} + E_{Oe} + E_{Oi} \qquad \textbf{(B-3)}$$

Soil mineral stocks ($E_{A/C}$) were calculated considering the contribution of the stones ($\chi_{i\ stones}$, vol.%) in the soils along the chronosequence, T_i, BD_i, and the elemental concentration in the stones (>2mm, $C_{Ei\ stones}$) and in the fine earth (fe <2mm, $C_{Ei\ fs}$), for the A and C horizons, respectively (**Eq. B-4**).

$$E_{A/C}\,(g\ m^{-2}) = E_{A/C\ stones}\,(g\ m^{-2}) \times \chi_{i\ stones} + E_{A/C\ fe}(g\ m^{-2}) \times (1-\chi_{i\ stones}) \quad (\mathbf{B\text{-}4})$$

where:

$$E_{A/C\ fe}\,(g\ m^{-2}) = CE_{i\ fe}\,(g\ g^{-1}) \times BD_i\,(g\ m^{-3}) \times T_i\,(m) \quad (\mathbf{B\text{-}5})$$

$$E_{A/C\ stones}\,(g\ m^{-2}) = CE_{i\ stones}\,(g\ g^{-1}) \times 2.65 \times 10^6\,(g\ m^{-3}) \times T_i\,(m) \quad (\mathbf{B\text{-}6})$$

Bulk densities (BD_i) and stone volume were taken from Zhou et al. (2016) and Wang et al. (2020c), who studied the same sites as in our study. The soil particle density was assumed as 2.65 g cm^{-3} (**Eq. B-6**; Zhou et al. 2016). To calculate stocks of the extractable cations in the mineral soil, we only considered the fine earth, assuming that no extractable cations were present in the stones.

To account for the decrease in bulk density of the A horizon related with the loosening of soil during pedogenesis by weathering and ecosystem succession, the thickness of the C horizon (T_C) underlying the A horizon was adjusted in our stock calculation using **Eq. B-7**,

$$T_C\,(m) = 0.1\,(m) - T_A\,(m) \times \frac{BD_A\,(g\ m^{-3})}{BD_C(g\ m^{-3})} \quad (\mathbf{B\text{-}7})$$

where T_A is the thickness of the A horizon, 0.1 m is the initial mineral soil depth and BD_A and BD_C are the field bulk densities of the local A and C horizons, respectively. Total mineral soil stock ($E_{mineral\ horizons}$) was calculated by summing up the individual A and C horizon stocks. Additionally, we calculated the stocks of the mineral soil assuming that the density of the C horizon was initially the same at all the sites (BD_C = BD_C at Site 1, along the chronosequence) (**Figure B-S4**). There were no significant differences between the two approaches so that we only present the results of **Eq. B-7**.

Total stock (g m^{-2}) at each plot was calculated by summing up the individual stocks of the different plant compartments, ($E_{plant\ compartment}$; leaves/needles, branch, trunk, bark and root) and organic and mineral horizons (**Eq. B-8**).

$$E_{total\ stock} = E_{plant\ compartment} + E_{organic\ horizons} + E_{mineral\ horizons} \quad (\mathbf{B\text{-}8})$$

Fluxes

Annual plant uptake of base metals was calculated by multiplying the annual net primary productivity (NPP) (**Table B-S3**) with the mass-weighted mean element concentration of the plant ($C_{E\ plant}$) (**Eq. B-9**). NPP was taken from Luo et al. (2004), who derived it from measurements of the tree diameter growth at breast height of all individual trees or shrubs on a study plot, which was translated into biomass growth with the help of the allometric equations of Zhong et al. (1997).

$$E_{plant\ uptake}\ (g\ m^{-2}\ year^{-1}) = NPP\ (g\ m^{-2}\ year^{-1}) \times C_{E\ plant}\ (g\ g^{-1}) \quad (\mathbf{B\text{-}9})$$

Total deposition (TD_E, g m^{-2} $year^{-1}$) for any element E was calculated with **Eq. B-10**

$$TD_E = BDep_E + DD_E \quad (\mathbf{B\text{-}10})$$

where $BDep_E$ represents the bulk deposition measured with a Hellmann-type rain collector and DD_E is the estimation of the fine particulate dry deposition. Data of $BDep_E$ were obtained from the Gongga Mountain Alpine Ecosystem Observation Station (3000 m above sea level), Chinese Academy of Sciences (Zhou et al. 2016), which is located in the Hailuogou river catchment, where our study sites are. Dry deposition (DD_E) was roughly estimated by multiplying the relationship $DD/BDep_E$ published by Wilcke et al. (2017), calculated using the canopy budget method from Ulrich (1983) in a tropical forest with similar precipitation than that in the Hailuogou area. Because the scavenging of fine particulates from the atmosphere is related with the size of the plant surface of the forest canopy (Freer-Smith et al. 2005; Song et al. 2015), we scaled the $DD/BDep_E$ ratio by multiplying with the ratio of biomass at each individual site to that at Site 7 (127 years). This assumes that only the forest at Site 7 had a similar $DD/BDep_E$ ratio than the native montane forest in Ecuador used as reference and that the scavenging surface of the canopy is proportional to the biomass.

Leaching of the element E (L_E) from the soil to the stream (= element export with the stream) was estimated from the concentration in the stream water ($C_{E\ SW}$, data from Zhou et al. 2016), the mean annual precipitation (Pr, data from Wu et al. 2013) and the fraction of rainfall lost via the stream (α) (**Eq. B-11**). The runoff coefficient α was individually adjusted to each of our sites by multiplying the transpiration of a mature forest taken from Sun et al. (2013) with the ratio of biomass at each individual site to that at Site 7. The canopy interception loss was also taken from Sun et al. (2013), who provided interception loss values for different succession stages of our chronosequence allowing for interpolating data for two sites for which no data were available (**Table B-S3**). The fraction of rainfall

lost via the stream near the glacier forefront was estimated at 86% (Brock et al. 2010; Small et al. 2018).

$$L_E \text{ (g m}^{-2} \text{ year}^{-1}) = C_{E\,SW} \text{ (g L}^{-1}) \text{ x Pr (L m}^{-2} \text{ year}^{-1}) \text{ x } \alpha \quad \textbf{(B-11)}$$

Our estimate of the base metal leaching losses is based on the assumptions that all water passes through the deep subsoil, which consists of the unchanged glacial debris at all study sites and that during this passage chemical equilibrium of the soil solution with the substrate is reached via almost instantaneous cation exchange and mineral precipitation processes because any water flow through the debris and soils takes long enough to reach these fast equilibria. This assumption is reasonable because the length of the water path from the study soils to the stream is at least in the range of >1 m so that even at a high water conductivity of 10^{-4} m s^{-1}, it would take the water >160 h to pass from the soil to the stream and thus long enough for equilibration. As a consequence, the base metal output of our study sites only depended on the fraction of water percolating through the subsoil to the stream described by α and the mean base metal concentration in stream water.

Mean depletion rates (g m^{-2} $year^{-1}$) of the Ca and Mg stocks in the total ecosystem along the first stage of the chronosequence (from 0 to 47 years) were approximated by fitting a linear relationship of the total stocks versus time. Mg and K release from the depletion of biotite and hornblende was estimated from mineral composition data taken from Zhou et al. (2016) for the same study sites.

In order to compare the budget of the independently estimated ecosystem fluxes (input: atmospheric deposition; outputs: loss with stream flow, accumulation in the organic layer and biomass; all in g m^{-2} $year^{-1}$) with the cumulative stock change in the mineral topsoil (uppermost 10 cm, in g m^{-2}), we multiplied the respective flux by the site age.

Statistical evaluation

Normal distribution of the data was checked with the Shapiro-Wilk test. Pearson correlation, linear regression, and non-linear function fitting were used to evaluate relationships between variables. Calculation of total stocks using (i) the local BDc (**Eq. B-7**) or (ii) assuming that the density of the C horizon was initially the same at all sites (i.e., equal to the glacial debris, 0 yr old site) were tested for significant differences with independent two-sample t-tests at each site. One-way analysis of variance (ANOVA) and a Tukey's HSD post-hoc test were applied to detect significant differences between total stocks among the various study sites. Normal distribution of residuals was visually

inspected. Homoscedasticity was confirmed for our data after applying the Levene's test. Statistical analyses were conducted with the statistical software R (R Core Team, 2019). Tukey's HSD post hoc tests following ANOVA were performed with the 'agricolae' package (de Mendiburu 2021). Significance was set at $p < 0.05$.

4. Results

4.1. Base metal depletion rates in the entire ecosystem

Total ecosystem stocks of Ca and Mg decreased along the chronosequence (**Figure B-1a, b).** Most of the depletion of Ca and Mg occurred during the first 47 years of soil exposure, paralleling the pH decrease from 8.0 to 5.8 in the mineral topsoil and the loss of carbonates (**Table B-1**), likely mainly calcite ($CaCO_3$) (Zhou et al. 2016). Ca and Mg stocks decreased at rates of 130 ± 10.6 g m^{-2} and 35 ± 3.1 g m^{-2} over the first 47 years of soil development, respectively. This entailed that 44% of the initial stock of Ca was leached during the first 47 years after glacier retreat, accompanied by 30% of the initial Mg stock. After most of the carbonates were dissolved and the pH decreased to the strong acid/aluminum oxide buffer range, the annual depletion of Ca and Mg slowed down (**Figure B-1a, b; Table B-1).**

Contrary to Ca and Mg, there was no clear relationship between K and Na total ecosystem stocks and development time (**Figure B-1c, d**). Instead, K and Na total stocks remained similar at on average 5162 ± 710 g m^{-2} K and 3530 ± 429 g m^{-2} Na along the chronosequence.

Table B-2. Fluxes of Ca, Mg, K and Na along the Hailuogou chronosequence (g m^{-2} $year^{-1}$) at each study site along the Hailuogou glacier retreat chronosequence. Atmospheric deposition includes bulk and estimated fine particulate dry deposition. Element release from carbonates was calculated from the difference in carbonate concentrations between two consecutive sites divided by the difference in site age in years, considering the amount of the inorganic C that is present as $CaCO_3$ or as $CaMg(CO_3)_2$ (Zhou et al. 2016). Carbonate export after >59 years was negligible (not detected, ND). Release from carbonates, plant uptake and accumulation in the organic layer (Oa + Oe + Oi) are presented as means ± single standard deviations (n=3).

	Site age (year)	**0**	**37**	**47**	**59**	**87**	**127**
Ca	Atmospheric deposition	1.3 ± 0.3	2.1 ± 0.3	2.3 ± 0.3	2.6 ± 0.3	3.0 ± 0.3	3.2 ± 0.3
	Plant uptake		31 ± 6	64 ± 6	62 ± 2.0	22 ± 3.0	39 ± 6.5
	Accumulation in the org. layer		6.8 ± 2.8	12.2 ± 0.6	8.0 ± 0.5	2.5 ± 0.5	3.7 ± 0.7
	Stream export	31	77	59	55	48	40
Mg	Atmospheric deposition	0.3 ± 0.2	0.5 ± 0.2	0.5 ± 0.2	0.6 ± 0.2	0.7 ± 0.2	0.7 ± 0.2
	Plant uptake		2.1 ± 0.2	4.8 ± 1.5	3.5 ± 0.2	2.4 ± 0.3	3.5 ± 0.3
	Accumulation in the org. layer		2.2 ± 1.4	4.0 ± 0.7	2.6 ± 0.8	0.7 ± 0.3	0.9 ± 0.2
	Stream export	0.8	5.5	4.8	5.2	5.5	4.1
K	Atmospheric deposition	3.6 ± 0.5	5.3 ± 0.5	6.0 ± 0.5	6.7 ± 0.6	7.5 ± 0.6	8.0 ± 0.6
	Plant uptake		34 ± 1.9	44.± 2.7	36 ± 5.8	29 ± 1.5	29 ± 3.6
	Accumulation in the org. layer		2.6 ± 2.0	5.5 ± 0.7	3.9 ± 1.5	1.2 ± 0.4	1.4 ± 0.3
	Stream export	5.0	7.0	5.9	6.2	4.7	2.7
Na	Atmospheric deposition	0.3 ± 0.1	0.5 ± 0.1	0.6 ± 0.1	0.6 ± 0.1	0.7 ± 0.1	0.8 ± 0.1
	Plant uptake		0.1	<0.1	<0.1	<0.1	<0.1
	Accumulation in the org. layer		1.7 ± 1.4	3.4 ± 0.7	2.1 ± 1.1	0.8 ± 0.5	0.6 ± 0.1
	Stream export	0.4	1.4	1.1	1.0	1.0	0.8

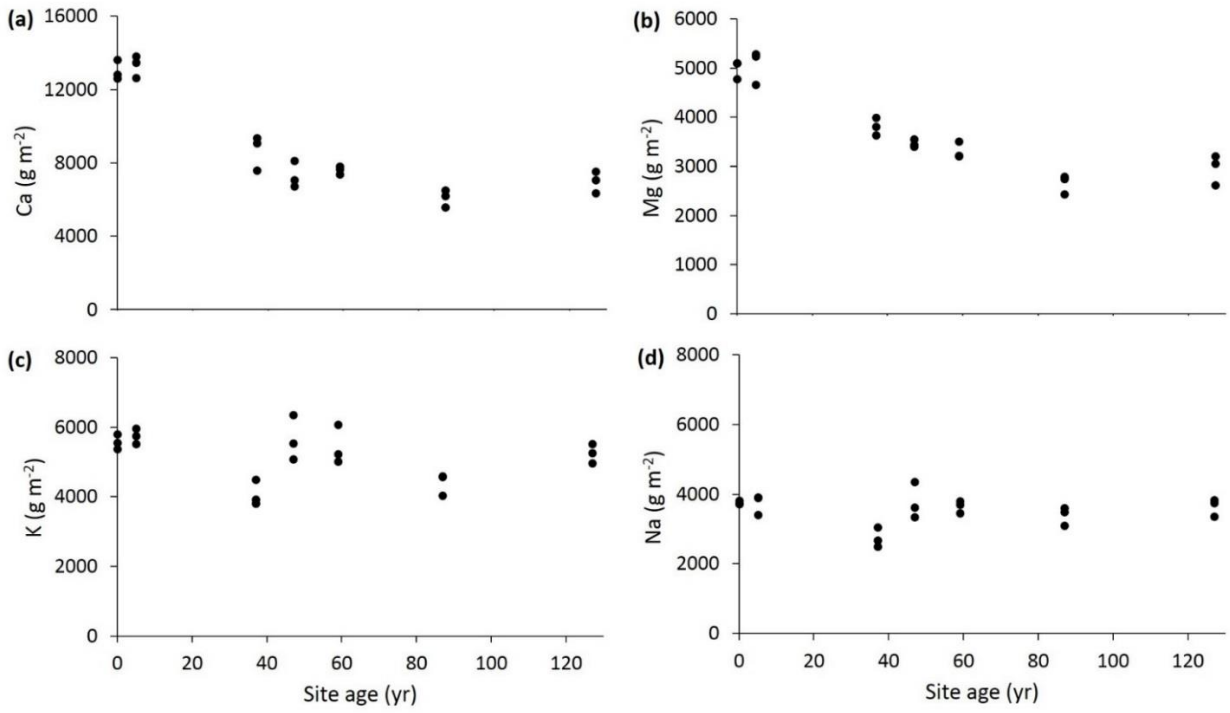

Figure B-1. Total stocks, including above and belowground biomass, the organic layer, and the upper 10 cm of the mineral soil (fine earth + stones), of Ca (**a**), Mg (**b**), K (**c**) and Na (**d**) along the Hailuogou chronosequence. Different points at each site age represent spatially independent replicates.

4.2. Base metal stocks in the soils

Most of the total element (i.e. Ca, Mg, K and Na) stock was stored in the mineral topsoil (0-10 cm; **Table B-S5**). The initial weathering of carbonates and subsequent loss of Ca (**Tables B-1 and B-2**) accounted for 40-60% of the total loss of Ca in the mineral topsoil along the chronosequence, compared to the immediate glacier forefield (0 yr-old site). Mg stocks in the mineral topsoil soil decreased from 4990 ± 196 g m^{-2} to 2620 ± 202 g m^{-2} over the first 47 years, and further decreased only slightly from 47 to 127 years (**Table B-S5**). K and Na mineral soil stocks remained similar at on average 5075 ± 700 g m^{-2} K and 3459 ± 420 g m^{-2} Na along the whole chronosequence.

The exchangeable Mg stock in the mineral soil consistently increased along the chronosequence from 0.7 ± 0.0 g m^{-2} to 2.3 ± 0.5 g m^{-2}, while no trend was found in the exchangeable K and Na concentrations with time (**Table B-S5**). It was not possible to quantify exchangeable Ca in the carbonate-containing soils, because of the partial dissolution of calcite in our extract (Tessier et al. 1979, Klimova et al. 2011).

The accumulation of organic matter on top of the mineral soil, which increased at a mean annual rate of 288 g m^{-2} over the studied time span, promoted the formation of an organic horizon of increasing thickness (**Table B-S2**) that stores a large amount of nutrients (**Table B-S5**). The strongest element accumulation in the combined organic horizons occurred from 37 to 47 years after glacier retreat (**Figure B-2**), accompanied by the establishment of a young *P. purdommii*-dominated forest. After the establishment of the coniferous forest, 87 years after deglaciation, the annual accumulation sharply decreased for all the studied elements (**Table B-2**). The mean concentration of the base metals in the organic horizons increased with depth (i.e., Oi < Oe < Oa) (**Figure B-2**).

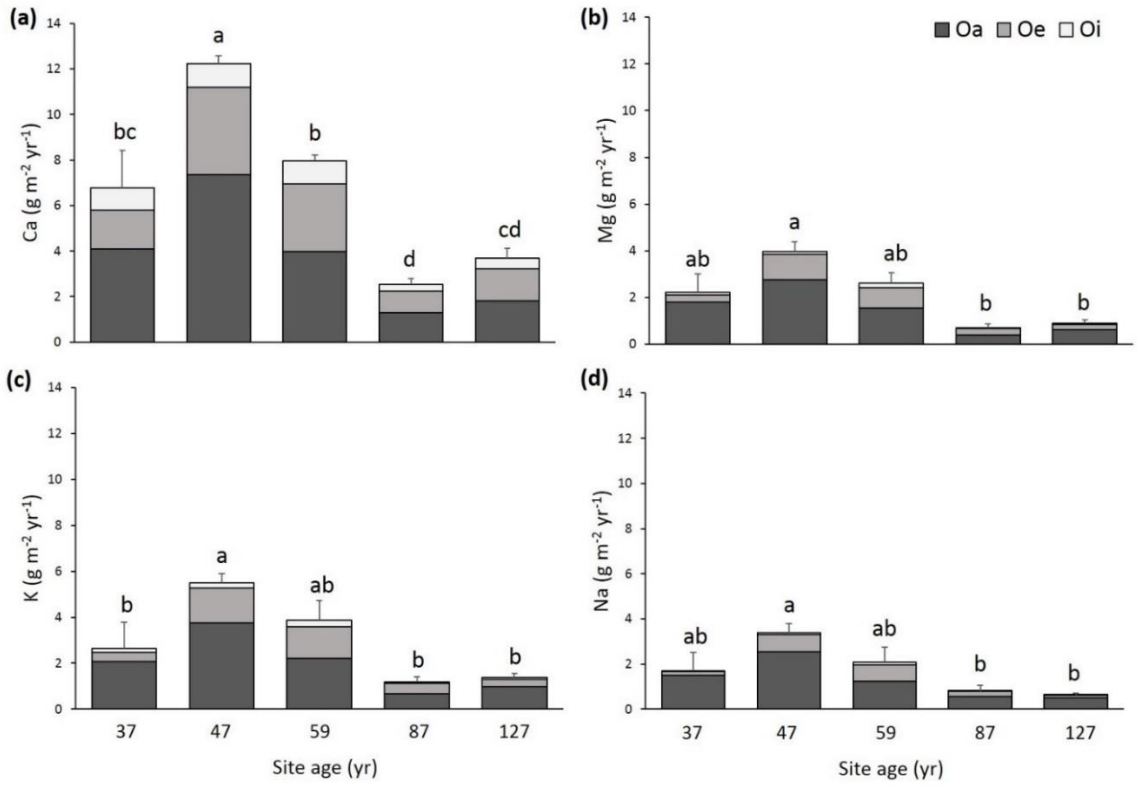

Figure B-2. Mean annual accumulation of Ca (**a**), Mg (**b**), K (**c**), and Na (**d**) in the different organic horizons: Oi (fresh litter), Oe (shredded litter) and Oa (dark layer of decomposed humus) along the Hailuogou chronosequence. Error bars represent single standard errors of the total annual accumulation of all organic layers combined (n = 3 spatially independent replicates). Letters indicate significant differences among the annual base metal accumulation along the chronosequence according to Tukey's HSD post-hoc test.

4.3. Base metal stocks in the plants

Total stocks in aboveground and belowground biomass ranged from 77 ± 17 to 259 ± 26 g m^{-2} Ca, 5.3 ± 0.7 to 18.6 ± 11.8 g m^{-2} Mg and 92 ± 7 to 144 ± 33 g m^{-2} K, and were consistently highest at the 47 and at the 59 year-old sites (**Table B-S5**). The distribution of base metals varied among different tree compartments with tree species and site (**Figure B-S2**). The largest stocks of Ca and Mg resided in the bark (Ca: 24-39% of the stock in the aboveground and belowground biomass, Mg: 8-24%), roots (Ca: 11-39%, Mg: 15-42%), and trunk (Ca: 5-35%, Mg: 5-53%), while K was mainly stored in branches (19-46%), trunk (4-29%) and roots (14-24%). The Na stocks in the different aboveground plant compartments were < 0.04 g m^{-2} and averaged 0.2 ± 0.1 g m^{-2} in the roots.

The plant compartment contributing most to the biomass was the trunk, which accounted for 45% of the total biomass in the shrub and the deciduous trees and 58% in the coniferous trees (**Table B-S4**), followed by the branches (23% in the shrub and deciduous trees and 13% in the coniferous trees). The leaves/needles contributed the least, accounting for only 4% of the total biomass in all considered tree and shrub species.

4.4. Base metal fluxes

Annual atmospheric deposition to the whole study area varied from 1.3 - 3.2 g m^{-2} Ca, 0.3 – 0.7 g m^{-2} Mg, 3.6 – 8.0 g m^{-2} K, and 0.3 – 0.8 g m^{-2} Na (**Table B-2**). The estimated dry deposition increased along the chronosequence, since the scavenging of fine particulates from the atmosphere by the vegetation increases with increasing surface area of the canopy (Freer-Smith et al. 2005; Song et al. 2015), which we approximated by biomass (**Table B-2)**. Annual losses of Ca and Mg via the stream were between one and two orders of magnitude higher than the estimated bulk deposition, while those of K and Na were in a similar range in bulk deposition and stream export (**Table B-2; Figure B-3**).

Total aboveground and belowground plant biomass increased with site age along the chronosequence (**Figure B-S5**) at rates of 380 ± 33 g m^{-2} $year^{-1}$. Annual plant uptake ranged from 22 - 64 g m^{-2} Ca, 2.1 - 4.8 g m^{-2} Mg and 29 - 44 g m^{-2} K, but did not show a consistent temporal trend along the chronosequence (**Table B-2)**. Because Ca, Mg, and K concentrations were considerably higher in *P. purdomii* foliage than in all other sampled tree species, sites where *P. purdomii* was growing usually showed the highest plant uptake

of base metals. Annual Na uptake ranged from not detected to 0.1 g m^{-2}. The accumulation of base metals in the organic horizons along the chronosequence generally decreased in the order Ca > K > Mg > Na (**Table B-2**).

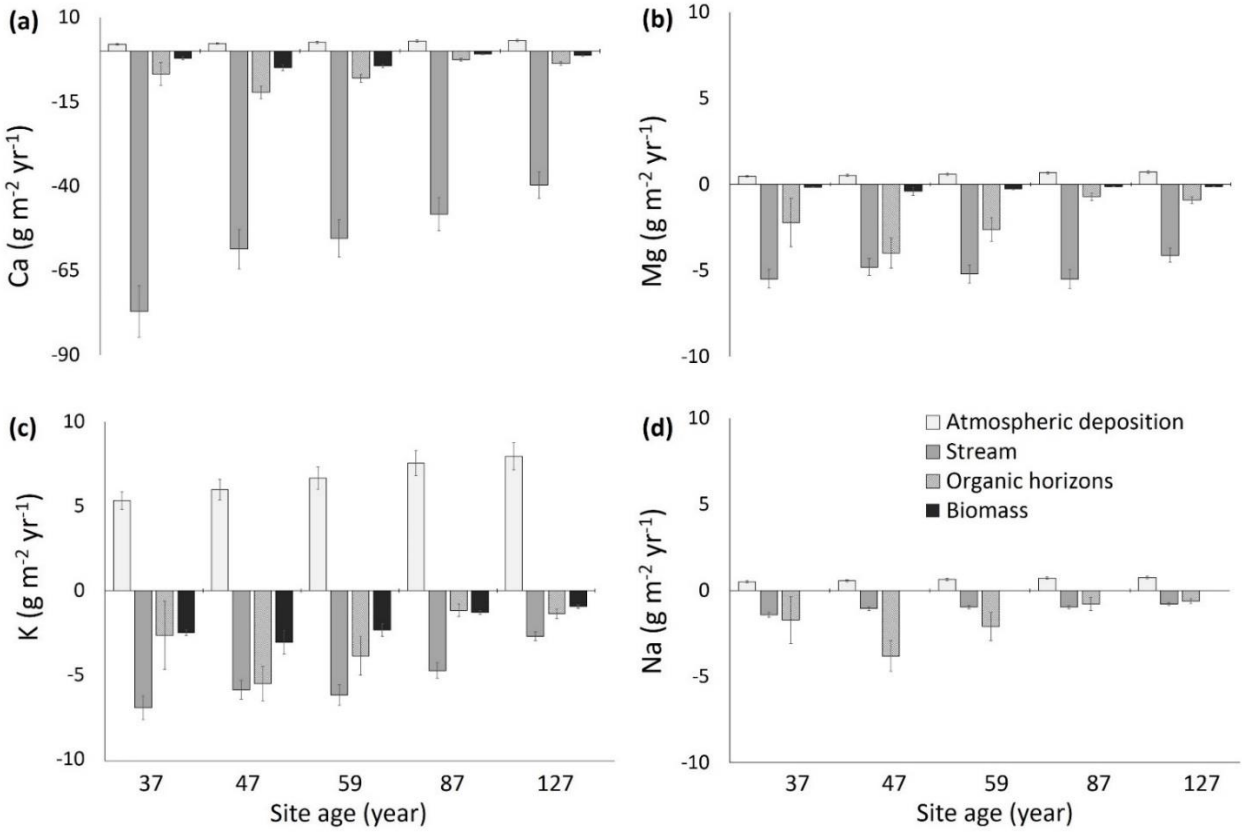

Figure B-3. Main fluxes of Ca (a), Mg (b), K (c) and Na (d) into and out of the uppermost 10 cm of the mineral soil along the Hailuogou chronosequence. Error bars in the columns represent single standard deviations (n=3). A standard deviation of 10% of the value was assumed for atmospheric deposition and stream. Inputs have positive and outputs negative values.

To determine whether the individual fluxes matched the total base metal loss, we compared the release of base metals in the mineral topsoil (0-10 cm), which represented the part of the mineral soil where most of the roots were located, with the budgets of the independently determined individual fluxes along the chronosequence (**Figure B-4**). Moreover, we included the part of the change in the Ca, Mg and K stocks, which was attributable to the loss of easily weatherable minerals (calcite, biotite and hornblende). The CO_3^{2-} concentrations decreased in the topsoil at a rate of 113 ± 15 g m^{-2} yr^{-1} CO_3^{2-} during

the first 47 years after glacier retreat and was then gone (**Table B-1**). This resulted in a Ca depletion of 79 g m^{-2} yr^{-1}. The Mg depletion in the mineral topsoil (0-10 cm) attributed to the loss of hornblende + biotite was 21 g m^{-2} yr^{-1} in the first 47 years of the chronosequence, during which the pH dropped markedly (**Table B-1**) and 8 g m^{-2} yr^{-1} in the later 80 years. The K depletion attributed to the loss of biotite was 19 g m^{-2} yr^{-1} (0-47 yr) and 6 g m^{-2} yr^{-1} (47-127 yr).

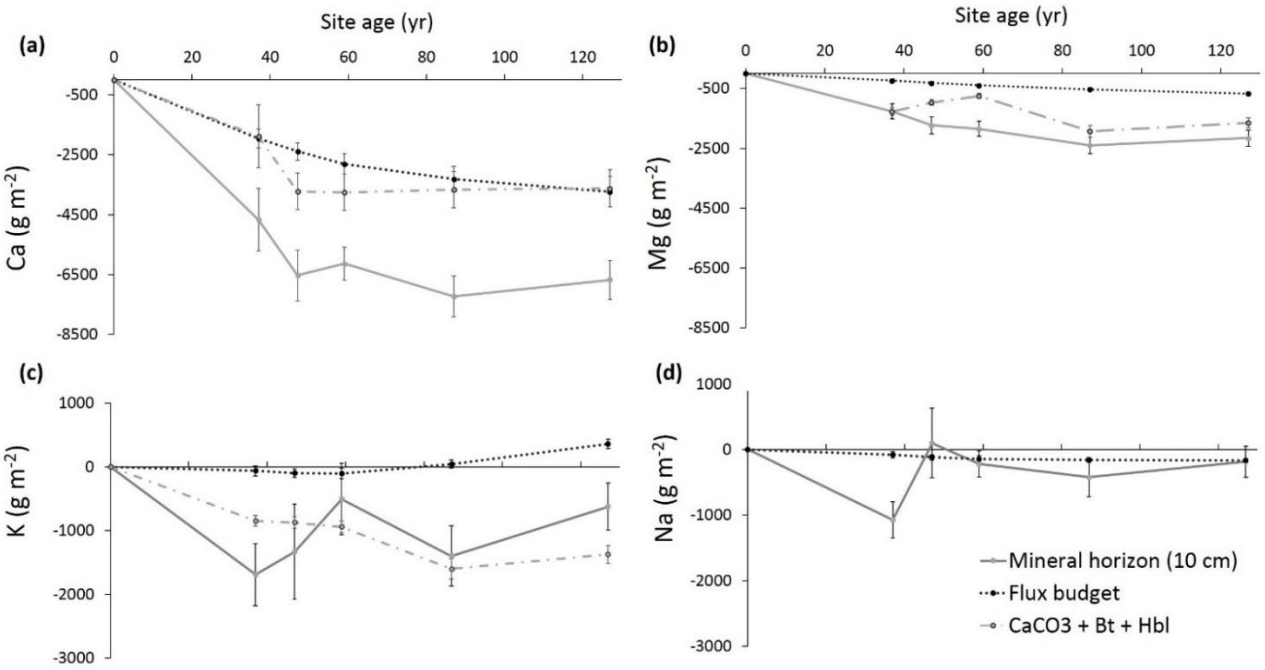

Figure B-4. Release of Ca (a), Mg (b), K (c) and Na (d) from the mineral topsoil (-10 cm) compared with the budget of the independently determined individual fluxes including the inputs atmospheric deposition and the outputs accumulation in the different tree compartments and organic layers and export with the stream (sum of the fluxes shown in **Figure B-3**). We also included the release of Ca, Mg and K attributed to calcite (Ca), biotite (Mg and K) and hornblende (Mg) depletion ($CaCO_3$ + Bt + Hbl) relative to the 0 yr-old site. Error bars represent single standard deviations of three replicate plots at each site, which was in the case of the flux budget calculated by Gaussian error propagation from the standard errors of the individual fluxes.

Other minerals included in the glacial debris and containing Mg or K, such as chlorite or K-feldspar, have not been included in this estimation because their concentration hardly changed after 127 years. The chlorite concentration decreased from 40 to 30 mg g^{-1} in the topsoil while that of K-feldspar varied inconsistently from 67 (37 year-old site) to 120 mg g^{-1} (87 year-old site, Zhou et al. 2016). **Figure B-4** illustrates that the budgets of the fluxes

shown in **Figure B-3** only explained a small part of the changes in the stocks of Ca and Mg, while the loss of the considered easily weatherable mineral explained a large part.

5. Discussion

5.1. Change in the total and soil base metal stocks and fluxes

The most rapidly depleted element from the mineral topsoil along the chronosequence was Ca, followed by Mg, while K and Na stocks remained similar (**Figure B-1**). We attribute the higher loss of Ca relative to the other elements to the depletion of carbonates (**Tables B-S2 and B-S5**), dominated by calcite ($CaCO_3$, Zhou et al. 2016). The CO_3^{2-} decrease rate in the topsoil of 113 ± 15 g m^{-2} yr^{-1} CO_3^{2-} during the first 47 years after glacier retreat was higher than in other soil chronosequences evolving from parent materials containing a broad range of $CaCO_3$ concentrations (20-340 mg g^{-1}), where the loss of CO_3^{2-} ranged from 14 to 65 g m^{-2} $year^{-1}$ (Van Breemen and Protz 1988). However, our CO_3^{2-} dissolution rate was in the range of that found in older soils (>10.000 years) in Switzerland (91 – 136 g m^{-2} $year^{-1}$ CO_3^{2-}; Egli and Fitze 2001) and slightly lower than in ~193 yr old Calcaric Regosols soils in the Alps, which, in contrast to our study site, originally contained more carbonates (70-180 mg g^{-1} of CO_3^{2-}) in the topsoil (Egli and Fitze 2001). The higher temperatures and higher precipitation together with the influence of the fast vegetation succession may have contributed to the more rapid CO_3^{2-} depletion at the Hailuogou chronosequence compared to other proglacial areas (**Table B-S1**). Because the dolomite concentrations remained constant at ca. 20 mg g^{-1} along the chronosequence (Yang et al. 2015; Zhou et al. 2016), the Mg release cannot be directly attributed to the carbonate weathering but must be related with other easily weatherable minerals (such as e.g., biotite and hornblende).

The order of the element release at the beginning of soil development was consistent with the order of mineral dissolution (i.e., carbonate minerals > ferromagnesian minerals > feldspars; Lichter 1998; White et al. 1996; Zhou et al. 2016). However, our findings are not consistent with the sequence of the ion release by weathering inferred from open-system element budgets at other chronosequences, where Na and K are the most easily leached ions (Bain et al. 1993, Harden 1988). We attribute this discrepancy to the low concentration of K and Na in easily weatherable minerals which release high quantities of Ca and Mg in the early stage of the chronosequence but little K and Na. Mg-rich minerals, such as

hornblende and biotite (which also contain K), are more readily weathered than those that contain high K and Na concentrations but little Mg, e.g., orthoclase and albite (Clow and Drever 1996; Wilson 2004). At the Hailuogou chronosequence, the dissolution of Mg-rich silicate minerals contributed to the faster decrease of Mg (**Figure B-S1b**) than K stocks (**Figure B-S1c**), which is in line with the findings of Zhou et al. (2016). Moreover, the release of Mg from hornblende and biotite had a similar size as the total Mg loss from the studied ecosystems (**Figure B-4**). The strong mineral soil acidification indicated by the drop in soil pH along the chronosequence (**Tables B-S2 and B-S5**), accompanied by the establishment of a coniferous forest, may have further intensified the weathering of silicate minerals in the older stages of the chronosequence, promoting Mg and K release.

The one order of magnitude higher K than Mg atmospheric deposition (**Table B-2**) but similar Mg and K export with the stream (**Figure B-3b, c**) kept K stocks nearly constant along the chronosequence (**Figure B-1c**), while those of Mg decreased (**Figure B-1b**). The accumulation of K in biomass and in the organic horizons (**Figure B-3c**) contributed to the slight decrease of K in the mineral soil along the chronosequence (**Figure B-4c**), but compensated the total ecosystem stocks which remained unrelated with ecosystem age (**Figure B-1c**). In line with our observations, Lichter (1998) reported that K showed a negligible depletion during the first 1,000 years of soil development but the K stock linearly decreased in the longer term (> 4,000 years) along a sand dune chronosequence in Wilderness State Park (Michigan, US), in which the dissolution of carbonates also promoted a rapid decrease in pH from 8.5 to 4.3.

Because of the low Ca and Mg deposition from the atmosphere, the accumulation of deposited Ca and Mg contributed little to the total stock of Ca and Mg (**Table B-2**). Annual losses of Ca and Mg via the stream were between one and two orders of magnitude higher than the estimated bulk deposition (**Table B-2**), which contributed to the stock decrease of both elements along the chronosequence (**Figure B-1a,b**). Na inputs and outputs were low (**Figure B-3d**) and fluxes hardly changed along the chronosequence (**Table B-2**) explaining that the Na stocks remained nearly unchanged (**Figure B-1d**). We attribute this to the prevalence of Na in little weatherable minerals such as e.g., albite.

The finding that the flux budget did not explain the total losses of Ca, Mg and K from the ecosystems of the Hailuogou chronosquence (**Figure B-4**) indicates that we missed output fluxes. We speculate that an important missing flux might be leaching into the

subsoil (i.e. the C horizons), where the elements are stored in the exchangeable pool or as re-precipitated minerals.

We explain the low K and Na stock 37 years after glacial retreat and the related apparent strong depletion of K and Na between 5 and 37 years and later accumulation between 37 and 47 years to the spatial heterogeneity of the glacial debris (**Figure B-1c, d**), which might have resulted in a locally lower initial stock of K and Na in the parent material of the 37 yr-old site (**Table B-1**). Because Ca and Mg are associated with other minerals (and rocks) than K and Na, the heterogeneity of the glacial debris does not necessarily affect all elements in the same way.

5.2. Biological stocks and fluxes of base metals

The high release of Ca from the intense initial carbonate weathering enabled the build-up of a large biomass stock of Ca (**Table B-S5**), which was supported by the release of sufficient Mg and K to soil solution via weathering of easily weatherable silicate minerals, such as biotite and hornblende. Ca and K stocks in the foliage of the tree species developing at Hailuogou ranged from 5.4 to 13.3 g m^{-2} and 7.2 to 18.8 g m^{-2}, respectively **(Table B-S5),** and were mostly higher than observed in different similarly aged forests of the temperate zone, for which we found comparison values, e.g., the 70 year-old forests in the Walker Branch watershed (Tennessee, US) on acidic soils developed from paleozoic dolomitic bedrock, while Mg stocks ranged from 0.6 to 2.1 g m^{-2} and were slightly below those in the Walker Branch watershed or in the same range (5.8 - 7.5 g m^{-2} Ca, 3.6 - 5.3 g m^{-2} K, 1.2 - 2.1 g m^{-2} Mg, Johnson & Henderson, 1989). Along the Hailuogou chronosequence, plant biomass reached up to 40,630 g m^{-2} within only 127 years of ecosystem development (calculated from Luo et al. 2004; **Figure B-S5**). Total biomass estimated at the different 70 year-old forests in the Walker Branch watershed ranged between 16,380 and 19,770 g m^{-2} (Edwards et al. 1989), which is less than the total biomass at the Hailuogou region within only 47 years (**Figure B-S5**). The higher biomass production and metal uptake at the Hailuogou chronosequence occurs in spite of less favorable climatic conditions for forest growth than at the Walker Branch watershed (mean annual precipitation of 1947 mm and mean annual temperature of 4.2°C at Hailuogou (Wu et al. 2013) vs. 1410 mm and 14°C at the Walker Branch watershed (Edwards et al. 1989). Cool temperature and a higher risk of waterlogging at the Hailuogou chronosequence should have reduced biomass production

(Eamus 2003). The aboveground biomass in another young (55 year-old) forest developed on glacial till originating from the local metasedimentary and magmatic rocks (Barton et al. 1997) in the Hubbard Brook Valley with a mean annual temperature of 3.7-6.7°C and a mean annual precipitation of 1326 to 1607 mm (Campbell, 2021), which should be again more favorable for forest growth than at the Hailuogou chronosequence showed also considerably lower element stocks (38.3 g m^{-2} Ca, 3.6 g m^{-2} Mg and 15.5 g m^{-2} K; Likens 2013) and, consequently, lower annual vegetation uptake (6.2 g m^{-2} $year^{-1}$ Ca, 0.9 g m^{-2} $year^{-1}$ Mg and 6.4 g m^{-2} $year^{-1}$ K; Likens 2013) than the >47 year-old Hailuogou sites. This comparison indicates that the vegetation along the Hailuogou glacial retreat chronosequence took up nutrients more rapidly than other young forests, which is strongly associated with the faster rate of biomass production. Moreover, nutrient release by weathering of the young carbonatic glacial debris was likely faster than on the older substrates at the forest sites used for comparison.

5.3. Coincidence of carbonate depletion and shift from deciduous to coniferous forest

After the reactive carbonates were leached as indicated by the drop of the mineral topsoil pH from 8.0 to 5.8 from the 0 yr to the 47 yr-old site (**Table B-S2**), net weathering rates decreased because less soluble minerals remained in the soil. This occurred in line with the vegetation change from deciduous to coniferous trees and their associated lower nutrient demand and slower nutrient cycling (**Table B-2**; Carnol and Bazgir 2013; Ericsson 1994). As a consequence, nutrient supply by weathering and nutrient demand by the vegetation seemed to match well. Because the differences in mean annual climatic conditions between the youngest and the oldest study site separated by ca. 130 m elevation difference were small (0.77°C, 4.5 mm), we assume that climate played a minor role in explaining the changing vegetation composition.

The most rapid elemental accumulation in organic horizons occurred between 37 and 47 years after glacier retreat, accompanied by the stabilization of a half-mature *P. purdommii* forest and sharply decreased after the stabilization of a coniferous forest, 87 years after deglaciation (**Figure B-2**), likely because of the lower element concentration in foliage of coniferous than deciduous trees (Richardson and Friedland 2016). The rapid initial accumulation of organic matter in the organic layer on top of the mineral soil created

an important reservoir of nutrients for the ecosystem, because the decomposition of organic matter mineralizes nutrients which can be reused for plant uptake (Lilienfein et al. 2001; Wilcke et al. 2002). Calcium availability in the forest floor has been shown to be directly related with tree growth (Baribault et al. 2010; Gradowski and Thomas 2008; Long et al. 1997) and K availability contributes to a higher N uptake (Stevens et al. 1993) and water-use efficiency (Bradbury and Malcolm 1977), promoting faster vegetation growth. The high K uptake in the early stage of the vegetation succession (0-47 yr) and the low K export with the stream at the older sites (47-127 yr) indicated that this nutrient was efficiently internally recycled in our study ecosystems. This together with the release of other essential nutrients from easily weatherable minerals, that we did not study, might have contributed to allow the likely N-limited forest to make full use of the fixed N_2 facilitating the fast establishment of a deciduous forest in the early stage of the chronosequence. The faster vegetation development than at many other glacier retreat chronosequences (**Table B-S1**) might have been further supported by the higher mean annual temperature at the Hailuogou sites.

6. Conclusions

The fast development from bare soil to mature forest along the 127-year old Hailuogou glacier retreat chronosequence was linked with a strong soil acidification and an intense loss of carbonates in the first 47 years of vegetation succession. This development was associated with a decrease in total stocks of Ca and Mg, mainly because of the dissolution of carbonates and easily weatherable Mg-containing minerals, while the stocks of K and Na changed little.

Part of the released Ca and Mg was incorporated into the growing aboveground biomass and thereby retained in the ecosystem. The smaller K release than that of Ca and Mg in the early stage of the chronosequence was compensated by higher K inputs with atmospheric deposition, which were in the same order of magnitude than K losses through the stream. We suggest that the strong supply of Ca and Mg and a closed K cycling contributed to the fast establishment of a deciduous forest, which contributed to allow the likely N-limited forest to make full use of the fixed N_2.

The slower element release by weathering after leaching of carbonates occurred synchronously with the vegetation change from deciduous to coniferous forest with its

lower nutrient demand, while climatic differences along the chronosequence were minor. The rapid vegetation development resulted in the formation of an organic layer on top of the mineral soils with increasing thickness along the chronosequence that stored a large quantity of nutrients. The storage of K in the organic layers was particularly important, since this element was internally cycled through the vegetation (i.e., via plant uptake and return to the soil via throughfall and litterfall). As a consequence, nutrient supply by weathering and nutrient demand by vegetation combined to promote a fast vegetation development along the Hailuogou chronosequence.

7. Acknowledgments

We thank J. Wang, H. Bing, J. Zhou, and Q. He, as well as numerous students from the Chinese Academy of Science for their support in the field during the sampling campaign. We acknowledge the funding by the German Research Foundation (DFG, Wi 1601/25-1). Furthermore, we thank three anonymous reviewers for their valuable comments, which helped us to improve the paper considerably.

8. Supplementary material

Table B-S1. Vegetation development and parent material geology in glacier forelands with similar age in the world.

No.	Site	Age (yr)	Elevation (m a.s.l.)	MAT (°C)	MAP (mm)	Parent material	Vegetation	Source
	Hailuogou	127	2800-3000	4.2	1947	Granite Calcite (~5.6%)	0 yr: coarse and gravelly sand 37 yr: *Hippophae rhamnoides* L. 47 yr: *Populus purdomii* Rehder 59 yr: *Abies fabri* (Mast.) Craib, *Populus purdomii* Rehder 87 yr: *A. fabri*, *Picea brachytyla* (Franch.) E.Pritz 127 yr: *P. brachytyla* , *A. fabri*	(Zhou et al. 2016)
1	Damma Glacier, Swiss Alps	140	1950-2150	0.5	2400	Granite	6-13 yr: scarce vegetation, with mosses lichens, forbs and grasses: *Agrostis gigantea* Roth, *Rumex scutatus* L., *Cerastium uniflorum* Thom. ex Reichb., and *Oxyria digyna* Hill 57-79 yr: *A. gigantea*, *Salix* spp; *Deschampsia cespitosa* (L.) Roem.& Schult., and *Athyrium alpestre* (Hoppe) Milde (57-79yrs). 108-140 yr: *Rhododendron ferrugineum* L., *Salix* spp. *A. gigantea* and *Festuca rubra* L.	(Bernasconi et al. 2011)
2	Morteratsch Glacier, Swiss Alps	150	1900-2150	0.5	1000-1300	Granite, granodiorite *Calcite (<1%)*	7 yr: *Epilobium fleischeri* Hochst. 12 yr: *Oxyrietum digynae* Lüdi 27 yr: *E. fleischeri* 77 yr: Larici-Pinetum cembrae	(Mavris et al. 2010)
3	Ried forefield, Swiss Alps	50	2060	6.4	NA Apr-Oct: 322 mm	Granitoid gneiss	Salicaceae species, subsequently replaced by *R. ferrugineum*, *L. decidua* ,	(Conen et al. 2007)
4	Skaftafellsjökull, Iceland	120	100	5.1	NA	Basalt, hyaloclastite, tephra	Mosses, dwarf shrubs and shrubs. 120 yr: willows (*Salix lanata* L. and *Salix phylicifolia* L.) and downy birch (*Betula pubescens* Ehrh.)	(Vilmundardóttir et al. 2014)
5	Werenskiold Glacier, Norway	80	25-75	-4.4	430	Metamorphic rocks: schists	1 yr: No vegetation 6 yr: *Saxifraga oppositifolia* L. *Saxifraga cespitosa* L. > 12 yr: *S. oppositifolia*, *S. caespitosa*, lichens	(Kabala and Zapart 2012)
6	Glacier Bay, Alaska	220	750-800	4.9	1800	Diorite, granite, volcanic rocks, schist, marble, dolomite, graywacke, argillite, and limestone	15-25 yr: woody species including *Dryas drummondii* Richards, several willows (including *Salix sitchensis* Sanson, *Salix barclayi* Anderss., *Salix commutata* Bebb., and *Salix alaxensis* Coville, black cottonwood, and Sitka alder (*Alnus sinuata* [Reg.] Rydb.). > 35: *A. sinuata* and shrubs.	(Fastie 1995)
7	Midui Glacier, China	90	3770-3810	8.7	835	Granite	<50 yr: Pioneer tree species (*H. rhamnoides*, *Populus pseudoglauca* Z.Wang & P.Y.Fu and *Populus davidiana* Dode). > 50 yr: *Abies georgei* Orr	(Wang et al. 2020b) (Liu et al. 2014)

Table B-S1. Extended.

No.	Site	Age (yr)	Elevation (m a.s.l.)	MAT (°C)	MAP (mm)	Parent material	Vegetation	Source
8	Santa Inés island, Chile	382	24-63	6.9	2777	Granitoid rocks	Shrubs, herbs and non-vascular vegetation. 33-83 yr: deciduous *Nothofagus antarctica* Oerst > 200 yr: evergreen *Nothofagus betuloides* Blume	(Pérez et al. 2014)
9	Alexandra Fiord, Ellesmere island, Canada	44	500-700	-15.2	100-200	Gneiss-granite	Mosses, graminoid-forb, deciduous shrub-moss, evergreen dwarf-shrub-moss.	(Labine 1994) (Jones and Henry 2003)
10	Robson Glacier, Rocky Mountain, Canada	193	~1976	2.1	737	Sedimentary rocks (quartzites, limestones and dolomites)	< 79 yr: Pioneer *Hedysarum mackenzii* Richardson, *Dryas octopetala* L., *Castilleja pullida*,Velenovsky, *Epilobium latifolia* Reiche and some willow species (e.g. *Salix glauca* L., *Salix vestita* Pursh., and *Salix brachycarpa* Nutt.) 79-193 yr: dispersed *Picea engelmannii* Engelm.,*Arctostaphylos rubra´*(Rehder & E.H.Wilson) Fernand, *Betual glandulosa*, Michx., *Aster alpinus* L., *Pyrola bracteata*, Hook., *Pedicularis bracteosa* Benth., *Carex scirpoidea* Michx.	(Sondheim and Standish 1983)
11	Midtre Lovénbreen, Svalbard	100	395	-6.3	386	Metamorphic rocks	<30 yr: pioneer species in small frequencies dominated by *S. oppositifolia* 30-70 yr: *Bistorta vivípara* (L.) Gray, *Carex nardina* Fr., *Pedicularis hirsuta* Haenke, *Arenaria pseudofrigida* (Ostenf. & O.C.Dahl) Juz. ex. Schischk. & Knorring, *Minuartia rubella* (Wahlenb.) Hiern and *Salix polaris* Wahlenb. 70-100 yr: *Silene acaulis* (L.) L., *A. pseudofrigida, S. polaris*. At this stage bryophytes and lichens have the same frequency.	(Moreau et al. 2008)
12	Frías Glacier, Argentina	140	~3100	7.6	4300	Granodiorite	<84 yr: pioneer lichens *Stereocaulon speciosum* I.M.Lamb, *Placopsis perrugosa*(Nyl.) Nyl., *Placopsis stenophylla* (Hue) I.M.Lamb and *Rhizocarpon geminatum*Körb. moss *Racomitrium lanuginosum* (Hedw.) Brid.,, *Andreaea* sp., small herbs *Senecio argyreus* Phil. and shrubs *Baccharis racemosa* DC. And *Gaultheria pumila* (L.f.) D.J.Middleton 84 yr: moss *Andreaea* sp. and *R. lanuginosum*, lichen *P. perrugosa, Placopsis bicolor* (Tuck.) B.de Lesd. *Cladonia lepidophora* Ahti. & Kashiw., *Stereocaulon* spp, *Rhizocarpon geographicum* (L.) DC, graminae *Rhytidosperma picta*, herbs *Senecio argyreus* Phil. and shrubs *G. pumila* 84-140 yr: moss *Andreaea* sp. and *R. lanuginosum*, lichen *P. perrugosa, C. lepidophora*, and *Stereocaulon* spp. 140 yr: lichen *Cladonia subchordalis* A.Evans, herb *Quinchamalium chilense* Willd., shrubs *G. pumila, Berberis buxifolia* Lam., and *Empetrum rubrum* Vahl ex. Willd	(Garibotti et al. 2011)

Table B-S1. Extended.

No.	Site	Age (yr)	Elevation (m a.s.l.)	MAT (°C)	MAP (mm)	Parent material	Vegetation	Source
13	Yanamarey Glacier, Cordillera Blanca, Perú	44	4600	2.1	800-1200	Metamorphic rocks (quartzite and hornfels)	Sparse mosses and grasses	(López-Moreno et al. 2017)
14	Lys Glacier, NW Italian Alps	260	1990-2480	-3	1200	Granitic gneiss with minor mafic inclusions	5-7 yr: pioneer *E. fleischeri* 7-60 yr: *Festuca varia* Haenke, *Trifolium pallescens* DC., *Myosotis alpestris* F.W.Schmidt, *Juncus trifidus* L., and *Vaccinium uliginosum* subsp. *gaultherioides* (Bigelow) S.B.Young 190 yr: herbs *M. alpestris* and *F. varia* 260 yr: shrubs *Loiseleuria procumbens* (L.) Desv. and *V. uliginosum* subsp. *gaultherioides*	(D'Amico et al. 2014)
15	Tyndall Glacier, Mount Kenya, Kenya	~90	4360-4520	0	2250-2500	Basalt, phonolite, trachyte, syenite	Pioneer *Senecio keniophytum* R.E.Fr., *Arabis alpine* Krock. ex Steudt, *R geographicum*, and *Agrostis trachyphylla*. Pilg. Scarce large plants as *Lobelia telekii* Schweinf. ex. Engl. and *Senecio keniodendron* R.E.Fr. & T.C.E.Fr.	(Mizuno 1998)
16	Lyman Glacier forefield, Washington, USA	~100	1100	NA	2750	Heterogeneous glacial till	20-30 yr: scattered individuals or small patches of *Juncus drummondii* E.Mey, *Juncus Mertensianus* Bong., *Luzula piperi*, M.E.Jones *Saxifraga ferruginea* Graham and *Saxifraga tolmiei* Torr. & A.Gray 30-70 yr: scattered willow shrubs (*Salix phylicifolia* L. and *Salix commutata* Bebb), and Pinaceae mixed with herbaceous communities 70-100 yr: transition from low herbaceous to early stages of the heath shrub and lush meadow parkland communities containing individuals of *Abies lasiocarpa* (Hook.) Nutt., *Larix lyallii* Parl and *Tsuga mertensiana* (Bong.) Sarg among patches dominated by several members of Ericaceae.	(Jumpponen et al. 1998)
17	Glacier 15α, Antisana, Ecuador	290	1854-5720	0.5-2	~1300	Heterogeneous volcanic material	Cushion plants and short-stem grasses with a patchy vegetation cover	(Moret et al. 2020)

MAT is mean annual temperature; MAP is mean annual precipitation; NA is not available.

Table B-S2. Soil properties along the Hailuogou chronosequence, SW China.

Site	Site age (yr)	Elevation (m a.s.l.)	Soil horizon / thickness (cm)	pH	CO_3^{2-} (mg g^{-1})	Bulk density (g cm^{-3})	Rock fragments (wt.%)	Organic C (g kg^{-1})	Total N (g kg^{-1})	Fine earth (<2 mm) (%)			ECEC ($mmol_c$ kg^{-1})
										Clay (<2μm)	Silt (2-63μm)	Sand (63-2000 μm)	
S1	0	2982	C1: 0.5 ± 0	8.0 ± 0	19 ± 1	1.80	20.5	6.5 ± 1.2	0.3 ± 0.1	3.0	22.8	74.2	138.7 ± 0.3
			C2: 9.5 ± 0 [a]	8.3 ± 0	25 ± 1	1.80	20.5	3.9 ± 0.1	0.1 ± 0.0	3.2	21.6	75.2	82.2 ± 0.2
S2	5	2948	A: 0.5 ± 0	8.1 ± 0	17 ± 1	1.84	20.5	11.6 ± 2.2	0.5 ± 0.1	3.0	24.3	72.7	81.2 ± 0.7
			C: 9.5 ± 0 [a]	8.3 ± 0	27 ± 1	1.84	20.5	3.5 ± 0.1	0.1 ± 0.0	3.5	24.0	72.5	68.1 ± 0.2
S3	37	2942	Oi: 1.5 ± 0.5	6.4 ± 0.1		0.12		447 ± 4	25 ± 2				
			Oe: 2.8 ± 0.8	5.8 ± 0.3		0.12		405 ± 16	25 ± 2				
			Oa: 2.3 ± 1.3	5.2 ± 0.3		0.22		181 ± 13	12 ± 2				
			A: 1 ± 0	6.1 ± 0.1	2 ± 1	0.96	21.4	16.9 ± 2.7	1 ± 0.1	2.1	18.9	79.1	46.1 ± 0.3
			C: 9.3 ± 0 [a]	6.9 ± 0.1	7 ± 3	1.37	27.5	7.8 ± 1.7	0.5 ± 0.2	1.6	12.8	85.5	31.7 ± 1.9
S4	47	2922	Oi: 1.3 ± 0.3	6.2 ± 0.1		0.18		449 ± 9	24 ± 1				
			Oe: 4.3 ± 0.9	5.6 ± 0.1		0.18		351 ± 27	22 ± 3				
			Oa: 4.7 ± 0.9	5.2 ± 0.2		0.29		254 ± 55	17 ± 3				
			A: 3.0 ± 0.6	5.8 ± 0.2	ND	0.35	16.8	14.1 ± 1.2	1.2 ± 0.3	3.6	18.5	77.9	171.9 ± 7.0
			C: 9.3 ± 0.1 [a]	6.0 ± 0.1	< 0.2	1.44	15.3	8.3 ± 0.7	0.0 ± 0.0	4.9	26.3	68.8	115.9 ± 8.9
S5	59	2912	Oi: 2.3 ± 0.3	5.9 ± 0.2		0.13		437 ± 22	20 ± 3				
			Oe: 5.7 ± 0.3	5.7 ± 0.3		0.13		357 ± 58	20 ± 3				
			Oa: 5.3 ± 0.3	5.4 ± 0.1		0.13		298 ± 39	20 ± 3				
			A: 3.7 ± 0.3	5.9 ± 0.1	ND	0.49	13.5	10.8 ± 2.8	0.8 ± 0.2	1.0	13.8	85.2	116.8 ± 23.1
			C: 8.7 ± 0.1 [a]	6.3 ± 0.1	< 0.2	1.43	11.2	3.8 ± 0.7	0.0 ± 0.0	3.4	29.6	67.1	59.2 ± 5.5
S6	87	2883	Oi: 1.5 ± 0.3	5.2 ± 0.2		0.12		468 ± 3	15 ± 2				
			Oe: 6.7 ± 0.7	4.6 ± 0.2		0.12		409 ± 29	16 ± 1				
			Oa: 4.7 ± 0.9	4.1 ± 0.2		0.13		327 ± 44	18 ± 2				
			A: 4.5 ± 0.8	4.9 ± 0.1	< 0.5	0.72	18.9	28.9 ± 10.4	1.9 ± 0.7	3.5	14.1	82.4	170.0 ± 33.0
			C: 7.4 ± 0.4 [a]	5.6 ± 0.1	0.6 ± 0.4	1.27	26.5	16.2 ± 4.6	0.7 ± 0.1	2.5	13.0	84.5	107.6 ± 6.6
S7	127	2855	Oi: 2.9 ± 0.1	5.8 ± 0.1		0.11		451 ± 7	20 ± 1				
			Oe: 9.0 ± 0.6	5.8 ± 0.1		0.11		435 ± 6	20 ± 0				
			Oa: 6.8 ± 0.2	5.0 ± 0.1		0.14		304 ± 26	19 ± 1				
			A: 6.0 ± 0.0	5.2 ± 0.2	0.2 ± 0.1	0.61	18.6	47.7 ± 20.5	3.4 ± 1.5	4.3	18.6	77.1	237.0 ± 34.3
			C: 7.2 ± 0.0 [a]	5.5 ± 0.1	0.2 ± 0.1	1.33	29.9	10.9 ± 1.3	0.7 ± 0.1	1.5	6.2	92.3	88.4 ± 12.4

Data are shown as means or mean ± standard error (n=3). [a] Thickness of the C horizon used in this study. Bulk density and weight% of rock fragments were taken from Zhou et al. (2016) and Wang et al. (2020c).

Table B-S3. Plant biomass, net primary productivity (NPP), age of the vegetation, and fraction of rainfall lost by transpiration, by canopy interception and by the stream (runoff coefficient α) calculated for our sites.

Site age (years)	0	37	47	59	87	127
Biomass (g m^{-2})	-	16282	22291	28539	36811	40626
NPP (g m^{-2} $year^{-1}$)	-	788.6	925.6	1052.0	1220.4	1287.1
Vegetation age (year)	-	25	35	47	74	112
Fraction of rainfall lost by transpiration	0.14	0.17	0.23	0.29	0.38	0.42
Fraction of rainfall lost by canopy interception	-	0.17[a*]	0.23[a]	0.16[b*]	0.21[b]	0.25[c]
α	0.86	0.66	0.54	0.55	0.41	0.33

Plant biomass and net primary productivity (NPP) calculated for our sites from data published by Luo et al. (2004) for the same study area (**Fig. B-S1**). Age of the vegetation was estimated from Zhou et al. (2013). Estimated fraction of rainfall lost via the stream (runoff coefficient α) was calculated by multiplying the transpiration of a mature forest at our study site taken from Sun et al. (2020), with the ratio of biomass at each ecosystem site to that at the 127 yr-old site. The fraction of rainfall lost via the stream at the glacier forefront was estimated at 86% (Brock et al. 2010; Small et al. 2018). Canopy interception was taken from Sun et al. (2013) for a young (30-40 yr) *A. fabri* and *P. purdomii* mixed forest (a), a middle-aged (70-80 yr) *A. fabri* dominant forest (b) and a mature (100-120 yr) *A. fabri* dominant forest (c). We interpolated the data for the 37-yr and 59-yr sites (*) considering the biomass. The runoff coefficient α represents the total fraction of rainfall lost via the stream.

Table B-S4. Proportional contribution of the different tree compartments to the total tree biomass. (Leaf, branch, trunk+bark and root: data from Zhou 2013; partitioning between trunk and bark: estimated for our study area from Wilcke and Lilienfein, 2004).

Tree compartments	Leaf	Branch	Trunk	Bark	Root
Coniferous trees[a]	4%	13%	58%	12%	13%
Evergreen and deciduous broad-leaved trees[b]	4%	23%	45%	9%	20%

a: used for *Abies fabri* (Mast.) Craib and *Picea brachytyla* (Franch.) E. Pritz.;
b: used for *Hippophae rhamnoides* L. and *Populus purdomii* Rehder

Table B-S5. Base metal stocks along the Hailuogou chronosequence (g m^{-2}).

Site age (years)	0	5	37	47	59	87	127
Ca							
Leaves			5.4 ± 1.6	13 ± 3.0	9.1 ± 1.9	8.5 ± 2.5	13 ± 1.3
Branches			10 ± 1.8	41 ± 10	31 ± 3.6	14 ± 3.3	19 ± 3.3
Trunk			3.6 ± 0.5	63 ± 34	90 ± 18	17 ± 0.5	44 ± 31
Bark			28 ± 13	54 ± 6.6	100 ± 18	22 ± 3.0	46 ± 18
Roots			30 ± 10	59 ± 23	28 ± 4.7	19 ± 15	40 ± 7.6
Total biomass			*77.0 ± 17*	*230 ± 43*	*260 ± 26*	*80 ± 16*	*160 ± 37*
Oi			35 ± 22	49 ± 19	60 ± 12	24 ± 11	60 ± 21
Oe			63 ± 20	180 ± 62	180 ± 51	84 ± 13	180 ± 26
Oa			152 ± 120	350 ± 59	235.0 ± 50.6	110 ± 41	230 ± 56
Total organic horizons			*250 ± 120*	*570 ± 87*	*470 ± 73*	*220 ± 45*	*470 ± 65*
Ca exchangeable	n.a.	n.a.	n.a.	5.7 ± 7.4	16 ± 3.5	21 ± 7.3	24 ± 6.7
Fine earth (0-10 cm)	9530 ± 130	9830 ± 770	5750 ± 620	5190 ± 400	5920 ± 380	4450 ± 380	4440 ± 300
Stones (0-10 cm)	3500 ± 390	3490 ± 160	2600 ± 700	1310 ± 290	970 ± 250	1340 ± 99	1900 ± 170
Total mineral soil (0-10 cm)	*13030 ± 410*	*13320 ± 780*	*8350. ± 930*	*6500 ± 500*	*6890 ± 460*	*5790 ± 390*	*6340 ± 350*
Mg							
Leaves			0.7 ± 0.1	2.1 ± 0.4	0.6 ± 0.1	0.7 ± 0.1	1.3 ± 0.2
Branches			1.2 ± 0.1	2.4 ± 0.2	2.7 ± 0.6	2.8 ± 0.7	3.2 ± 0.5
Trunk			0.2 ± 0.1	9.8 ± 11.7	6.0 ± 0.9	1.8 ± 0.1	3.1 ± 1.5
Bark			1.0 ± 0.5	1.6 ± 0.2	3.7 ± 0.5	1.4 ± 0.4	1.9 ± 0.5
Roots			2.2 ± 0.5	2.8 ± 1.6	2.7 ± 0.3	2.4 ± 0.9	4.3 ± 0.6
Total biomass			*5.3 + 0.7*	*19 ± 12*	*16 ± 1.2*	*9.1 ± 1.2*	*14 ± 1.7*
Oi			4.2 ± 2.4	6.1 ± 3.7	11 ± 2.2	3.2 ± 1.0	6.5 ± 0.2
Oe			11 ± 2.5	51 ± 14	52 ± 33	24 ± 7.4	31 ± 3.5
Oa			67 ± 52	130 ± 39	91 ± 23	35 ± 17	78 ± 25
Total organic horizons			*82 ± 52*	*190 ± 41*	*150 ± 40*	*62 ± 19*	*120 ± 25*
Mg exchangeable	0.7 ± 0.0	0.7 ± 0.0	0.8 ± 0.2	0.7 ± 0.5	0.8 ± 0.2	1.6 ± 0.5	2.3 ± 0.5
Fine earth (0-10 cm)	3740 ± 22	3770 ± 319	2870 ± 85	2620 ± 202	2660 ± 251	1950 ± 176	1960 ± 213
Stones (0-10 cm)	1260 ± 190	1290 ± 31	853 ± 84	640 ± 64	480 ± 96	638 ± 60	872 ± 65
Total mineral soil (0-10 cm)	*4990 ± 196*	*5060 ± 320*	*3720 ± 119*	*3260 ± 212*	*3140 ± 268*	*2590 ± 186*	*2830 ± 223*
K							
Leaves			10 ± 1.3	19 ± 5.9	7.2 ± 0.9	9.4 ± 1.6	9.8 ± 0.9
Branches			42 ± 5.2	55 ± 9.5	45 ± 19	43 ± 5.2	24 ± 2.2
Trunk			4.1 ± 1.6	31 ± 30	40 ± 8.6	28 ± 5.6	33 ± 5.1
Bark			13 ± 3.4	13 ± 4.6	27 ± 3.8	18 ± 4.1	23 ± 3.4
Roots			23 ± 2.2	27 ± 3.6	20 ± 1.9	15 ± 4.9	33 ± 12
Total biomass			*92 ± 6.9*	*144 ± 33.*	*138 ± 22*	*113 ± 10*	*121 ± 13*
Oi			6.4 ± 4.0	11 ± 7.3	16 ± 4.0	4.7 ± 1.1	8.2 ± 2.0
Oe			14 ± 3.2	72 ± 17	82 ± 59	39 ± 12	42 ± 8.3
Oa			77 ± 75	177.0 ± 43	130 ± 32	58 ± 230	125 ± 35
Total organic horizons			*98 ± 75*	*260 ± 47*	*230 ± 67*	*100 ± 32*	*175 ± 36*
K exchangeable	0.6 ± 0.0	0.7 ± 0.0	0.8 ± 0.3	0.7 ± 0.2	0.6 ± 0.3	0.4 ± 0.2	0.6 ± 0.1
Fine earth (0-10 cm)	4190 ± 182	4240 ± 262	2910 ± 340	4130 ± 573	4310 ± 534	3250 ± 369	3520 ± 301
Stones (0-10 cm)	1390 ± 148	1500 ± 76	971 ± 110	1121 ± 154	762 ± 25	931 ± 92	1430 ± 69
Total mineral soil (0-10 cm)	*5580 ± 234*	*5740 ± 273*	*3890 ± 357*	*5250 ± 594*	*5070 ± 535*	*4180 ± 381*	*4960 ± 309*
Na							
Roots			0.2 ± 0.0	0.2 ± 0.1	0.2 ± 0.0	0.1 ± 0.1	0.1 ± 0.0
Oi			2.0 ± 1.7	3.5 ± 2.6	7.0 ± 3.7	1.1 ± 0.3	1.8 ± 0.6
Oe			5.7 ± 1.1	36 ± 11	44 ± 41	20 ± 11	15 ± 3.2
Oa			56 ± 50	120 ± 40	73 ± 25	48 ± 32	63 ± 18
Total organic horizons			*63 ± 50*	*160 ± 41*	*123 ± 49*	*69 ± 34*	*79 ± 18*
Na exchangeable	0.1 ± 0.0	0.1 ± 0.0	0.1 ± 0.0	0.0 ± 0.0	0.1 ± 0.0	0.1 ± 0.0	0.1 ± 0.0
Fine earth (0-10 cm)	2750 ± 23	2720 ± 244	2050 ± 155	2870 ± 435	3020 ± 216	2670 ± 245	2620 ± 168
Stones (0-10 cm)	1010 ± 44	1020 ± 160	630 ± 120	746 ± 100	511 ± 50	659 ± 97	952 ± 76
Total mineral soil (0-10 cm)	*3750 ± 49*	*3740 ± 296*	*2680 ±196*	*3620 ± 446*	*3530 ± 222*	*3330 ± 264*	*35670 ± 184*

Na stocks in the different organs of the aboveground biomass were < 0.04 g m^{-2}. n.a. is not analyzed.

O_x represent the different organic horizons: Oi (fresh litter), Oe (shredded litter) and Oa (dark layer of decomposed humus).

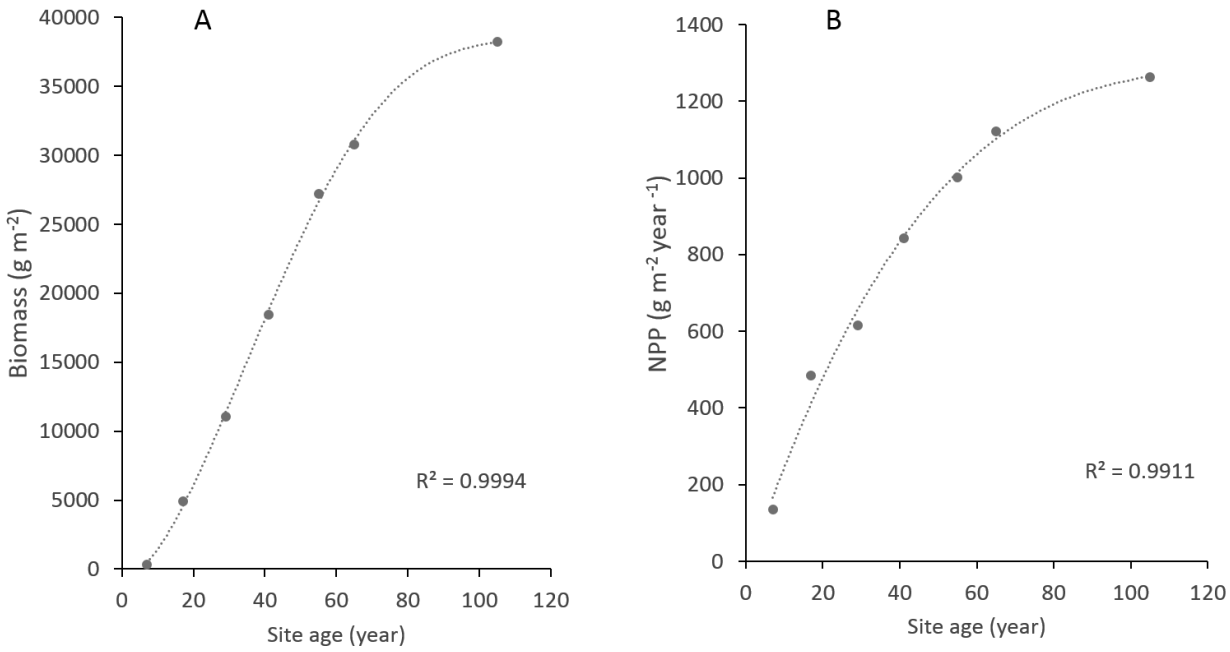

Figure B-S1. Logistic fitting of the relationship between site age and biomass (A) and between site age and net primary production (B) along the Hailuogou chronosequence. Data from Luo et al. (2004).

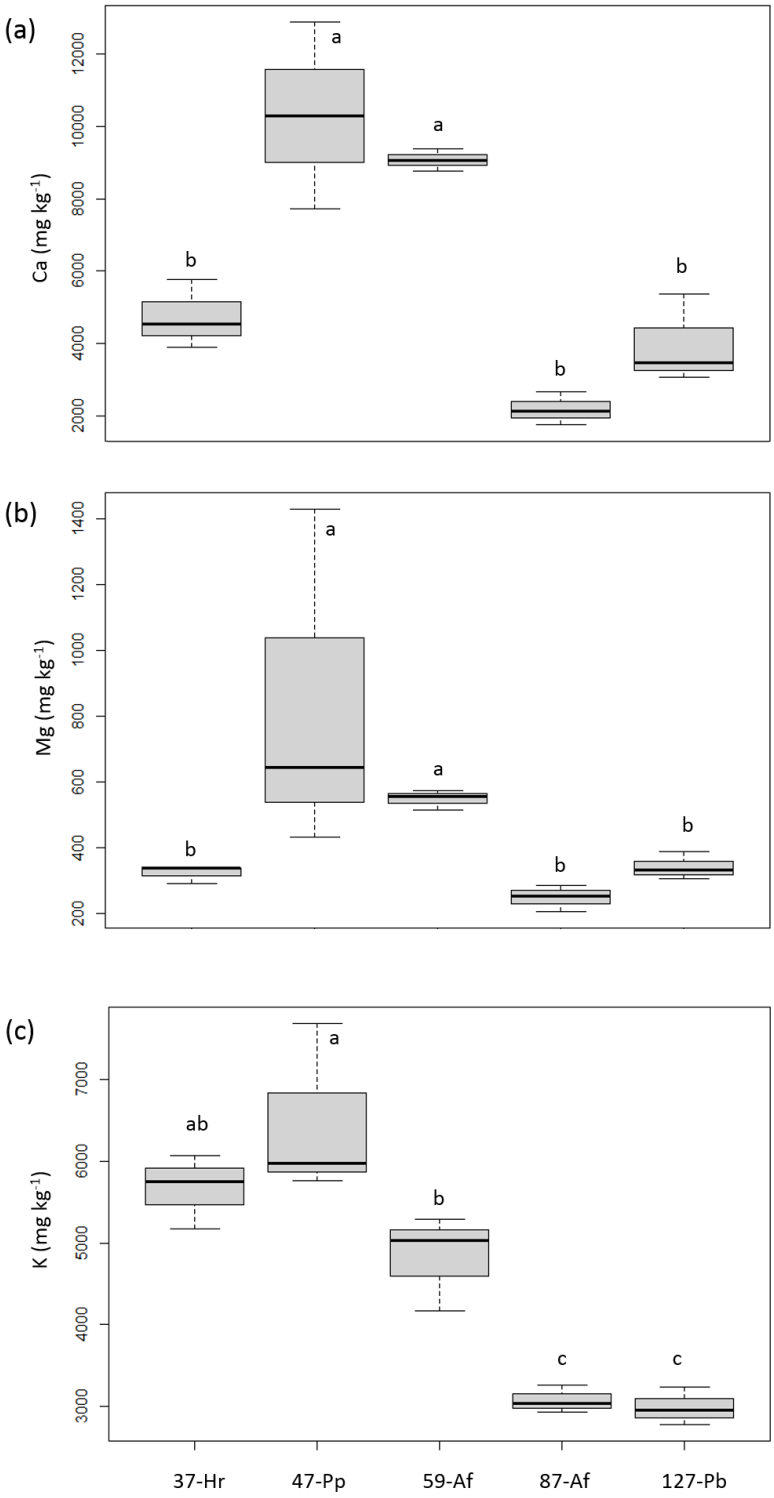

Figure B-S2. Mass-weighted mean concentrations of Ca (a), Mg (b), and K(c) in the dominant tree and shrub species along the Hailuogou chronosequence, i.e., *Hippophae rhamnoides* L. (Hr; 37 yr), *Populus purdomii* Rehder (Pp; 47 yr), *Abies fabri* (Mast.) Craib (Af; 59 yr and 87 yr) and *Picea brachytyla* (Franch.) E.Pritz (Pb; 127 yr). Letters indicate significant differences according to Tukey's HSD post-hoc test.

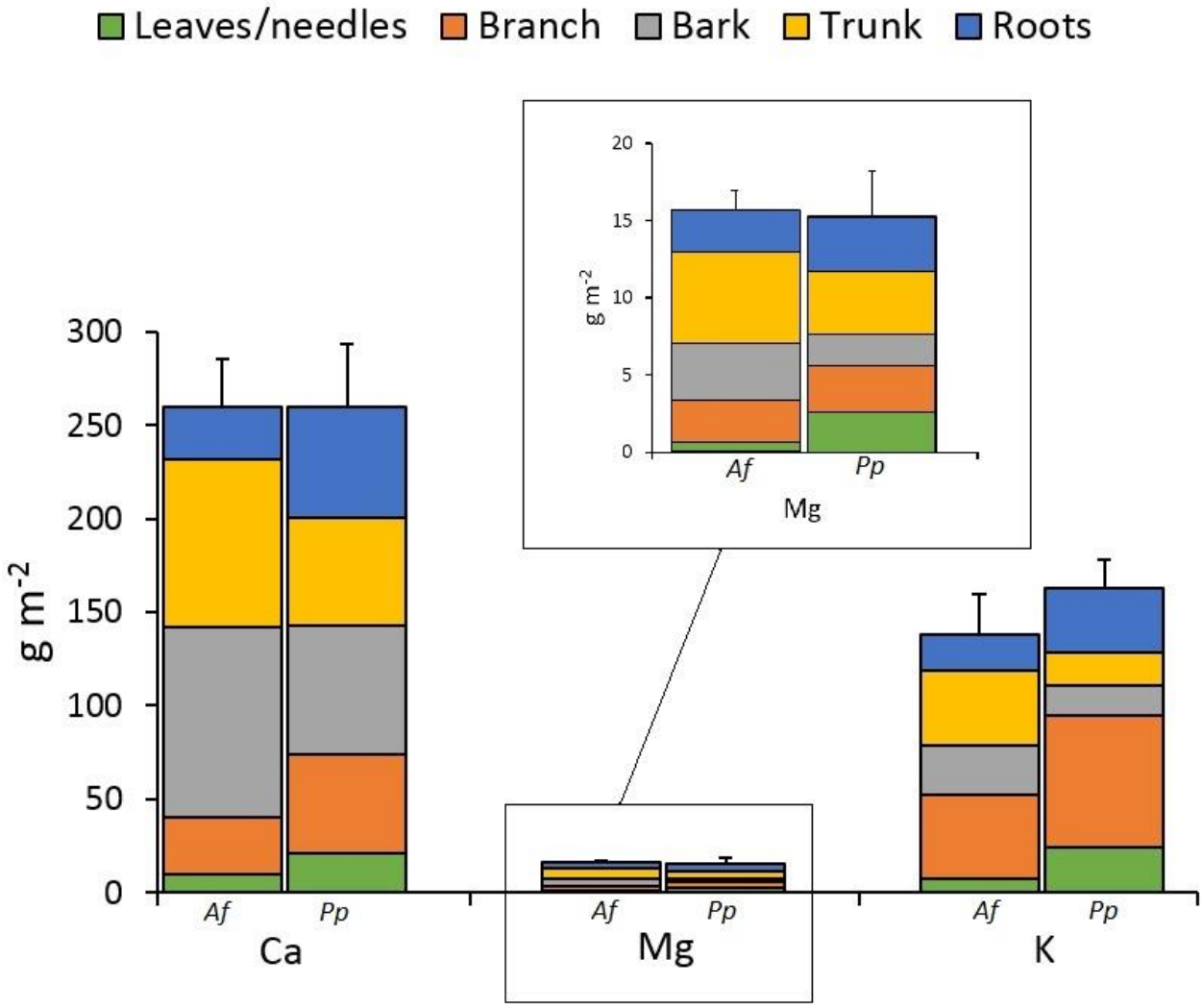

Figure B-S3. Stocks of Ca, Mg and K in the different plant compartments of the trees at Site 5 (59 years) of the Hailuogou chronosequence assuming a cover of 100% *Abies fabri* (Mast.) Craib (Af, left bars) and *Populus purdomii* Rehder (Pp, right bars). The data for *P. purdormii* were taken from Site 4 except for the leaves, which were sampled on Site 5. The element concentrations of the leaves of *P. purdomii* did not significantly differ between Sites 4 and 5 (t-test). Error lines represent single standard deviations calculated by Gaussian error propagation

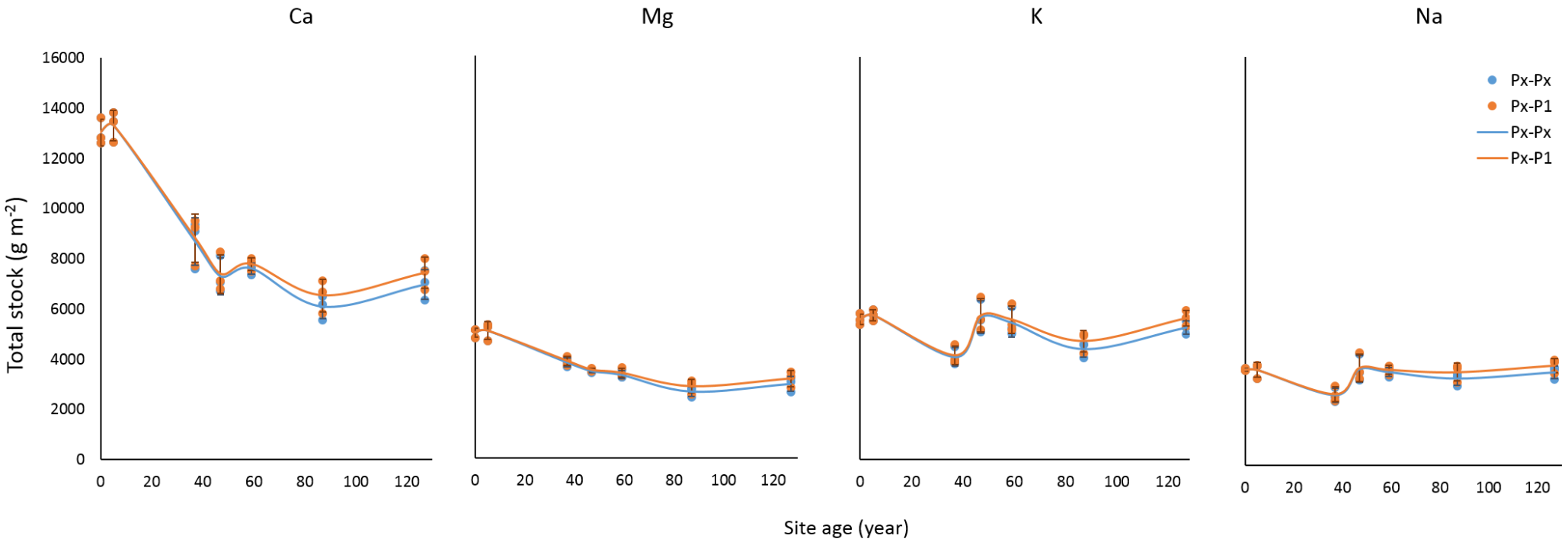

Figure B-S4. Comparison of total stocks calculated by adjusting the thickness of the C horizon in the different plots with the help of the local C horizon density at each site (Px-Px) and by assuming that the density of the C horizon did not change along the chronosequence and equaled that of the local C horizon density of the original glacial debris at Site 1 (Px-P1). Error bars represent standard deviations (n=3).

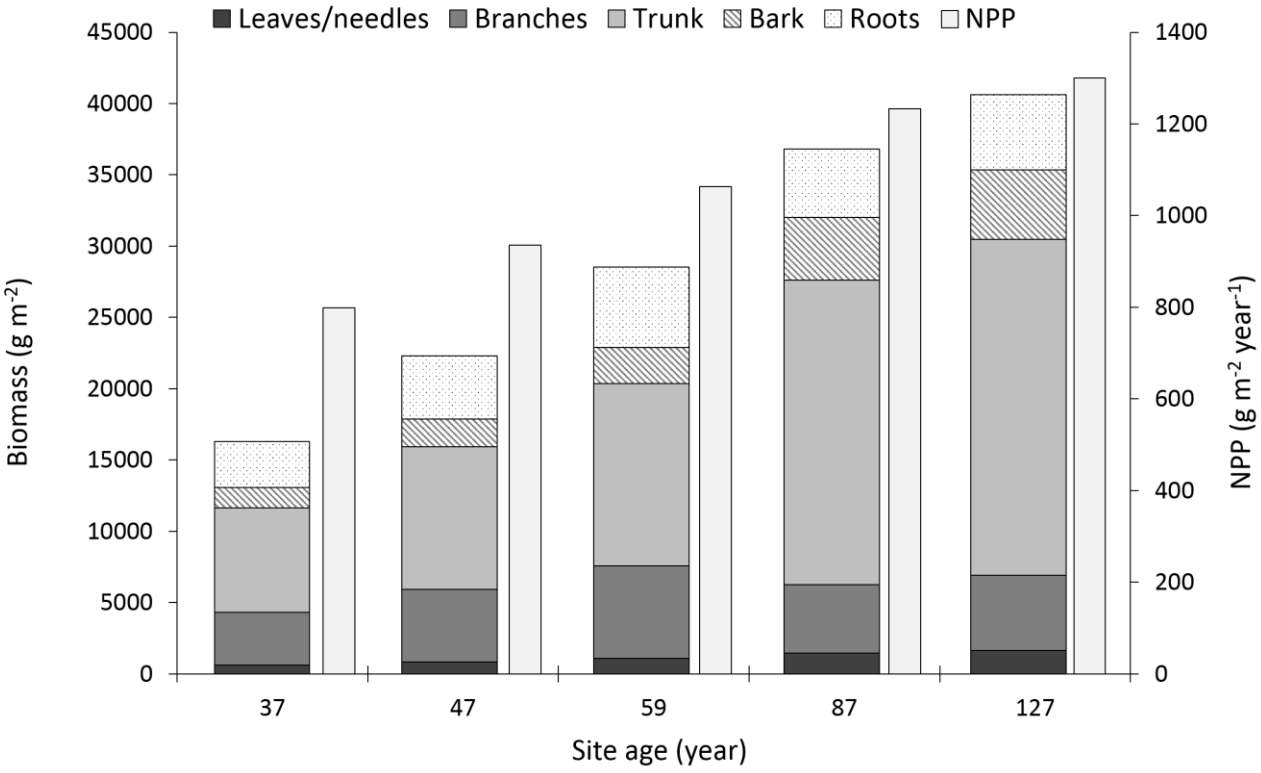

Figure B-S5. Biomass development individually specified for the different tree organs (g m^{-2}; **Tables B-S3 and B-S4**) and net primary production, NPP (g m^{-2} $year^{-1}$; **Table B-S3**) along the Hailuogou chronosequence. Biomass and NPP data were calculated for our study sites from Luo et al. (2004; **Figure B-S1**) and proportional contributions of the different tree organs to total tree biomass from Zhou (2013) and Wilcke and Lilienfein (2004, partitioning between trunk and bark).

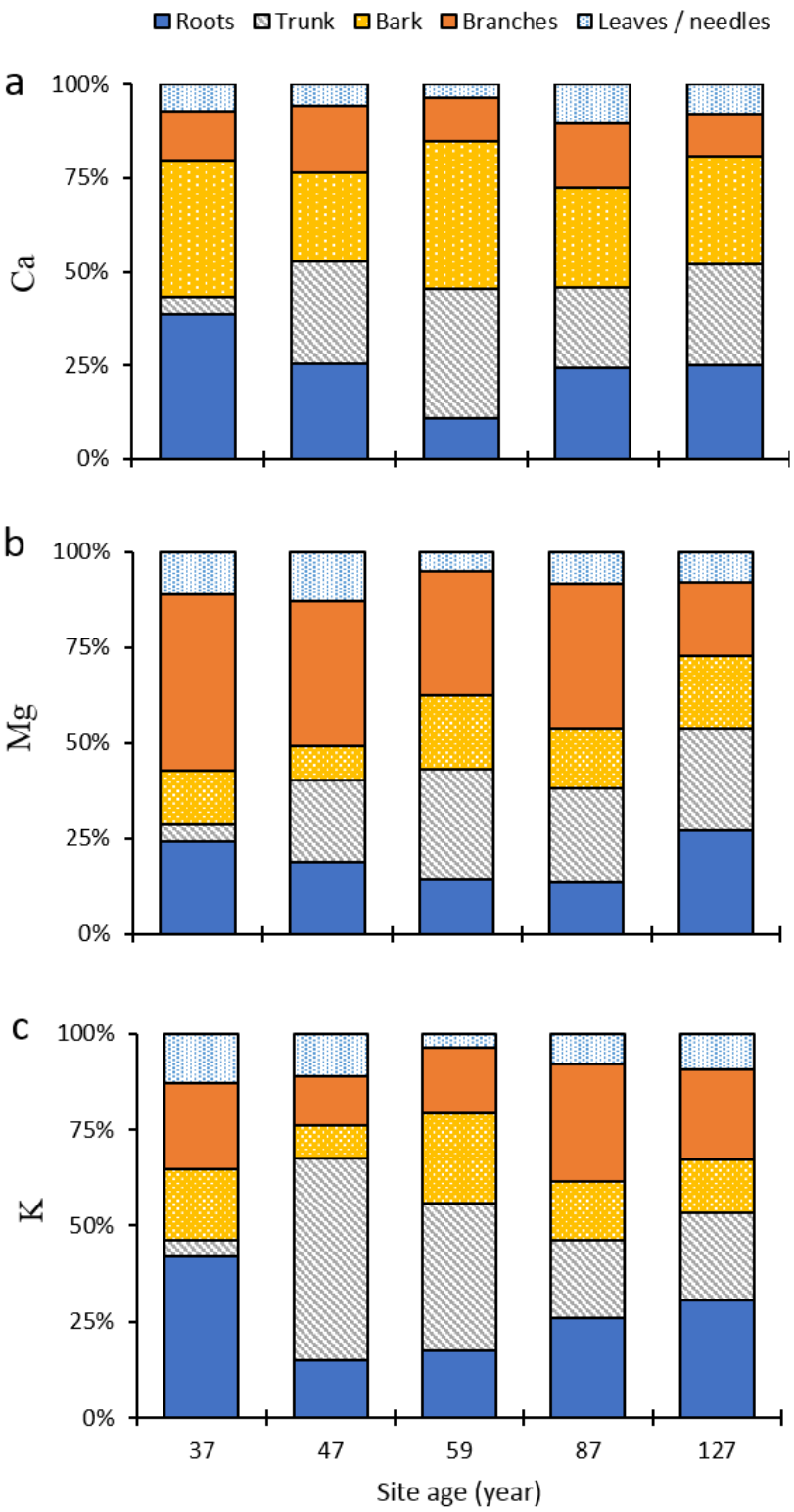

Figure B-S6. Mean distribution of base metals (a: Ca, b: Mg, c: K) among the different tree organs of the dominant tree species along the Hailuogou chronosequence, i.e., *Hippophae rhamnoides* L. (37-yr), *Populus purdomii* Rehder (47-yr), *Abies fabri* (Mast.) Craib (59-yr and 87-yr) and *Picea brachytyla* (Franch.) E.Pritz (127-yr).

9. References

Amtmann A, Sanders D (**1999**) Mechanism of Na^+ uptake by plant cells. Advances in Botanical Research 29:75–112. https://doi.org/10.1016/S0065-2296(08)60310-9

Bain DC, Mellor A, Robertson-Rintoul MSE, Buckland ST (**1993**) Variations in weathering processes and rates with time in a chronosequence of soils from Glen Feshie, Scotland. Geoderma 57:275–293. https://doi.org/10.1016/0016-7061(93)90010-I

Baribault TW, Kobe RK, Rothstein DE (**2010**) Soil calcium, nitrogen, and water are correlated with aboveground net primary production in northern hardwood forests. Forest Ecology and Management 260:723–733. https://doi.org/10.1016/j.foreco.2010.05.029

Baribault TW, Kobe RK, Finley AO (**2012**) Tropical tree growth is correlated with soil phosphorus, potassium, and calcium, though not for legumes. Ecol Monogr 82:189–203. https://doi.org/10.2307/41739364

Barton CC, Carmelo RH, Bailey SW (**1997**) Bedrock geologic map of Hubbard Brook Experimental Forest and maps of fractures and geology in roadcuts along Interstate-93, Grafton County, New Hampshire. Sheet 1, Scale 1:12,000; Sheet 2, Scale 1:200. US Geological Survey, Miscellaneous Investigations Series, Map I-2562.

Bernasconi SM., Bauder A, Bourdon B, Brunner I, Bünemann E, Chris I, Derungs N, Edwards P, Farinotti D, Frey B, Frossard E, Furrer G, Gierga M, Göransson H, Gülland K, Hagedorn F, Hajdas I, Hindshaw R, Ivy-Ochs S, Jansa J, Jonas T, Kiczka M, Kretzschmar R, Lemarchand E, Luster J, Magnusson J, Mitchell EAD, Venterink HO, Plötze M, Reynolds B, Smittenberg RH, Stähli M, Tamburini F, Tipper ET, Wacker L, Welc M, Wiederhold JG, Zeyer J, Zimmermann S, Zumsteg A (**2011**) Chemical and Biological Gradients along the Damma Glacier Soil Chronosequence, Switzerland. Vadose Zone Journal 10:867. https://doi.org/10.2136/vzj2010.0129

Berner EK, Berner RA, Moulton KL (**2004**) Plants and mineral weathering: present and past, in: J.I. Drever (Ed.), Surface and Gound Water, Weathering, and Soils. pp. 169–188. https://doi.org/10.1016/B0-08-043751-6/05175-6

Bing H, Wu Y, Zhou J, Liang J, Wang J, Yang Z (**2016a**) Mobility and eco-risk of trace metals in soils at the Hailuogou Glacier foreland in eastern Tibetan Plateau. Environmental Science and Pollution Research 23:5721–5732. https://doi.org/10.1007/s11356-015-5592-2

Bing H, Wu Y, Zhou J, Sun H, Luo J, Wang J, Yu D (**2016b**) Stoichiometric variation of carbon, nitrogen, and phosphorus in soils and its implication for nutrient limitation in alpine ecosystem of Eastern Tibetan Plateau. J Soils Sediments 16:405–416. https://doi.org/10.1007/s11368-015-1200-9

Bing H, Wu Y, Li J, Xiang Z, Luo X, Zhou J, Sun H, Zhang G (**2019**) Biomonitoring trace element contamination impacted by atmospheric deposition in China's remote mountains. Atmospheric Research 224:30–41. https://doi.org/10.1016/j.atmosres.2019.03.018

Bradbury IK, Malcolm DC (**1977**) The Effect of Phosphorus and Potassium on Transpiration, Leaf Diffusive Resistance and Water-Use Efficiency in Sitka Spruce (Picea sitchensis) Seedlings. Journal of Applied Ecology 14:631. https://doi.org/10.2307/2402573

Brock BW, Mihalcea C, Kirkbride MP, Diolaiuti G, Cutler MEJ, Smiraglia C (**2010**) Meteorology and surface energy fluxes in the 2005 – 2007 ablation seasons at the Miage debris - covered glacier, Mont Blanc Massif, Italian Alps. Journal of Geophysical Research - Atmospheres 115:1–16. https://doi.org/10.1029/2009JD013224

Burga CA, Krüsi B, Egli M, Wernli M, Elsener S, Ziefle M, Fischer T, Mavris C (**2010**) Plant succession and soil development on the foreland of the Morteratsch glacier (Pontresina, Switzerland): Straight forward or chaotic? Flora Morphology, Distribution, Functional Ecology of Plants 205:561–576. https://doi.org/10.1016/j.flora.2009.10.001

Burstrom HG (**1968**) Calcium and plant growth. Biol Rev 43(3):287–316. https://doi.org/10.1111/j.1469-185X.1968.tb00962.x

Cambell J (**2021**) Chapter 08: Climate Change. *In* Online Book: A Synthesis of Scientific Research at Hubbard Brook. https://hubbardbrook.org/online-book/online-book, visited on 23/11/2021.

Chadwick OA, Derry LA, Vitousek PM, Huebert BJ, Hedin LO (**1999**) Changing sources of nutrients during four million years of ecosystem development. Nature, 397-491:497. https://doi.org/10.1038/17276

Clow DW, Drever JI (**1996**) Weathering rates as a function of flow through an alpine soil. Chemical Geology 132:131-141. https://doi.org/10.1016/S0009-2541(96)00048-4

Coaz J (**1887**) Erste Ansiedlung phanerogamer Pflanzen auf vom Gletscher verlassenen Boden. Mitteilungen der Naturforschenden Gesellschaft in Bern 1886:3-12

Cole DW, Rapp M (**1981**) Elemental cycling in forest ecosystems. Dynamic Principles of Forest Ecosystems, Cambridge University Press, Cambridge.

Conen F, Yakutin MV, Zumbrunn T, Leifeld J (**2007**) Organic carbon and microbial biomass in two soil development chronosequences following glacial retreat. European Journal of Soil Science 58:758–762. https://doi.org/10.1111/j.1365-2389.2006.00864.x

Crocker RL, Major J (**1955**) Soil Development in Relation to Vegetation and Surface Age at Glacier Bay, Alaska. Journal of Ecology 43(2):427-448. https://doi.org/10.2307/2257005

Crozier MJ (**2010**) Deciphering the effect of climate change on landslide activity: A review. Geomorphology 124:260–267. https://doi.org/10.1016/j.geomorph.2010.04.009

Cullen NJ, Sirguey P, Mölg T, Kaser G, Winkler M, Fitzsimons SJ (**2013**) A century of ice retreat on Kilimanjaro: the mapping reloaded, The Cryosphere 7:419–431. https://doi.org/10.5194/tc-7-419-2013

D'Amico ME, Freppaz M, Filippa G, Zanini E (**2014**) Vegetation influence on soil formation rate in a proglacial chronosequence (Lys Glacier, NW Italian Alps). Catena 113:122–137. https://doi.org/ 10.1016/j.catena.2013.10.001

de Mendiburu F (**2021**) Package 'agricolae'. R package version, 1.3–5.

Dickson BA, Crocker RL (**1953**) A chronosequence of soils and vegetation near Mount Shasta, California; I. Definition of the ecosystem investigated and features of the plant succession. Journal of Soil Science 4:123-141. https://doi.org/10.1111/j.1365-2389.1953.tb00650.x

Diem B, Godbold DL (**1993**) Potassium, calcium and magnesium antagonism in clones of Popolus trichocarpa. Plant Soil 155(156):411-414. https://doi.org/10.1007/BF00025070

Drever JI, Stillings LL (**1997**) The role of organic acids in mineral weathering. Colloids Surf A Physicochem Eng Aspects 120:167–181. https://doi.org/10.1016/S0927-7757(96)03720-X

Eamus D (**2003**) How does ecosystem water balance affect net primary productivity of woody ecosystems? – Functional Plant Biology 30: 187–205. https://doi.org/10.1071/FP02084

Edwards NT, Johnson DW, McLaughlin SB, Harris WF (**1989**) Carbon dynamics and productivity. In Analysis of biogeochemical cycling processes in Walker Branch Watershed, ed. D. W. Johnson and R. I. Van Hook. New York: Springer-Verlag, pp. 197–232.

Egli M, Fitze P (**2001**) Quantitative aspects of carbonate leaching of soils with differing ages and climates. Catena 46:35–62. https://doi.org/10.1016/S0341-8162(01)00154-0

Elser JJ, Bracken MES, Cleland EE, Grunder S, Harpole WS, Hillebrandt H, Ngai JT, Seabloom EW, Shurin JB, Smith JE (**2007**) Global analysis of nitrogen and phosphorus limitation of primary producers in freshwater, marine and terrestrial ecosystems. Ecology Letters 10(12):1135–1142. https://doi.org/10.1111/j.1461-0248.2007.01113.x

Epron D, Laclau J-P, Almeida JCR, Gonçalves JLM, Ponton S, Sette CR, Delgado-Rojas JS, Bouillet J-P, Nouvellon Y (**2012**) Do changes in carbon allocation account for the growth response to potassium and sodium applications in tropical Eucalyptus plantations? Tree Physiol 32:667–679. https://doi.org/10.1093/treephys/tpr107

Epron D, Cabral OMR, Laclau J-P, Dannoura M, Packer AP, Plain C, et al. (**2015**) In situ 13_{CO2} pulse labelling of field-grown eucalypt trees revealed the effects of potassium nutrition and throughfall exclusion on phloem transport of photosynthetic carbon. Tree Physiology,36:6–21. https://doi.org/10.1093/treephys/tpv090

Ericsson T (**1994**) Nutrient dynamics and requirements of forests crops. New Zealand Journal of Forestry Science 24:133-68

Ertiftik H, Zengin M (**2017**) Response of maize for grain to potassium and magnesium fertilizers in soils with high lime contents. Journal of Plant Nutrition 40:93–103. https://doi.org/10.1080/01904167.2016.1201493

Fageria NK (**1983**) Ionic Interactions in Rice Plants from Dilute Solutions. Plant Soil 70: 309–316. https://doi.org/10.1007/BF02374887

Fastie CL (**1995**) Causes and Ecosystem Consequences of Multiple Pathways of Primary Succession at Glacier Bay, Alaska. Ecology 76:1899–1916. https://doi.org/10.2307/1940722

Federer CA, Hornbeck JW, Tritton LM, Martin CW, Pierce RS, Smith CT (**1989**) Long-term depletion of calcium and other nutrients in eastern US forests. Environ Manag 13:593–601. https://doi.org/10.1007/BF01874965

Freer-Smith PH, Beckett KP, Taylor G (**2005**) Deposition velocities to *Sorbus aria*, *Acer campestre*, *Populus deltoides* × *trichocarpa* 'Beaupré', *Pinus nigra* and × *Cupressocyparis leylandii* for coarse, fine and ultra-fine particles in the urban environment. Environmental Pollution 133:157-167. https://doi.org/10.1016/j.envpol.2004.03.031

Friedel H (**1938**) Die Pflanzenbesiedlung im Vorfeld des Hintereisferners. Zeitschrift für Gletscherkunde 26:215-239

Garibotti I, Pissolito C, Villalba R (**2011**) Vegetation development on deglaciated rock outcrops from Glaciar frías, Argentina. Arctic, Antarctic, and Alpine Research 43:35–45. https://doi.org/ 10.1657/1938-4246-43.1.35

Gradowski T, Thomas SC (**2008**) Responses of Acer saccharum canopy trees and saplings to P, K and lime additions under high N deposition. Tree Physiology 28:173–185. https://doi.org/10.1093/treephys/28.2.173

Haeberli W, Schaub Y, Huggel C (**2017**) Increasing risks related to landslides from degrading permafrost into new lakes in de-glaciating mountain ranges. Geomorphology 293:405–417. https://doi.org/10.1016/j.geomorph.2016.02.009

Harden JW (**1988**) Genetic interpretations of elemental and chemical differences in a soil chronosequence, California. Geoderma 43:179–193. https://doi.org/10.1016/0016-7061(88)90042-0

He L, Tang Y (**2008**) Soil development along primary succession sequences on moraines of Hailuogou Glacier, Gongga Mountain, Sichuan, China. Catena 72:259–269. https://doi.org/10.1016/j.catena.2007.05.010

Hock R, Rasul G, Adler C, et al (**2019**) High Mountain Areas. In: IPCC Special Report on the Ocean and Cryosphere in a Changing Climate [H.-O. Pörtner, D.C. Roberts, V. Masson-Delmotte, P. Zhai, M. Tignor, E. Poloczanska, K. Mintenbeck, A. Alegría, M. Nicolai, A. Okem, J. Petzold, B. Rama, N.M.

IPCC (**2021**) Climate Change 2021: The Physical Science Basis. Contribution of Working Group I to the Sixth Assessment Report of the Intergovernmental Panel on Climate Change[Masson-Delmotte, V., P. Zhai, A. Pirani, S.L. Connors, C. Péan, S. Berger, N. Caud, Y. Chen, L. Goldfarb, M.I. Gomis, M. Huang, K. Leitzell, E. Lonnoy, J.B.R. Matthews, T.K. Maycock, T. Waterfield, O. Yelekçi, R. Yu,and B. Zhou (eds.)]. Cambridge University Press, Cambridge, United Kingdom and New York, NY, USA, 2391 pp. https://doi.org/10.1017/9781009157896.

IUSS Working Group WRB (**2014**) World Reference Base for Soil Resources 2014. International soil classification system for naming soils and creating legends for soil maps. World Soil Resource Reports No. 106. FAO, Rome

Jia Y, Kong X, Weiser MD, Lv Y, Akbar S, Jia X, et al. (**2015**) Sodium limits litter decomposition rates in a subtropical forest: additional tests of the sodium ecosystem respiration hypothesis. Appl Soil Ecol 93:98e104. https://doi.org/10.1016/j.apsoil.2015.04.012

Johnson DW, Henderson GS (**1989**) Terrestrial nutrient cycling. In Analysis of biogeochemical cycling processes in Walker Branch Watershed, ed. D. W. Johnson and R. I. Van Hook. New York: Springer-Verlag, pp.233–300

Jones GA, Henry GHR (**2003**) Primary plant succession on recently deglaciated terrain in the Canadian High Arctic. Journal of Biogeography 30:277–296. https://doi.org/10.1046/j.1365-2699.2003. 00818.x

Jumpponen A, Mattson K, Trappe JM, Ohtonen R (**1998**) Effects of established willows on primary succession on Lyman Glacier forefront, North Cascade Range, Washington, USA: evidence for simultaneous canopy inhibition and soil facilitation. Arctic, Antarctic, and Alpine Research 30: 31-39. https:/doi.org/10.2307/1551743

Kabala C, Zapart J (**2012**) Initial soil development and carbon accumulation on moraines of the rapidly retreating Werenskiold Glacier, SW Spitsbergen, Svalbard archipelago. Geoderma, 175–176:9–20. https://doi.org/10.1016/j.geoderma.2012.01.025

Kaspari M., Yanoviak SP, Dudley R, Yuan M, Clay NA (**2009**) Sodium shortage as a constraint on the carbon cycle in an inland tropical rainforest. Proc Natl Acad Sci USA 106: 19405e19409. https://doi.org/10.1073/pnas.0906448106

Kaspari M, Clay NA, Donoso DA, Yanoviak SP (**2014**) Sodium fertilization increases termites and enhances decomposition in an Amazonian forest. Ecology 95:795e800. https://doi.org/10.1890/13-1274.1

Keiler M, Knight J, Harrison S (**2010**) Climate change and geomorphological hazards in the eastern European Alps. Philos Trans R Soc A Math Phys Eng Sci 368:2461–2479. https://doi.org/10.1098/rsta.2010.0047

Klimova I, Kaljuvee T, Türn L, Bender V, Trikkel A, Kuusik R (**2011**) Interactions of ammonium nitrate with different additives. J Therm Anal Calorim 105:13–26. https://doi.org/10.1007/s10973-011-1514-9

Labine C (**1994**) Meteorology and climatology of the Alexandra Fiord lowland. In Svoboda, J., and Freedman, B. (eds.), Ecology of a Polar Oasis: Alexandra Fiord, Ellesmere Island, Canada. Toronto: Captus Press, 23–39.

Larcher W (**2003**) Physiological Plant Ecology: Ecophysiology and Stress Physiology of Functional Groups, third ed. Springer, Berlin.

LeBauer DS, Treseder KK (**2008**) Nitrogen limitation of net primary productivity in terrestrial ecosystems is globally distributed. Ecology 89:379–379. https://doi.org/10.1890/06-2057.1

Lei Y, Du L, Chen K, Plenkocić-Moraj, Sun G (**2021**) Optimizing foliar allocation of limiting nutrients and fast-slow economic strategies drive forest succession along a glacier retreating chronosequence in the eastern Tibetan Plateau. Plant Soil 462, 159–174. https://doi.org/10.1007/s11104-020-04827-3

Li Z, He Y, Yang X, Theakstone WH, Jia W, Pu T, Liu Q, He X, Song B, Zhang N, Wang S, Du J (**2010**) Changes of the Hailuogou glacier, Mt. Gongga, China, against the background of climate change during the Holocene. Quaternary International 218:166–175. https://doi.org/10.1016/j.quaint.2008.09.005

Lichter J (**1998**) Rates of weathering and chemical depletion in soils across a chronosequence of Lake Michigan sand dunes. Geoderma 85:255–282. https://doi.org/10.1016/S0016-7061(98)00026-3

Likens GE (**2013**) Biogeochemistry of a forested ecosystem, 3rd edn. Springer, New York.

Lilienfein J, Wilcke W, Thomas R, Vilela L, Lima SdC, Zech W (**2001**) Effects of Pinus caribaea plantations on the C, N, P, and S status of Brazilian savanna Oxisols. Forest Ecology and Management 147:171-182. https://doi.org/10.1016/S0378-1127(00)00472-2

Liu JJ, Cheng ZL, Li Y (**2014**) The 1988 glacial lake outburst flood in Guangxieco Lake, Tibet, China. Natural Hazards and Earth System Sciences 14:3065–3075. https://doi.org/10.5194/nhess-14-3065-2014

Long RP, Horsley SB, Lilja PR (**1997**) Impact of forest liming on growth and crown vigor of sugar maple and associated hardwoods. Canadian Journal of Forest Research 27:1560-1573. https://doi.org/10.1139/x97-074

López-Moreno JI, Valero-Garcés B, Mark B, Condom T, Revuelto J, Azorín-Molina C, Bazo J, Frugone M., Vicente-Serrano SM, Alejo-Cochachin J (**2017**) Hydrological and depositional processes associated with recent glacier recession in Yanamarey catchment, Cordillera Blanca (Peru). Science of the Total Environment 579: 272–282. https://doi.org/10.1016/j.scitotenv.2016.11.107

Luo J, Li W, Liao X, He Z (**2004**) CO_2 emissions from soils of the deglaciered region on Hailuogou glacier in the past 100 years. Journal of Mountain Research 22:421-427.

Luo J, Tang R, Sun S, Yang D, She J, Yang P (**2015**) Lead distribution and possible sources along vertical zone spectrum of typical ecosystems in the Gongga Mountain, eastern Tibetan Plateau. Atmospheric Environment 115:132–140. https://doi.org/10.1016/j.atmosenv.2015.05.022

Marschner P (**2012**) Marschner's Mineral Nutrition of Higher Plants. Edition No. 3.

Mavris C, Egli M, Plötze M, Blum JD, Mirabella A, Giaccai D, Haeberli W (**2010**) Initial stages of weathering and soil formation in the Morteratsch proglacial area. Geoderma 155:359–371. https://doi.org/10.1016/j.geoderma.2009.12.019

McLaughlin SB, Wimmer R (**1999**) Tansley review No. 104. Calcium physiology and terrestrial ecosystem processes. New Phytol 142(3):373– 417. https://doi.org/10.1046/j.1469-8137.1999.00420.x

Mizuno K (**1998**). Succession processes of alpine vegetation in response to glacial fluctuations of tyndall glacier, Mt. Kenya, Kenya. Arctic and Alpine Research 30: 340–348. https://doi.org/ 10.2307/1552006

Moreau M, Mercier D, Laffly D, Roussel E (**2008**) Impacts of recent paraglacial dynamics on plant colonization: A case study on Midtre Lovénbreen foreland, Spitsbergen (79°N). Geomorphology 95:48–60. https://doi.org/10.1016/j.geomorph.2006.07.031

Moret P, Barragán Á, Moreno E, Cauvy-Fraunié S, Gobbi M (**2020**) When the ice has gone: colonisation of equatorial glacier forelands by ground beetles (Coleoptera: Carabidae). Neotropical Entomology 49:213–226. https://doi.org/10.1007/s13744-019-00753-x

Nogués-Bravo D, Araújo MB, Errea MP, Martínez-Rica JP (**2007**) Exposure of global mountain systems to climate warming during the 21st Century. Glob Environ Chang 17:420–428. https://doi.org/10.1016/j.gloenvcha.2006.11.007

Paoli GD, Curran LM (**2007**) Soil nutrients limit fine litter production and tree growth in mature lowland forest of southwestern Borneo. Ecosystems 10:503–18. https://doi.org/10.1007/s10021-007-9042-y

Pérez CA, Aravena JC, Silva WA, Enríquez JM, Fariña JM, Armesto JJ (**2014**) Ecosystem development in short-term postglacial chronosequences: N and P limitation in glacier forelands from Santa Inés Island, Magellan Strait. Austral Ecology 39:288–303. https://doi.org/10.1111/aec.12078

Pickett STA (**1989**) Space-for-Time Substitution as an alternative to long-term studies. In: Likens G.E. (eds) Long-term studies in ecology. Springer, New York, NY.

Portes R, Dahms D, Brandová D, et al (**2018**) Evolution of soil erosion rates in alpine soils of the Central Rocky Mountains using fallout Pu and $\delta^{13}C$. Earth Planet Sci Lett 496:257–269. https://doi.org/10.1016/j.epsl.2018.06.002

Rhodes R, Miles N, Hughes, JC (**2018**) Interactions between potassium, calcium and magnesium in sugarcane grown on two contrasting soils in South Africa. Field Crops Research,223:1–11. https://doi.org/10.1016/j.fcr.2018.01.001

Richardson SD, Reynolds JM (**2000**) An overview of glacial hazards in the Himalayas. Quat Int 65–66:31–47. https://doi.org/10.1016/S1040-6182(99)00035-X

Richardson JB, Friedland AJ (**2016**) Influence of coniferous and deciduous vegetation on major and trace metals in forests of northern New England, USA. Plant Soil 402:363–378. https://doi.org/10.1007/s11104-016-2805-5

Seehaus T, Malz P, Sommer C, Lippl S, Cochachin A, Braun M (**2019**) Changes of the tropical glaciers throughout Peru between 2000 and 2016 - Mass balance and area fluctuations. The Cryosphere 13:2537–2556. https://doi.org/10.5194/tc-13-2537-2019

Small EE, Badger AM, Abolafia-Rosenzweig R, Livneh B (**2018**) Estimating soil evaporation using drying rates determined from satellite-based soil moisture records. Remote Sensing 10:1945. https://doi.org/10.3390/rs10121945

Sondheim MW, Standish JT (**1983**) Numerical Analysis of a Chronosequence Including an Assessment of Variability. Canadian Journal of Soil Science 63:501–517. https://doi.org/10.4141/cjss83-052

Song Y, Maher BA, Li F, Wang X, Sun X, Zhang H (**2015**) Particulate matter deposited on leaf of five evergreen species in Beijing, China: Source identification and size distribution. Atmospheric environment 105:53-60. https://doi.org/10.1016/j.atmosenv.2015.01.032

Stevens PA, Harrison AF, Jones HE, Williams TG, Hughes S (**1993**) Nitrate leaching from a Sitka spruce plantation and the effect of fertilisation with phosphorus and potassium. Forest Ecology and Management 58:233–247. https://doi.org/10.1016/0378-1127(93)90147-F

Sun J, Sun X, Hu Z, Wang G (**2020**) Exploring the influence of environmental factors in partitioning evapotranspiration along an elevation gradient on Mount Gongga, eastern edge of the Qinghai-Tibet Platea, China. Journal of Mountain Science 17:384–396. https://doi.org/10.1007/s11629-019-5687-1

Sun X, Wang G, Lin Y, Liu L, Gao Y (**2013**) Intercepted rainfall in Abies fabri forest with different-aged stands in southwestern China. Turkish Journal of Agriculture and Forestry 37:495–504. https://doi.org/10.3906/tar-1207-36

Tavakkoli E, Rengasamy P, McDonald GK (**2010**) High concentrations of Na^+ and Cl^- ions in soil solution have simultaneous detrimental effects on growth of faba bean under salinity stress. Journal of experimental botany 61(15):4449–4459. https://doi.org/10.1093/jxb/erq251

Tessier A, Campbell PGC, Bisson M (**1979**) Sequential Extraction Procedure for the Speciation of Particulate Trace Metals. Anal Chem 51:844-851. https://doi.org/10.1021/ac50043a017

Ulrich B (**1983**) Interactions of forest canopies with atmospheric constituents: SO2, alkali and earth alkali cations and chloride. In: Ulrich B, Pankrath J (eds) Effects of accumulation of air pollutants in forest ecosystems. D. Reidel Publishing, Dordrecht, pp 33–45

Van Breemen N, Protz R (**1988**) Rates of calcium carbonate removal from soils. Canadian Journal of Soil Science 68(2):449–454. https://doi.org/10.4141/cjss88-042

Vilmundardóttir OK, Gísladóttir G, Lal R (**2014**) Early stage development of selected soil properties along the proglacial moraines of Skaftafellsjökull glacier, SE-Iceland. Catena 121:142–150. https://doi.org/10.1016/j.catena.2014.04.020

Vilmundardóttir OK, Gísladóttir G, Lal R (**2015**) Between ice and ocean; soil development along an age chronosequence formed by the retreating Breidamerkurjökull glacier, SE-Iceland. Geoderma 259–260:310–320. https://doi.org/10.1016/j.geoderma.2015.06.016

Vitousek PM, Howarth RW (**1991**) Nitrogen limitation on land and in the sea—How can it occur. Biogeochemistry 13:87– 115. https://doi.org/10.1007/BF00002772

Vogt KA, Grier CC, Vogt DJ (**1986**) Production, turnover, and nutrient dynamics of above- and belowground detritus of world forests. Adv Ecol Res 15:303–377. https://doi.org/10.1016/S0065-2504(08)60122-1

Wang J, He Q, Wu Y, Zhu H, Sun H, Zhou J, Wang D, Li J, Bing H (**2021**) Effects of pioneer N2-fixing plants on the resource status and establishment of neighboring non-N_2-fixing plants in a newly formed glacier floodplain, eastern Tibetan Plateau. Plant Soil 458:261–276. https://doi.org/10.1007/s11104-020-04462-y

Wang X, Luo J, Lin C, Wang D, Yuan W (**2020a**) Elevated cadmium pollution since 1890s recorded by forest chronosequence in deglaciated region of Gongga, China. Environmental Pollution 260:114082. https://doi.org/10.1016/j.envpol.2020.114082

Wang X, Luo J, Yuan W, Lin CJ, Wang F, Liu C, Wang G, Feng X (**2020b**) Global warming accelerates uptake of atmospheric mercury in regions experiencing glacier retreat. Proceedings of the National Academy of Sciences of the United States of America 117:2049–2055. https://doi.org/ 10.1073/pnas.1906930117

Wang J, Wu Y, Zhou J, Bing H, Sun H, He Q (**2020c**) Soil microbes become a major pool of biological phosphorus during the early stage of soil development with little evidence of competition for phosphorus with plants. Plant and Soil 446:259–274. https://doi.org/10.1007/s11104-019-04329-x

White AF, Blum AE, Schulz MS, Bullen TD, Harden JW, Peterson ML (**1996**) Chemical Weathering of a Soil Chronosequence on Granite Alluvium I. Reaction Rates Based on Changes in Soil Mineralogy. Geochimica et Cosmochimica Acta 60:2533–2550. https://doi.org/10.1016/0016-7037(96)00106-8

Wietrzyk P, Rola K, Osyczka P, Nicia P, Szymański W, Węgrzyn M (**2018**) The relationships between soil chemical properties and vegetation succession in the aspect of changes of distance from the glacier forehead and time elapsed after glacier retreat in the Irenebreen foreland (NW Svalbard). Plant and Soil 428:195–211. https://doi.org/10.1007/s11104-018-3660-3

Wilcke W, Lilienfein J (**2004**) Element storage in native, agri-, and silvicultural ecosystems of the Brazilian savanna. II. Metals. Plant and Soil 258:31–41. https://doi.org/10.1023/B:PLSO.0000016503.59527.ea

Wilcke W, Yasin S, Abramowski U, Valarezo C, Zech W (**2002**) Nutrient storage and turnover in organic layers under tropical montane rain forest in Ecuador. European Journal of Soil Science 53:15-27. https://doi.org/10.1046/j.1365-2389.2002.00411.x

Wilcke W, Velescu A, Leimer S, Bigalke M, Boy J, Valarezo C (**2017**) Biological versus geochemical control and environmental change drivers of the base metal budgets of a tropical montane forest in Ecuador during 15 years. Biogeochemistry 136:167–189. https://doi.org/10.1007/s10533-017-0386-x

Wilson MJ (**2004**) Weathering of the primary rock-forming minerals: processes, products and rates. Clay Minerals 39:233–266. https://doi.org/10.1180/0009855043930133

Wright SJ, Yavitt JB, Wurzburger N, Turner BL, Tanner EVJ, Sayer EJ, Santiago LS, Kaspari M, Hedin LO, Harms KE, Garcia MN, Corre MD (**2011**) Potassium, phosphorus, or nitrogen limit root allocation, tree growth, or litter production in a lowland tropical forest. Ecology 92:1616-16. https://doi.org/10.1890/10-1558.1

Wu Y, Li W, Zhou J, Cao Y (**2013**) Temperature and precipitation variations at two meteorological stations on eastern slope of Gongga Mountain, SW China in the past two decades. Journal of Mountain Science 10:370–377. https://doi.org/10.1007/s11629-013-2328-y

Wu Y, Zhou J, Bing H, Sun H., Wang J (**2015**) Rapid loss of phosphorus during early pedogenesis along a glacier retreat choronosequence, Gongga Mountain (SW China). PeerJ 3:e1377. https://doi.org/10.7717/peerj.1377

Yang Z, Bing H, Zhou J, Wu Y, Sun H, Luo J, Sun S, Wang J (**2015**) Variation of mineral composition along the soil chronosequence at the Hailuogou glacier foreland of Gongga Mountain Acta Pedologica Sinica 52(3):507–516. https://doi.org/10.11766/trxb201406180301

Yang D, Luo J, Peng P, Li W, Shi W, Jia L, et al. (**2021**) Dynamics of nitrogen and phosphorus accumulation and their stoichiometry along a chronosequence of forest primary succession in the Hailuogou Glacier retreat area, eastern Tibetan Plateau. PLoS ONE 16(2): e0246433. https://doi.org/10.1371/journal.pone.0246433

Zeien H, Brümmer GW (**1989**) Chemische Extraktion zur Bestimmung der Schwermetall-bindungsformen in Böden; Mittlgn. Dtsch. Bodenkundl. Gesellsch. Sonderh. 59/I, Kongreßbd. Münster, 505–510

Zemp M, Paul F, Hoelzle M, Haeberli W (**2008**) Glacier fluctuations in the European Alps 1850-2000: an overview and spatio-temporal analysis of available data. Darkening Peaks: Glacier Retreat, Science, and Society (Berkeley and Los Angeles: University of California Press, 2008), pages 152-167.

Zhang J, Luo J, DeLuca TH, Wang G, Sun S, Sun X, Hu Z, Zhang W (**2021**) Biogeochemical stoichiometry of soil and plant functional groups along a primary successional gradient following glacial retreat on the eastern Tibetan plateau. Global Ecology and Conservation 26:e01491. https://doi.org/10.1016/j.gecco.2021.e01491

Zhong XH, Luo J, Wu N (**1997**) Researches of the forest ecosystems on Gongga Mountain. Chengdu University of Science and Technology Press, Chengdu.

Zhong XH, Zhang WJ, Luo J (**1999**) The characteristics of the mountain ecosystem and environment in the Gongga Mountain region. Ambio 28 (8), 648–654.

Zhou J, Wu YH, Prietzel J, Bing H, Yu D, Sun S, Luo J, Sun H (**2013**) Changes of soil phosphorus speciation along a 120-year soil chronosequence in the Hailuogou Glacier retreat area (Gongga Mountain, SW China). Geoderma 195–196:251–259. https://doi.org/10.1016/j.geoderma.2012.12.010

Zhou J, Bing H, Wu YH, Yang Z, Wang J, Sun H, Luo J, Liang J (**2016**) Rapid weathering processes of a 120-year-old chronosequence in the Hailuogou Glacier foreland, Mt. Gongga, SW China. Geoderma 267:78–91. https://doi.org/10.1016/j.geoderma.2015.12.024

Zhou J, Bing H, Wu YH, Sun H, Wang J (**2018**) Weathering of primary mineral phosphate in the early stages of ecosystem development in the Hailuogou Glacier foreland chronosequence. European Journal of Soil Science, 69:450– 461. https://doi.org/10.1111/ejss.12536

Zhou P (**2013**) The differentiation and influence factors of carbon sequestration of typical vegetation types in altitudinal belts of Gongga Mountain. Master thesis, University of Chinese Academy of Sciences, Beijing, China, pp 32

C. Base cations release

Base cations release in soils along the 127-year Hailuogou glacial retreat chronosequence

Nuria Basdediós[1], Yanhong Wu[2], Wolfgang Wilcke[1]

[1]Karlsruhe Institute of Technology (KIT), Institute of Geography and Geoecology, Reinhard-Baumeister-Platz 1, 76131 Karlsruhe, Germany

[2]Key Laboratory of Mountain Surface Processes and Ecological Regulation, Institute of Mountain Hazards and Environment, Chinese Academy of Sciences, Chengdu 610041, China

Soil Science Society of America Journal (2022): 86, 1692–1706

DOI: 10.1002/saj2.20473

1. Abstract

At the Hailuogou glacial retreat chronosequence, a mature forest has surprisingly fast developed in ~120 years, although the glacial debris is dominated by nutrient-poor granite with a small contribution of carbonate minerals. In previous work, we hypothesized that the fast vegetation development is synchronized with initial fast carbonate weathering followed by slow silicate weathering. To test this hypothesis, we (i) characterized the composition of the glacial debris to elucidate the sources of base cations and (ii) determined the base cation release kinetics from topsoils (0-10 cm) along the chronosequence with a weathering experiment at a constant pH value (pH_{stat}). Besides granitic rocks, the glacial debris contained some meta-sedimentary and meta-volcanic calc-silicate rocks, amphibolite, mica schist, and quartzite. Although the total Ca concentration of the glacial debris was only about double that of Mg, K, and Na, during the first day of the pH_{stat} experiment, the released mass of Ca was >10 times higher than that of Mg and K, and even ca. 100 times higher than that of Na. The size of the fast-reacting Ca-carbonate pool decreased quickly in the first ca. 40 yr, after which a slow-reacting Ca-silicate pool matched the fast-reacting pool with a size of 1.9±0.6 mg g^{-1} Ca. In contrast, for Mg, K, and Na the slow-reacting pool dominated from the beginning, suggesting that these elements mainly originated from silicate weathering. Our findings support the view that the well-synchronized interplay between carbonate and silicate weathering facilitated the fast vegetation succession.

Core ideas:

Calcite occurred in the mainly granitic substrate of the Hailuogou chronosequence.

The calcite originated from meta-sedimentary and meta-volcanic rocks in the glacial debris.

Carbonate weathering determined the rapid initial Ca but not Mg release.

The main sources of weathered Mg, K, and Na were silicate minerals.

Base cation release kinetics followed the order, Ca>>Mg>K>>Na.

2. Introduction

Chronosequences and associated space-for-time substitutions have been widely used to study the soil development and plant succession across multiple time scales and many landscapes (Bockheim, 1980; Huggett, 1998; Walker et al., 2010). The parent material determines the original element concentrations of the evolved soils and directly influences the balance between nutrient availability, loss, and retention (Anderson, 1988; Eimil-Fraga et al., 2014; Jesse Hahm et al., 2014; Augusto et al., 2017). The weathering of parent materials releases nutrients into the soil solution at variable rates, depending on mineral properties, climatic conditions, topographic position, time and biota (Jenny, 1941; Harley and Gilkes, 2000; Wilson, 2004). Except for N which usually enters the soil via microbial fixation from the atmosphere, mineral weathering releases all macronutrients (i.e. K, Ca, Mg, P, and S) as well as trace elements which are necessary for plant growth (Barker et al., 1997; Marschner, 2012; Tripler et al., 2006; Vitousek and Sanford, 1986; White and Broadley, 2003).

In the subtropical high mountainous Gongga region, located at the southeastern edge of the Tibetan Plateau, the decrease in the mean annual precipitation and increase in the mean annual temperature in the past two decades (Wu et al., 2013) accelerated the retreat of the Hailuogou glacier, one of the largest glaciers at the foot of the Gongga Mountain (Zhou et al., 2013), which started in the late 19th century (Li et al., 2010). The successive ecosystem development created a natural soil and vegetation chronosequence, which has been little disturbed by human activities. The fast vegetation succession is surprising, because the Gongga Mountain and the derived glacial debris is mainly composed of granite (Searle et al., 2016), a nutrient-poor substrate, particularly with respect to Ca and Mg (Schmitt et al., 2012). However, the Hailuogou glacial debris also contains carbonates originating from meta-sedimentary rocks (Roger et al., 1995; Searle et al., 2016), which are leached out of the topsoil in 47 years after glacial retreat (Basdediós et al., 2022).

The major rock-forming mineral groups in the Earth's crust are quartz, feldspars (i.e., K-feldspar and plagioclase) and ferromagnesian minerals (e.g., biotite and hornblende). Quartz contains low concentrations of plant nutrients and is little weatherable (Barker et al., 1997). Feldspars persist in strongly weathered soils in which other primary minerals have been altered to secondary minerals, providing a slow release of K and Ca (Allen and Hajek, 1989). In contrast, ferromagnesian minerals are considered to be relatively unstable

among the common rock minerals and can release large quantities of Mg and K (Allen and Hajek, 1989). Minerals with higher solubility in water than silicates, such as carbonates, are the most easily weathered (Smith and Huyck, 1999). Fast initial weathering of $CaCO_3$ and the subsequent release of available nutrients may contribute to the development of primary vegetation successions, especially in glacial environments, because chemical weathering is strongly influenced by carbonate minerals even if they are present in only small amounts (~1%) in the parent material (Blum et al., 1998).

The presence of carbonate minerals buffers the pH near neutral values and usually releases Ca and if dolomite or magnesite are present also Mg at high rates through weathering (Mavris et al., 2010; Zamanian et al., 2016). The soil pH influences many biogeochemical processes which drive vegetation succession, such as microbial turnover of organic matter and related N release (Andersson and Nilsson, 2001), P availability (Hinsinger, 2001; Sohrt et al., 2017), and the release of nutrient cations by mineral weathering (Chadwick and Chorover 2001). Weathering of carbonate and silicate minerals can be described as an acid-base reaction, with the difference that carbonate minerals dissolve completely whereas silicate weathering usually results in the formation of secondary clay minerals outside the inner (per-)humid tropics with their desilicating weathering regime. A mix of mineral constituents in the parent material, e.g., carbonates and easily weatherable silicates, might release a wide variety of nutrients through weathering that become easily available for plant uptake. Once a soil organic layer is established, it can store and supply a large quantity of the nutrients required by the vegetation (Basdediós et al., 2022; Jobbágy and Jackson, 2004; Lilienfein et al., 2001; Wilcke et al., 2002). Because at the beginning of the vegetation succession on glacial debris the soil is usually free of organic matter, mineral weathering together with the nutrient input by atmospheric deposition drives the supply of all macronutrients but N, which is acquired by microbial N_2 fixation from the atmosphere except in bituminous sediments and metamorphites (Houlton et al., 2018). Therefore, weathering rates play a crucial role in enabling plant growth. Likewise, plants can influence weathering rates compared with the rates when plants are absent (Berner et al., 2004). Plants cause physical weathering by root growth and influence chemical weathering of minerals to mobilize nutrients from the soil, partly assisted by mycorrhizal fungi with which plant roots are associated. Roots can also excrete organic acids and chelates into the rhizosphere, which help plants to access specific nutrients or to form non-toxic complexes in soils (Drever and Stillings, 1997; Meyer et al.,

2009). In a previous study at the Hailuogou glacial retreat chronosequence, Basdediós et al. (2022) suggested that the synchronization of weathering rates with vegetation development facilitated the fast succession. They hypothesized that in the early phase of the ecosystem succession, weathering of carbonates and easily weatherable silicates released high amounts of Ca and to a lesser degree Mg. After carbonates were dissolved, the onset of slower silicate weathering concurring with the shift from deciduous to coniferous forest slowed the nutrient cycle. While the total stocks of Ca and Mg decreased along the chronosequence in response to the loss of carbonates and easily weatherable silicates within a few decades, those of K and Na were unrelated with ecosystem age. To explain the lack of a relationship between ecosystem age and K and Na stocks, Basdediós et al. (2022) suggested that K and Na were constantly released from silicate mineral pools at low rates which were taken up by the organisms of the ecosystem with little losses.

Batch and column techniques are used to examine buffer capacities and reaction kinetics of rocks and soils (Selim and Amacher, 1997; Alt et al., 2013; Hacker et al., 2017). Frequently, the analyzed mineral material is exposed to a constant elevated H^+ pressure in so-called pH_{stat} experiments, which can be realized in automatic titroprocessors or as batch experiment with ion exchangers. In automatic titroprocessors, the proton activity in the reaction solution is kept constant at a higher level than soil equilibrium pH by measuring pH continuously and replacing buffered protons by the addition of mineral acid (Süsser, 1987; van de Sand and Fischer, 1994). In experiments with tritroprocessors, the released ions accumulate in the solution with the risk that secondary mineral precipitation occurs if dissolution constants are surpassed. Titroprocessor experiments therefore mimic conditions with a stagnant solution phase. In the pH_{stat} method of Kaupenjohann and Wilcke (1995) ions released into solution during H^+ buffering are removed from the system with the help of ion exchange resins and therefore do not affect further reactions. Ion exchange resin approaches mimic conditions in which water percolates through the soil and removes weathering products (Schwarz et al., 1999; Alt et al., 2013; Hacker et al., 2017). Süsser (1987) described buffer reactions in soils during pH_{stat} experiments as the sum of two independent reactions both following first order kinetics. This allows to distinguish a fast- and a slow-reacting mineral pool and release rate constants associated with these pools.

Our overall objective was to (i) identify the origin of the carbonate minerals in the granite-dominates glacial debris of the Hailuogou glacier and test the hypotheses that (ii) $CaCO_3$ determines initial Ca release and contributes, to a minor degree, to that of Mg, (iii) the weathering release rates of Ca and Mg decrease with increasing soil age, because of the fast loss of initially present carbonates and easily weatherable silicate minerals as reflected by strongly decreasing fast-reacting Ca and Mg pools. Once the carbonates are gone, the slower silicate weathering takes over and releases Ca and Mg at lower rates than initially, which is synchronized with the ecosystem development from deciduous to coniferous forest. (iv) K and Na are only weathered from silicate minerals such as mica during the whole ecosystem development and thus show constant release rates and slightly decreasing pool sizes.

3. Materials and methods

3.1. Study area

The Gongga Mountain (summit: 7556 m a.s.l., **Figure A-3**) is formed from the Gongga batholith, which extends for more than 100 km in the transition zone of the Sichuan Basin and the Tibetan Plateau, Southwest China. The massif is mainly composed of a granitoid complex (i.e., granite and granodiorite) intruded into the Palaeozoic-Triassic meta-sediments and meta-volcanic rocks of the Songpan-Ganze terrane (Roger et al., 1995; Searle et al., 2016). Located on the eastern slope of the Gongga Mountain, the Hailuogou Glacier has markedly retreated since late 19th century (Li et al., 2010), developing a 2 km long and 50–200 m wide chronosequence, which spans an elevational range from 2800-2950 m a.s.l.. The short time of pedogenesis (<130 years) formed soils without B horizon classified from youngest to oldest as Leptic Calcaric to Folic Dystric Regosols (IUSS Working Group WRB 2014). The parent material of soil formation is moraine and consists mainly of a mixture of silicates (87%), including plagioclase (28.5%), quartz (24.5%), biotite (12%), hornblende (12%) and K-feldspar (10%), carbonates (<10%), and a minor contribution of apatite (<2.1%) (Yang et al., 2015; Zhou et al., 2016). The mean annual temperature and precipitation are 4.2 °C and 1947 mm, respectively. Rain falls mainly during the summer growing season (May to September, Wu et al., 2013).

Our study included seven sites, de-glaciated between 0 (Site 1; 2982 m a.s.l.) and 127 years ago (Site 7; 2855 m a.s.l.; **Figure A-3**), previously described by Zhou et al. (2013). A primary vegetation succession has developed along the chronosequence, from pioneer shrubs (i.e., *Hippophae rhamnoides* L., Site 3: 37 yr), over half mature broad-leaved tree forests dominated by poplar (*Populus purdomii* Rehder; Site 4: 47 yr), to a full conifer forest dominated by Faber's fir (*Abies fabri* (Mast.) Craib; Sites 5 and 6: 59 and 87 yr, respectively) and Sargent spruce (*Picea brachytyla* (Franch.) E. Pritz.; Site 7: 127 yr). With increasing time, the soils have developed A and O horizons of increasing thickness. The intense carbonate weathering in the early stage of the chronosequence and the rapid establishment of the vegetation decreased soil pH from 8.0 to 5.8 in only 47 years (Basdediós et al., 2022).

3.2. Field sampling

At all seven study sites, we collected samples of the A and C horizons and from the 0-10 cm topsoil layer, which included the uppermost part of the C horizons because the morphologically recognizable A horizons were only 0.5-6.5 cm thick or even absent at Site 1 in August 2017 (**Figure A-2; Table C-1**). Each ecosystem succession stage was sampled in triplicate. The distance between the sampled soil profiles was at least 20 m, except at Sites 1 and 2, where the distance was reduced to 10 m because of the narrower valley in the proximity of the glacier. Mineral soil samples were air-dried to constant weight and sieved to two different fractions: fine earth (<2 mm) and stones (>2mm). Plant residues were removed manually. At Site 1 (0 yr), we additionally collected 16 different rock samples from the surface which we considered as representative of the composition of the glacial debris forming the substrate for soil development.

3.3. Optical and chemical analyses

To determine the type of the collected rocks, photomicrographs of thin sections (30 µm thick) were taken with an Axiocam 105 attached to a Zeiss Axiolab optical microscope (1.5x; Carl Zeiss AG, Oberkochen, Germany). To collect unweathered rock material, we removed the outer shell of each rock sample by cutting with an automated core slabbing saw. Aliquots of the soil samples were ground using a Retsch MM 400 ball mill (Retsch

GmbH, Haan, Germany). The stone fraction of the soils (>2 mm) and the rock samples were ground in an agate grinding set using a vibratory disk mill (Siebtechnik GmbH, Mülheim an der Ruhr, Germany).

Table C-1. Mean loss on ignition (LOI) and element concentrations with standard errors in parentheses (n=3) of the stone fraction (>2mm) in the soil profiles along the Hailuogou chronosequence.

Site age	Soil horizon	LOI	Inorganic C	S	Ca	Mg	K	Na
(yr)		(%)			(g kg^{-1})			
5	A	4.38 (1.5)	7.4 (1.0)	0.7 (0.2)	74.5 (4.2)	32.1 (1.2)	36.1 (3.0)	26.1 (1.3)
37	A	0.51 (0.0)	7.3 (0.8)	0.3 (0.2)	70.2 (9.6)	36.3 (5.1)	36.5 (3.4)	24.3 (2.2)
47	A	0.69 (0.1)	2.0 (0.7)	0.1 (0.0)	65.7 (2.2)	31.2 (0.6)	49.2 (2.9)	36.8 (4.5)
59	A	1.27 (0.3)	2.6 (0.7)	0.3 (0.1)	57.1 (5.5)	30.4 (4.1)	40.4 (4.0)	26.9 (3.3)
87	A	1.68 (0.8)	1.5 (0.2)	0.2 (0.1)	45.3 (1.3)	20.5 (2.2)	28.4 (1.9)	21.5 (0.9)
127	A	5.59 (4.5)	2.0 (0.3)	0.3 (0.1)	42.9 (4.7)	19.2 (2.3)	28.9 (0.6)	19.2 (0.9)
5	C	0.20 (0.0)	9.7 (0.2)	0.7 (0.3)	87.4 (2.4)	32.2 (0.5)	37.6 (1.1)	25.3 (2.4)
37	C	0.45 (0.1)	10.2 (3.7)	0.3 (0.1)	60.3 (10.0)	21.8 (4.0)	21.9 (1.6)	14.2 (1.7)
47	C	0.27 (0.1)	1.6 (0.7)	0.1 (0.0)	53.6 (8.1)	26.2 (1.8)	46.6 (3.5)	30.6 (2.4)
59	C	0.57 (0.0)	3.4 (1.1)	0.2 (0.1)	57.7 (6.7)	27.7 (3.0)	39.9 (3.6)	26.4 (3.0)
87	C	0.73 (0.2)	2.4 (0.6)	0.2 (0.1)	35.3 (1.5)	17.0 (0.9)	25.2 (1.9)	17.4 (1.5)
127	C	0.37 (0.1)	1.8 (0.7)	0.3 (0.2)	46.2 (2.7)	21.2 (1.0)	35.5 (1.2)	23.6 (1.3)
0	C1	1.58 (0.3)	6.7 (0.8)	0.3 (0.1)	79.7 (11.5)	31.4 (2.9)	34.1 (3.0)	28.5 (1.7)
0	C2	0.41 (0.1)	9.5 (2.8)	0.5 (0.3)	88.9 (6.0)	31.8 (3.0)	35.2 (2.3)	25.3 (0.7)

Total element concentrations in fine earth (<2 mm), the stone fraction (> 2mm), and rocks from the glacial debris, were determined after total digestion with concentrated HNO_3/HF/H_2O_2 (4:1.5:1, v/v) in a microwave oven (MARS6Xpress, CEM) by measurement with an inductively-coupled plasma optical-emission spectrometer (ICP-OES, 5100 VDV, Agilent). Accuracy was assessed by the analysis of a certified reference material (BCR-2, Basalt, Columbia River). Average recoveries±standard deviations were 100±10% for all certified elements.

Soil pH, effective cation-exchange capacity (ECEC), concentrations of exchangeable Ca, Mg, K, and Na, and Ca carbonate concentrations were taken from Basdediós et al. (2022). The inorganic C (i.e., after muffling the samples at 550°C to remove organic matter) and total S concentrations of the stone fraction were determined by combustion in a CNS Elemental Analyzer (EuroEA, HEKAtech GmbH). The inorganic C concentrations and $\delta^{13}C$ values in the rocks were determined with an Elemental Analyzer – Isotope Ratio Mass Spectrometer (Flash 2000 HT Plus-Delta V Advantage, ThermoFisher Scientific) after

muffling the samples at 550°C. Loss on ignition (LOI) was determined by weighing before and after muffling the samples at 550°C.

To determine the release kinetics of the base cations (i.e., Ca, Mg, K, and Na) we followed the method of Schwarz et al. (1999) and included modifications of Alt et al. (2013) to handle the carbonates. We inserted 2 g of a mixed ion-exchange resin (Amberlite MB-20, Rohm and Haas, Philadelphia, PA, USA) into 3 cm-wide 4 cm-long homemade polyethylene (PE) bags, which were permeable to fluids (mesh width 100 µm). Before starting the experiment, the resin was saturated with HNO_3 and rinsed with deionized water (DI, >18 MΩ cm^{-1}) to remove free acid. We added 100 mL of DI water to 1 g of fine earth in a 125- mL PE bottle. The soil-water suspension was shaken during 1 hour and the initial pH was measured. The resin bag and 1 mL of $Ba(NO_3)_2$ of varying concentrations were added at the same time to the soil-water suspension in equilibrium to start the experiment. We supplied as many Ba equivalents as were theoretically necessary to lower the pH to 3.0 by releasing exchanged H^+ from the resin. Ba equivalents were calculated as the H^+ concentration in the solution at pH 3.0 minus that in the equilibrium soil suspension, assuming that each mol of Ba^{2+} releases 2 mol of H^+. The bottles were shaken during 10 min, 30 min, 1 h, 2 h, 4 h, 12 h, 24 h, 48 h, 96 h and 168 h, respectively, to determine the element release over time. Therefore, 10 PE bottles were prepared per soil sample. At each site age, we analyzed three independent soil samples collected from the uppermost 10 cm of the soils. In total, 7 sites x 3 replicates x 10 aliquots for the different shaking times = 210 samples were processed. After the extraction time had passed, the resin bags were removed and the pH of the soil suspension was immediately measured in an aliquot that was afterwards discarded because of the release of K by the glass electrode. After rinsing the resin bags thoroughly with DI water, the ions adsorbed to the resin were extracted in three steps with 30 mL of 2M HNO_3 for 10 min in the first and second step and for 30 min in the last one. Exchanged element concentrations were determined by ICP-OES. Preliminary tests of the element recovery from the resins with standard solutions were satisfying for all studied elements (Ca: 101±3%, Mg: 99±1%, K: 106±3%, Na: 99±1%; n=3).

3.4. Calculations and statistical analyses

The initial number of moles of H^+ that had to be released from the resin to decrease the initial pH (pHi) to 3.0 by exchange with Ba^{2+} ions was calculated with **Equation C-1**.

$$H^+ = (10^{-3} - 10^{-pHi}) / 2 \quad \textbf{(C-1)}$$

The base cation release kinetics were described by a two-step first-order reaction (**Equation C-2**, Süsser, 1987; Schwarz et al., 1999).

$$Y(t) = \text{Pool A } (1\text{-}e^{-ka\,t}) + \text{Pool B } (1\text{-}e^{-kb\,t}) \quad \textbf{(C-2)}$$

where Y(t) represents the element release from soil (mg kg^{-1}) at time *t*. Pool A and Pool B are the estimates of the two differently reactive pools (slow/fast; mg kg^{-1}) and k_a and k_b are the corresponding rate constants (h^{-1}) of each pool, estimated by a nonlinear regression model using sequential quadratic optimization. We used the coefficient of determination (R^2) as measure of the fit between our data and the function.

Linear regression and Pearson correlation were used to evaluate the relationships between variables. Significant differences between the fast-reacting pool (Pool A) of each base cation (i.e., Ca, Mg, K, and Na) and its respective exchangeable element concentration extracted with 1M NH_4NO_3 were tested with independent two-sample t-tests at each site. One-way analysis of variance (ANOVA) and Tukey's HSD post-hoc test were applied to find significant differences in Pool A, Pool B, k_a and k_b among the seven study sites. Normal distribution of residuals was visually inspected. Homoscedasticity was tested with Levene's test. Statistical analyses were conducted with the statistical software R (R Core Team, 2019). Significance was set at $p < 0.05$.

4. Results

4.1. Rock types and source of carbonates

The 16 rocks we collected at Site 1 included four samples of granite, six samples of calc-silicate rocks of which five were meta-sedimentary (MS) and one meta-volcanic (MV), three samples of amphibolite, one sample of mica schist and one sample of quartzite. Our

visual impression in the field was that meta-volcanic rocks occurred rarely in the study area, while metasedimentary rocks were more frequent.

We detected inorganic C in all collected rock types (**Figure C-1**). Assuming that all the inorganic C is present as calcite ($CaCO_3$), the studied rocks contained up to 19% of calcite. The sample with the highest calcite concentration was the meta-volcanic rock (MV, **Figure C-1**). The second highest inorganic C concentrations were detected in the more frequent metasedimentary rocks (MS). In these rocks, calcite was present together with quartz and amphibole (**Figure C-2a**), epidote (**Figure C-2b**), biotite (**Figure C-2c**), and traces of zoisite (**Figure C-2d**). Optical microscopy images revealed that the calcite occurred mainly in the pores of the rocks, as interstitial calcite between the grains (**Figure C-2e**). The meta-volcanic rock was characterized by layering mainly consisting of calcite, plagioclase, amphibole, feldspar, and traces of quartz (**Figure C-2f**).

Total metal concentrations of the rocks varied widely (**Figure C-1**). Calcium concentrations correlated significantly with the inorganic C concentrations in the calc-silicate rocks and granites ($r = 0.88$, $p < 0.001$, $n = 10$). However, this was not the case in amphibolite, mica-schist, or quartzite. The total Mg, K, and Na concentration in rocks did not correlate with the inorganic C concentrations. The $\delta^{13}C$ values ranged from -2.43 to -10.4‰ in all rocks except for amphibolite and mica schist, which were lower (–11.5 to -22.5‰). The rapid carbonate depletion from the parent material was reflected by the fast decrease in inorganic C concentrations in the stone fraction along the chronosequence, which fell by one order of magnitude during the first 47 years (**Table C-1**).

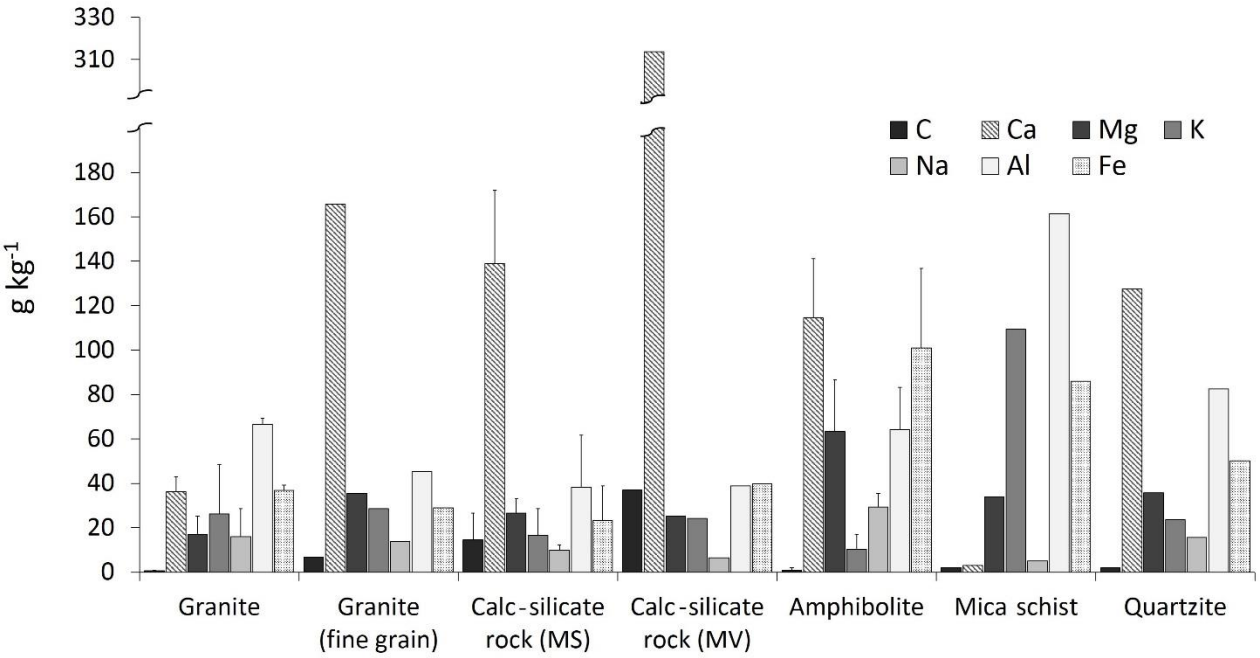

Figure C-1. Mean concentrations of inorganic C, Ca, Mg, K, Na, Al, and Fe in the sampled rock types of the Hailuogou glacial debris. Error bars indicate the standard deviation of three (granite and amphibolite) or six (calc-silicate rock) replicate samples. Lacking error bars indicate that only one sample was available. MS, metasedimentary rock; MV, metavolcanic rock.

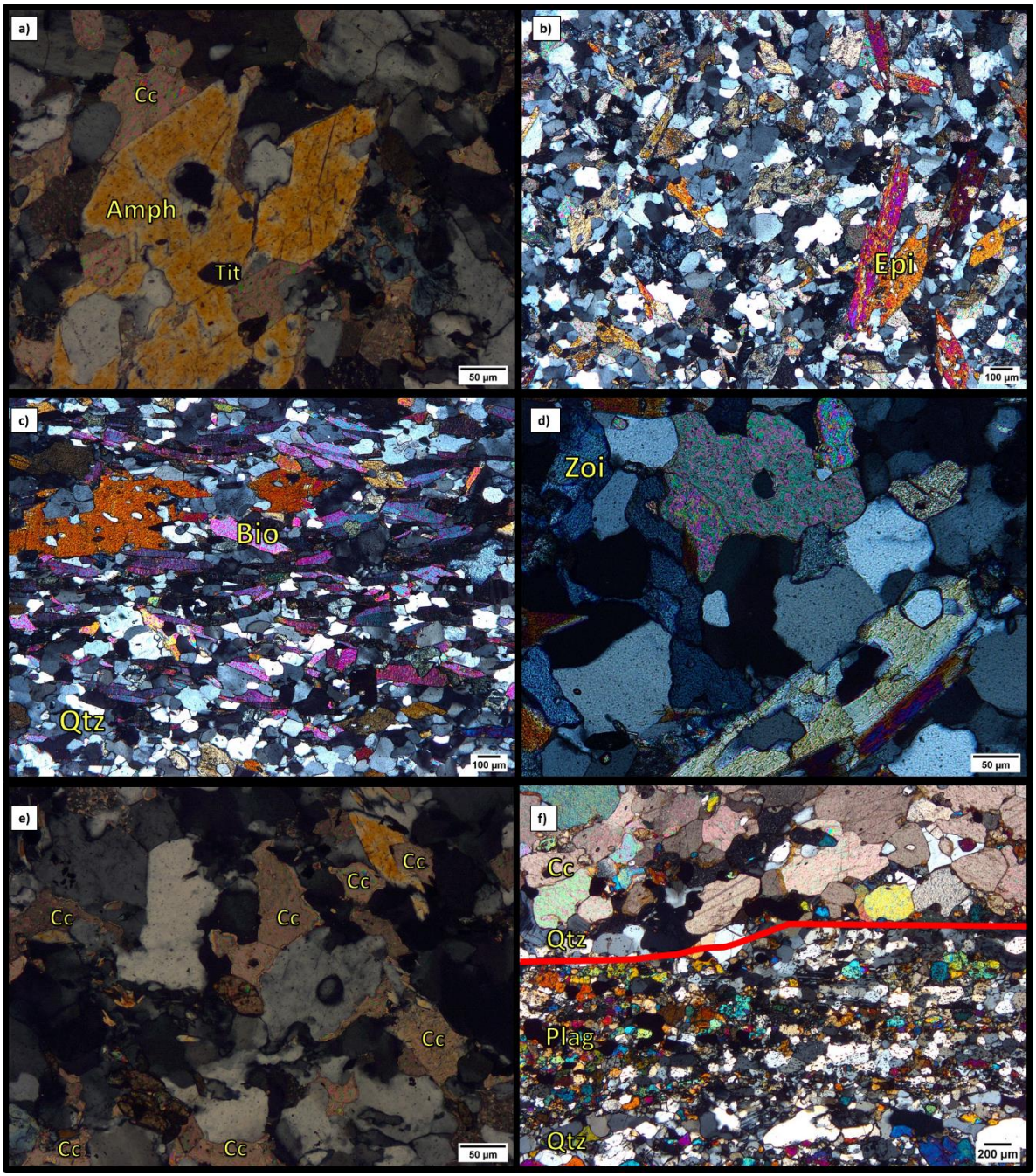

Figure C-2. Photomicrograph of thin sections of selected rocks collected from the Hailuogou glacial debris. Metasedimentary rocks (a–e) contained (a) calcite (Cc), amphibole (Amph), and titanite (Tit), (b) Epidote (Epi), (c) biotite (Bio), and quartz (Qtz), (d) some zoisite (Zoi), and (e) high amounts of interstitial calcite between the grains. (f) The only meta-volcanic rock collected contained a carbonate layer (Cc), few quartz layers (Qtz) and plagioclase (Plag). The red line in f illustrates the banding/layering by separating the coarser grained upper part from the finer grained lower part of the photomicrograph of the meta-volcanic rock

4.2. Base cation release kinetics

From Site 1 to Site 3 (soils containing carbonates), the target pH of 3.0 was reached in 4 to 12 hours after starting the experiment, while from Site 4 to Site 7, the target pH was reached in 30 minutes to 1 hour. At Sites 1 (0 yr) and 2 (5 yr), the release kinetics of Ca were converged to a one-pool kinetic equation instead of to a two-pool kinetic equation (Pool B = 0 or k_a=k_b). The goodness of the fit (R^2 values) ranged from 0.89 to 0.99, 0.97 to 0.99, 0.96 to 0.99 and 0.96 to 0.99 for Ca, Mg, K, and Na, respectively (**Figure C-3**).

The size of the fast-reacting pool (Pool A) of Ca dropped substantially along the chronosequence (**Figure C-4a**) and correlated significantly positively with the $CaCO_3$ and exchangeable and total Ca concentrations (**Table C-2**). Pool A of Mg, K, and Na did not change with site age and was generally smaller than their corresponding slow-reacting Pool B (**Figure C-4b, c, d**). Pools A of Mg and K were significantly and marginally significantly ($p < 0.1$) correlated with the exchangeable Mg and K concentrations in soil, respectively (**Table C-2**). Pool B of K correlated positively with the exchangeable K concentrations (**Table C-2**). Pool B of Na increased significantly with decreasing $CaCO_3$ concentrations.

The modeled release rate constant associated with the fast-reacting Pool A, k_a, did not significantly change with site age for any of the studied elements and varied from 0.3-0.7, 1.7–8.2, 0.4–0.8, and 0.1–39 h^{-1} for Ca, Mg, K and Na, respectively. Similarly, the modeled release rate constant associated with the slow-reacting Pool B, k_b, of Ca, Mg and Na was not correlated with site age, and varied from 0.02-0.04, 0.01–0.02 and 0.01-0.03 h^{-1}, respectively. Only k_b of K decreased significantly with site age**,** from 0.08 (Site 1, 0 yr) to 0.02 h^{-1} (Site 7, 127 yr). The k_a values of Ca correlated significantly negatively with the total Ca concentrations, while the k_a values of Na correlated significantly negatively with the $CaCO_3$ concentrations. The k_b values of Mg and K correlated significantly positively with pH and $CaCO_3$ concentrations (r and p values shown in **Table C-2**).

Table C-2. Pearson coefficient (r) and p values of the correlations of site age, exchangeable element concentrations (exch.) extracted with 1M NH_4NO_3, $CaCO_3$ concentration, and total element concentrations in the fine earth (soil <2 mm) with Pools A and B and release rate constants k_a and k_b, which were modeled based on the results of a pH_{stat} experiment at pH 3 on the topsoils (0-10 cm) along the Hailuogou chronosequence.

						Release rate constants (h^{-1})			
		Pool A (mg kg^{-1})		**Pool B (mg kg^{-1})**		**k_a**		**k_b**	
	Properties	**r**	**p**	**r**	**p**	**r**	**p**	**r**	**p**
Ca	Site age (yr)	-0.81	< 0.001	-0.50	0.06	0.42	0.06	0.23	0.40
	Exch. Ca (mg kg^{-1})	0.93	< 0.001	0.58	< 0.05	-0.38	0.09	0.29	0.29
	$CaCO_3$ (g kg^{-1})	0.99	< 0.001	0.47	0.08	-0.38	0.08	0.35	0.20
	Total Ca soil (g kg^{-1})	0.94	< 0.001	0.58	< 0.05	-0.54	< 0.05	-0.06	0.84
Mg	Site age (yr)	0.17	0.47	-0.27	0.24	-0.32	0.16	-0.40	0.07
	Exch. Mg (mg kg^{-1})	0.54	< 0.05	-0.12	0.61	-0.38	0.09	-0.18	0.43
	$CaCO_3$ (g kg^{-1})	0.04	0.86	-0.10	0.67	0.17	0.47	0.47	< 0.05
	Total Mg soil (g kg^{-1})	-0.18	0.45	0.28	0.22	0.13	0.56	0.30	0.19
K	Site age (yr)	-0.32	0.16	-0.40	0.07	-0.26	0.25	-0.62	< 0.05
	Exch. K (mg kg^{-1})	0.38	0.09	0.50	< 0.05	0.15	0.53	-0.02	0.93
	$CaCO_3$ (g kg^{-1})	0.07	0.76	-0.04	0.88	0.35	0.12	0.74	< 0.001
	Total K soil (g kg^{-1})	-0.21	0.37	-0.12	0.60	0.11	0.62	-0.25	0.27
Na	Site age (yr)	0.16	0.49	0.32	0.16	0.26	0.26	-0.31	0.17
	Exch. Na (mg kg^{-1})	-0.06	0.81	-0.21	0.36	0.36	0.11	0.18	0.44
	$CaCO_3$ (g kg^{-1})	0.00	0.99	-0.50	< 0.05	-0.48	< 0.05	0.30	0.18
	Total Na soil (g kg^{-1})	-0.13	0.57	0.40	0.07	0.28	0.21	-0.21	0.37

The size of the Pools A of Ca and Mg generally did not significantly differ from the respective size of the exchangeable element concentrations at most sites (**Figure C-5a, b**). However, at Sites 1 and 2 the Pool A of Mg was significantly larger than the exchangeable Mg concentration and at Site 5 Pools A of Ca and Mg were significantly larger than the respective exchangeable element concentrations. The exchangeable Ca concentration in the carbonate-containing soils (Site 1 to 3) could not be determined with the used standard method because of the partial dissolution of calcite in the extract. The size of Pools A of K and Na was significantly larger than the respective exchangeable concentrations at all study sites (**Figure C-5c, d**).

The slow-reacting Pool B of Mg only started to release Mg after 4-12 h and was significantly correlated with the total Mg concentration in the soil (r = 0.59). Pools B of Mg and K correlated significantly with each other (r = 0.65, p = 0.001) but not with those of Ca or Na. At the end of the experiment (t = 168 h), the total mass of released Mg strongly

correlated with that of Fe ($r = 0.96$, $p < 0.001$), Al ($r = 0.89$, $p < 0.001$), and K ($r = 0.84$, $p < 0.001$). However, there was no correlation between the total mass of released Ca and Na and that of Fe or Al. The released K:Mg ratio 1 h after starting the experiment linearly decreased from 3.1 ± 0.3 (Site 1) to 0.9 ± 0.2 (Site 7, $r = 0.79$, $p < 0.005$), while it averaged 0.4±0.1 at the end of the experiment with little variation (**Figure C-6a**). Similarly, the molar K:Mg ratio in aboveground biomass tended to decrease from Site 3 to 7, although the correlation between site age and molar K:Mg ratio was not significant (**Figure C-6b**). The molar K:Mg ratio varied little with site age in the organic layer and the mineral soil (0-10 cm).

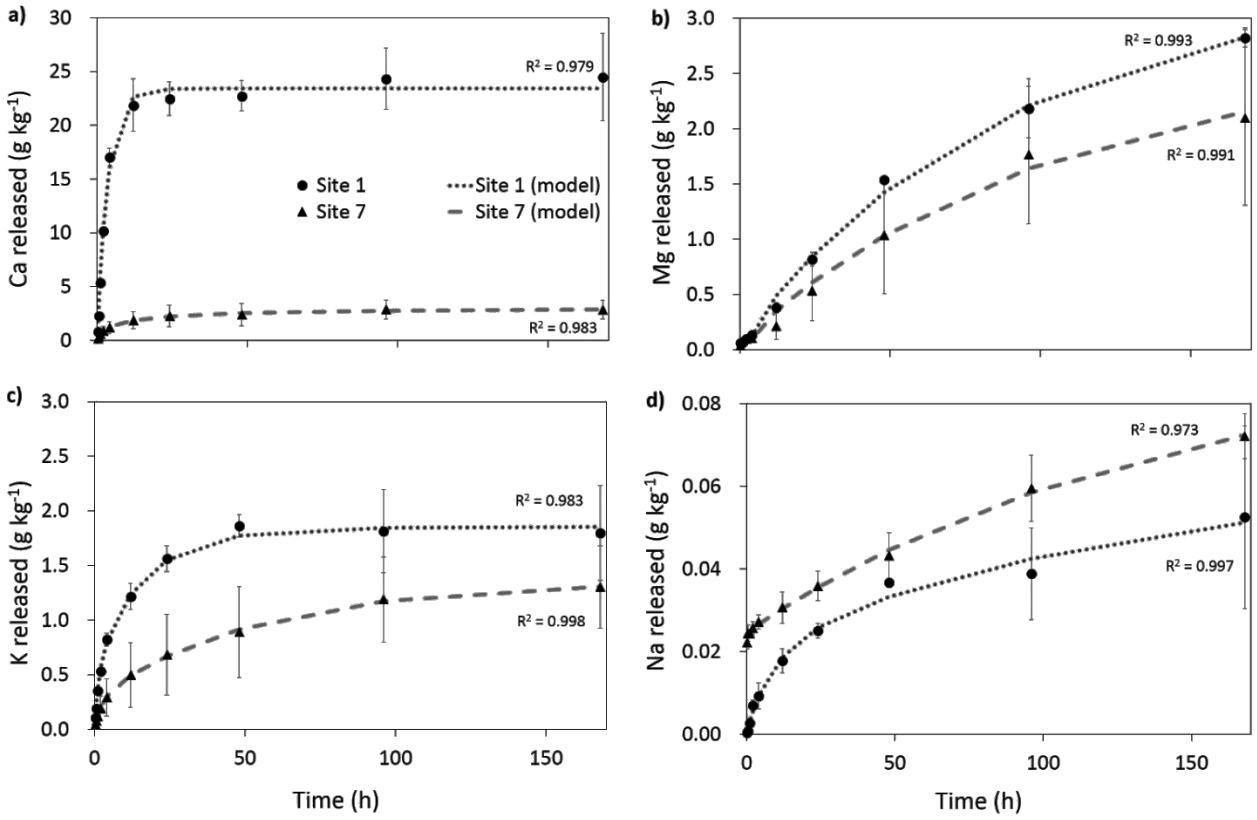

Figure C-3. Release kinetics of (a) Ca, (b) Mg, (c) K, and (d) Na during a pH_{stat} experiment at pH 3 in topsoils (0–10 cm) from Site 1 (0 yr) to Site 7 (127 yr) of the Hailuogou chronosequence. Error bars represent standard errors (n = 3). The dotted and dashed lines illustrate the biexponential fit.

5. Discussion

5.1. Source of carbonates

The plutonic component of the Hailuogou glacial debris was expected from geological maps showing that the Gongga Mountain peak is composed of granitic rocks. Paleozoic sedimentary rocks with high-grade metamorphism can be found in the surroundings, ~10 km from the main peak (Roger et al., 1995). Searle et al. (2016) also reported the presence of metasediments at the eastern margin of the Gongga batholith, which also belongs to the source area of the Hailuogou glacial debris.

Our suggestion that the inorganic carbon detected in all sampled rocks (**Figure C-1**) was mainly calcite (**Figure C-2**) is supported by its $\delta^{13}C$ values, which was similar to that reported for carbonates in metamorphic and igneous rocks of -11.9 to +3.1‰ (Deines and Gold, 1973) and of -16 to +2‰ in calc-silicate rocks (Schwarcz, 1969). However, the amphibolite and mica schist samples which had $\delta^{13}C$ values <-16‰, may have contained graphite, for which $\delta^{13}C$ values down to -41‰ are reported (Deines, 1980; Ghent and O'Neil, 1985). This assumption is supported by the finding that no strong reaction was observed after application of diluted HCl to the amphibolite and mica schist samples.

Optical microscopy images revealed that calcite was mainly present in the pores of the metasedimentary rocks as interstitial calcite between the grains (**Figure C-2e**), which is in line with findings of White et al. (1999) who reported that calcite can occur as fillings in cracks and microfractures within the silicate matrix. Moreover, in some of our samples the saussuritization process by which primary rock-forming plagioclase is partially transformed into other minerals, such as epidote, zoisite, albite, or calcite could also have occurred. Saussuritization was observed in other mainly granitic proglacial areas such as the Morteratsch glacial retreat area in the Canton of Grisons, Switzerland (Mavris et al., 2010). The Morteratsch glacial retreat area is one of the few locations we know of, where similar to the Hailuogou region, a fast vegetation cover has developed within few decades after glacial retreat. However, the $CaCO_3$ concentration in the Morteratsch glacial debris is with only 0.2±0.3% (Mavris et al., 2010) one order of magnitude lower than at Hailuogou (5.6%, Zhou et al., 2016).

We even detected low concentrations of carbonates in the abundant coarse-grained granites (3 - 7 mg g^{-1} $CaCO_3$, **Figure C-1**) and higher ones in the fine-grained granite from the Hailuogou area (57 mg g^{-1} $CaCO_3$, **Figure C-1**). Up to now, the petrogenesis of calcite in granitoid rocks has received little attention. White et al. (2005) stated that calcite is universally present in granitoid rocks in a concentration ranging from 0.028 to 18.8 mg g^{-1}, with a mean of 2.52 mg g^{-1}. To explain the ubiquitous presence of accessory calcite in granitoid rocks, White et al. (2005) suggested that calcite might be included during late-magmatic growth or subsolidus replacement during magmatic processes. However, specific calcite occurrences can also be related to external inputs, such as from carbonate wall rocks or hydrothermal alteration (White et al., 2005). Geothermal mid-temperate springs (T~60°C) are scattered across the Hailuogou National Forest Park (Qi et al., 2017). Because of the presence of Paleozoic sedimentary rocks in the eastern catchment area of the Hailuogou glacier (Searle et al., 2016) in combination with hydrothermal sources in the surroundings of the study area (Qi et al., 2017), we suggest that the detected inorganic C in the granite samples of the Hailuogou chronosequence can be attributed to a mix of magmatic processes and external inputs.

5.2. Role of carbonates and easily weatherable silicates for the release of Ca and Mg

The release of all studied base cations by acid hydrolysis initially proceeded fast, followed by a slower reaction (**Figure C-3**). Although the total Ca concentration of the parent substrate was only about double that of Mg, K, and Na (**Table C-1**), during the first day of the pH_{stat} experiment, a >10 times higher mass of Ca was released than of Mg and K and even a ca. 100 times higher mass of Ca than of Na (**Figure C-3**). Rapid element release at the beginning of a pH_{stat} experiment is likely related to cation-exchange reactions and unstable solid phases that are easily dissolved upon acidification, e.g., carbonates (Cappuyns and Swennen, 2008, Alt et al., 2013). The fact that along the Hailuogou chronosequence, the size of the fast-reacting Ca pool (Pool A) correlated positively with the carbonate (CO_3^{2-}), exchangeable Ca, and total Ca concentrations in soil, while the fast-reacting Mg pool only correlated with the exchangeable Mg concentrations in soil (**Table C-2**), suggested that the Mg release along the chronosequence was not associated

with the weathering of Mg-containing carbonate minerals, such as dolomite or magnesite, but with cation-exchange reactions.

Along the chronosequence, the size of the fast-reacting Ca and Mg pools did not significantly differ from the respective sizes of the exchangeable element pools (**Figure C-5a, b**), except for Mg in the younger soils (Sites 1-2), where the Pool A was larger than the exchangeable Mg concentrations (**Figure C-5b**). This may be attributed to the release of Mg from other labile minerals, such as chlorite (Zhou et al., 2016) during the pH_{stat} experiment.

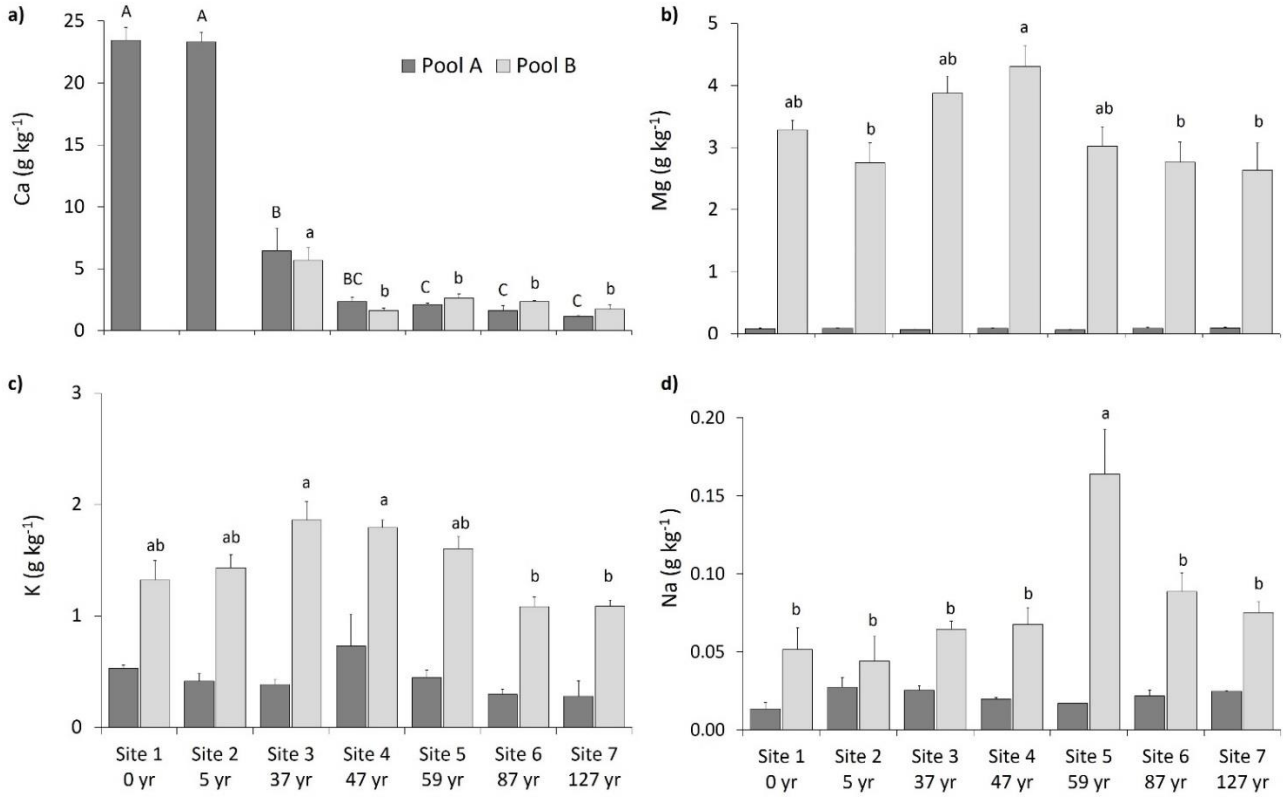

Figure C-4. Sizes of (a) Ca, (b) Mg, (c) K, and (d) Na Pools A (fast) and B (slow) in topsoils (0–10 cm) calculated with the biexponential function in Equation 2 along the Hailuogou chronosequence. Uppercase and lowercase letters denote significant differences in the sizes of Pools A and B, respectively, among the sites ($p < .05$). Error bars represent standard errors ($n = 3$).

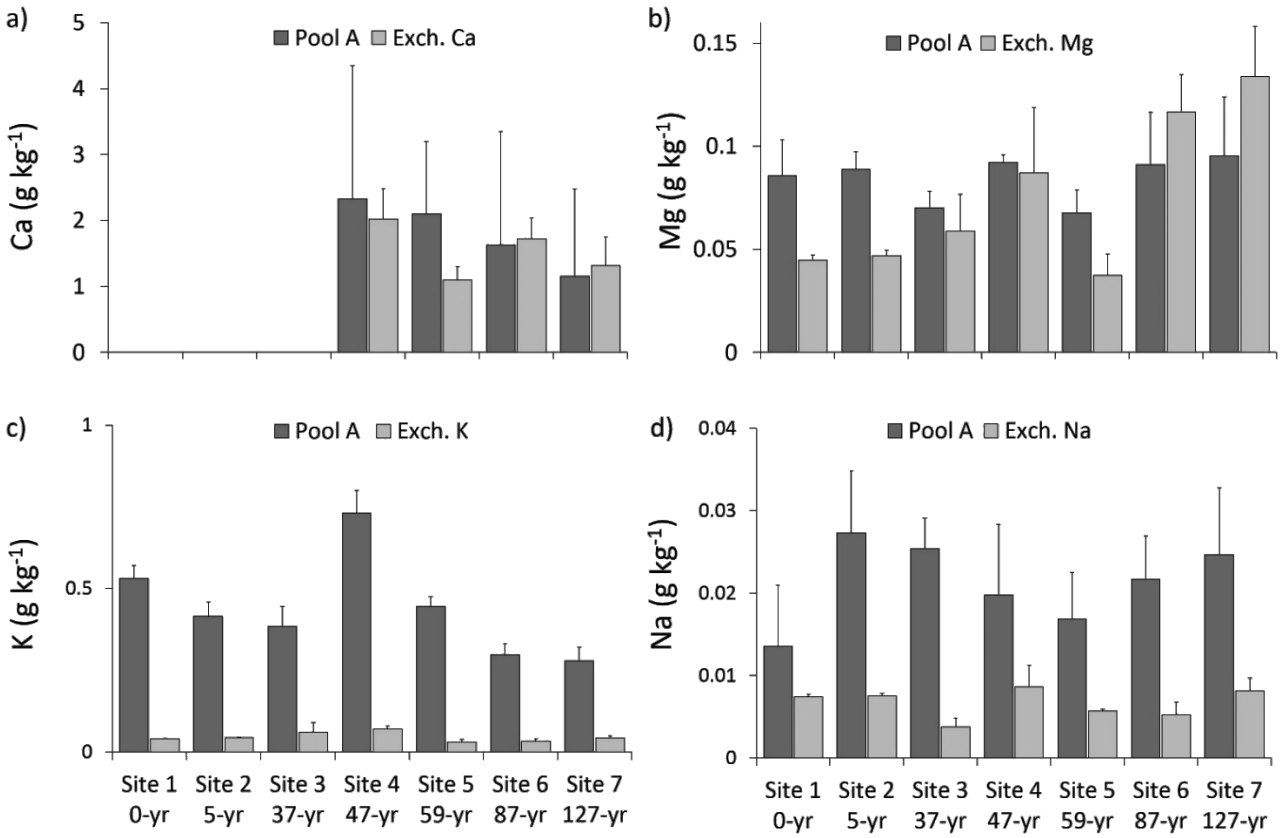

Figure C-5. Sizes of the fast-reacting Pool A of (a) Ca, (b) Mg, (c) K, and (d) Na and size of the respective exchangeable element pools extracted with 1 M NH4NO3 from topsoils (0–10 cm). The exchangeable Ca concentration in the carbonate-containing soils (Sites 1-3) could not be determined with the used standard method because of the partial dissolution of calcite in the extract.

5.3. Changes of Ca and Mg weathering rates with ecosystem development

The comparison of the release kinetics of the four base cations between Site 1 and Site 7 revealed a general slowdown of the weathering for all studied elements, except for Na (**Figure C-3**). However, the difference in the release kinetics between Sites 1 and 7 was particularly pronounced for Ca and comparatively weak and similar for the other three elements. We attribute this to the loss of carbonates within a few decades, from which only Ca was released to a considerable extent.

The release rate constant associated with the fast-reacting Ca pool, k_{a_Ca}, increased with decreasing Ca concentration in soil and marginally significantly with soil age

(**Table C-2**). This occurred in line with the rapid weathering of carbonates reported by Basdediós et al. (2022). After carbonates were leached (>47 yr), the size of the fast-reacting Ca pool was comparable to that of the exchangeable Ca pool (**Figure C-5a).** The release rate constant associated with the slow-reacting Pool B of Ca, $k_{b\_Ca,}$ did not significantly change with increasing site age, although the size of Pool B tended to decrease (**Table C-2).** This indicated that the slow-reacting Ca pool was weathered at a constant rate along the chronosequence. We suggest that Ca-Al sorosilicates, such as titanite and epidote (**Figure C-2a, b**), contributed to the slow-reacting pool of Ca (**Figure C-4a**).

The release rate constant associated with the fast-reacting Mg pool, k_{a_Mg}, did not significantly change along the chronosequence, while that associated with the slow-reacting Mg pool, k_{b_Mg}, marginally significantly ($p < 0.1$) decreased with time. Unexpectedly, the slow-reacting Mg pool seemed to only become active 4-12 hours after the start of the experiment and not simultaneously with the fast pool as was the case for Ca, K, and Na (**Figure C-3**), which may indicate that Mg was more strongly bound in soil, e.g., by association with highly insoluble soil constituents (Cappuyns and Swennens, 2008). The acid target pH of 3.0 in our pH_{stat} experiment intensified the weathering of minerals such as the micas biotite and muscovite leading to a release of Mg and K into soil solution, which may have contributed to the large slow-reacting pool of both elements. Weathering of micas is a gradual transformation of their structures by removal of Mg, Fe and K (Stoch and Sikora, 1976). During biotite weathering in the pH range of 2 to 6, Mg and Fe are preferentially released (Bray et al., 2015), likely together with K. In the Hailuogou region, the Mg release was closely correlated with that of Fe and Al, but not with the CO_3^{2-} concentrations indicating that most of the released Mg was associated with silicate weathering.

Contrary to our hypothesis, the fast-reacting Pool A of Mg did not significantly change with time and was consistently smaller than the slow-reacting Pool B of Mg along the chronosequence (**Figure C-4b**). The size of Pool A of Mg correlated with the exchangeable Mg concentration in soil (**Table C-2**). Only in the younger soils (Sites 1 and 2), Pool A was significantly larger than the exchangeable Mg pool, which we attribute to a slightly higher chlorite concentration at Sites 1 and 2 (4%, Zhou et al., 2016), because chlorite is easily weatherable and can be quickly lost from the topsoil (Terhorst et al., 2012). The finding that 2 h after the start, before the slow-reacting pool of Mg was activated, the

molar K : Mg ratio significantly decreased with site age from 3.4±0.2 (Site 1) to 1.2±0.3 (Site 7) (**Figure C-6**), while after 168 h the K : Mg ratios did not correlate with site age anymore indicated that more Mg was leached relative to K, although more K than Mg was originally stored in the mineral soil (K : Mg ratio in the mineral soil: 1.3±0.1, **Figure C-6b**). This was in line with the findings of Basdediós et al. (2022), who reported a decrease in the total stocks of Mg along the chronosequence, while those of K were not related to ecosystem age.

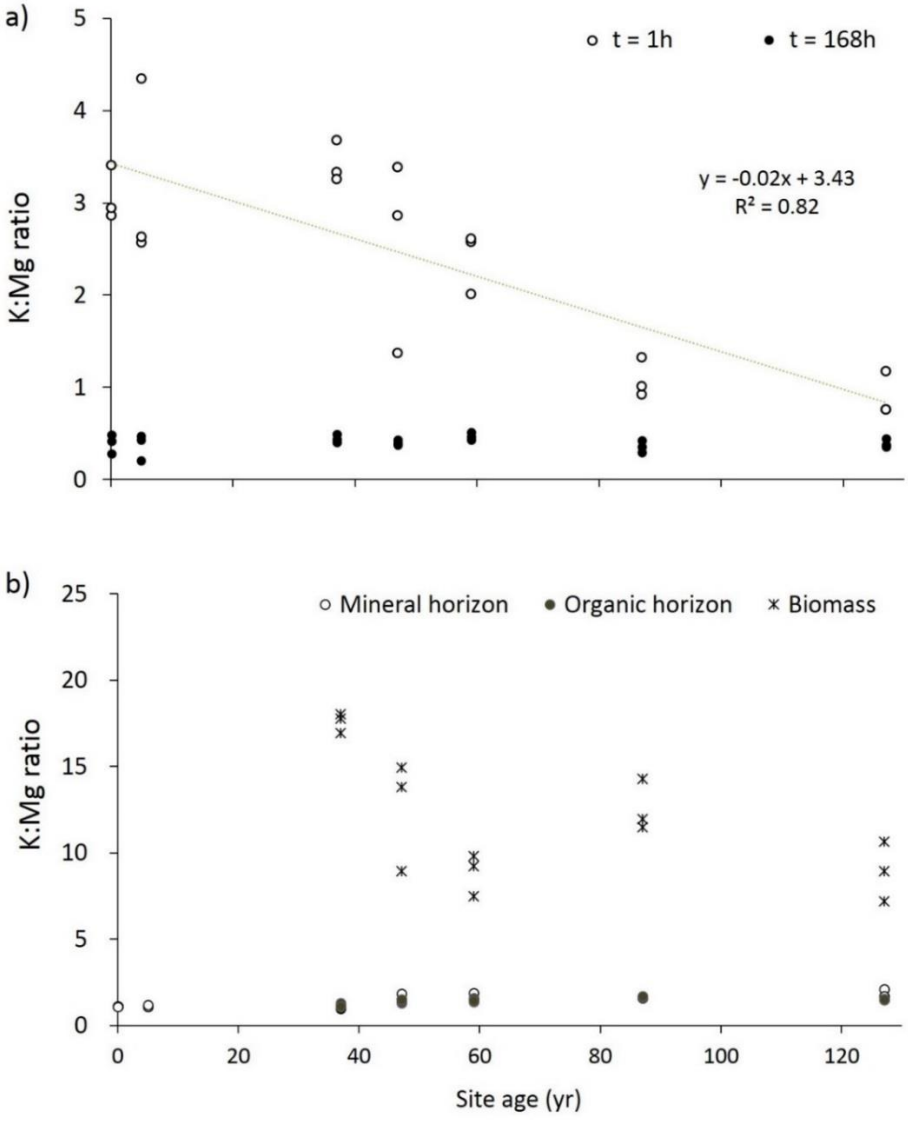

Figure C-6. (a) Released molar K/Mg ratios 1 and 168 h after starting the pH_{stat} experiment and (b) molar K/Mg ratios in the upper 10 cm of the mineral soil, the organic layer, and the aboveground biomass along the chronosequence. For each site age, we ran three independent batch experiments and collected three independent samples, which are individually shown. The regression line in a was calculated for the means of each site age. Data of b were taken from Basdediós et al. (2022).

We suggest that Ca was initially mainly released from calcite, while Mg was released from chlorite. At later stages of the chronosequence, bioavailable (fast-reacting) Ca and Mg were stored in the exchangeable pools, which was replenished by the slow weathering of silicate minerals of intermediate stability such as titanite for Ca and hornblende and biotite for Mg. After 127 yr, the contributions of hornblende and biotite to the total mineral mass had decreased from 11.8 to 8.5% and from 18.0 to 9.0% (Zhou et al., 2016), respectively, from which we infer that these two minerals contributed to the slow-reacting Pool B of Mg (**Figure C-4**).

5.4. Source minerals of K and Na release

The release of K was one order of magnitude higher than that of Na (**Figure C-3**), although the total concentrations of both elements were similar in the parent material (**Table C-1**). In line with the findings of Basdediós et al. (2022), the size of the Pools A and B of both elements did not correlate with increasing site age, although the slow-reacting Pool B of K showed a marginally significant ($p < 0.1$) decreasing trend that may become more pronounced in the longer term (e.g., Lichter, 1998).

The finding that the fast-reacting Pools A of K and Na were consistently larger than their respective exchangeable pools (**Figure C-5c, d**), indicated the presence of reactive K and Na pools in the soil that were not salt-extractable. A possible source of this reactive K might be the interlayers of clay minerals, which can contain substantial, not salt-extractable K concentrations but can be easily weathered (Falk Øgaard and Krogstad, 2005). Extensive depletion of interlayer K in clay minerals might also have contributed to the decrease in the K release rate constants of the slow-reacting K pool (k_{b_K}) with age (**Table C-2**), because the release of interlayer K usually decreases when the concentration of K in soil solution increases (Hinsinger and Jaillard, 1993). The small fast-reacting pool of Na might be related to the presence of low concentration of Na carbonates in the glacial debris (Zhou et al., 2016).

With increasing site age, the K release from the slow-reacting K pool decreased (**Table C-2**) indicating that less primary K was delivered into the soil solution. We attribute the large slow-reacting K pool to the weathering of minerals such as biotite, which also released Mg (**Figure C-4b, c**) and muscovite. The slow-reacting Na pool was also

consistently larger than the fast-reacting Na pool and increased marginally significantly with increasing Na concentrations in the soil indicating that most of the Na present in the study soils was associated with weathering-resistant minerals, such as Na-rich feldspar and augite. Interestingly, the significantly largest Pool B of Na at the 57-year site (**Figure C-4**) was consistent with the report of Zhou et al. (2016) that at this site the augite concentration in topsoil was with 5.9% the highest along the chronosequence. The other soils only contained 2.1-3.1% of augite. This supports our assumption that augite contributed to the slow-reacting Pool B of Na. Moreover, in granitic substrates, plagioclases (Ca and Na feldspars) are usually faster weathered than K-feldspars (Grant, 1962), while the Ca-rich end member of the plagioclases dissolves faster than the Na-rich end-member (Palandri and Kharaka, 2004), contributing to the more rapid release of Ca than Na along the chronosequence (**Figure C-3**). The faster release of Ca might also explain why stream water samples in the Hailuogou region were dominated by Ca, while Na only accounted for a small proportion of the dissolved base cations (Zhou et al., 2016). Therefore, we infer that the weathering of Na-containing minerals along the Hailuogou chronosequence released much less Na than other base cations (**Figure C-3**). As a consequence, the Na stocks remained almost constant along the chronosequence (Basdediós et al., 2022).

6. Conclusions

Although the Gongga peak is mainly composed of granite and granitoid rocks, sedimentary rocks in the eastern catchment area of the Hailuogou glacier contribute $CaCO_3$ to the Hailuogou glacial debris, from which the studied chronosequence developed. Calcite was mainly present in the pores of the metasedimentary rocks as interstitial calcite in the silicate matrix. We have detected carbonates even in the granitoid rocks, which we attribute to a combination of magmatic processes with external inputs during rock formation.

The fast initial weathering of carbonates determined the rapid initial Ca release. The Mg release was, in contrast, closely correlated with Fe and Al release, but not with the carbonate concentrations, indicating that most of the released Mg was associated with silicate weathering. The sizes of the fast-reacting pools of Ca and Mg mostly matched the sizes of their respective exchangeable pools. The slow-reacting pool of Mg was considerably larger than the fast-reacting pool of Mg, which indicated that Mg was generally stored in more stable minerals than Ca, such as in biotite and hornblende.

The main sources of weathered K and Na were silicate minerals. The release of K was one order of magnitude higher than that of Na, although the total concentration of both elements were similar in the parent material. With increasing site age, the K release from the slow-reacting K pool slowed down so that increasingly less primary K was delivered into the soil solution. The weathering of Na-containing minerals along the Hailuogou chronosequence released little Na so that the Na stocks remained nearly constant during the 127-yr succession.

Our results suggest that the fast weathering of carbonates in the otherwise acidic, granite-dominated glacial till allowed for a fast initial delivery of Ca, succeeded by an increasing weathering of silicates with decreasing pH and a subsequent delivery of other nutrients including K and Mg could have facilitated the fast vegetation succession. The slower base cation release after the carbonates had been completely leached, fell together with a change of the forest composition from deciduous to coniferous with a lower nutrient demand. Thus, the vegetation development seemed to be synchronized with the weathering regime.

7. Acknowledgments

We thank Z. Zhong, J. Wang, H. Bing, J. Zhou, and Q. He, as well as many students from the Chinese Academy of Science for their support in the field during the sampling campaign, Stephan Unrein for providing the thin sections, and Armin Zeh for his help in classifying the rocks, taking the photomicrographs and evaluating the mineral composition. We are indebted to the German Research Foundation (DFG, Wi 1601/25-1) and to the International Partnership Program of Chinese Academy of Sciences (131551KYSB20190028) for funding this study.

8. References

Allen, B.L. and B.F. Hajek. **1989**. Mineral occurrence in soil environments. In: Dixon JB & Weed SB (eds) Soils in Mineral Environments, pp 199-278, 2nd edn. Soil Science Society of America, Madison, Wisc. https://doi.org/10.2136/sssabookser1.2ed.c5

Alt, F., Y. Oelmann, I. Schoning and W. Wilcke. **2013**. Phosphate release kinetics in calcareous grassland and forest soils in response to H+ addition. Soil Sci. Soc. Am. J. 77:2060‑2070. doi:10.2136/sssaj2013.02.0072

Anderson, D.W. **1988**. The effect of parent material and soil development on nutrient cycling in temperate ecosystems. Biogeochemistry 5, 71–97. https://doi.org/10.1007/BF02180318

Andersson, S. and S.I. Nilsson. **2001**. Influence of pH and temperature on microbial activity, substrate availability of soil-solution bacteria and leaching of dissolved organic carbon in a mor humus. Soil Biol. Biochem. 33:1181–1191. https://doi.org/10.1016/S0038-0717(01)00022-0

Augusto, L., D.L. Achat, M. Jonard, D. Vidal and B. Ringeval. **2017**. Soil parent material—A major driver of plant nutrient limitations in terrestrial ecosystems. Glob. Change Biol. 23: 3808– 3824. https://doi.org/10.1111/gcb.13691

Basdediós, N., Z. Zhong, Y. Wu and W. Wilcke. **2022**. Initial carbonate weathering is linked with vegetation development along a 127-year glacial retreat chronosequence in the subtropical high mountainous Hailuogou region (SW China). Plant Soil 471: 609–628. https://doi.org/10.1007/s11104-021-05250-y

Barker, W.W., S.A. Welch and J.F. Banfield. **1997**. Biogeochemical weathering of silicate minerals. In: Banfield JF & Nealson KH (eds) Geomicrobiology: Interactions Between Microbes and Minerals, Rev. Min. 35: 391–428. Mineralogical Society of America, Washington.

Berner, E.K., R.A. Berner and K.L. Moulton. **2004**. Plants and mineral weathering: past and present. In: Drever, J.I. (Ed.), Surface and gound water, weathering, and soils. Treatise on Geochemistry 5. Elsevier, San Diego, pp. 169–188.https://doi.org/10.1016/B0-08-043751-6/05175-6

Blum, J.D., C.A. Gazis, A.D. Jacobson and C.P. Chamberlain. **1998**. Carbonate versus silicate weathering in the Raikhot watershed within the high Himalayan crystalline series. Geology 265, 411– 414. https://doi.org/10.1130/0091-7613(1998)026<0411:CVSWIT>2.3.CO;2

Bockheim, J.G. **1980**. Solution and use of chronofunctions in studying soil development. Geoderma 24:71–85. https://doi.org/10.1016/0016-7061(80)90035-X

Bray, A.W., E.H. Oelkers, S. Bonneville, D. Wolff-Boenisch, N.J. Potts, G. Fones and L.G. Benning. **2015**. The effect of pH, grain size, and organic ligands on biotite weathering rates. Geochim. Cosmochim. Acta 164, 127–145. https://doi.org/10.1016/j.gca.2015.04.048

Cappuynus, V. and R. Swennen. **2008**. The application of pH_{stat} leaching tests to assess the pH-dependent release of trace metals from soils, sediments and waste materials. J. Hazard. Mater. 158, 185–195.https://doi.org/10.1016/j.jhazmat.2008.01.058

Chadwick, O.A. and J. Chorover. **2001**. The chemistry of pedogenic thresholds. Geoderma 100:321–353. https://doi.org/10.1016/S0016-7061(01)00027-1

Deines, P. and D.P. Gold. **1973**. The isotopic composition of carbonatite and kimberlite carbonates and their bearing on the isotopic composition of deep-seated carbon: Geochimica et Cosmochimica Acta, v. 37, p. 1709–1733.

Deines, P. **1980**. The isotopic composition of reduced organic carbon, in Fritz, P., and Fontes, J.Ch., eds., Handbook of Environmental Isotope Geochemistry, Volume 1, The Terrestrial Environment, A: Amsterdam, The Netherlands, Elsevier Scientific Publishing Co., p. 329–402.

Drever, J.I. and L.L. Stillings. **1997**. The role of organic acids in mineral weathering. Colloids Surf A Physicochem Eng Aspects 120:167–181. https://doi.org/10.1016/S0927-7757(96)03720-X

Eimil-Fraga, C., R. Rodríguez-Soalleiro, F. Sánchez-Rodríguez, C. Pérez-Cruzado and E. Álvarez-Rodríguez. **2014**. Significance of bedrock as a site factor determining nutritional status and growth of maritime pine. Forest Ecology and Management 331, 19-24. http://dx.doi.org/10.1016/j.foreco.2014.07.024

Falk Øgaard, A. and T. Krogstad. **2005**. Release of interlayer potassium in Norwegian grassland soils. J. Plant Nutr. Soil Sc., 168, 80–88. https://doi.org/10.1002/jpln.200421454

Ghent, E.D. and J.R. O'Neil. **1985**. Late Precambrian marbles of unusual carbon-isotope composition, southeastern British Columbia: Canadian Journal Earth Science, v. 22, p. 324–329. https://doi.org/10.1139/e85-032

Grant, W. H. **1962**. Weathering of Stone Mountain Granite. Clays and Clay Minerals, 11(1), 65–73. doi:10.1346/ccmn.1962.0110106

Hacker, N., G. Gleixner, M. Lange, W. Wilcke and Y. Oelmann. **2017**. Phosphorus release from mineral soil by acid hydrolysis: method development, kinetics, and plant community composition effects. Soil Sci. Soc. Am. J. 81:1389–1400. https://doi.org/10.2136/sssaj2017.02.0064

Harley, A. and R. Gilkes. **2000**. Factors influencing the release of plant nutrient elements from silicate rock powders: a geochemical overview. Nutrient Cycling in Agroecosystems 56, 11–36. https://doi.org/10.1023/A:1009859309453

Hinsinger, P. **2001**. Bioavailability of soil inorganic P in the rhizosphere as affected by root-induced chemical changes: a review. Plant and Soil, 237, 173-195. https://doi.org/10.1023/A:1013351617532

Hinsinger, P. and B. Jaillard. **1993**. Root-induced release of interlayer potassium and vermiculitization of phlogopite as related to potassium depletion in the rhizosphere of ryegrass. Journal of Soil Science, 44: 525-534. https://doi.org/10.1111/j.1365-2389.1993.tb00474.x

Houlton, B.Z., S.L. Morford and R.A. Dahlgren. **2018**. Convergent evidence for widespread rock nitrogen sources in Earth's surface environment. Science 360, 58-62. https://doi.org/10.1126/science.aan4399

Huggett, R.J. **1998**. Soil chronosequences, soil development, and soil evolution: A critical review. Catena 32:155–172. https://doi.org/10.1016/S0341-8162(98)00053-8

IUSS Working Group WRB. **2014**. World Reference Base for soil resources. International soil classification system for naming soils and creating legends for soil maps. World Soil Resource Reports No. 106. FAO, Rome.

Jenny, H. **1941**. Factors of Soil Formation: A System of Quantitative Pedology. McGraw Hill, New York, 281 pp.

Jesse Hahm, W., C.S. Riebe, C.E. Lukens and S. Araki. **2014**. Bedrock composition regulates mountain ecosystems and landscape evolution. Proceedings of the National Academy of Sciences Mar 2014, 111 (9) 3338-3343 https://doi.org/10.1073/pnas.1315667111

Jobbágy, E. G. and R.B. Jackson. **2004**. The uplift of soil nutrients by plants: biogeochemical consequences across scales. Ecology 85, 2380–2389. https://doi.org/10.1890/03-0245

Kaupenjohann, M. & W. Wilcke. **1995**. Heavy metal release from a serpentine soil using a pH- stat technique. Soil Sci. Soc. Am. J. 59, 1027-1031. https://doi.org/10.2136/sssaj1995.03615995005900040010x

Li, Z., Y. He, X. Yang, et al. **2010**. Changes of the Hailuogou glacier, Mt. Gongga, China, against the background of climate change during the Holocene. Quat Int 218:166–175. https://doi.org/10.1016/j.quaint.2008.09.005

Lichter, J. **1998**. Rates of weathering and chemical depletion in soils across a chronosequence of Lake Michigan sand dunes. Geoderma 85:255–282. https://doi.org/10.1016/S0016-7061(98)00026-3

Lilienfein, J. W. Wilcke, R. Thomas, L. Vilela, S.C. Lima and W. Zech. **2001**. Efects of Pinus caribaea plantations on the C, N, P, and S status of Brazilian savanna Oxisols. For Ecol Manag 147:171–182. https://doi.org/10.1016/S0378- 1127(00)00472-2

Marschner, P. **2012**. Marschner's Mineral Nutrition of Higher Plants. Edition No.3

Mavris, C., M. Egli, M. Plötze, et al. **2010**. Initial stages of weathering and soil formation in the Morteratsch proglacial area. Geoderma 155:359–371. https://doi.org/10.1016/j.geoderma.2009.12.019

Meyer, S., A. De Angeli, A.R. Fernie and E. Martinoia. **2009**. Intra- and extra-cellular excretion of carboxylates. Trends Plant Sci.15, 40-47. https://doi.org/10.1016/j.tplants.2009.10.002

Palandri, J. L. and Y. K. Kharaka. **2004**. A compilation of rate parameters of water-mineral interaction kinetics for application to geochemical modeling, in U.S. Geological

Survey 2004–1068 (Menlo Park, CA), 71. https://doi.org/10.3133/ofr20041068

Qi, J., M. Xu, C. An, M. Wu, Y. Zhang, X. Li, Q. Zhang and G. Lu. **2017**. Characterizations of geothermal springs along the Moxi deep fault in the western Sichuan plateau, China. Physics of the Earth and Planetary Interiors 263, 12–22 http://dx.doi.org/10.1016/j.pepi.2017.01.001

R Core Team. **2019**. R: a language and environment for statistical computing. R Foundation for Statistical Computing, Vienna, Austria. https://www.R-project.org.

Roger, F., S. Calassou, J. Lancelot, J. Malavieille, M. Mattauer, X. Zhiqin, H. Ziwen and H. Liwei. **1995**. Miocene emplacement and deformation of the Konga Shan granite (Xianshui He fault, west Sichuan, China): Geodynamicimplications. Earth and Planetary Science Letters, 130:201 – 216. https://doi.org/10.1016/0012-821X(94)00252-T

Schmitt, A.D., N. Vigier, D. Lemarchand, et al. **2012**. Processes controlling the stable isotope compositions of Li, B, Mg and Ca in plants, soils and waters: A review. Comptes Rendus - Geosci 344:704–722. https://doi.org/10.1016/j.crte.2012.10.002

Schwarcz, H.P. **1969**. Carbon, in Wedepohl, K.H., ed., Handbook of Geochemistry: Berlin, Springer-Verlag, Section B-I, The Stable Isotopes of Carbon, p. 6-B-1–6-B-15.

Schwarz, A., W. Wilcke, J. Styk and W. Zech. **1999**. Heavy metal release from soils in batch pH(stat) experiments. Soil Sci. Soc. Am. J. 63:290‑296. https://doi.org/10.2136/sssaj1999.03615995006300020006x

Searle, M.P., N.M.W. Roberts, S.L. Chung, et al. **2016**. Age and anatomy of the Gongga Shan batholith, eastern Tibetan Plateau, and its relationship to the active Xianshui-he fault. Geosphere 12:948–970. https://doi.org/10.1130/GES01244.1

Selim, H.M. and M.C. Amacher. **1997**. Reactivity and transport of heavy metals in soils. CRC press, Boca Raton, FL.

Smith, K.S. and H.L.O. Huyck. **1999**. An Overview of the Abundance, Relative Mobility, Bioavailability, and Human Toxicity of Metals. In G.S. Plumlee and M.J. Logsdon (Eds.). The Environmental Chemistry of Mineral Deposits, reviews in Economic Geology, Volume 6A, pp. 29-70.

Sohrt, J., F. Lang and M. Weiler. **2017**. Quantifying components of the phosphorus cycle in temperate forests. WIREs Water, 4(6), e1243. https://doi.org/10.1002/wat2.1243

Stoch, L. and W. Sikora. **1976**. Transformations of micas in the process of kaolinitization of granites and gneisses. Clays Clay Miner. 24, 156–162. https://doi.org/10.1346/CCMN.1976.0240402

Süsser, P. **1987**. Art, Menge und Wirkungsweise von Puffersubstanzen in Mineralbodenhorizonten forstlich genutzter Böden des Fichtelgebirges. Dissertation am Lehrstuhl für Bodenkunde, Technische Universität München-Weihenstephan.

Terhorst, B., F. Ottner and K. Wriessnig. **2012**. Weathering intensity and pedostratigraphy of the Middle to Upper Pleistocene loess/palaeosol sequence of Wels-Aschet (Upper Austria). Quaternary International 265, 142-154. https://doi.org/10.1016/j.quaint.2011.08.042

Tripler, C.E., S.S. Kaushal, G.E. Likens and M. Todd Walter. **2006**. Patterns in potassium dynamics in forest ecosystems. Ecol. Lett. 9 (4), 451–466. https://doi.org/10.1111/j.1461-0248.2006.00891.x

van de Sand, M. and W.R. Fischer. **1994**. Quantifizierung der wichtigsten Mechanismen zur Säurepufferung carbonatfreier Böden. Z. Pflanzenernähr. Bodenk., 157, 369-373.

Vitousek, P. M. and R.L. Sanford. **1986**. Nutrient cycling in moist tropical forest. Annual Review of Ecology and Systematics, 17, 137–167. https://doi.org/10.1146/annurev.es.17.110186.001033

Walker, L.R., D.A. Wardle, R.D. Bardgett and B.D. Clarkson. **2010**. The use of chronosequences in studies of ecological succession and soil development. J. Ecol. 98:725–736. https://doi.org/10.1111/j.1365-2745.2010.01664.x

White, A.F., T.D. Bullen, D.V. Vivit, et al. **1999**. The role of disseminated calcite in the chemical weathering of granitoid rocks. Geochim. Cosmochim. Acta 63:1939–1953. https://doi.org/10.1016/S0016-7037(99)00082-4

White, A.F., M.S. Schulz, J.B. Lowenstern, et al. **2005**. The ubiquitous nature of accessory calcite in granitoid rocks: Implications for weathering, solute evolution, and petrogenesis. Geochim. Cosmochim. Acta 69:1455–1471. https://doi.org/10.1016/j.gca.2004.09.012

White, P.J. and M.R. Broadley. **2003**. Calcium in plants. Ann. Bot. 92 (4) 487–511. https://doi.org/10.1093/aob/mcg164

Wilcke, W., S. Yasin, U. Abramowski, C. Valarezo and W. Zech. **2002**. Nutrient storage and turnover in organic layers under tropical montane rain forest in Ecuador. European Journal of Soil Science 53, 15-27. https://doi.org/10.1046/j.1365-2389.2002.00411.x

Wilson, M. **2004**. Weathering of the primary rock-forming minerals: Processes, products and rates. Clay Minerals, 39(3), 233-266. doi:10.1180/0009855043930133

Wu,Y., W. Li, J. Zhou and Y. Cao. **2013**. Temperature and precipitation variations at two meteorological stations on eastern slope of Gongga Mountain, SW China in the past two decades. J. Mt. Sci. 10:370–377. https://doi.org/10.1007/s11629-013-2328-y

Yang, Z., H. Bing, J. Zhou, et al. **2015**. Variation of mineral composition along the soil chronosequence at the Hailuogou glacier foreland of Gongga Mountain. Acta Pedol. Sin. 52:39–48. https://doi.org/10.11766/trxb201406180301

Zamanian, K., K. Pustovoytov and Y. Kuzyakov. **2016**. Pedogenic carbonates: Forms and formation processes. Earth-Science Rev 157:1–17. https://doi.org/10.1016/j.earscirev.2016.03.003

Zhou, J., H. Bing, Y. Wu, et al. **2016**. Rapid weathering processes of a 120-year-old chronosequence in the Hailuogou Glacier foreland, Mt. Gongga, SW China. Geoderma 267:78–91. https://doi.org/10.1016/j.geoderma.2015.12.024

Zhou, J., Y. Wu, J. Prietzel, et al. **2013**. Changes of soil phosphorus speciation along a 120-year soil chronosequence in the Hailuogou Glacier retreat area (Gongga Mountain, SW China). Geoderma 195–196:251–259. https://doi.org/10.1016/j.geoderma.2012.12.010

D. Magnesium isotope ratios

Magnesium isotope ratios reflect the size and sources of Mg loss along a glacial retreat chronosequence

Nuria Basdediós[1], Yanhong Wu[2], Wolfgang Wilcke[1]

[1]Karlsruhe Institute of Technology (KIT), Institute of Geography and Geoecology, Reinhard-Baumeister-Platz 1, 76131 Karlsruhe, Germany

[2] Key Laboratory of Mountain Surface Processes and Ecological Regulation, Institute of Mountain Hazards and Environment, Chinese Academy of Sciences, Chengdu 610041, China

ACS Earth and Space Chemistry 7, 1151–1161

DOI: 10.1021/acsearthspacechem.3c00049

1. Abstract

Magnesium (Mg) stable isotope ratios reflect Mg turnover in ecosystems. At the Hailuogou glacial retreat chronosequence in SW China about one third of the initially present Mg was lost from the topsoil in 127 yr. We determined bulk soil and exchangeable δ^{26}Mg values at six sites exposed by the glacier from 0-127 yr ago. Moreover, we conducted a weathering experiment (pH_{stat}) at the youngest (0 years) and the oldest (127 years) sites and measured δ^{26}Mg values in differently reactive pools. We found a close correlation between the δ^{26}Mg values of the bulk topsoils (0-10 cm) and the Mg depletion rates ($r=0.98$, $p<0.001$, $n=5$). The particularly fast Mg loss in the first 37 yr was attributable to leaching of exchangeable Mg and the fast dissolution of chlorite as revealed by the lower δ^{26}Mg values of the fast (-1.28±0.10‰) than the slow reacting (-0.64±0.11‰) pool at the 0 yr-old site in our pH_{stat} experiment. The low δ^{26}Mg values of the fast-reacting pool matched those reported for chlorite. Our results demonstrate that the δ^{26}Mg values might be used as proxy of Mg loss and to identify the mineral sources of this loss.

2. Introduction

As one of the most abundant elements in the Earth's continental crust, magnesium (Mg) is widely distributed among the lithosphere, hydrosphere, and biosphere (Rudnik and Gao, 2003; Taylor and McLennan, 1985). Magnesium has a great influence on the global atmospheric CO_2 concentration through the formation and chemical weathering of Mg-bearing minerals (Berner et al., 1983). In nature, Mg isotopes are fractionated through diverse processes, such as weathering of the continental crust (Pogge von Strandmann et al., 2008; Teng et al., 2010; Tipper et al., 2006), Mg incorporation in secondary Mg-bearing minerals (Opfergelt et al., 2012), biomineralization (Chang et al., 2004), magma differentiation (Teng et al., 2007; Richter et al., 2008; Ryu et al., 2011), petrogenesis (Wang et al., 2015), plant uptake (Black et al., 2008; Bolou-Bi et al., 2010), and chlorophyll biosynthesis (Black et al., 2006). The resulting natural variation in Mg isotope ratios of different mineral and ecosystem pools may be used to elucidate the origin of Mg pools with different isotopic composition and to trace ecosystem processes (Court et al., 2021; Uhlig et al. 2017).

The different dissolution rates of the diverse minerals in the parent material of soils have an effect on the fractionation of Mg isotopes in soil through weathering. The more rapid dissolution of carbonate than of silicate minerals (Lasaga, 1984) cause rivers draining carbonate watersheds to have a Mg isotope composition similar to the carbonate bedrock (Galy et al., 2002; Tipper et al., 2008), while Mg in watersheds draining silicate bedrock is usually isotopically lighter than the silicate substrate (Brenot et al., 2008, Lee et al., 2014; Tipper et al., 2008). Three main findings have been discussed to explain the latter: the preferential uptake of the heavy Mg isotopes by the vegetation (Black et al., 2008; Bolou-Bi et al., 2010, 2012; Mavromatis et al., 2014; Uhlig et al., 2017), the preferential incorporation of heavy Mg isotopes in secondary minerals (Opfergelt et al., 2012), and the adsorption of heavy Mg onto clays (Huang et al., 2012; Pogge von Strandmann et al., 2012). Conversely, some studies reported no isotopic fractionation between runoff and weathered educts (Novak et al., 2020) or even that during silicate weathering lighter Mg isotopes are preferentially incorporated into secondary phases resulting in higher δ^{26}Mg values in solution (Opfergelt et al., 2014; Pogge von Strandmann et al., 2008; Wimpenny et al., 2010). This suggests that the direction of Mg isotope fractionation during weathering might depend on the dissolution and neoformation of specific minerals (Pogge von Strandmann

et al., 2008; Hindshaw et al., 2019), likely related to the Mg-O bond lengths of the secondary minerals formed (Hindshaw et al., 2020; Li et al., 2014).

The literature about a possible fractionation of Mg isotopes associated with cation exchange in soil is also not consistent. Some studies suggest that cation exchange enriches isotopically light Mg in the exchangeable Mg pool because of the preferential removal of heavy Mg isotopes during adsorption-desorption processes (Gao et al., 2018; Huang et al., 2012; Opfergelt et al., 2014). However, Wimpenny et al. (2014a) reported a negligible Mg isotope fractionation during Mg exchange on clay minerals, which has been corroborated by an experiment of Cai et al. (2022). If the latter was true, Mg isotope fractionation in soils would be mainly attributable to secondary mineral formation or plant uptake.

Plant growth experiments in the laboratory showed that Mg in plant roots is isotopically heavier than the plant-available Mg pool (Black et al., 2008; Bolou-Bi et al., 2010; Kimmig et al., 2018). However, Kimmig et al. (2018) showed that maple trees growing on natural soils did not fractionate Mg isotopes during plant uptake while the same tree species growing in laboratory pot experiments did. This was tentatively attributed to the presence of mycorrhizal fungi that colonize plant roots in the field, which were absent in the sterile soils used in lab experiments. Further studies showed that the direction of Mg isotope fractionation by fungi is species-specific (Fahad et al., 2016; Pokharel et al., 2017). Inside the plant, the light isotopes are preferentially incorporated into chlorophyll and thus accumulate in leaves and nonwoody shoots (Black et al., 2008; Bolou-Bi et al., 2010, 2012). The return of this isotopically light Mg pool via litterfall can influence the Mg isotope composition of the topsoils.

Along the 127 year old Hailuogou glacial retreat chronosequence in Sichuan, southwest China, total Mg stocks in the mineral topsoil (0-10 cm) decreased from 4990 ± 196 g m^{-2} to 2830 ± 223 g m^{-2} in only 127 years, while the exchangeable Mg stock consistently increased from 0.7 ± 0.0 g m^{-2} to 2.3 ± 0.5 g m^{-2} (Basdediós et al., 2022a). To explore the reasons for the fast depletion of Mg in only a few decades, Basdediós et al. (2022b) conducted a weathering experiment using the resin-based pH_{stat} approach of of Kaupenjohann and Wilcke (1995), in which ions are released into solution during H^+ buffering at constant pH and removed from the system using ion exchange resins. This method allowed to distinguish a fast- and a slow-reacting mineral pool and the release rate constants associated with each of them. The size of the fast-reacting pool of Mg did not

significantly change with site age and was consistently smaller than the slow-reacting pool (Basdediós et al., 2022b). The size of the fast-reacting pool mostly matched the size of the exchangeable Mg pool except for the young soils (< 37 years old), where the fast-reacting pool was larger than the respective exchangeable Mg pool (Basdediós et al., 2022b). Basdediós et al. (2022b) suggested that Mg was initially released from chlorite. At the later stages of the chronosequence the fast-reacting Mg pool consisted entirely of exchangeable Mg, which was fed by the slow weathering of silicate minerals of intermediate stability such as hornblende and biotite. The reported substantially lower δ^{26}Mg value of chlorite (-1.82 ± 0.07 ‰) than of hornblende (-0.32 ± 0.09 ‰) and biotite (-0.29 ± 0.08 ‰) in granites (Ryu et al., 2011) provides an opportunity to test this hypothesis by measuring the δ^{26}Mg value of the fast-reacting pool.

We aimed to reveal if Mg isotope ratios can be used to elucidate the mineral sources of Mg release by weathering and as tracer of Mg loss from the soil at a 127-yr old glacial retreat chronosequence in China. We hypothesized that (i) the large Mg depletion in the mineral topsoil in only 127 years is associated with an increase in the δ^{26}Mg value of bulk topsoil as a consequence of the preferred (a) leaching (i.e., vertical transport) of ^{24}Mg during silicate weathering and (b) dissolution of a reactive fraction of Mg-isotopically light chlorite in the early phase of soil development along the chronosequence, while (ii) the δ^{26}Mg value of the slow-reacting Mg pool increases with increasing soil age because of the depletion of the Mg-isotopically heavier biotite and hornblende relative to a little reactive fraction of the Mg-isotopically lighter chlorite.

3. Materials and methods

3.1. Study area

Located on the eastern slope of the Gongga Mountain, in the transition zone of the Sichuan Basin and the Tibetan Plateau (southwest China), the Hailuogou Glacier had markedly retreated since the late 19th century (Li et al., 2010b), resulting in the development of an approximately 2 km-long, 50–200 m wide soil chronosequence, at an elevation of 2850-3000 m above sea level (a.s.l.). The short time of pedogenesis (<130 years) resulted in the formation of initial soils without B horizon classified from the youngest to the oldest soils as Leptic Calcaric to Folic Dystric Regosols according to the World Reference Base for Soil Resources (IUSS Working Group WRB, 2022). With increasing time, the soils

have developed A and O horizons of increasing thickness. The mean annual temperature and precipitation rates are 4.2 °C and 1947 mm, respectively (Zhou et al., 2013). A primary vegetation succession has developed along this chronosequence, from pioneer shrubs (i.e. *Hippophae rhamnoides* L.), over half mature broad-leaved tree forests dominated by *Populus purdomii* Rehder, to a full conifer forest dominated by *Abies fabri* (Mast.) Craib and *Picea brachytyla* (Franch.) E. Pritz. in only 127 years.

We included six sites with varying ecosystem ages (**Figure A-3**), deglaciated between 0 (Site 1; 2982 m a.s.l.) and 127 years ago (Site 6; 2855 m a.s.l.). The parent material of soil formation consists of a mixture of silicates (~90%) with a small contribution of carbonates (< 10%) which are lost from the topsoil by weathering and subsequent leaching within 47 years (Basdediós et al., 2022a). The mineral composition of the C horizons is dominated by quartz, plagioclase, K-feldspar, biotite, and hornblende, with the presence of minor minerals such as chlorite and apatite (Zhou et al., 2016). The intense carbonate weathering in the early stage of the chronosequence and the rapid establishment of the vegetation decreased soil pH from 8.0 to 5.8 in only 47 years (**Table D-1**), promoting a more intense biogeochemical weathering in the later stage of the chronosequence (Zhou et al., 2016).

3.2. Field sampling

Soil samples were collected in August 2017. Each of the six included ecosystem succession stages was sampled in triplicate. To guarantee spatial statistical independence, the distance between the sampled soil profiles was at least 20 m, except at Site 1, where the distance was reduced to 10 m because the studied area is narrower in the proximity of the glacier. Soil profiles were hand-dug and two soil horizons sampled: A (surface mineral soil with humus enrichment), and C (weathered soil parent material). Soil samples were air-dried to constant weight and sieved to <2 mm to collect the fine earth. Aliquots of all samples were ground using a ball mill equipped with a zirconium oxide jar (PM 200, Retsch, Haan, Germany).

3.3. Chemical analyses

3.3.1. Sample preparation

Exchangeable cations in the A horizons were extracted with 1 M NH_4NO_3 at a 1:25 soil to solution ratio following the method described by Zeien and Brümmer (1989) and measured by atomic absorption spectroscopy (AAS). Five of these extracts were chosen for Mg isotope analysis corresponding to one of the three replicate soil samples collected at each ecosystem succession stage, from 37 to 127 years. Aliquots of the exchangeable cation extracts containing ~10 µg of Mg were dried down and treated with HCl-HNO_3 (3:1, v:v) at 120°C for 24 h in order to digest the high salt content of the matrix (1 M NH_4NO_3), before redissolution in 10 M HCl. Soil samples (70-100 mg) were digested with concentrated HF-HNO_3 (3:1) in Teflon Savillex screw-top beakers on a hot plate at 120°C for 72 h and dried down. The remaining residues were treated with concentrated HCl-HNO_3 (3:1) at 120°C for 24 h, evaporated to dryness, and redissolved in 1 M HNO_3.

To determine the Mg release kinetics, we conducted a weathering experiment using the resin-based pH_{stat} approach of Schwarz et al. (1999) including modifications of Alt et al. (2013), as described in Basdediós et al (2022b). Mg^{2+} was released from the fine earth into solution during H^+ buffering at constant pH and removed from the system using ion-exchange resins. The pH_{stat} extracts after 30 min, 48 h, and 168 h experimental duration of the three replicate soil samples collected at the 0 year and 127 year old sites were selected for Mg isotope analysis. Magnesium concentrations were determined by inductively coupled plasma atomic emission spectroscopy (ICP-OES, 5100 VDV, Agilent, Waldbronn, Germany). Mg recovery from the pH_{stat}-resin with standard solutions was 99 ± 1% (n = 3).

Sample preparation, purification and Mg isotope ratio analyses were performed in a clean-air laboratory to avoid sample contamination. We used distilled acids (DST-1000 Savillex ®) to remove any impurities. All labware used during sample treatment was previously acid-cleaned and rinsed with ultrapure water (>18.2 MΩ cm^{-1}).

Table D-1. Mean chemical and physical soil properties of the fine earth (< 2mm) along the Hailuogou chronosequence with standard error (SE) in parentheses if available (n=3)[a].

Site age (yr)	Elevation (m a.s.l.)	Soil horizon	Thickness (cm)	pH (H_2O)	CO_3^{2-} (mg g^{-1})	Bulk density (g cm^{-3})[c]	Organic C (g kg^{-1})	Total N (g kg^{-1})	Particle-size distribution (%)			Mg stock (g m^{-2})	δ^{26}Mg (‰)
									Clay (<2μm)	Silt (2-63μm)	Sand (63-2000 μm)		
0	2982	C1	0.5 (0.0)	8.0 (0.0)	19 ± 1	1.80	6.5 (1.2)	0.3 (0.1)	3.0	22.8	74.2	245 (7)	-0.34 (0.01)
		C2	9.5 (0.0)[b]	8.3 (0.0)	25 ± 1	1.80	3.9 (0.1)	0.1 (0.0)	3.2	21.6	75.2	4750 (113)	-0.35 (0.08)
		0-10 cm										*4990 (196)*	*-0.35 (0.08)*
37	2942	A	1 (0.0)	6.1 (0.1)	2 ± 1	0.96	16.9 (2.7)	1 (0.1)	2.1	18.9	79.1	301 (13)	-0.29 (0.06)
		C	9.3 (0.0)[b]	6.9 (0.1)	7 ± 3	1.37	7.8 (1.7)	0.5 (0.2)	1.6	12.8	85.5	3420 (68)	-0.33 (0.02)
		0-10 cm										*3720 (119)*	*-0.32 (0.02)*
47	2922	A	3.0 (0.6)	5.8 (0.2)	n.d.	0.35	14.1 (1.2)	1.2 (0.3)	3.6	18.5	77.9	326 (66)	-0.31 (0.04)
		C	9.3 (0.1)[b]	6.0 (0.1)	< 0.2	1.44	8.3 (0.7)	0.0 (0.0)	4.9	26.3	68.8	2930 (103)	-0.31 (0.05)
		0-10 cm										*3260 (212)*	*-0.30 (0.05)*
59	2912	A	3.7 (0.3)	5.9 (0.1)	n.d.	0.49	10.8 (2.8)	0.8 (0.2)	1.0	13.8	85.2	468 (37)	-0.31 (0.02)
		C	8.7 (0.1)[b]	6.3 (0.1)	< 0.2	1.43	3.8 (0.7)	0.0 (0.0)	3.4	29.6	67.1	2680 (151)	-0.35 (0.02)
		0-10 cm										*3140 (268)*	*-0.35 (0.02)*
87	2883	A	4.5 (0.8)	4.9 (0.1)	< 0.5	0.72	28.9 (10.4)	1.9 (0.7)	3.5	14.1	82.4	650 (87)	-0.28 (0.03)
		C	7.4 (0.4)[b]	5.6 (0.1)	0.6 (0.4)	1.27	16.2 (4.6)	0.7 (0.1)	2.5	13.0	84.5	1940 (63)	-0.34 (0.05)
		0-10 cm										*2590 (186)*	*-0.33 (0.04)*
127	2855	A	6.0 (0.0)	5.2 ± 0.2	0.2 (0.1)	0.61	47.7 (20.5)	3.4 (1.5)	4.3	18.6	77.1	778 (55)	-0.32 (0.01)
		C	7.2 (0.0)[b]	5.5 (0.1)	0.2 (0.1)	1.33	10.9 (1.3)	0.7 (0.1)	1.5	6.2	92.3	2050 (116)	-0.38 (0.03)
		0-10 cm										*2830 (223)*	*-0.36 (0.03)*

[a]The δ^{26}Mg values of the upper 10 cm have been calculated per soil profile using **Eq. D-5** and averaged per site age (n = 3). Calculated values are shown in italics. n.d = not detected. [b]Thickness of the C horizon used in this study. [c]Data from Zhou et al. (2016) and Wang et al. (2020).

3.3.2. Sample purification to remove potential interferences in the Mg isotope analysis

A fraction of each sample containing 10-15 µg of Mg was evaporated and redissolved in the acid needed for purification (i.e., 2 mL 1 M HNO_3 or 0.25 mL 10 M HCl). Separation of Mg from matrix elements was achieved by cation-exchange chromatography, using Bio-Rad AG50W-X8 resin, previously cleaned with 1 M HCl, 4 M HCl, 1 M HNO_3, and deionized water >18.2 MΩ cm^{-1} before filled into columns (10 mL Bio-Rad® polypropylene columns). The resins were not reused for different samples. We followed two different methods to purify the Mg fraction of the samples, depending on the sample matrix.

Resin extracts derived from the pH_{stat} experiment were purified according to the procedure described by Teng et al. (2007) in which we used slightly longer columns (filled with 1.2 mL of resin instead of 1 mL). The resin was further cleaned in the columns with 20 mL of 4 M HCl and 10 mL of deionized water before it was conditioned with 1 M HNO_3 prior to loading the sample. The Mg fraction and the potential interferences (e.g., Na, Ca or Ti), were eluted from the column with 1 M HNO_3. Sodium was eluted with the first 10 mL after loading the sample, Mg was collected in the next 16 mL, and Ca was last eluted (**Figure A-5**). The procedure was repeated 2-3 times for each sample to obtain a pure Mg solution (i.e., showing a ratio of the concentration of the interferences to that of Mg <0.05).

We tested the purification method of Teng et al. (2007) for our soil samples but found that part of the Ti was always eluted at the same time as Mg, which potentially creates an interference on the stable isotope ratio of Mg because the double charged ions of Ti ($^{48}Ti^{2+}$, $^{50}Ti^{2+}$) have the same mass/charge ratio as Mg isotopes. Therefore, soil samples and soil exchangeable fractions were purified following the two-step method described by Opfergelt et al. (2012), in which the first step removes most of the Fe and Ca using 10 M HCl as eluent and the second step separates Mg from the rest of the matrix with successively 0.4 M HCl, 0.15 M HF, 95% acetone/0.5 M HCl and 1 M HCl as eluents (**Figure A-6**).

Mg isotopes can be fractionated during ion-exchange reactions with heavy Mg isotopes eluted first from the column (Teng et al., 2007); therefore, it is essential to obtain a Mg yield of ~ 100%. Purified samples were only accepted if the Mg recovery was >95%. Elution pattern and Mg yields were determined by inductively coupled plasma mass spectrometry (ICP-MS, 7900 Agilent, Waldbronn, Germany). The ^{24}Mg signal of the

procedural blanks was < 0.5% of the total ^{24}Mg signal and was therefore considered negligible.

3.3.3. Isotope ratio analysis

Mg isotope signals (^{24}Mg, ^{25}Mg and ^{26}Mg) were measured simultaneously with a Thermo Scientific *Neptune plus* multicollector ICP-MS (MC-ICP-MS) on Faraday detectors using a 10^{11} Ohm Faraday cup current amplifier in five blocks of 30 cycles per block, with an integration time of 4 s per cycle. Since differences in the Mg concentrations between samples and standards can affect instrumental mass bias (Teng and Yang, 2014), all samples and standards were introduced into the plasma dissolved in 0.37 M HNO_3 at Mg concentrations of 500 ppb using the standard-sample bracketing technique. Magnesium isotope data are reported relative to DSM-3 (Galy et al., 2003, **Eq. D-1**):

$$\delta^{x}Mg = \{[^{x}Mg/^{24}Mg)_{sample} / (^{x}Mg/^{24}Mg)_{DSM3}] -1\} \times 10^{3} \quad (\mathbf{D\text{-}1})$$

where *x* is either mass 26 or 25.

We used an in-house $Mg(NO_3)_2$ standard for our bracketing. The composition of the in-house $Mg(NO_3)_2$ standard was determined relative to ERM-AE143 (Galy et al., 2003; Vogl et al., 2016) and normalized to the international DSM-3 Mg standard scale according to González de Vega et al. (2020). The long-term reproducibility of our Mg isotope ratio measurements was checked by performing repeated measurements of the in-house $Mg(NO_3)_2$ standard of the Observatoire Midi-Pyrenées/Laboratoire Geosciences Environnement Toulouse (GET), France. Our values of $\delta^{26}Mg = 0.28\pm0.13‰$ and $\delta^{25}Mg = 0.18\pm0.09‰$ matched those reported by Stamm et al. (2022) well ($\delta^{26}Mg = 0.32\pm0.14‰$ and $\delta^{25}Mg = 0.16\pm0.08‰$). Accuracy and precision of the whole procedure was assessed by digestion and purification of the certified reference material BCR-2 (Basalt Columbia River). The results obtained with our method were $\delta^{26}Mg = -0.25\pm0.12‰$ and $\delta^{25}Mg = -0.10\pm0.04‰$ (2SD, n=13), in close agreement with corresponding measurements reported by previous studies ($\delta^{26}Mg = -0.16‰$ to $-0.36‰$ and $\delta^{25}Mg = -0.18‰$ to $-0.08‰$; An et al., 2014, Teng et al., 2007).

3.4. Calculations and statistical analyses

A linear regression of the $\delta^{26}Mg$ on the $\delta^{25}Mg$ values resulted in a slope of 0.521 ± 0.016 (2SD, **Figure A-8**), in line with the theoretical kinetic slope of 0.511 and the theoretical equilibrium slope of 0.521 (Young and Galy, 2004) and similar to the slopes reported in previous studies on terrestrial samples (e.g., 0.509 ± 0.023, Brenot et al., 2008; 0.518 ± 0.038, Galy et al., 2001; 0.516 ± 0.006, Kimmig et al., 2018). Therefore, only the $\delta^{26}Mg$ value will be used further.

The release kinetics of Mg in soils was described as a two-step first-order reaction by Süsser (1987) and reported by Basdediós et al. (2021b) for the same samples as used here after applying **Eq. D-2**

$$Y(t) = \text{Pool A}\ (1-e^{-kat}) + \text{Pool B}\ (1-e^{-kbt}) \quad \textbf{(D-2)}$$

where $Y(t)$ represents the Mg release from soil (mg kg^{-1}) at time t, Pool A and Pool B are the estimates of the two differently reactive pools (slow/fast; mg kg^{-1}) and k_a and k_b are the corresponding rate constants (h^{-1}) of each pool, estimated by a nonlinear regression model using sequential quadratic optimization.

Since the slow-reacting Mg pool (Pool B) only started to release Mg after 4-12 h (Basdediós et al., 2022b), the $\delta^{26}Mg$ value of the fast-reacting Mg pool (Pool A) has been acquired from the pH_{stat} experiment by direct measurement of the resin extract after shaking for 30 min (n=3). The slow reacting Mg pool was calculated by applying a two-pool mixing model (**Eq. D-3**), after shaking for 48 h and 168 h (n=3), respectively. There were no significant differences between the two values for 48 and 168 h according to a t test for independent samples, so we only present the results of 168 h.

$$\delta^{26}Mg_{Pool\_B} = (\delta^{26}Mg_{Total} - (\delta^{26}Mg_{Pool\ A} * f_{Pool\_A})) / f_{Pool\_B} \quad \textbf{(D-3)}$$

where f represents the fractions (calculated in mg g^{-1}) of the involved pools A and B ($f_{Pool\_A} + f_{Pool\_B} = 1$). The use of $\delta^{26}Mg$ values in our mixing model instead of the $^{26}Mg/^{24}Mg$ isotope ratios seemed to be justified given the small variation of the Mg isotope ratios in our study.

Because we were unable to directly measure the $\delta^{26}Mg$ value of chlorite in our study soils, we estimated this value by assuming that the $\delta^{26}Mg$ values of our study soils are determined by the mixture of the only three Mg-bearing minerals that were detected by Zhou et al. (2016) in the parent material, i.e., biotite, hornblende, and chlorite (**Eq. D-4**).

The $\delta^{26}Mg$ value of chlorite has been estimated using **Eq. D-4**, where χ represents the contribution of the mineral *i*, i.e. biotite (Bio), hornblende (Hbl) or chlorite (Chl), to the total Mg-containing minerals concentration (Bio+Hbl+Chl). We used the maximum and minimum $\delta^{26}Mg$ values for coexisting biotite and hornblende in granitoids in the continental crust of central China published by Liu et al. (2010) as end-members of the mixing model.

$$\delta^{26}Mg_{Chl} = (\delta^{26}Mg_{Bulk\ soil} * \chi_{Bio+Hbl+Chl} - \delta^{26}Mg_{Bio} * \chi_{Bio} - \delta^{26}Mg_{Hbl} * \chi_{Hbl}) / \chi_{Chl} \quad \textbf{(D-4)}$$

A mixing model was applied to calculate the $\delta^{26}Mg$ of the upper 10 cm of the mineral soil ($\delta^{26}Mg_{10\text{-}cm}$), including the A and part of the C horizon (the A horizon was ≤ 6 cm thick along the chronosequence; **Table D-1**) at each site along the chronosequence (**Eq. D-5)**:

$$\delta^{26}Mg_{10\text{-}cm} = ((\delta^{26}Mg_{A} * \chi_{A}) + (\delta^{26}Mg_{C} * \chi_{C})) / \chi_{10\text{-}cm} \quad \textbf{(D-5)}$$

where $\delta^{26}Mg_A$ and $\delta^{26}Mg_C$ represent the Mg isotope compositions of the mineral A and C horizons, respectively, and χ_A and χ_C represent the contribution of each horizon to the total stock, in g m^{-2} ($\chi_{10\text{-}cm}$).

The annual Mg depletion rate (g m^{-2} yr^{-1}) was calculated as the difference in the total Mg stock (0−10 cm, g m^{-2}, **Table D-1**) between two consecutive sites, divided by the site age difference (yr).

The $\delta^{26}Mg$ values of the mineral A and C horizons at each study site were tested for significant differences using a paired sample *t* test. Independent pools (e.g., $\delta^{26}Mg$ of the mineral soil vs $\delta^{26}Mg$ of the exchangeable Mg fraction or pH_{stat} extracts) were tested for significant differences using a paired *t* test assuming equal variances. Statistical analyses were conducted with the statistical software R (R Core Team, 2019). Significance was set at $p < 0.05$.

4. Results

The $\delta^{26}Mg$ values of the bulk soils along the chronosequence varied from -0.34 to -0.28‰, and from -0.38 to -0.31‰ for the A and C horizons, respectively (**Figure D-1**). The C horizon was consistently enriched in the light Mg isotopes compared to the respective A horizon ($p < 0.05$) and the $\delta^{26}Mg$ values of the C horizons tended to decrease with site age ($r = 0.85$, $p = 0.07$; **Figure D-1**), while the $\delta^{26}Mg$ value of the A horizons

were not correlated with site age. The δ^{26}Mg values of the topsoil (0-10 cm) were significantly negatively correlated with the annual Mg depletion rates (r = 0.98, p < 0.001; **Figure D-2**).

The fast-reacting Mg pool at Site 1 (0 yr) as derived from our pH_{stat} experiment (δ^{26}Mg=-1.28±0.10 ‰, **Table D-2**) was significantly depleted in the heavy Mg isotopes compared to that at the 127 year-old site (-0.74±0.13 ‰, n=3, p<0.05). However, this was not the case for the slow-reacting Mg pool, which showed similar δ^{26}Mg values with on average -0.54±0.25 ‰ at both sites (**Figure D-3**). The fast-reacting Mg pool at Site 1 was significantly depleted in ^{26}Mg compared to the slow-reacting Mg pool (δ^{26}Mg=-0.64±0.11 ‰, **Table D-2**). There were no significant differences in the δ^{26}Mg values between the fast- and slow-reacting Mg pools at the 127 year site (**Figure D-3**). The size of the slow-reacting Mg pool was positively correlated with the biotite + hornblende to chlorite ratios (r=0.82, p<0.05), and the δ^{26}Mg values of the topsoil (0 - 10 cm) tended to decrease with decreasing size of the slow-reacting pool (**Figure D-4**).

The exchangeable Mg fraction showed δ^{26}Mg values of -0.86 ± 0.13 ‰ (n=5) and was considerably depleted in ^{26}Mg compared to the bulk soils (**Figure D-3**). The δ^{26}Mg values of the exchangeable Mg fraction correlated with the release rate constant of the slow-reacting pool, k_b (r=0.99, p<0.01; **Figure D-5**).

Table D-2. Size of the fast-reacting and exchangeable Mg pools, stock of the exchangeable Mg and respective δ^{26}Mg along the Hailuogou chronosequence. Data are shown as mean with standard error (SE) in parenthesis (n=3). δ^{26}Mg values of the exchangeable Mg are shown as mean with 2SE in parenthesis of measurements performed within the same analytical session.

Site age	Fast-reacting Mg pool (g kg^{-1})	Exchangeable Mg pool (g kg^{-1})	Stock exch. Mg, 0-10 cm (g m^{-2})	δ^{26}Mg exchangeable Mg (‰)	δ^{26}Mg fast reacting Mg pool (‰)	δ^{26}Mg slow reacting pool (‰)
0	0.09 (0.02)	0.04 (0.0)	0.7 (0.2)	n.a.	-1.28 (0.10)	-0.64 (0.11)
37	0.07 (0.01)	0.06 (0.02)	0.8 (0.2)	-0.87 (0.05)	n.a.	n.a.
47	0.09 (0.01)	0.09 (0.03)	0.7 (0.5)	-0.80 (0.05)	n.a.	n.a.
59	0.07 (0.01)	0.04 (0.01)	0.8 (0.2)	-0.88 (0.05)	n.a.	n.a.
87	0.09 (0.03)	0.12 (0.02)	1.6 (0.5)	-0.76 (0.07)	n.a.	n.a.
127	0.10 (0.03)	0.13 (0.02)	2.3 (0.5)	-1.00 (0.05)	-0.74 (0.13)	-0.44 (0.17)

n.a. = not available

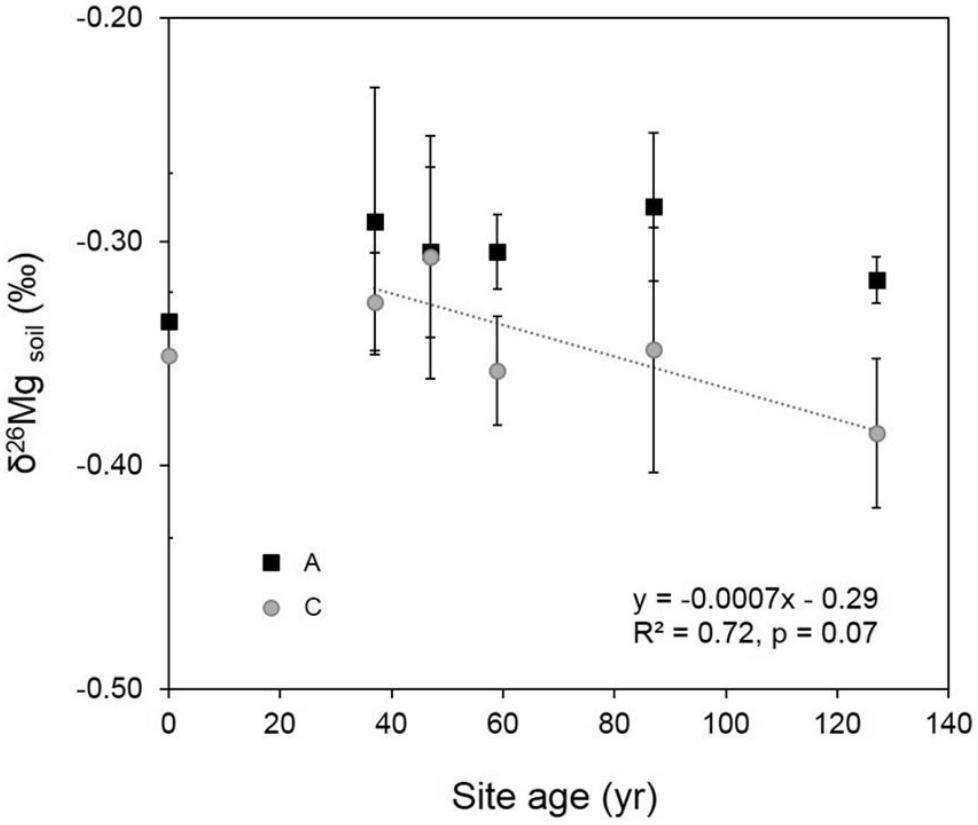

Figure D-1. Magnesium isotope compositions (δ^{26}Mg values) of bulk soils (<2 mm) of the mineral A (squares) and C (circles) horizons or C1 (square) and C2 (circle) horizons at Site 1 (0 yr) where no A horizon had developed along the Hailuogou retreat chronosequence. The dotted regression line represents a marginally significant correlation between the δ26Mg values of the mineral C horizon with increasing site age, excluding Site 1. Error bars represent standard errors (SE) of three replicate soil samples considered spatially independent.

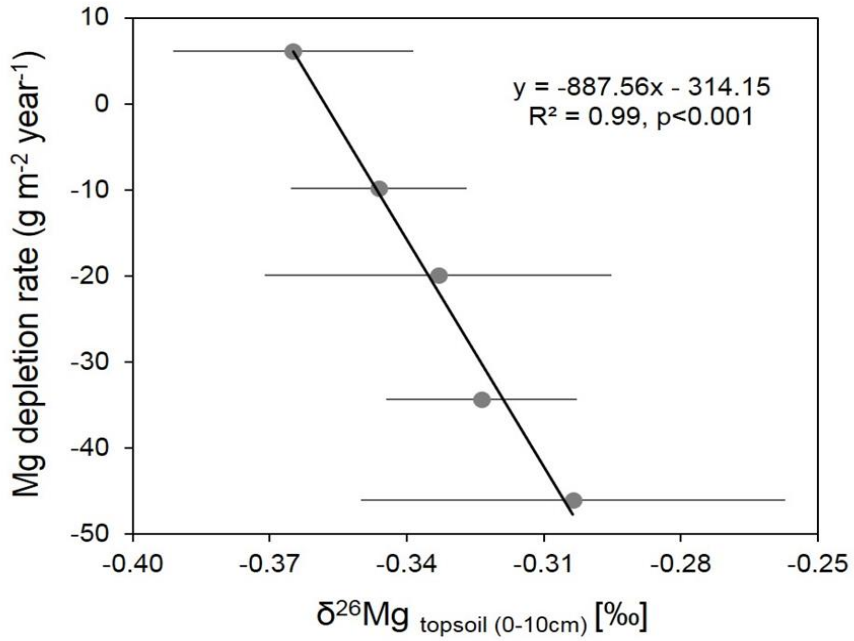

Figure D-2. Relationship between the Mg isotope composition (δ^{26}Mg values) of the upper 10 cm of the mineral soil and the Mg depletion rates of the entire ecosystem (to a soil depth of 10 cm) along the Hailuogou Chronosequence taken from Basdediós et al.2022a. Error bars represent standard errors (SE) of three spatial replicates and thus the spatial heterogeneity of the study soils.

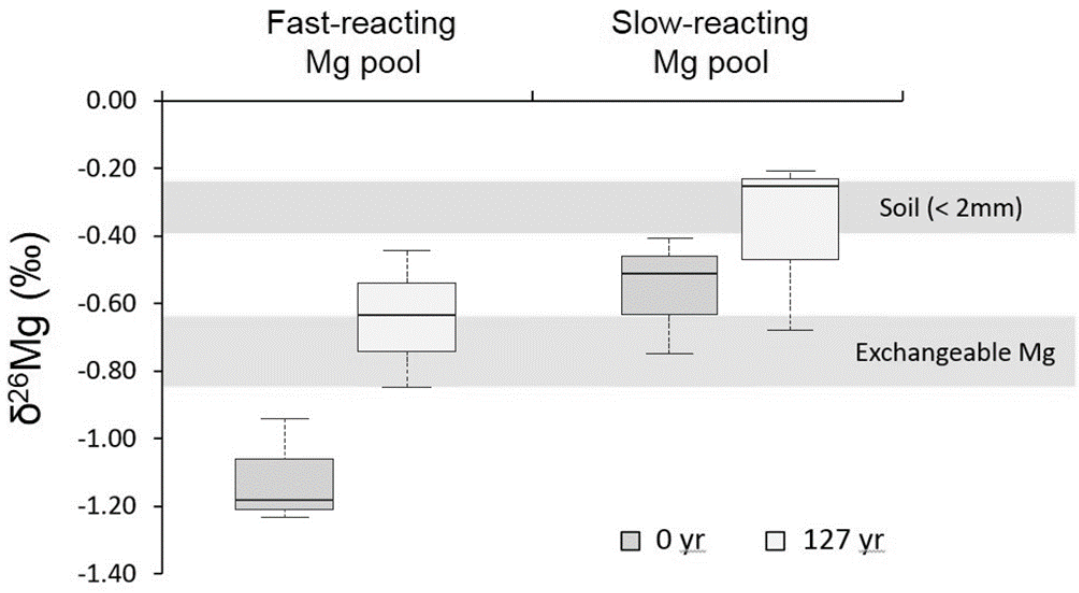

Figure D-3. Magnesium isotope compositions (δ^{26}Mg values) of bulk soils (<2 mm) and the exchangeable Mg fraction along the Hailuogou glacier retreat chronosequence, together with those of the fast- and slow-reacting Mg pools at the youngest (0 years, dark boxes) and oldest sites (127 years, light boxes). The boxes and whiskers show the medians, the 25th and 75th percentiles, and minima and maxima.

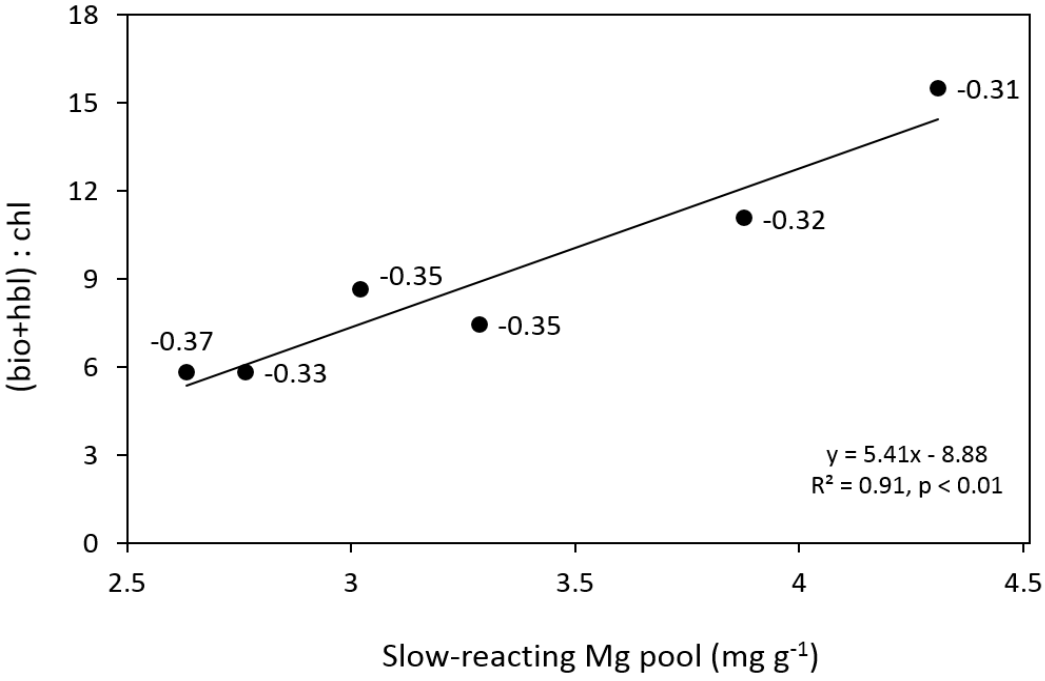

Figure D-4. Relationship between the size of the slow-reacting Mg pool along the Hailuogou chronosequence and the biotite (bio) + hornblende (hbl) to chlorite (chl) concentration ratios. Labels represent δ^{26}Mg values of the upper 10 cm of the mineral soil at each ecosystem site age calculated with **Eq. D-5**. Error bars represent standard errors (SE) of three spatial replicates and thus spatial heterogeneity.

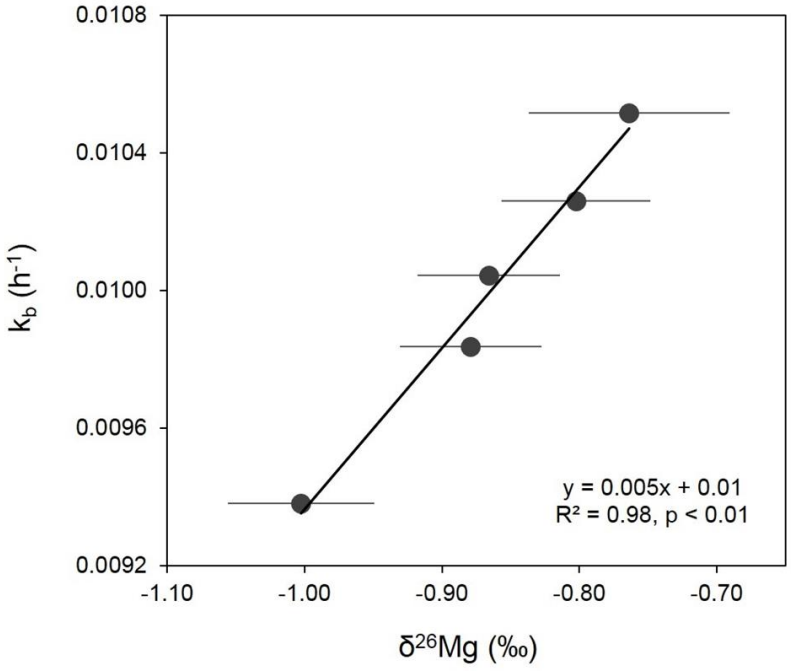

Figure D-5. Relationship between the Mg isotope compositions (δ^{26}Mg values) of the exchangeable Mg along the Hailuogou chronosequence and the release rate constants associated with the slow-reacting Mg pool, kb. Error bars represent two standard errors (2SE) of the same sample analyzed within the same analytical session as measure of the analytical precision.

5. Discussion

The δ^{26}Mg values of the fine earth (<2mm) in the mineral topsoils (0-10 cm) along the chronosequence averaged -0.34±0.02 ‰ (SE, n=6), which is Mg-isotopically lighter than the average value of the upper continental crust (-0.22‰, Li et al., 2010a), but similar to reported δ^{26}Mg values of biotite (-0.29±0.08 ‰) and hornblende (-0.32±0.09 ‰; Ryu et al., 2011), which are the main Mg-containing minerals in the topsoils of the Hailuogou glacial retreat area (13±2 % and 12±2 % of the total mineral composition, respectively) together with chlorite (3±1%; Zhou et al., 2016). Newly formed soils originating from granitic rocks have usually a similar isotopic composition as the parent material from which they evolve (Ryu et al., 2021). The parent rocks along the Hailuogou chronosequence originate from the eastern slope of the Gongga Mountain, a granitoid massif intruded into Triassic and Paleozoic metasedimentary and metavolcanic rocks (Searle et al., 2016). The Mg isotopic composition of granitic substrates located in the upper continental crust differ widely (i.e., from -0.40 to 0.44 ‰; Shen et al., 2009), with an average value of -0.21±0.07 ‰ in central China (Liu et al., 2010), and a range of -0.35 to -0.16 ‰ in eastern China (Li et al., 2010a). Thus, the δ^{26}Mg value of our study soils is close to the lower end of the reported range for China.

5.1. Relationship of the δ^{26}Mg values in bulk soils with soil age and Mg depletion

In spite of the increasing Mg depletion from the topsoil (0-10 cm) with soil age, the δ^{26}Mg values of the topsoils (**Table D-1**) were not related with site age. Thus, our first hypothesis could be falsified. Studies on basaltic soils along a Hawaiian chronosequence reported that the δ^{26}Mg values of the soils did not significantly differ from those of the parent material during the first 300 yr (Ryu et al., 2021), in line with our findings. However, older soils (≥ 20.000 yr) showed higher δ^{26}Mg values than the parent materials, which the authors attributed to secondary mineral formation favoring heavy isotopes. Comparable temporal trends have been reported for other metal isotope ratios in the same Hawaiian chronosequence: the δ^{7}Li and δ^{30}Si values of 300 year old soils were the same as in the fresh basalt, respectively, despite a Li loss of ~30% by weathering and subsequent leaching (Ryu et al., 2014; Ziegler et al., 2005). In soils of the ~150 year old Damma glacial retreat

area in Switzerland with granitic parent materials, the $\delta^{44/42}$Ca and δ^{56}Fe values were similarly unrelated with ecosystem age (Hindshaw et al., 2011; Kiczka et al., 2011).

However, we found a close and significant correlation between the Mg depletion rate quantified by Basdedios et al. (2022a) and the δ^{26}Mg values of the topsoils (0-10 cm, **Figure D-2**). The lack of a relationship between the δ^{26}Mg values of the soils and the soil age is probably explained by heterogeneities in the mineral composition of the parent substrate, which are better reflected by the Mg depletion rates than by soil age. The 37 and 47 year old sites had higher hornblende and slightly lower chlorite concentrations in the topsoils (0-10 cm; >15.6 and 2-3%, respectively) than the other sites (<12 and 3-4%; Zhou et al., 2016). Similar results were reported by Ryu et al. (2011), who simulated granite weathering in a laboratory experiment and concluded that the mineral-specific surface area and mineral concentration caused elemental release rates to vary, and that the different δ^{26}Mg values reflect a conservative mixing of Mg released from the different minerals. Our results suggest that the δ^{26}Mg value of bulk soils may serve as a proxy for natural ecosystem budgets of young ecosystems and thus may allow to determine change rates of element concentrations. However, our findings are based on a limited number of sites along a comparatively homogeneous chronosequence of young ecosystems. Therefore, future research should address the question whether these findings can be extrapolated to more diverse soils and longer time scales.

5.1.1. Role of Mg leaching

The finding that the C horizons had significantly lower δ^{26}Mg values than the corresponding A horizons according to the *t* test for paired samples could be explained by the increasing preferred transfer of ^{24}Mg from the A horizon to the upper C horizon by leaching (i.e., vertical transport), which supports our hypothesis. This is further corroborated by our finding that the δ^{26}Mg values of the fast-reacting pool, which can be assumed to primarily feed the leaching from the A to the C horizon, were considerably lower than those of the slow-reacting pool and the bulk soil, particularly at the youngest study site (**Figures D-1 and D-3**) in line with previous findings that weathering promotes the release of light Mg isotopes, leaving an isotopically heavy residue (e.g., Bolou-Bi et al., 2012; Schmitt et al., 2012; Tipper et al., 2006, 2012; Wimpenny et al., 2010, 2011).

The marginally significant decrease of the δ^{26}Mg values of the C horizons with increasing site age (**Figure D-1**) is surprising, since the opposite trend has usually been observed (Schmitt et al., 2012; Tipper et al., 2006, 2012; Wimpenny et al. 2010, 2011). However, our results are consistent with the finding of Ma et al. (2015), who reported an accumulation of light Mg isotopes during silicate dissolution (particulary of illite and chlorite) and reprecipitation as Mg-isotopically light vermiculite.The increasing accumulation of the light Mg isotopes in the C horizon with increasing site age might also be attributed to the preferential loss of isotopically heavy Mg in particles as suspended sediments during subsurface erosion, as occurred in the Shale Hills catchment in Pennsylvania (Ma et al., 2015). The gradual increase in the exchangeable Mg stocks (Basdediós et al., 2022a) might also contribute to decrease the δ^{26}Mg values of the C horizons as a consequence of the preferential retention of light Mg isotopes on the cation exchange sites (Opfergelt et al., 2012, 2014). However, the stock of exchangeable Mg ($< 2.3 \pm 0.5$ g Mg m^{-2}, Basdediós et al., 2022a) was small relative to the total Mg stock in the mineral topsoil (0-10 cm; $> 2830 \pm 223$ g Mg m^{-2}, **Table D-1**). The formation of pedogenic carbonates can also potentially decrease δ^{26}Mg values in bulk soils (Galy et al., 2002; Immenhauser et al., 2010; Wimpenny et al., 2014b) but this is probably not the case in our study area because of the low CO_3^{2-} concentrations in the >47 year-old soils (**Table D-1**).

Similarly, a substantial influence of preferential plant uptake of the heavy Mg isotopes (Black et al., 2008; Bolou-Bi et al., 2010, 2012) seems unlikely, because of the scarcity of roots in the C horizon. Moreover, Basdediós et al. (2022a) reported that the annual plant uptake of Mg was with $<4.8 \pm 1.5$ g m^{-2} yr^{-1} one order of magnitude lower than the Mg released by weathering in the mineral topsoil (0−10 cm; ~ 21 g m^{-2} yr^{-1}; Basdediós et al., 2022b), resulting in only a small effect of plant uptake on the δ^{26}Mg values in the topsoils (0−10 cm) and likely an even smaller one in the C horizons.

5.1.2. Role of chlorite dissolution

The different δ^{26}Mg values of the fast-reacting Mg pool in the youngest and the oldest soil (**Figure D-3**) indicated that the mineral sources of this pool changed with time along the chronosequence. Basdediós et al. (2022b) reported that the size of the fast-reacting Mg pool matched the size of the exchangeable Mg pool along the chronosequence, except in the

<37 year old soils, where the fast-reacting was larger than the exchangeable Mg pool. The much lower δ^{26}Mg value of the fast-reacting Mg pool at the youngest site (0 yr) than the mean δ^{26}Mg value of the exchangeable Mg pool along the chronosequence ($\Delta^{26}Mg_{PoolA-ExchMg}$ = 0.42; **Figure D-3**) suggested that the fast-reacting Mg pool was fed by a mineral with a particularly light Mg isotope composition. The fact that several authors reported low δ^{26}Mg values for chlorite in granitic environments (e.g., −0.78‰, Kimmig et al., 2018; and −1.82‰, Ryu et al., 2011) suggested that chlorite, that is present in the parent material of our study soils and the concentration of which decreased from 4% to 2% in less than 50 years (Zhou et al., 2016), could be this mineral. We assume that the high δ^{26}Mg value of 0.40 ‰ ± 0.22 in a highly weathered andesitic catchment in Puerto Rico reported by Chapela Lara et al. (2017) is specific for the volcanic setting of their study. Hornblende and biotite have a similar Mg isotope composition, although recent studies suggest that hornblendes might be slightly lighter than coexisting biotites in granitoid rocks ($\Delta^{26}Mg_{Hbl-Bt}$ = -0.06 ‰ ± 0.08, 2SD, Liu et al., 2010). For our mixing model, we used the maximum and minimum δ^{26}Mg values for coexisting biotite and hornblende in granitoids in the continental crust of central China published by Liu et al (2010) and solved **Eq. D-4** for the δ^{26}Mg value of chlorite in all soils along the Hailuogou chronosequence. This yielded a potential range of δ^{26}Mg values of -0.89 ‰ to -1.82 ‰ for chlorite at our study sites. Thus, the weathering of a reactive fraction of chlorite could indeed explain, why the size of the fast-reacting Mg pool in the young soils was larger than that of the exchangeable Mg supporting our hypothesis that chlorite was an important source of plant-available Mg released in the young soils of the studied glacial retreat chronosequence. A faster weathering rate of chlorite than of hornblende and biotite is in line with the literature (Malmström et al., 1996; Swoboda-Colberg & Drever 1993).

5.2. Relationship of the δ^{26}Mg values of the slow-reacting Mg pool with mineralogical composition and soil age

The δ^{26}Mg values of the slow-reacting Mg pool at the 0 and 127 year old sites did not significantly differ (**Figure D-3**), although there was a noticeable tendency towards higher δ^{26}Mg values that might become more pronounced in a longer term (i.e., > 127 years). The δ^{26}Mg values of the slow-reacting Mg pool were similar to those of the bulk soils

(**Figure D-3**), which further supports the finding of Basdediós et al. (2022b) that the slow-reacting Mg pool dominates the total Mg pool in the study soils.

The size of the slow-reacting Mg pool correlated significantly with the contribution of biotite+hornblende to chlorite concentration ratios (**Figure D-4**). This result further emphasizes that the mineral composition of soils is an important driver of their Mg isotope composition and of the Mg isotope fractionation during weathering. The finding that the δ^{26}Mg values of the exchangeable Mg pool correlated significantly with the release rate constant of the slow-reacting pool in the five oldest soils illustrated that the exchangeable Mg pool was mostly fed by the weathering of biotite+hornblende, once the reactive fraction of the chlorite had been dissolved. However, in our study soils the contribution of chlorite seems to be too low to significantly influence the δ^{26}Mg values of the slow-reacting pool so that our hypothesis ii is not fully supported. Despite this, the use of Mg isotope ratios helped us in constraining the roles of different Mg-bearing soil minerals in providing plant-available Mg during the early phase of soil development, which would not have been possible with elemental budgets alone.

6. Acknowledgments

We thank Z. Zhong, J. Wang, H. Bing, J. Zhou, and Q. He, as well as multiple students from the Chinese Academy of Science for their support in the field during the sampling campaign; L. Saller, T. Kunzmann and A. Ismagilov for their support during the Mg purification of the pH extracts; M. Kull for the supervision during the extraction of the exchangeable cations in the mineral topsoil and subsequent AAS measurement, and F. Stamm for her guidance in δ^{26}Mg measurements and for providing us with an aliquot of her in-house $Mg(NO_3)_2$ standard measured at the Observatoire Midi-Pyrenées/Laboratoire Geosciences Environnement Toulouse (GET), France. We are indebted to the German Research Foundation (DFG) for funding this study (Wi 1601/25-1).

7. References

Alt, F.; Oelmann, Y.; Schoning, I.; Wilcke, W. Phosphate release kinetics in calcareous grassland and forest soils in response to H+ addition. *Soil Sci. Soc. Am. J.* **2013**, 77, 2060–2070. https://doi.org/10.2136/sssaj2013.02.0072

An, Y.; Wu, F.; Xiang, Y.; Nan, X.; Yu, X.; Yang, J.; Yu, H.; Xie, L.; Huang, F. High-precision Mg isotope analyses of low-Mg rocks by MC-ICP-MS. *Chemical Geology* **2014**, 390, 9–21. https://doi.org/10.1016/j.chemgeo.2014.09.014

Basdediós, N.; Zhong, Z.; Wu, Y.; Wilcke, W. Initial carbonate weathering is linked with vegetation development along a 127-year glacial retreat chronosequence in the subtropical high mountainous Hailuogou region (SW China). *Plant and Soil* **2022a**, 471, 609–628. https://doi.org/10.1007/s11104-021-05250-y

Basdediós, N.; Wu, Y.; Wilcke, W. Base cations release in soils along the 127-year Hailuogou glacial retreat chronosequence. *Soil Sci. Soc. Am. J.* **2022b**, 86, 1692–1706. https://doi.org/10.1002/saj2.20473

Berner, R. A.; Lasaga, A. C.; Garrels, R. M. The carbonate-silicate geochemical cycle and its effect on atmospheric carbon-dioxide over the past 100 million years. *Am. J. Sci.* **1983**, 283, 641–683. https://doi.org/10.2475/ajs.283.7.641

Black, J.R.; Yin, Q.Z.; Casey, W.H. An experimental study of magnesium-isotope fraction in chlorophyll-a photosynthesis. *Geochim. Cosmochim. Acta* **2006**, 70, 4072-4079. https://doi.org/10.1016/j.gca.2006.06.010

Black, J.R.; Epstein, E.; Rains, W.D., Yin, Q.Z.; Casey, W.H. Magnesium-Isotope fractionation during plant growth. *Environmental Science and Technology* **2008**, 42 (21), 7831-7836. https://doi.org/10.1021/es8012722

Bolou-Bi, E. B.; Poszwa, A.; Leyval, C.; Vigier, N. Experimental determination of magnesium isotope fractionation during higher plant growth. *Geochim. Cosmochim. Acta* **2010**, 74(9), 2523-2537. https://doi.org/10.1016/j.gca.2010.02.010

Bolou-Bi, E. B.; Vigier, N.; Poszwa, A.; Boudot, J.P.; Dambrine, E. Effects of biogeochemical processes on magnesium isotope variations in a forested catchment in the Vosges Mountains (France). *Geochim. Cosmochim. Acta* **2012,** 87, 341–355. https://doi.org/10.1016/j.gca.2012.04.005

Brenot, A.; Cloquet, C.; Vigier, N.; Carignan, J.; France-Lanord C. Magnesium isotope systematics of the lithologically varied Moselle river basin, France. *Geochim. Cosmochim. Acta* **2008,** 72, 5070–5089. https://doi.org/10.1016/j.gca.2008.07.027

Cai, D.; Henehan, M. J.; Uhlig, D.; von Blanckenburg, F. Mg isotope composition of runoff is buffered by the regolith exchangeable pool. *Geochim. Cosmochim. Acta* **2022**, 321, 99−114. https://doi.org/10.1016/j.gca.2022.01.011

Chang, V. T. C.; Williams, R. J. P.; Makishima, A.; Belshawl, N. S.; O'Nions, R. K. Mg and Ca isotope fractionation during $CaCO_3$ biomineralisation. *Biochemical and biophysical research communications*, **2004**, *323*(1), 79-85. https://doi.org/10.1016/j.bbrc.2004.08.053

Chapela Lara, M.; Buss, H. L.; Pogge von Strandmann, P. A. E.; Schuessler, J.; Moore, O. W. The influence of critical zone processes on the Mg isotope budget in a tropical, highly weathered andesitic catchment. *Geochim. Cosmochim. Acta* **2017,** 202, 77–100. https://doi.org/10.1016/j.gca.2016.12.032

Court, M.; van der Heijden, G.; Louvat, P.; et al. Mg isotope composition in beech forest ecosystems and variations induced by liming: insights from four experimental sites in Northern France. *Biogeochemistry* **2021**, 153, 115−134. https://doi.org/10.1007/s10533-021-00766-y

Fahad, Z. A.; Bolou-Bi, E. B.; Köhler, S. J.; Finlay, R. D.; Mahmood, S. Fractionation and assimilation of Mg isotopes by fungi is species dependent. *Environ. Microbiol. Rep.* **2016**, 8, 956−965. https://doi.org/10.1111/1758-2229.12459

Galy, A.; Belshaw, N.S.; Halicz, L.; O'Nions R.K. High-precision measurement of magnesium isotopes by multiple-collector inductively coupled plasma mass spectrometry. *Int. J. Mass Spectrom.* **2001**, 208, 89-98. https://doi.org/10.1016/S1387-3806(01)00380-3

Galy, A.; Bar-Matthews, M.; Halicz, L.; O'Nions R.K. Mg isotopic composition of carbonate: insight from speleothem formation. *Earth and Planetary Science Letters* **2002**, 201(1):105-115. https://doi.org/10.1016/S0012-821X(02)00675-1

Galy, A.; Yoffe, O.; Janney, P.E.; Williams, R.W.; Cloquet, C.; Alard, O.; Halicz, L.; Wadhwa, M.; Hutcheon, I.D.; Ramon, E.; Carignan, J. Magnesium isotope

heterogeneity of the isotopic standard SRM980 and new reference materials for magnesium-isotope-ratio measurements. *J Anal At Spectrom* **2003**, 18:1352. https://doi.org/10.1039/b309273a

Gao, T.; Ke, S.; Wang, S. J.; Li, F. B.; Liu, C. S.; Lei, J.; Liao, C.; Wu, F. Contrasting Mg isotopic compositions between Fe-Mn nodules and surrounding soils: accumulation of light Mg isotopes by Mg-depleted clay minerals and Fe oxides. *Geochim. Cosmochim. Acta* **2018**, 237, 205–222. https://doi.org/10.1016/j.gca.2018.06.028

González de Vega, C.; Chernonozhkin, S.M.; Grigoryan, R.; Costas-Rodríguez, M.; Vanhaecke, F. Characterization of the new isotopic reference materials IRMM-524A and ERM-AE143 for Fe and Mg isotopic analysis of geological and biological samples. *J. Anal. At. Spectrom.* **2020,** 35:2517-2529. https://doi.org/10.1039/D0JA00225A

Hindshaw, R.S.; Reynolds, B.C.; Wiederhold, J.G.; Kretzschmar, R.; Bourdon, B. Calcium isotopes in a proglacial weathering environment: Damma glacier, Switzerland. *Geochim. Cosmochim. Acta* **2011**, 75, 106-118. https://doi.org/10.1016/j.gca.2010.09.038

Hindshaw, R.S.; Rickli, J.; Leuthold, J. Mg and Li stable isotope ratios of rocks, minerals, and water in an outlet glacier of the Greenland Ice Sheet. *Frontier in Earth Science* **2019,** 7: 316. https://doi.org/10.3389/feart.2019.00316

Hindshaw, R.S.; Tosca, R.; Tosca, N.J.; Tipper, E.T. Experimental constraints on Mg isotope fractionation during clay formation: Implications for the global biogeochemical cycle of Mg. *Earth Planet Sc. Lett.* **2020,** 531, 115980. https://doi.org/10.1016/j.epsl.2019.115980

Huang, K.J.; Teng, F.Z.; Wei, G.J.; Ma, J.L.; Bao, Z.Y. Adsorption- and desorption-controlled magnesium isotope fractionation during extreme weathering of basalt in Hainan Island, China. *Earth Planet. Sci. Lett.* **2012**, 359–360, 73–83. https://doi.org/10.1016/j.epsl.2012.10.007

Immenhauser, A.; Buhl, D.; Richter, D.; Niedermayr, A.; Riechelmann, D.; Dietzel, M.; Schulte, U. Magnesium-isotope fractionation during low-Mg calcite precipitation in a limestone cave - Field study and experiments. *Geochim. Cosmochim. Acta* **2010**, 74, 4346−4364. https://doi.org/10.1016/j.gca.2010.05.006

IUSS Working Group WRB. **2022**. World Reference Base for Soil Resources. International soil classification system for naming soils and creating legends for soil maps. 4th edition. International Union of Soil Sciences (IUSS), Vienna, Austria.

Kaupenjohann, M.; Wilcke W. Heavy metal release from a serpentine soil using a pH- stat technique. *Soil Sci. Soc. Am. J.* **1995**, 59, 1027-1031. https://doi.org/10.2136/sssaj1995.03615995005900040010x

Kiczka, M.; Wiederhold, J.G.; Frommer, J.; Voegelin, A.; Kraemer, S.M.; Bourdon, B.; Kretzschmar, R. Iron speciation and isotope fractionation during silicate weathering and soil formation in an alpine glacier forefield chronosequence. *Geochim. Cosmochim. Acta* **2011**, 75 (19), 5559-5573. https://doi.org/10.1016/j.gca.2011.07.008

Kimmig, S.R.; Holmden, C.; Bélanger, N. Biogeochemical cycling of Mg and its isotopes in a sugar maple forest in Québec. *Geochim. Cosmochim. Acta* **2018**, 230, 60-82. https://doi.org/10.1016/j.gca.2018.03.020

Lasaga, A.C. Chemical kinetics of water-rock interactions. *Journal of Geophysical Research: Solid Earth* **1984**, 89, B6 4009:4025. https://doi.org/10.1029/JB089iB06p04009

Lee, S.W.; Ryu, J.S.; Lee, K.S. Magnesium isotope geochemistry in the Han River, South Korea. *Chem. Geol.* **2014**, 364: 9–19. https://doi.org/10.1016/j.chemgeo.2013.11.022

Li, W.; Beard, B. L.; Li, C.; Johnson, C. M. Magnesium isotope fractionation between brucite [Mg $(OH)_2$] and Mg aqueous species: Implications for silicate weathering and biogeochemical processes. *Earth Planet. Sci. Lett.* **2014**, 394, 82−93. https://doi.org/10.1016/j.epsl.2014.03.022

Li, W.Y.; Teng, F.Z.; Ke, S.; Rudnick, R.L.; Gao, S.; Wu, F.Y.; Chappell, B.W. Heterogeneous magnesium isotopic composition of the upper continental crust. *Geochim. Cosmochim. Acta* **2010a,** 74: 6867–6884. https://doi.org/10.1016/j.gca.2010.08.030

Li, Z.; He, Y.; Yang, X.; Theakstone, W.H.; Jia, W.; Pu, T.; Liu, Q.; He, X.; Song, B.; Zhang, N.; Wang, S.; Du, J. Changes of the Hailuogou glacier, Mt. Gongga, China,

against the background of climate change during the Holocene. *Quat. Int.* **2010b,** 218:166–175. https://doi.org/10.1016/j.quaint.2008.09.005

Liu, S.A.; Teng, F.Z.; He, Y.; Ke, S.; Li, S. Investigation of magnesium isotope fractionation during granite differentiation: Implication for Mg isotopic composition of the continental crust. *Earth Planet. Sci. Lett.* **2010,** 297:646-654. https://doi.org/10.1016/j.epsl.2010.07.019

Ma, L.; Teng, F. Z.; Jin, L.; Ke, S.; Yang, W.; Gu, H.; Brantley, S. L. Magnesium isotope fractionation during shale weathering in the Shale Hills Critical Zone Observatory: Accumulation of light Mg isotopes in soils by clay mineral transformation. *Chem. Geol.* **2015**, 397, 37−50. https://doi.org/10.1016/j.chemgeo.2015.01.010

Malmström M.; Banwart, S.; Lewenhagen, J.; Duro., L. Bruno, J. The dissolution of biotite and chlorite at 25°C in the near-neutral pH region. *Journal of Contaminant Hydrology* **1996**, 21, 201-213. https://doi.org/10.1016/0169-7722(95)00047-X

Mavromatis, V.; Prokushkin, A. S.; Pokrovsky, O. S.; Viers, J.; Korets, M. A. Magnesium isotopes in permafrost-dominated Central Siberian larch forest watersheds. *Geochim. Cosmochim. Acta* **2014**, 147, 76−89. https://doi.org/10.1016/j.gca.2014.10.009

Novak, M.; Farkas, J.; Kram, P.; Hruska, J.; Stepanova, M.; Veselovsky, F.; Curik, J.; Andronikov, A. V.; Sebek, O.; Simecek, M.; Fottova, D.; Bohdalkova, L.; Prechova, E.; Koubova, M.; Vitkova, H. Controls on δ^{26}Mg variability in three Central European headwater catchments characterized by contrasting bedrock chemistry and contrasting inputs of atmospheric pollutants. *PLoS One* **2020**, 15, No. e0242915. https://doi.org/10.1371/journal.pone.0242915

Opfergelt, S.; Georg, R.B.; Delvaux, B.; Cabidoche, Y.M.; Burton, K.W.; Halliday, A.N. Mechanisms of magnesium isotope fractionation in volcanic soil weathering sequences, Guadeloupe. *Earth Planet. Sci. Lett.* **2012**, 341-344, 176-185. https://doi.org/10.1016/j.epsl.2012.06.010

Opfergelt, S.; Burton, K.W.; Georg, R.B.; West, A.J.; Guicharnaud, R.A.; Sigfusson, B.; Siebert, C.; Gislason, S.R.; Halliday, A.N. Magnesium retention on the soil exchange complex controlling Mg isotope variations in soils, soil solutions and vegetation in volcanic soils, Iceland. *Geochim. Cosmochim. Acta* **2014,** 125, 110:130. https://doi.org/10.1016/j.gca.2013.09.036

Pogge von Strandmann, P.A.; Burton, K.W.; James, R.H.; van Calsteren, P.; Gislason, S.R.; Sigfússon, B. The influence of weathering processes on riverine magnesium isotopes in a basaltic terrain. *Earth Planet. Sci. Lett.* **2008**, *276*(1-2), 187-197. https://doi.org/10.1016/j.epsl.2008.09.020

Pogge von Strandmann, P. A.; Opfergelt, S.; Lai, Y. J.; Sigfusson, B.; Gislason, S. R.; Burton, K. W. Lithium, magnesium and silicon isotope behavior accompanying weathering in a basaltic soil and pore water profile in Iceland. *Earth Planet. Sci. Lett.* **2012**, 339−340, 11−23. https://doi.org/10.1016/j.epsl.2012.05.035

Pokharel, R.; Gerrits, R.; Schuessler, J. A.; Floor, G. H.; Gorbushina, A. A.; von Blanckenburg, F. Mg isotope fractionation during uptake by a rock-inhabiting, model microcolonial fungus Knufia petricola at acidic and neutral pH. *Environ. Sci. Technol.* **2017**, 51, 9691−9699. https://doi.org/10.1021/acs.est.7b01798

R Core Team. **2019**. R: A language and environment for statistical computing. R Foundation for Statistical Computing. https://www.R-project.org

Richter, F.M.; Watson, E.B.; Mendybaev, R.A.; Teng, F.Z.; Janney, P.E. Magnesium isotope fractionation in silicate melts by chemical and thermal diffusion. *Geochim. Cosmochim. Acta* **2008**, *72*(1), 206-220. https://doi.org/10.1016/j.gca.2007.10.016

Rudnick, R.L.; Gao, S. The Composition of the Continental Crust. In: Holland, H.D. and Turekian, K.K., Eds., Treatise on Geochemistry, Vol. 3, The Crust, Elsevier-Pergamon, Oxford, **2003,** 1-64. http://dx.doi.org/10.1016/b0-08-043751-6/03016-4

Ryu, J.S.; Jacobson, A.D.; Holmden, C.; Lundstrom, C.; Zhang, Z. The major ion, δ 44/40 Ca, δ 44/42 Ca, and δ 26/24 Mg geochemistry of granite weathering at pH = 1 and T =25°C: power-law processes and the relative reactivity of minerals. *Geochim. Cosmochim. Acta* **2011,** 75(20), 6004–6026. https://doi.org/10.1016/j.gca.2011.07.025

Ryu, J.S.; Vigier, N.; Lee, S.W.; Lee, K.S.; Chadwick, O.A. Variation of lithium isotope geochemistry during basalt weathering and secondary mineral transformations in Hawaii. *Geochim. Cosmochim. Acta* **2014,** 145, 103–115. https://doi.org/10.1016/j.gca.2014.08.030

Ryu, J. S.; Vigier, N.; Derry, L.; Chadwick, O. A. Variations of Mg isotope geochemistry in soils over a Hawaiian 4 Myr chronosequence. *Geochim. Cosmochim. Acta* **2021**, 292, 94–114. https://doi.org/10.1016/j.gca.2020.09.024

Schmitt, A.D.; Vigier, N.; Lemarchand, D.; Millot, R.; Stille, P.; Chabaux, F. Processes controlling the stable isotope compositions of Li, B, Mg and Ca in plants, soils and waters: A review. *Comptes Rendus Geoscience* **2012**, 344(11-12),704-722. https://doi.org/10.1016/j.crte.2012.10.002

Schwarz, A.; Wilcke, W.; Styk, J.; Zech, W. Heavy metal release from soils in batch pH(stat) experiments. *Soil Sci. Soc. Am. J.* **1999**, 63, 290–296. https://doi.org/10.2136/sssaj1999.03615995006300020006x

Searle, M.P.; Roberts, N.M.W.; Chung, S.L.; Lee, Y.H.; Cook, K.L.; Elliott, J.R.; Weller, O.M.; St-Onge, M.R.; Xu, X.W.; Tan, X.B.; Li, K. Age and anatomy of the Gongga Shan batholith, eastern Tibetan Plateau, and its relationship to the active Xianshui-he fault. *Geosphere* **2016**, 12, 948–970. https://doi.org/10.1130/GES01244.1

Shen, B.; Jacobsen, B.; Lee, C.T.A.; Yin, Q.Z.; Morton, D.M. The Mg isotopic systematics of granitoids in continental arcs and implications for the role of chemical weathering in crust formation. *Proc. Natl. Acad. Sci.* **2009,** 106 (49), 20652–20657. https://doi.org/10.1073/pnas.091066310

Stamm, F.M.; Méheut, M.; Zambardi, T.; Chmeleff, J.; Schott, J.; Oelkers E.H. Determination of the equilibrium magnesium isotope fractionation factors between brucite and aqueous inorganic and organic species. *Geochim. Cosmochim. Acta* **2022,** 336, 33–49. https://doi.org/10.1016/j.gca.2022.09.003

Süsser, P. Art, Menge und Wirkungsweise von Puffersubstanzen in Mineralbodenhorizonten forstlich genutzter Böden des Fichtelgebirges. PhD Thesis, Technical University München-Weihenstephan, Germany, **1987.**

Swoboda-Colberg, N.G.; Drever, J.I. Mineral dissolution rates in plot-scale field and laboratory experiments, *Chem. Geol.* **1993,** 105 (1-3), 51–69. https://doi.org/10.1016/0009-2541(93)90118-3

Taylor, S.R.; McLennan, S.M. The Continental Crust: Its Composition and Evolution. Blackwell, Oxford **1985**, 1-312.

Teng, F.Z.; Wadhwa, M.; Helz, R.T. Investigation of magnesium isotope fractionation during basalt differentiation: implications for a chondritic composition of the terrestrial mantle. *Earth Planet. Sci. Lett.* **2007**, 261(1-2), 84-92. https://doi.org/10.1016/j.epsl.2007.06.004

Teng, F.Z.; Li, W.Y.; Rudnick, R.L.; Gardner, L.R. Contrasting lithium and magnesium isotope fractionation during continental weathering. *Earth Planet. Sci. Lett.* **2010**, 300 (1–2), 63-71. https://doi.org/10.1016/j.epsl.2010.09.036

Teng, F.Z.; Yang, W. Comparison of factors affecting the accuracy of high-precision magnesium isotope analysis by multi-collector inductively coupled plasma mass spectrometry. *Rapid Commun. Mass Spectrom.* **2014**, 28 (1), 19-24. https://doi.org/10.1002/rcm.6752

Tipper, E. T.; Galy, A.; Gaillardet, J.; Bickle, M. J.; Elderfield, H.; Carder, E. A. The magnesium isotope budget of the modern ocean: constraints from riverine magnesium isotope ratios. *Earth Planet. Sci. Lett.* **2006,** 250(1-2), 241-253. https://doi.org/10.1016/j.epsl.2006.07.037

Tipper, E.T.; Galy, A.; Bickle, M.J. Calcium and magnesium isotope systematics in rivers draining the Himalaya–Tibetan–Plateau region: lithological or fractionation control? *Geochim. Cosmochim. Acta* **2008,** 72, 1057–1075. https://doi.org/10.1016/j.gca.2007.11.029

Tipper, E.T.; Lemarchand, E.; Hindshaw, R.S.; Reynolds, B.C.; Bourdon, B. Seasonal sensitivity of weathering processes: Hints from magnesium isotopes in a glacial stream. *Chemical Geology* **2012**, 312–313, 80–92. https://doi.org/10.1016/j.chemgeo.2012.04.002

Uhlig, D.; Schuessler, J. A.; Bouchez, J.; Dixon, J. L.; von Blanckenburg, F. Quantifying nutrient uptake as driver of rock weathering in forest ecosystems by magnesium stable isotopes. *Biogeosciences* **2017**, 14 (12), 3111−3128. https://doi.org/10.5194/bg-14-3111-2017

Vogl, J., Brandt, B., Noordmann, J., Rienitz, O., Malinovskiy, D. Characterization of a series of absolute isotope reference materials for magnesium: ab initio calibration of the mass spectrometers, and determination of isotopic compositions and relative

atomic weights. *J. Anal. At. Spectrom.* **2016,** 31, 1440. https://doi.org/10.1039/c6ja00013d

Wang, J.; Wu, Y.; Zhou, J.; Bing, H.; Sun, H.; He, Q. Soil microbes become a major pool of biological phosphorus during the early stage of soil development with little evidence of competition for phosphorus with plants. *Plant and Soil* **2020**, 446:259–274. https://doi.org/10.1007/s11104-019-04329-x

Wang, S.J.; Teng, F.Z.; Bea, F. Magnesium isotopic systematics of metapelite in the deep crust and implications for granite petrogenesis. *Geochemical Perspectives Letters* **2015** v1, n1. https://doi.org/10.7185/geochemlet.1508

Wimpenny, J.; Gíslason, S.R.; James, R.H.; Gannoun, A.; Pogge Von Strandmann, P.A.E.; Burton, K.W. The behaviour of Li and Mg isotopes during primary phase dissolution and secondary mineral formation in basalt. *Geochim. Cosmochim. Acta* **2010,** 74, 5259–5279. https://doi.org/10.1016/j.gca.2010.06.028

Wimpenny, J.; Burton, K.W.; James, R.H.; Gannoun, A.; Mokadem, F.; Gíslason, S.R. The behaviour of magnesium and its isotopes during glacial weathering in an ancient shield terrain in West Greenland. *Earth Planet. Sci. Lett.* **2011**, 304, 260-269. https://doi.org/10.1016/j.epsl.2011.02.008

Wimpenny, J.; Colla, C. A.; Yin, Q. Z.; Rustad, J. R.; Casey, W.H. Investigating the behaviour of Mg isotopes during the formation of clay minerals. *Geochim. Cosmochim. Acta* **2014a**, 128, 178−194. https://doi.org/10.1016/j.gca.2013.12.012

Wimpenny, J.; Yin, Q.; Tollstrup, D.; Xie, L.; Sun, J. Using Mg isotope ratios to trace Cenozoic weathering changes: A case study from the Chinese Loess Plateau. *Chem. Geol.* **2014b**, 376, 31−43. https://doi.org/10.1016/j.chemgeo.2014.03.008

Young, E.; Galy, A. The isotope geochemistry and cosmochemistry of magnesium. *Rev. Mineral. Geochem. Miner. Soc. Am.* **2004,** 55, 197–230. https://doi.org/10.2138/gsrmg.55.1.197

Zeien, H.; Brümmer, G.W. Chemische Extraktion zur Bestimmung der Schwermetallbindungsformen in Böden. Mittlgn. Dtsch. Bodenkundl. Gesellsch. Sonderh. 59/I, Kongreßbd. Münster **1989**, 505–510

Zhou, J.; Wu, Y.H.; Prietzel, J.; Bing, H.; Yu, D.; Sun, S.; Luo, J.; Sun, H. Changes of soil phosphorus speciation along a 120-year soil chronosequence in the Hailuogou glacier retreat area (Gongga Mountain, SW China). *Geoderma* **2013**, 195–196:251–259. https://doi.org/10.1016/j.geoderma.2012.12.010

Zhou, J.; Bing, H.; Wu, Y.; Yang, Z.; Wang, J.; Sun, H.; Luo, J.; Liang, J. Rapid weathering processes of a 120-year-old chronosequence in the Hailuogou glacier foreland, Mt. Gongga, SW China. *Geoderma* **2016,** 267:78–91. https://doi.org/10.1016/j.geoderma.2015.12.024

Ziegler, K.; Chadwick, O.A.; Brzezinski, M.A.; Kelly, E.F. Natural variations of $\delta^{30}Si$ ratios during progressive basalt weathering, Hawaiian Islands. *Geochim. Cosmochim. Acta* **2005**, 69, 4597–4610. https://doi.org/10.1016/j.gca.2005.05.008

E. Appendix

The appendix is attached on an USB stick containing the following files:

01_ICP_Biomass.xlsx: Element concentrations (Ca, Mg, K, Na; in g kg^{-1}) of plant biomass, i.e., leaf, needle (1 and 3 years old), bark, branch, trunk and root, of the dominant tree species along the Hailuogou chronosequence, determined by ICP-OES after total digestion with concentrated HNO_3 and H_2O_2 in a microwave oven (**Section B**).

02_ICP_Soil.xlsx: Element concentrations (Ca, Mg, K, Na; in g kg^{-1}) of the five soil horizons sampled along the Hailuogou chronosequence: Oi (fresh litter), Oe (shredded litter), Oa (dark layer of decomposed humus), A (surface mineral soil with humus enrichment), and C (weathered soil parent material). Fine earth (<2 mm) and stones (soil > 2 mm) of the mineral horizons were analyzed separately. Concentrations were determined by ICP-OES after total digestion with concentrated HNO_3/HF/H_2O_2 in a microwave oven (**Section B**).

03_pHstat.xlsx: Ca, Mg, K and Na release over time during a pH_{stat} experiment at pH 3 in topsoils (0-10cm) from Site 1 (0 yr) to Site 7 (127 yr) of the Hailuogou chronosequence, expressed in mmol kg^{-1} (**Section C**).

04_pHstat_Ca.xlsx: Modelled sizes of the fast-reacting Ca pool (Pool A) and the slow-reacting Ca pool (Pool B) in mg kg^{-1} and release rate constant associated to each pool, (k_a and k_b, respectively: h^{-1}) in topsoils (0-10 cm) at each study site along the Hailuogou chronosequence. The coefficient of determination (R^2) describes the goodness of the fit between my data and the modelled function (**Section C**).

05_ pHstat_Mg.xlsx: Modelled sizes of the fast-reacting Mg pool (Pool A) and the slow-reacting Mg pool (Pool B) in mg kg^{-1} and release rate constants associated to each pool, (k_a and k_b, respectively: h^{-1}) in topsoils (0-10 cm) at each study site along the Hailuogou chronosequence. The coefficient of determination (R^2) describes the goodness of the fit between my data and the modelled function (**Section C**).

06_ pHstat_K.xlsx: Modelled sizes of the fast-reacting K pool (Pool A) and the slow-reacting K pool (Pool B) in mg kg^{-1} and release rate constants associated to each pool, (k_a and k_b, respectively: h^{-1}) in topsoils (0-10 cm) at each study site along the Hailuogou chronosequence. The coefficient of determination (R^2) describes the goodness of the fit between my data and the modelled function (**Section C**).

07_pHstat_Na.xlsx: Modelled sizes of the fast-reacting Na pool (Pool A) and the slow-reacting Na pool (Pool B) in mg kg^{-1} and release rate constant associated to each pool, (k_a and k_b, respectively: h^{-1}) in topsoils (0-10 cm) at each study site along the Hailuogou chronosequence. The coefficient of determination (R^2) describes the goodness of the fit between my data and the modelled function (**Section C**).

08_InHouseMgSTD.xlsx: Values of repeated measurements (n=45) of our bracketing in-house $Mg(NO_3)_2$ standard relative to ERM-AE143 over the course of this study (**Section D**).

09_Mg_Iso.xlsx: Measured Mg isotope ratios of mineral soil samples, exchangeable Mg fraction, extracts derived from the pH_{stat} experiment and standards (**Section D**).

10_Mg_Iso_org.xlsx: Measured Mg isotope ratios in biomass, i.e., leaf, needle (1 and 3 years old) and root, and organic horizons along the Hailuogou chronosequence, and standards (**Section D**).